Correlation functions in turbulence : numerical simulations and comparison with the functional renormalization group analysis

Anastasiia Gorbunova

Université Grenoble Alpes

THÈSE

Pour obtenir le grade de

DOCTEUR DE L'UNIVERSITÉ GRENOBLE ALPES

Spécialité : Physique Théorique

Arrêtée ministériel : 25 mai 2016

Présentée par

Anastasiia GORBUNOVA

Thèse dirigée par **Vincent ROSSETTO-GIACCHERINO,** Chargé de recherche, CNRS Délégation Alpes
et codirigée par **Guillaume BALARAC,** Professeur des Universités, Grenoble INP, Université Grenoble Alpes
et **Léonie CANET,** Professeure des Universités, Université Grenoble Alpes

préparée au sein du **Laboratoire de Physique et de Modélisation des Milieux Condensés**
et **Laboratoire des Écoulements Géophysiques et Industrielles**
dans **l'École Doctorale de Physique**

Fonctions de corrélation en turbulence

Simulations numériques et comparaison avec l'analyse par le groupe de renormalisation fonctionnel

Correlation functions in turbulence

Numerical simulations and comparison with the functional renormalization group analysis

Thèse soutenue publiquement le **19 Novembre 2021**,
devant le jury composé de :

Monsieur Emmanuel LÉVÊQUE
Directeur de recherche, CNRS Délégation Rhône-Auvergne, Rapporteur

Monsieur John Christos VASSILICOS
Directeur de recherche, CNRS Délégation Hauts-de-France, Rapporteur

Monsieur Achim WIRTH
Directeur de recherche, CNRS Délégation Alpes, Président

Monsieur Marc BRACHET
Directeur de recherche émérite, CNRS Délégation Paris-Centre, Examinateur

Monsieur Giorgio KRSTULOVIC
Chargé de recherche, CNRS Délégation Côte d'Azur, Examinateur

Abstract

The aim of this thesis is a comparison of the data from direct numerical simulations (DNS) of a three-dimensional homogeneous isotropic turbulent flow with recent analytical predictions obtained by means of the functional renormalization group (FRG) approach. The main results of the thesis concern the spatio-temporal correlation function of velocity, which is expected to decay as a Gaussian function of time at small time lags and as an exponential at large time lags. The numerical results show that the two-point correlation function of the Fourier modes of velocity indeed decays as a Gaussian in time at small time lags. The same behavior is observed for triple velocity correlations, which can be linked to the spectral energy transfer function. However, the behavior at large time delays is indiscernible due to the low-level magnitude of the correlation functions.

Another important result of the thesis concerns the spatio-temporal correlations in passive scalar turbulence. The simulations of a scalar in a Navier-Stokes velocity field demonstrate a Gaussian decay as well for the scalar correlation function at small time delays, similar to the velocity correlation. The influence of the velocity temporal correlations on the scalar is studied in simulations with synthetic velocity fields. In the case of a random white-in-time velocity (also known as Kraichnan's model), the scalar correlations demonstrate a purely exponential decay in time. Adding a finite correlation time to the synthetic velocity leads to the emergence of a portion of Gaussian decay at small time lags in the scalar correlation function, while it turns to the exponential at time delays larger than the typical velocity correlation time. These results reveal the crossover between the two temporal correlation regimes, as predicted by the FRG.

The last part of the thesis presents a preliminary study of the shell model of random passive scalar advection with the use of the FRG approach. The normal scaling of the second-order scalar structure is obtained, and the possible directions for studying the anomalous scaling are discussed.

Keywords: Fluid mechanics, Turbulence, Numerical simulations

Résumé

L'objectif de cette thèse est une comparaison des données de simulations numériques directes (DNS) d'un écoulement turbulent isotrope homogène en trois dimensions avec des prédictions analytiques récentes obtenues au moyen de l'approche du groupe de renormalisation fonctionnel (FRG). Les principaux résultats de la thèse concernent la fonction de corrélation spatio-temporelle de la vitesse, qui devrait décroître comme une fonction gaussienne du temps aux petits décalages et exponentiellement aux grands décalages temporels. Les résultats numériques montrent que la fonction de corrélation à deux points des modes de Fourier de vitesse décroît effectivement comme une gaussienne dans le temps aux petits décalages temporels. Le même comportement est observé pour les corrélations triples de la vitesse, qui peuvent être liées à la fonction de transfert d'énergie spectrale. Cependant, le comportement aux grands décalages temporels est indiscernable en raison des amplitudes faibles des fonctions de corrélation.

Un autre résultat important de la thèse concerne les corrélations spatio-temporelles dans la turbulence du scalaire passif. Les simulations d'une quantité scalaire dans un champ de vitesse gouverné pas l'équation de Navier-Stokes démontrent également une décroissance gaussienne pour la fonction de corrélation du scalaire à de petits décalages, similaire à la corrélation de vitesse. L'influence des corrélations temporelles de vitesse sur le scalaire est étudiée dans des simulations avec des champs de vitesse synthétiques. Dans le cas d'une vitesse aléatoire delta-corrélée en temps (également connue sous le nom de modèle de Kraichnan), les corrélations du scalaire démontrent une décroissance purement exponentielle dans le temps. L'ajout d'un temps de corrélation fini à la vitesse synthétique conduit à l'émergence d'une partie gaussienne à de petits décalages temporels dans la décroissance de la fonction de corrélation scalaire, tandis qu'elle devient exponentielle à des décalages temporels plus grands que le temps de corrélation de vitesse typique. Ces résultats révèlent la transition entre les deux régimes de corrélation temporelle, comme prédit par le FRG.

La dernière partie de la thèse présente une étude préliminaire du modèle en couches de l'advection aléatoire du scalaire passif avec l'utilisation de l'approche FRG. La loi d'échelle normale dans la fonction de structure de second ordre du scalaire est obtenue, et les directions possibles d'études des lois d'échelle anormales sont discutées.

Mots clés : Mécanique des fluides, Turbulence, Simulations numériques

Acknowledgments

First of all, I would like to express my gratitude to the members of the jury Achim Wirth, Marc Brachet, and Giorgio Krstulovic and to referees Emmanuel Lévêque and John Christos Vassilicos for participating in the jury and making valuable comments regarding the thesis.

This work would be impossible without my thesis supervisors Vincent Rossetto, Guillaume Balarac, and Léonie Canet, I am profoundly grateful to them. It was my good fortune to participate in this fruitful collaboration on such a challenging and exciting subject such as fundamental aspects of turbulence. Their involvement and enthusiasm are the main driving forces of this research, and it is a big pleasure for me to work with them.

I am thankful to Vincent for guiding me in this way and his encouragement. He always finds time to listen when I am blocked and helps to rethink the problem under a new angle and to find new ways to explore. I found also a lot of support from Guillaume, who is always ready to help out and finds time to go even into particular technical issues. A lot of things that in the beginning appear extremely complicated and almost impossible to implement become clear and feasible after a brief conversation with Guillaume. I would also like to thank sincerely Léonie for her support and motivation. Each conversation with her brings up a lot of clarifications and new interesting questions. I also appreciate a lot exciting journey into the world of theory of renormalization group, which actually appears to be not so frightening as it sounds with the help of such an excellent teacher.

I would like also to thank sincerely Christophe Baudet and Mathieu Gibert for following my work during these years and bringing new interesting ideas and questions. Many thanks also go to Gregory Eyink for the collaboration and thought-provoking discussions.

My sincere thanks to Carlo Pagani for his patience in explaining me the basics of the field theory and for his involvement. I have learned a lot and I feel really lucky to have the opportunity to work with him.

In addition, I would also like to express deep gratitude to all members of the lab LPMMC, especially to the directors, Anna Minguzzi and Serguey Skipetrov, for their welcome. It was an honor and pleasure for me to be part of the lab during these three years. Of course, the warmest greetings to all my colleagues, PhD students, and postdocs, and thanks for all their efforts to keep being a team even in complicated circumstances. This time for me was a lot of work, but also a lot of fun.

I would also like to express my gratitude to the members of LEGI and in particular to the directors, Achim Wirth and Joel Sommeria. Big thanks to my colleagues from the MOST team, especially to our team engineer, Patrick Begou, who rescued my computer many times and made my life and work on supercomputers extremely efficient and smooth.

I would also like to acknowledge the École doctorale de physique de Grenoble and Université Grenoble Alpes for giving the opportunity to work and study turbulence and providing a scholarship for my thesis.

Lastly but not last, I would like to thank warmly my family who have always been supporting me on distance from Russia, and of course my husband, Luis, who is taking all this path together with me.

Table of Contents

Introduction

Turbulence is a complex and ubiquitous phenomenon. One of its most stunning features is its universality. At first sight, fluid flows can be drastically different, varying from planetary storms and accretion of galaxies to a jet from the water tap, or a flow behind a fish - all share some common universal statistical properties at small scales. Universality is determined by the multiscale dynamics of turbulence in three dimensions: the eddies of various sizes form a hierarchy of scales, in which the energy cascades from the large scale, corresponding to the scale of energy injection, towards small scales, at which the viscous dissipation occurs. If these two typical length scales are strongly separated, there exists a range of intermediate scales, called the inertial range, over which the energy cascade develops. The viscous dissipation in the inertial range is negligible, and the large-scale flow imposed by the energy injection can be considered as slowly varying in space and time, so the statistical properties in the inertial range become independent on the details of the mechanisms of energy injection and dissipation, i.e. they become universal. By assuming a standard scale invariance in the inertial range, Kolmogorov in 1941 proposed a statistical description of turbulence, which is one of the most important milestones in turbulence research. In particular, it explains the emergence of power laws in the statistics of velocity increments, which were observed experimentally.

However, an analytical deduction of the observed power laws from first principles, which in the case of fluid flow is the Navier-Stokes equation, is still a challenge. Various analytical approaches describing the statistical properties of turbulence have been developed over the years (Frisch, 1995 ; Zhou, 2021). Significant advance in this direction has been achieved by applying the functional renormalization group (FRG) approach to the problem of turbulence. Historically, the renormalization group methods have been largely used in the study of critical phenomena. Turbulence shares some common features with critical phenomena such as universality and emergence of power laws. However, early attempts of application of perturbative RG methods to Navier-Stokes equations encountered obstacles related to the choice and limitation of a small parameter needed for a perturbative expansion. The functional reformulation of the RG method allows to avoid this problem as it enables a non-perturbative analysis. Another significant advantage of FRG is that it provides a statistical description of turbulent flows in terms of n-point space-time Eulerian correlation functions of the hydrodynamic fields.

Although understanding the spatio-temporal statistical properties of turbulence is essential in many problems in fluid mechanics, they are studied much less compared to the purely spatial properties. They are important, for instance, for developing closure schemes in statistical and numerical models of turbulence or for data analysis of experimentally measured turbulent signals. In addition, the knowledge of the space-time correlations is needed in any problem involving some multiscale dynamics in fluid flows, such as the propagation of waves in turbulent media or turbulent particle dispersion.

Another important tool in turbulence research are direct numerical simulations (DNS). The word "direct" here means that the simulation does not rely on any model parametrizing small-scale dynamics and is based purely on the Navier-Stokes equation solved over a large span of scales from the forcing scale to the viscous dissipation scale, which is necessary to obtain an accurate description of a turbulent flow. Its main limitations consist in its restriction to simple geometries and high computational costs. The maximal Reynolds number accessible in DNS is mainly limited by the computational resources. However, with

the recent development of high-performance computing facilities, it is already possible to reach Reynolds numbers comparable to the ones in laboratory experiments of the developed turbulent flow. The main advantage of DNS is that it allows to compute a large variety of statistical properties of a flow, such as spectra, velocity increments, correlation functions, probability distribution, and others.

The aim of the present thesis is to combine recent theoretical results obtained within the FRG framework with the numerical data collected from DNS, which is possible thanks to the computational power of supercomputers. The main results consist in the validation of the FRG results for the space-time correlation functions with the use of DNS and establishing the range of applicability of the theoretical results to numerical simulations.

Structure of the manuscript. This manuscript consists of five chapters. The chapter 1 presents a summary of previous works dedicated to the FRG analysis of the spatio-temporal correlation functions in turbulent flows. It contains a schematic description of the main steps of the derivation with a particular focus on the points that are essential for understanding the results and their numerical validation. At the end of the first chapter, an interpretation of the FRG results in terms of single-particle dispersion is proposed. The chapter 2 presents the pseudo-spectral DNS solver used in this study. In particular, the method implemented for the computation and averaging of space-time correlation functions is described.

The two following chapters contain the results of the numerical simulations representing the main contribution of this thesis. Chapter 3 concerns the two- and three-point space-time correlation functions of velocity, which are compared with the FRG prediction. In addition, the correlation function of the velocity moduli is studied, which is not covered by the theoretical predictions. The final section of the third chapter is dedicated to the numerical validation of the FRG result for the kinetic energy spectrum in the near-dissipative range, which is also estimated within the FRG framework.

The next chapter 4 extends the study of the Eulerian correlation function by adding to the simulated flow a passive scalar, whose dynamics is governed by the advection-diffusion equation. The space-time correlation functions of the passive scalar are measured in the velocity field governed by the Navier-Stokes equations, as well as in random synthetic velocity fields. The synthetic velocity field is implemented with an approximately white-in-time covariance, which enables comparison with the theoretical results for Kraichnan's model of random advection, and with a correlated-in-time covariance. These two types of synthetic flow allow to study the influence of the velocity temporal covariance on the behavior of the scalar space-time correlation functions.

The following chapter 5 contains a preliminary analytical FRG study of the shell model of random passive advection. It gives a more detailed description of the steps of the FRG derivation, which is considerably simpler in the case of this shell model compared to the Navier-Stokes equation, and allows to access the scalar structure functions. Finally, the main text of the manuscript ends with general conclusions and perspectives.

Part of the results presented in this thesis have been published in the following articles:

— Gorbunova, A., G. Balarac, M. Bourgoin, L. Canet, N. Mordant, and V. Rossetto (2020). "Analysis of the Dissipative Range of the Energy Spectrum in Grid Turbulence and in Direct Numerical Simulations". In: *Physical Review Fluids* 5.4, 044604.

— Gorbunova, A., G. Balarac, L. Canet, G. Eyink, and V. Rossetto (2021a). "Spatio-Temporal Correlations in Three-Dimensional Homogeneous and Isotropic Turbulence". In: *Physics of Fluids* 33.4, 045114.

— Gorbunova, A., C. Pagani, G. Balarac, L. Canet, and V. Rossetto (2021b). "Eulerian spatiotemporal correlations in passive scalar turbulence". In: *Physical Review Fluids*, 6(12), 124606.

Introduction (Version française)

La turbulence est un phénomène complexe et omniprésent. L'une de ses caractéristiques les plus étonnantes est son universalité. À première vue, les écoulements de fluides peuvent être radicalement différents, allant des tourbillons planétaires et de l'accrétion de galaxies à un jet du robinet d'eau, ou un sillage derrière un poisson; cependant, tous partagent des propriétés statistiques universelles communes à petite échelle. L'universalité est déterminée par la dynamique multi-échelle de la turbulence en trois dimensions : les tourbillons de différentes tailles forment une hiérarchie, dans laquelle l'énergie cascade de la grande échelle, correspondant à l'injection d'énergie, vers les petites échelles, auxquelles la dissipation visqueuse se produit. Si ces deux échelles caractéristiques sont fortement séparées, il existe une zone d'échelles intermédiaires, appelée zone inertielle, sur laquelle se développe la cascade énergétique. La dissipation visqueuse dans la zone inertielle est négligeable, et l'écoulement à grande échelle imposé par l'injection d'énergie peut être considéré comme variant lentement dans l'espace et le temps, de sorte que les propriétés statistiques dans la zone inertielle deviennent indépendantes des détails des mécanismes de l'injection et dissipation de l'énergie, c'est-à-dire qu'elles deviennent universelles. En supposant une invariance d'échelle standard dans la zone inertielle, Kolmogorov a proposé en 1941 une description statistique de la turbulence, qui est l'un des jalons les plus importants de la recherche sur la turbulence. Cette description explique notamment l'émergence de lois de puissance dans les statistiques des incréments de vitesse, qui ont été observées expérimentalement.

Cependant, une déduction analytique des lois de puissance observées à partir des premiers principes, qui dans le cas de l'écoulement fluide sont les équations de Navier-Stokes, est toujours un défi. Diverses approches analytiques décrivant les propriétés statistiques de la turbulence ont été développées au cours des années (Frisch, 1995 ; Zhou, 2021). Des progrès significatifs dans cette direction ont été réalisés à l'aide de l'approche du groupe de renormalisation fonctionnelle (FRG). Historiquement, les méthodes du groupes de renormalisation ont été largement utilisées dans l'étude des phénomènes critiques. La turbulence partage certaines caractéristiques communes avec des phénomènes critiques telles que l'universalité et l'émergence de lois de puissance. Cependant, les premières tentatives d'application des méthodes RG perturbatives aux équations de Navier-Stokes ont rencontré des obstacles liés au choix et à la limitation d'un petit paramètre nécessaire pour une expansion perturbative. La reformulation fonctionnelle de la méthode RG permet d'éviter ce problème car elle permet une analyse non perturbative. Un autre avantage significatif du FRG est le fait qu'il fournit une description statistique des écoulements turbulents en termes de fonctions de corrélation eulériennes spatio-temporelles de n-points des champs hydrodynamiques.

Bien que la compréhension des propriétés statistiques spatio-temporelles de la turbulence soit essentielle dans de nombreux problèmes de mécanique des fluides, elles sont beaucoup moins étudiées que les propriétés purement spatiales. Or, elles sont importantes, par exemple, pour développer des schémas de fermeture dans des modèles statistiques et numériques de turbulence ou pour l'analyse de données de signaux turbulents mesurés expérimentalement. De plus, la connaissance des corrélations spatio-temporelles est nécessaire dans tout problème impliquant des dynamiques multi-échelles dans les écoulements fluides, comme la propagation d'ondes dans des milieux turbulents ou la dispersion turbulente de particules.

Un autre outil important dans la recherche sur la turbulence sont les simulations numériques directes (DNS). Le mot "direct" signifie ici que la simulation ne repose sur aucun modèle paramétrant la dynamique à petite échelle et est basée uniquement sur l'équation de Navier-Stokes résolue sur une large gamme d'échelles allant de l'échelle de forçage à l'échelle de dissipation visqueuse, qui est nécessaire pour obtenir une description précise

d'un écoulement turbulent. Ses principales limites consistent en sa restriction à des géométries simples et des coûts de calcul élevés. Le nombre de Reynolds maximal accessible par les simulations DNS est surtout limité par les ressources de calcul. Cependant, avec le développement récent d'installations de calcul à haute performance, il est déjà possible d'atteindre des nombres de Reynolds comparables à ceux des expériences de laboratoire de l'écoulement turbulent développé. Le principal avantage des simulations DNS est qu'elles permettent de calculer une grande variété de propriétés statistiques d'un écoulement, par exemple, les spectres, les incréments de vitesse, les fonctions de corrélation, la distribution de probabilité, etc.

L'objectif de cette thèse est de combiner des résultats théoriques récents obtenus dans le cadre de FRG avec les données numériques issues des DNS, ce qui est possible grâce à la puissance des supercalculateurs. Les principaux résultats consistent en la validation des résultats du FRG pour les fonctions de corrélation spatio-temporelles avec l'utilisation des simulations DNS et en l'établissement de la plage d'applicabilité des résultats théoriques aux simulations numériques. Les corrélations spatio-temporelles du scalaire passif sont également calculées dans le cas de la vitesse régie par les équations de Navier-Stokes, ainsi que dans les champs de vitesse synthétiques avec des statistiques prescrites, pour analyser l'influence de la covariance temporelle de vitesse sur les corrélations du scalaire.

Structure du manuscrit. Ce manuscrit est composé de cinq chapitres. Le chapitre 1 présente une synthèse des travaux antérieurs consacrés à l'analyse FRG des fonctions de corrélation spatio-temporelles dans les écoulements turbulents. Il contient une description schématique des principales étapes de la dérivation avec un accent particulier sur les points essentiels à la compréhension des résultats et à leur validation numérique. À la fin du premier chapitre, une interprétation mécanique des résultats du FRG en termes de dispersion des particules est proposée. Le chapitre 2 présente le solveur DNS pseudo-spectral utilisé dans cette étude. En particulier, la méthode mise en œuvre pour le calcul et le moyennage des fonctions de corrélation espace-temps est décrite.

Les deux chapitres suivants contiennent les résultats des simulations numériques représentant la principale contribution de cette thèse. Le chapitre 3 concerne les fonctions de corrélation spatio-temporelles de la vitesse à deux et trois points, qui sont comparées à la prédiction FRG. De plus, la fonction de corrélation des modules de vitesse est étudiée, ce qui n'est pas couvert par les prédictions théoriques. La dernière section du troisième chapitre est consacrée à la validation numérique du résultat FRG pour le spectre d'énergie cinétique dans le domaine dissipatif-proche, qui est également estimé dans le cadre FRG.

Le chapitre 4, étend l'étude de la fonction de corrélation eulérienne en ajoutant à l'écoulement simulé un scalaire passif, dont la dynamique est régie par l'équation d'advection-diffusion. Les fonctions de corrélation spatio-temporelle du scalaire passif sont mesurées dans le champ de vitesse régi par les équations de Navier-Stokes, ainsi que dans des champs de vitesse synthétiques aléatoires. Le champ de vitesse synthétique est implémenté avec une covariance approximativement bruit-blanc dans le temps, ce qui permet une comparaison avec les résultats théoriques du modèle d'advection aléatoire de Kraichnan, ainsi qu'avec une corrélation temporelle. Ces deux types d'écoulement synthétique permettent d'étudier l'influence de la covariance temporelle de la vitesse sur le comportement des fonctions de corrélation spatio-temporelles du scalaire.

Le chapitre 5, contient une étude analytique FRG préliminaire du modèle en couches d'advection passive aléatoire. Il donne une description plus détaillée des étapes de la dérivation FRG, qui est considérablement plus simple dans le cas de ce modèle en couches par rapport à l'équation de Navier-Stokes, et permet d'accéder aux fonctions de structure scalaire. Enfin, le texte principal du manuscrit se termine par des conclusions générales et des perspectives.

1 Theoretical framework

The present chapter introduces the theoretical framework of the functional renormalization group (FRG), which is used to obtain the analytical results tested numerically in this thesis. A brief description of the FRG method in application to Navier-Stokes and advection-diffusion equations is provided, with highlights on principal results concerning the Eulerian space-time correlation functions.

Contents

Abstract

This chapter provides a brief summary of the previous works dedicated to the statistical analysis of turbulence within the functional renormalization group (FRG) framework (Canet et al., 2016 ; Tarpin et al., 2018 ; Pagani and Canet, 2021). Its aim is to present the motivation behind the application of FRG to turbulence, its main ideas, and the principal points of the analytical derivation, which are essential for understanding the resulting expressions for the space-time correlation functions and their numerical validation. For this reason, a particular focus of this chapter is on the expressions resulting from FRG and enabling numerical tests, as well as on the range of validity of these expressions and their fluid-mechanical interpretation. This chapter does not contain any new results, but defines the theoretical framework and the motivation for the numerical study provided in the following chapters.

Résumé en français

Ce chapitre fournit un bref résumé des travaux précédents consacrés à l'analyse statistique de la turbulence dans le cadre de l'approche du groupe de renormalisation fonctionnelle (FRG) (Canet et al., 2016 ; Tarpin et al., 2018 ; Pagani and Canet, 2021). Son objectif est de présenter la motivation derrière l'application du FRG à la turbulence, ses idées générales, et les principaux points de la dérivation analytique, qui sont essentiels pour comprendre les résultats obtenus pour les fonctions de corrélation spatio-temporelle et leur validation numérique. Pour cette raison, un accent particulier de ce chapitre est fait sur les expressions résultant du FRG et permettant des tests numériques, ainsi que sur le domaine de validité de ces expressions et leur interprétation mécanique. Ce chapitre ne contient pas de résultats nouveaux, mais définit le cadre théorique et la motivation de l'étude numérique qui sera fournie dans les chapitres suivants.

1.1 Background

Renormalization group (RG). The renormalization group (RG) is a framework largely used in different branches of physics to study the dynamics of strongly correlated systems with many degrees of freedom. In the seminal work of Wilson and Kogut, 1974 a modern formulation of RG has been proposed. The core idea of RG is the progressive integration of small-scale fluctuations to obtain an effective description at large scales. It is a sequence of scale-dependent effective models from micro- to macro-scales, as the fluctuations are being averaged out. This sequence is called RG flow. The RG framework is used in high-energy physics, quantum many-body systems, and statistical physics. In particular, it appears to be a very powerful tool for the analysis of critical phenomena such as phase transitions, for which it explains the universality and allows to compute critical exponents.

Turbulence and RG. Hydrodynamic turbulence shares some particular features with critical phenomena, such as strong interscale correlations and non-Gaussian fluctuations. Other remarkable properties of turbulent flows are universality and power laws in the inertial range, which are the indications of the scale invariance. The hypothesis of scale invariance is the core assumption in statistical models of turbulence, the most celebrated of which is the theory of Kolmogorov, 1941.

This similitude between turbulence and critical phenomena thus calls for a theoretical

study of turbulence within the RG framework. The first works dedicated to the application of RG to turbulence date back to the eighties (DeDominicis and Martin, 1979 ; Fournier and Frisch, 1983 ; Yakhot and Orszag, 1986). However, the first applications of RG are based on perturbative approaches, which require establishing a small parameter for perturbative expansion. Finding a suitable small parameter in turbulence is a nontrivial task. In addition, the condition of the smallness of a parameter puts important limitations on the applicability and interpretation of the results (Eyink, 1994). The advances and obstacles in the application of perturbative RG in fluid mechanics are summarized in the reviews (Smith and Woodruff, 1998 ; Adzhemyan and Antonov, 1998 ; Zhou, 2010).

Functional renormalization group (FRG). The functional renormalization group (FRG) follows the approach of the Wilsonian RG of progressively averaging fluctuations and proposes a reformulation in terms of functionals of the fields. It provides a method of derivation of a flow equation for a scale-dependent "effective action" functional. The "effective action" functional can be interpreted as a coarse-grained free energy of the fluctuations at scales smaller than the renormalization scale. The functional formulation enables the construction of non-perturbative approximations, for this reason in the literature this framework is also referred to as "non-perturbative RG". The FRG has turned out to be a powerful tool to compute the properties of strongly correlated systems in a wide range of applications from high-energy physics, condensed matter, quantum gravity, and statistical physics (Dupuis et al., 2021).

Turbulence and FRG. The opportunity to develop non-perturbative approximations makes the FRG a promising analytical approach for the statistical description of turbulence. The FRG approach has been applied to the Navier-Stokes equation (Tomassini, 1997 ; Mejía-Monasterio and Muratore-Ginanneschi, 2012 ; Canet et al., 2015 ; Tarpin et al., 2018), as well as to the passive scalar advection-diffusion problem (Pagani, 2015 ; Pagani and Canet, 2021).

One of the most substantial novelties of the FRG results is that it provides access to generic n-point space-time correlation functions. Another important feature of the FRG approach is that it is based purely on the Navier-Stokes equation. It does not require any strong phenomenological hypothesis and the approximations in the derivation are well controlled. The FRG provides exact results for the time dependence of multipoint space-time Eulerian correlation functions in the limit of large wavenumbers for the cases of 3D (Tarpin et al., 2018) and 2D (Tarpin et al., 2019) stationary homogeneous isotropic turbulence governed by the Navier-Stokes equations.

Results of FRG. The derivation of exact results in the limit of large wavenumbers appeared to be possible through the exploitation of the extended symmetries of the field theory associated with Navier-Stokes equation (Canet et al., 2015 ; Canet et al., 2016). The resulting Eulerian correlation functions of the velocity field (Canet et al., 2017 ; Tarpin et al., 2018 ; Tarpin, 2018) can be compared with the already known results in turbulence as well as with new numerical and experimental data. In particular, Kolmogorov 5/3 law for the inertial range of the spectrum of the kinetic energy is obtained as the leading-order behavior. In addition, FRG demonstrates clearly that the leading behavior of the space-time correlation functions of velocity is determined by the sweeping effect, which is consistent with the available experimental and numerical results, but was not captured by the perturbative RG models. The new results concern, in particular, the extension of the dominance of the sweeping effect to n-point correlation functions and the prediction of a large-time-lag regime in the space-time correlation functions.

Structure of the chapter. This chapter serves to introduce the principal features and steps of the FRG analysis, but is mainly focused on the presentation of the main results obtained in previous works (Canet et al., 2016; Tarpin et al., 2018; Pagani and Canet, 2021) for the space-time correlation functions, as these results are tested numerically in the present thesis. First, the FRG in application to the Navier-Stokes equations is discussed, and the analytical results for the two- and three-point correlation function of velocity are presented. Next, in section 1.3, a brief description of the results of FRG analysis of passive scalar turbulence is presented. Two cases of dynamics of the passive scalar are discussed: advected by a random Gaussian velocity field and by a turbulent velocity field governed by the Navier-Stokes equations. The following section 1.4 proposes a physical interpretation of the FRG results through the problem of single-particle dispersion. The chapter is concluded by a general summary of the theoretical results.

1.2 Functional renormalization group approach in application to Navier-Stokes equations

1.2.1 Field theory for Navier-Stokes equation

The starting point of the FRG analysis are the 3D incompressible Navier-Stokes equations with external forcing, which in FRG terms correspond to the "microscopic theory":

$$\frac{\partial \vec{\mathbf{v}}(\vec{\mathbf{x}},t)}{\partial t} + [\vec{\mathbf{v}}(\vec{\mathbf{x}},t)\cdot\boldsymbol{\nabla}]\vec{\mathbf{v}}(\vec{\mathbf{x}},t) = -\boldsymbol{\nabla}p(\vec{\mathbf{x}},t) + \nu\nabla^2\vec{\mathbf{v}}(\vec{\mathbf{x}},t) + \vec{\mathbf{f}}(\vec{\mathbf{x}},t), \tag{1.1}$$

$$\boldsymbol{\nabla}\cdot\vec{\mathbf{v}}(\vec{\mathbf{x}},t) = 0, \tag{1.2}$$

where $\vec{\mathbf{v}}$ is the velocity vector, p - pressure, $\vec{\mathbf{f}}$ - external forcing, ν is the kinematic viscosity of the fluid.

The external forcing drives the fluid flow into a stationary state. To study the universal properties of the flow, which do not depend on the details of the forcing mechanism, the forcing is considered stochastic, and the flow is studied in terms of averages over the ensemble of forcing realizations. This random forcing is chosen to have a Gaussian distribution with zero mean and covariance:

$$\left\langle f_i(\vec{\mathbf{x}},t) f_j(\vec{\mathbf{x}'},t')\right\rangle = \delta_{ij}\delta(t-t')N_f(|\vec{\mathbf{x}}-\vec{\mathbf{x}'}|), \tag{1.3}$$

where $\langle\cdot\rangle$ denotes the ensemble average. Such a choice of the forcing covariance is local in time and preserves Galilean invariance. The spatial covariance $N_f(|\vec{\mathbf{x}}-\vec{\mathbf{x}'}|)$ is assumed to be concentrated at large scales, so in Fourier space it peaks at the wavenumber $k = L^{-1}$, where L is the integral length. It can be chosen diagonal in the components, without loss of generality because of incompressibility.

Path integral. The stochastic NS equation (1.1) can be reformulated in terms of a path integral following a standard procedure called Martin-Siggia-Rose-Janssen-de Dominicis (MSRJD) response functional formalism (Martin et al., 1973; Janssen, 1976; DeDominicis, 1976). The detailed explanation of the MSRJD procedure in application to the stochastic NS equation can be found in the works of Canet et al., 2015; Tarpin, 2018. The goal is to find the generating functional $\mathcal{Z}[j]$ of the correlation functions of the fields ϕ (velocity, pressure, response fields). The expression for the generating functional takes the form:

$$\mathcal{Z}\left[\vec{\mathbf{J}},\bar{\vec{\mathbf{J}}},J^p,\bar{J}^p\right] = \int \mathcal{D}\left[\vec{\mathbf{v}},\bar{\vec{\mathbf{v}}},p,\bar{p}\right]\exp\left\{-\mathcal{S}\left[\vec{\mathbf{v}},\bar{\vec{\mathbf{v}}},p,\bar{p}\right] + \int \mathrm{d}t\,\mathrm{d}\vec{\mathbf{x}}\, j_i\phi_i\right\}, \tag{1.4}$$

where the response fields are denoted with a bar, the letter ϕ denotes the fields and the response fields $\phi = \left\{\vec{\mathbf{v}}, \bar{\vec{\mathbf{v}}}, p, \bar{p}\right\}$, the letter j corresponds to the sources associated with the fields $j = \left\{\vec{\mathbf{J}}, \bar{\vec{\mathbf{J}}}, J^p, \bar{J}^p\right\}$. The symbol $\mathcal{D}$ denotes the functional measure of integration. The functional $\mathcal{S}[\phi]$ represents the action, which for the stochastic Navier-Stokes equation is given by (Canet et al., 2015):

$$\mathcal{S}\left[\vec{\mathbf{v}}, \bar{\vec{\mathbf{v}}}, p, \bar{p}\right] = \int \mathrm{d}t\, \mathrm{d}\vec{\mathbf{x}}\, \bar{v}_\alpha \left[\partial_t v_\alpha + v_\beta \partial_\beta v_\alpha - \nu \nabla^2 v_\alpha + \partial_\alpha p\right] - \bar{p}\partial_\alpha v_\alpha - \int \mathrm{d}t\, \mathrm{d}\vec{\mathbf{x}}\, \mathrm{d}\vec{\mathbf{x}}'\, \bar{v}_\alpha(t, \vec{\mathbf{x}}) N_f(|\vec{\mathbf{x}} - \vec{\mathbf{x}}'|) \bar{v}_\alpha(t, \vec{\mathbf{x}}'). \quad (1.5)$$

Here the Einstein summation convention is used.

The advantage of this formulation is that it provides a straightforward access to a n-point space-time correlation function in Eulerian frame of reference. The generating functional $\mathcal{Z}$ is analogous to the moment-generating function in probability theory: the n-th functional derivative of the generating functional with respect to the sources j gives the n-point correlation function, which can be written as:

$$G^{(n)}_{\alpha_1,\ldots,\alpha_n}(t_1, .., t_n, \vec{\mathbf{x}}_1, ..., \vec{\mathbf{x}}_n) = \frac{\delta^n \mathcal{Z}[j]}{\delta j_{\alpha_1}(t_1, \vec{\mathbf{x}}_1) \ldots \delta j_{\alpha_n}(t_n, \vec{\mathbf{x}}_n)}. \quad (1.6)$$

The analogue of the generating functional $\mathcal{Z}$ in statistical mechanics of equilibrium systems is the partition function. Its logarithm $W[j] = \ln \mathcal{Z}[j]$ is the generating functional of connected correlation functions (equivalent to cumulants). The analogue of the functional $W[j]$ in equilibrium systems is the Helmholz free energy.

Regulator. The generating functional (1.4) represents a functional integral which is impossible to compute via direct integration. At this point, the main idea of the RG comes into play: to perform the integration over the fluctuations progressively, scale-by-scale, starting from the microscopic scale up to the large-scale effective model. Within the FRG approach, this progressive integration of fluctuation modes is achieved by including in the generating functional $\mathcal{Z}$ a filtering term $\Delta\mathcal{S}_K[\phi]$ depending on a running wavenumber K which corresponds to the renormalization scale. Now, since the filtering term $\Delta\mathcal{S}_K$ depends on the renormalization scale K, the modified partition function also becomes scale dependent and can be denoted as $\mathcal{Z}_K$:

$$\mathcal{Z}_K[j] = \int \mathcal{D}[\phi] \exp\left\{-\mathcal{S}[\phi] - \Delta\mathcal{S}_K[\phi] + \int \mathrm{d}t\, \mathrm{d}\vec{\mathbf{x}}\, j_i \phi_i\right\}. \quad (1.7)$$

The filtering term ensures the selective integration of the fluctuations over wavenumbers larger than K. For this purpose, $\Delta\mathcal{S}_K[\phi]$ has to fulfill the following requirements:

— Smooth function.

— Large scales have to be suppressed in the path integral, so the filtering term has to be large for modes of wavenumbers smaller than the running renormalization scale $|\vec{\mathbf{q}}| \lesssim K$.

— Small scales should not be affected, as their contribution is integrated, so the filtering term has to vanish for modes with $|\vec{\mathbf{q}}| \gtrsim K$.

This filtering term is quadratic in fields. In the case of NS equation, it consists of two parts, which can be interpreted, respectively, as an effective forcing and an effective viscosity:

$$\Delta\mathcal{S}_K[\vec{\mathbf{v}}, \bar{\vec{\mathbf{v}}}] = -\int_{t,\vec{\mathbf{x}},\vec{\mathbf{x}}'} \bar{v}_\alpha(t, \vec{\mathbf{x}}) N_K(|\vec{\mathbf{x}} - \vec{\mathbf{x}}'|) \bar{v}_\alpha(t, \vec{\mathbf{x}}') + \int_{t,\vec{\mathbf{x}},\vec{\mathbf{x}}'} \bar{v}_\alpha(t, \vec{\mathbf{x}}) R_K(|\vec{\mathbf{x}} - \vec{\mathbf{x}}'|) v_\alpha(t, \vec{\mathbf{x}}'). \quad (1.8)$$

The effective forcing is just the forcing term N_K in the NS action (1.5) where the inverse integral scale is replaced by the running RG scale K. The physical forcing is restored when K crosses L^{-1} such that all nontrivial fluctuations have been integrated over. The most important property of the regulator functions N_K and R_K is that they vanish rapidly at large wavenumbers $|\vec{\mathbf{q}}| > K$. Clearly, there is no unique choice fulfilling these criteria, but the idea is that the final result does not depend on the details of the regulator, as its influence disappears when the renormalization scale is moved to $K \to 0$.

Effective average action. At the next step, the "effective average action" functional $\Gamma_K[\psi]$ is introduced. It is defined as the Legendre transform of the scale-dependent generating functional $W_K[j]$, modified by the filtering term:

$$\Gamma_K[\psi] = -W_K[j] + \int_{t,\vec{\mathbf{x}}} \psi_i j_i - \int_{t,\vec{\mathbf{x}},\vec{\mathbf{x}}'} [\bar{u}_\alpha R_K u_\alpha - \bar{u}_\alpha N_K \bar{u}_\alpha], \tag{1.9}$$

where $\psi = \langle \phi \rangle$ denotes the average fields, $\vec{\mathbf{u}} = \langle \vec{\mathbf{v}} \rangle$, $\bar{\vec{\mathbf{u}}} = \langle \bar{\vec{\mathbf{v}}} \rangle$ and j are the corresponding sources. In terms of statistical physics, Γ_K corresponds to the Gibbs free energy in equilibrium systems, it is also referred to as the generating functional of one-particle irreducible (1PI) vertices. The scale-dependent Γ_K gives then the integrated free energy of the small-scale fluctuations at wavenumbers $|\vec{\mathbf{q}}| > K$. Thus, by changing the renormalization (or filtering) wavenumber K from a certain large $K = \Lambda$, corresponding to the FRG microscale, to the integral scale of the system $K = L^{-1}$, one can actually perform the progressive integration of all fluctuations. Instead of the integration of the partition function $\mathcal{Z}$ itself, one can analyze the evolution of the effective action Γ_K with the renormalization scale wavenumber K approaching zero.

The properties of the filtering term $\Delta\mathcal{S}_K$ listed above ensure that, at the microscopic scale $K = \Lambda$, the effective action coincides with the NS action (1.5), so that $\Gamma_{K=\Lambda} = \mathcal{S}$. In the opposite limit of large scales $K \to 0$, all the fluctuations are averaged out and the regulator term vanishes, so $\Gamma_{K=0}$ becomes the full effective action Γ of the system.

RG flow equation. The effective average action Γ_K obeys an exact differential functional RG equation, which gives its evolution with the RG scale K (Wetterich, 1993). In Fourier space, it takes the form:

$$\partial_K \Gamma_K[\psi] = \frac{1}{2} \operatorname{Tr} \int_{\vec{\mathbf{q}}} \partial_K \mathcal{R}_K(\vec{\mathbf{q}}) \left[\Gamma_K^{(2)}[\psi] + \mathcal{R}_K(\vec{\mathbf{q}}) \right]^{-1}. \tag{1.10}$$

The equation is given in matrix form, so $[\mathcal{R}_K]$ is the regulator matrix of size 4×4 (by the number of fields), with non-zero elements $[\mathcal{R}_K]_{22} = N_K$ and $[\mathcal{R}_K]_{12} = [\mathcal{R}_K]_{21} = R_K$, the matrix $\Gamma_K^{(2)}$ is the Hessian matrix, so it contains the second-order functional derivatives of Γ_K. The integration occurs in the Fourier space.

Taking n-th functional derivatives of (1.10) with respect to the corresponding fields provides the exact flow equation of the vertices $\Gamma_K^{(n)}$. Since the effective average action Γ_K and the generating functional W_K are related through the Legendre transform (1.9), the solution of the flow equation for $\Gamma_K^{(n)}$ can be transformed into $W_K^{(n)}$, which is needed for computation of a n-point connected correlation function.

Fixed point. If one traces the evolution of the effective average action Γ_K with the renormalization scale wavenumber K changing from the microscale $K = \Lambda$ to small wavenumbers $K \to 0$, once the inverse integral length scale is passed $K = L^{-1}$, all fluctuations are averaged out. That also means that the effective average action Γ_K does not vary anymore at $K \lesssim L^{-1}$, and the solution of the flow equation reaches a fixed point. To compute

the observables of the physical system, such as correlation functions, one has to obtain the solution of the flow equation at the fixed point.

This fixed-point solution corresponds to stationary fully developed turbulence in the presence of large-scale forcing (Canet et al., 2016). The correlation functions evaluated at the fixed point are thus the universal properties of stationary turbulence.

Closure problem. The RG flow equation (1.10) and equations generated from it by taking functional derivatives are exact, however, they are not closed. The equation for a given $\Gamma_K^{(n)}$ contains derivatives $\Gamma_K^{(n+1)}$ and $\Gamma_K^{(n+2)}$, which in their turn are governed by their own flow equations involving higher-order derivatives and so on. That is to say that one has to consider actually an infinite hierarchy of flow equations. Thus, some approximations are needed to simplify or truncate these flow equations. One of the possible approximation schemes within the FRG is the derivative expansion (Delamotte, 2012), which consists in an expansion of Γ_K in series of gradients and time derivatives. However, in the case of hydrodynamic turbulence, the symmetries of the incompressible Navier-Stokes equations allow to express some vertices $\Gamma_K^{(n)}$ through lower-order vertices or to nullify them, and therefore to obtain a closure without any truncation in the limit of the large wavenumbers.

Extended symmetries. The symmetries of the NS field theory are the time-dependent Galilean symmetry and the time-dependent shift of the response fields, unveiled in the work of Canet et al., 2015. The two symmetries are extended symmetries, in the sense that the NS action (1.5) is not strictly invariant under these transformations, but has a variation which is linear in the fields.

The time-dependent Galilean symmetry corresponds to the following infinitesimal transformation:

$$\delta v_\alpha(\vec{\mathbf{x}}) = -\dot{\epsilon}_\alpha(t) + \epsilon_\beta(t)\partial_\beta v_\alpha(\vec{\mathbf{x}}), \qquad \delta p\,(\vec{\mathbf{x}}) = \epsilon_\beta(t)\partial_\beta p(\vec{\mathbf{x}}), \tag{1.11}$$

$$\delta \bar{v}_\alpha(\vec{\mathbf{x}}) = \epsilon_\beta(t)\partial_\beta \bar{v}_\alpha(\vec{\mathbf{x}}), \qquad \delta \bar{p}\,(\vec{\mathbf{x}}) = \epsilon_\beta(t)\partial_\beta \bar{p}(\vec{\mathbf{x}}). \tag{1.12}$$

If one sets $\vec{\epsilon}(t) = \vec{\epsilon}t$ it turns into the standard (global) Galilean transformation.

The time-dependent shift symmetry of the response fields corresponds to the following transformations:

$$\delta \bar{v}_\alpha(\vec{\mathbf{x}}) = \bar{\epsilon}_\alpha(t), \quad \delta \bar{p}\,(\vec{\mathbf{x}}) = v_\beta(\vec{\mathbf{x}})\bar{\epsilon}_\beta(t). \tag{1.13}$$

Based on these two symmetries, one can derive exact Ward identities providing relations between the vertex functions. The Ward identities and their derivation can be found in the works of Canet et al., 2015 ; Tarpin, 2018. The main result that follows from the analysis of the Ward identities is that all the vertices $\Gamma_K^{(n)}(\omega_1, ..., \omega_n, \vec{\mathbf{k}}_1, ..., \vec{\mathbf{k}}_n)$ that have at least one zero wave-vector $\vec{\mathbf{k}} = 0$ vanish or can be expressed exactly through the lower-order vertices.

Large-wavenumber closure. For turbulence, the flow equations can be simplified with the use of the Blaizot-Mendez-Galain-Wschebor (BMW) scheme (Blaizot et al., 2006), which relies essentially on the properties of the regulator. The presence of the derivative of the regulator $\partial_K \mathcal{R}_K(\vec{\mathbf{q}})$ in the flow equation (1.10) ensures that the integral over the internal wavenumber $\vec{\mathbf{q}}$ can be cut to $|\vec{\mathbf{q}}| \leq K$, since the larger wavenumbers simply do not contribute to the integral, as they are filtered out by the regulator derivative $\partial_K \mathcal{R}_K$. Thus, if one considers the limit where all external wavenumbers $\vec{\mathbf{k}}_i$ of the vertices $\Gamma_K^{(n)}$ are significantly larger compared to the renormalization running wavenumber K, $|\vec{\mathbf{k}}_i| \gg K$, then internal wavenumber (of the integration) is negligible with respect to the external ones $|\vec{\mathbf{q}}| \ll |\vec{\mathbf{k}}_i|$. One can thus expand the vertices of the flow equation in powers of $|\vec{\mathbf{q}}|$.

The unique feature of the NS field theory, which is related to Ward identities, is that the vertices with at least one wavenumber equal to zero can be expressed exactly through the lower-order vertices. As a consequence, the flow equation for any n-point correlation function of the NS turbulent fluid can be closed without truncation at the leading order of the expansion in powers of $|\vec{\mathbf{q}}|$ with the use of the above-mentioned Ward identities. The vertex expansion resulting from the BMW scheme is rigorously controlled, and it becomes exact at infinite wavenumbers.

To make the limit of the "large" wavenumbers more precise, the wavevectors $\vec{\mathbf{k}}$ should be considered with respect to the integral length scale wavenumber, as at this scale the RG flow stops, so the limit $K \to 0$ can be approximated by $K \approx L^{-1}$, and thus the results obtained in the large-wavenumber limit are valid for the wavevectors $|\vec{\mathbf{k}}| \gg L^{-1}$.

Flow equation for the correlation function. The two-point correlation function of the velocity in the Eulerian frame of reference in a stationary flow is defined as:

$$C^{(2)}(t,\vec{\mathbf{k}}) \equiv \mathrm{FT}[\langle u_i(t_0,\vec{\mathbf{r}}_0)u_i(t_0+t,\vec{\mathbf{r}}_0+\vec{\mathbf{r}})\rangle] = \left\langle \hat{u}_i(t_0,\vec{\mathbf{k}})\hat{u}_i^*(t_0+t,\vec{\mathbf{k}})\right\rangle, \tag{1.14}$$

where FT denotes the spatial Fourier transform, and the brackets denote the averaging over the statistical ensemble of the forcing realizations. The translational invariance in space and time of the correlation function follows from the assumptions of homogeneity and stationarity. Following the described closure scheme based on the NS symmetries and the assumption of large wavenumbers, one can obtain the closed flow equations for the scale-dependent version of the two-point correlation function $C_K(t,\vec{\mathbf{k}})$. The flow equation then takes the form (Canet et al., 2017; Tarpin et al., 2018):

$$K\partial_K C_K(t,\vec{\mathbf{k}}) = -\frac{2}{3}k^2 C_K(t,\vec{\mathbf{k}}) \int \frac{\cos(\omega t)-1}{\omega^2}\mathcal{J}_K(\omega)\frac{\mathrm{d}\omega}{2\pi}, \tag{1.15}$$

$$\mathcal{J}_K(\omega) = -2\int \mathrm{d}^3\vec{\mathbf{q}}\big[K\partial_K N_K(\vec{\mathbf{q}})|G_K(\omega,\vec{\mathbf{q}})|^2 - K\partial_K R_K(\vec{\mathbf{q}})C_K(\omega,\vec{\mathbf{q}})\mathrm{Re}\left[G_K(\omega,\vec{\mathbf{q}})\right]\big],$$

where the function $G_K(\omega,\vec{\mathbf{q}})$ is the Fourier transform of the scale-dependent response function defined as $G_K(t,\vec{\mathbf{x}}) \equiv \left\langle \vec{\mathbf{u}}(t_0+t,\vec{\mathbf{x}}_0+\vec{\mathbf{x}})\cdot\bar{\vec{\mathbf{u}}}(t,\vec{\mathbf{x}})\right\rangle_K$. Note that this equation becomes exact in the limit of infinite wavenumbers $|\vec{\mathbf{k}}| \to \infty$.

Similar flow equations can be obtained in the general case of n-point space-time correlation functions of velocity $C_K^{(n)}(t_1,...,t_n,\vec{\mathbf{k}}_1,...,\vec{\mathbf{k}}_n)$. These flow equations are linear in $C_K^{(n)}(t,\vec{\mathbf{k}})$, so they can be solved analytically at the fixed point, which corresponds to the velocity correlation in a stationary turbulent state. The fixed-point solutions are denoted by $C^{(n)}$ without index K. Moreover, their expressions can be simplified in the limit of short and large time delays t. For the case of the two-point correlation function $C^{(2)}$, the simplified expressions are provided in the next section.

1.2.2 Eulerian spatio-temporal correlation function of velocity

The general solution of the flow equation (1.15) takes a complicated form, but it can be simplified if one considers the limits of small and large time lags. The smallness of the time delays should be considered with respect to the typical integral (or large-scale eddy-turnover) time scale of the flow $\tau_0 \sim (L^2/\epsilon)^{1/3} \approx L/U_{rms}$ where ϵ is the mean energy dissipation rate, U_{rms} - the root-mean-square velocity.

Small time lags. At small time lags t, the expression of the integrand in the right-hand side of (1.15) can be approximated as $[\cos(\omega t) - 1]/\omega^2 \sim -t^2/2$. The expression for the two-point correlation function at the fixed-point solution of the Eq. (1.15) then takes the form (Tarpin et al., 2018):

$$C_S^{(2)}(t, \vec{\mathbf{k}}) = C_{0S}\epsilon^{2/3}k^{-11/3} \exp\left[-\alpha_S(L/\tau_0)^2 t^2 k^2 + \mathcal{O}(kL)\right], \quad t \ll \tau_0. \tag{1.16}$$

The subscript S refers to the "short"-time expression. Here, C_{0S} and α_S are non-universal constants, in the sense that their values depend on the forcing profile (1.3).

The result (1.16) clearly shows that the correlation function depends on the scaling variable tk as a Gaussian function. This scaling is different from the scaling $tk^{2/3}$ that results from dimensional arguments similar to K41 applied to the space-time correlations. In particular, it means that the characteristic decorrelation time of a velocity Fourier mode depends on the wavenumber as $\tau_D \sim k^{-1}$. Note that the prefactor in the exponential of the expression (1.16) can be related to the root-mean-square velocity of turbulent fluctuations as $u_{RMS} \sim L/\tau_0$, which is mainly determined by the large-scale velocity field.

This result has been already known phenomenologically as the random "sweeping" effect, a term introduced by Tennekes, 1975. This scaling arises from the random advection (or sweeping) of the small-scale eddies of the flow by a slow, random, large-scale velocity field. This result found its validation in numerical simulations and some experiments, but a systematic analytical derivation was lacking. The random sweeping effect will be discussed with more details in section 3.1. The numerical results validating the Gaussian time decorrelation in tk-variable (1.16) are provided in section 3.2.

Large time lags. Considering the large time lags $t \gg \tau_0$, one can show that Eq. (1.15) simplifies to the following expression (Tarpin et al., 2018):

$$K\partial_K C_K^{(2)}(t, \vec{\mathbf{k}}) = \frac{1}{3}\mathcal{J}_K(0) C_K(t, \vec{\mathbf{k}}) k^2 |t|. \tag{1.17}$$

The fixed point solution for the two-point correlation function then takes the form:

$$C_L^{(2)}(t, \vec{\mathbf{k}}) = C_{0L}\epsilon^{2/3}k^{-11/3} \exp\left[-\alpha_L(L^2/\tau_0)|t|k^2 + \mathcal{O}(kL)\right], \quad t \gg \tau_0. \tag{1.18}$$

The subscript L refers to the "large"-time expression. As previously in the case of small time lags, C_{0L} and α_L are non-universal constants depending on the forcing profile. The result (1.18) shows that the two-point correlation function changes its behavior from a Gaussian of the variable tk at small time lags (1.16) to an exponential of a variable tk^2 at large time lags (1.18).

In the numerical results presented in this thesis, the large-time regime (1.18) was not captured. The analysis of correlation functions at large time lags is complicated due to the weak amplitudes of the signals (see section 3.2.2). A similar behavior has been observed in the correlation function of a passive scalar. The FRG results for the passive scalar advection are discussed in the next section 1.3, and the numerical result will be provided in chapter 4. Additionally, a physical interpretation of the exponential decay at large time lags from the point of view of turbulent particle dispersion is proposed in the final section 1.4 of the present chapter.

Validity of the approximation. The results for the velocity correlation functions presented above are obtained in the limit of large wavenumbers. This assumption requires that all wavenumbers k_i involved in a given correlation function (and all partial sums of the wavenumbers) are large compared to the running RG wavenumber K.

The physical quantities, such as correlation functions, are obtained from the RG flow at the fixed point when the running renormalization wavenumber becomes smaller than the integral-scale wavenumber $K \lesssim L^{-1}$. Thus, a "large wavenumber" in the present analysis means $|\vec{\mathbf{k}}| \gg L^{-1}$. One can show that the factors in square brackets in Eqs. (1.16), (1.18) are exact in the limit of the large wavenumber, which implies that the corrections to these terms are at most of order $\mathcal{O}(kL)$ (Tarpin et al., 2018). In contrast, the terms that multiply the exponential in Eq. (1.16) are not exact in these expressions, as they can be corrected by higher-order contributions neglected in the large wavenumber expansion. That is to say that the exponent 11/3, corresponding to K41 scaling, can be rectified by the next-order term in the expansion, which would correspond to intermittency corrections.

Spatial spectrum of the kinetic energy. The inertial range of the three-dimensional spatial spectrum of the kinetic energy can be obtained simply by evaluating the two-point correlation function (1.16) at equal times (or at zero time lag). Due to the isotropy of the flow, the energy density function takes form:

$$E(k) = 4\pi k^2 C(t=0, \vec{\mathbf{k}}) = 4\pi C_{0S} \epsilon^{2/3} k^{-5/3}. \tag{1.19}$$

Therefore, one obtains the well-known K41 5/3 spectrum power law, which can be also deduced from the dimensional analysis (Frisch, 1995).

Interestingly, if instead of nullifying the time lag t, one takes a limit of the correlation function at the time lag tending to a characteristic Kolmogorov's time scale $t \to \tau_\eta = (\nu/\epsilon)^{1/2}$, and still considering the large-wavenumber limit $k \gg L^{-1}$, it is possible to obtain the spatial spectrum in the near-dissipative range. Under some assumptions, it takes the form of a stretched exponential function: (Canet et al., 2017):

$$E_{dissip}(k) = 4\pi k^2 C(t \to \tau_\eta, \vec{\mathbf{k}}) = 4\pi C_{0S} \epsilon^{2/3} k^{-5/3} \exp\left[-\mu k^{2/3}\right], \tag{1.20}$$

where μ is a non-universal constant.

It should be noted that such an approximation is expected to be valid only in the near-dissipative range, where there is an interplay between the nonlinear advection and the viscous diffusion, while in the far-dissipative range the spectrum is regularized by the viscosity. The form of the kinetic energy spectrum in the near-dissipative range has been studied numerically and compared with the FRG result, this study is provided in section 3.5.

Frequency spectrum of the kinetic energy. The frequency spectrum of the kinetic energy can be estimated by evaluating the temporal Fourier transform of the correlation function (1.16) at a single point in the physical space, which is equivalent to integrating over the wavevectors (Canet et al., 2017):

$$E(\omega) = \int_0^\infty \mathrm{d}k\, 4\pi k^2 \int_{-\infty}^{\infty} \mathrm{d}t\, C(t, \vec{\mathbf{k}}) e^{i\omega t} = 2^{8/3}\pi^{3/2}\Gamma\left(\frac{5}{6}\right) C_{0S} \alpha_S^{1/3} \left(\frac{\epsilon L}{\tau_0}\right)^{2/3} \omega^{-5/3}. \tag{1.21}$$

The power law $-5/3$ and its prefactor $(\epsilon L/\tau_0)^{2/3} \sim (\epsilon u_{RMS})^{2/3}$ can be also deduced from the dimensional arguments based on the random sweeping of the small vortices by large-scale velocity field (Tennekes, 1975).

This power law is also consistent with the experimental measurements of the kinetic energy spectra in Eulerian frame of reference in experiments (Kit et al., 1995) and numerical simulations (Chevillard et al., 2005; Lévêque et al., 2007). Hence, the FRG provides a correct prediction of the power laws in the inertial range of frequency and wavenumber spectra of kinetic energy.

Three-point correlation function. As it has been mentioned above, in the end of the section 1.2.1, the FRG approach yields a more general result: the spatio-temporal dependence of any multipoint correlation function of the turbulent velocity field in the limit of large wavenumbers. The general expression for the n-point correlation function can be found in the article of Tarpin et al., 2018. However, in the present work, only the three-point correlation function is studied, as is it possible to access it in numerical simulations. A three-point space-time correlation function of a velocity Fourier mode is defined as follows:

$$\begin{aligned} C^{(3)}_{\alpha\beta\gamma}\left(t_1,\vec{\mathbf{k}}_1,t_2,\vec{\mathbf{k}}_2\right) &\equiv \mathrm{FT}[\langle u_\alpha(t_0+t_1,\vec{\mathbf{r}}_0+\vec{\mathbf{r}}_1)u_\beta(t_0+t_2,\vec{\mathbf{r}}_0+\vec{\mathbf{r}}_2)u_\gamma(t_0,\vec{\mathbf{r}}_0)\rangle] \\ &= \left\langle \hat{u}_\alpha\left(t_0+t_1,\vec{\mathbf{k}}_1\right)\hat{u}_\beta\left(t_0+t_2,\vec{\mathbf{k}}_2\right)\hat{u}^*_\gamma\left(t_0,\vec{\mathbf{k}}_1+\vec{\mathbf{k}}_2\right)\right\rangle . \end{aligned} \tag{1.22}$$

In the limit where all wavenumbers k_1, k_2, $|\vec{\mathbf{k}}_1+\vec{\mathbf{k}}_2|$ are large with respect to L^{-1}, the FRG calculation leads to the following form at small time delays t_1 and t_2

$$C^{(3)}_{\alpha\beta\gamma}\left(t_1,\vec{\mathbf{k}}_1,t_2,\vec{\mathbf{k}}_2\right) = C^{(3)}_{\alpha\beta\gamma}\left(0,\vec{\mathbf{k}}_1,0,\vec{\mathbf{k}}_2\right)\exp\left\{-\alpha_S(L/\tau_0)^2\left|\vec{\mathbf{k}}_1 t_1+\vec{\mathbf{k}}_2 t_2\right|^2\right\}, \tag{1.23}$$

with α_S the same constant as in Eq. (1.16). Note that a similar expression as Eq. (1.18) is also available for large time delays. The simplified case of equal time delays is considered $t=t_1=t_2$, thus aiming at testing the theoretical form:

$$C^{(3)}_{\alpha\beta\gamma}\left(t,\vec{\mathbf{k}}_1,t,\vec{\mathbf{k}}_2\right) \sim \exp\left\{-\alpha_S(L/\tau_0)^2\left|\vec{\mathbf{k}}_1+\vec{\mathbf{k}}_2\right|^2 t^2\right\}, \quad t\ll\tau_0. \tag{1.24}$$

This expression shows that the three-point correlation function at large wavenumbers is also a Gaussian function of a variable $|\vec{\mathbf{k}}_1+\vec{\mathbf{k}}_2|t$ for small t, with the same prefactor α_S as in the two-point correlation function.

The fact that the resulting three-point correlation function is a function of the norm of the wavenumber of wavevectors $|\vec{\mathbf{k}}_1+\vec{\mathbf{k}}_2|$ allows to exploit the properties of the convolution in Fourier space and facilitate the numerical computation of $C^{(3)}$. Direct computation of the expression (1.24) in parallelized numerical simulation is a nontrivial task. In this work, a three-point statistical quantity is obtained by computing the correlation between the nonlinear term of the NS equation and the filtered velocity fields. To approach the limit of the large wavenumbers required by the FRG approximation, the velocity fields are filtered before computation. The method for the numerical estimation of the three-point correlation function is presented in detail in section 3.3, followed by the results of the numerical simulations.

1.3 Functional renormalization group in application to the advection of a passive scalar

This section provides a brief summary of the results of the FRG analysis applied to the problem of a passive scalar advected by a turbulent velocity flow (Pagani and Canet, 2021).

A scalar quantity θ is said to be passive if it does not have any back-reaction on the fluid flow, or its influence on the flow can be neglected. A passive scalar can represent different physical quantities such as the concentration of chemical species, variations of

salinity in the ocean, or small fluctuations of temperature or humidity. The evolution of a passive scalar quantity θ is governed by the advection-diffusion equation with external forcing:

$$\partial_t \theta(\vec{\mathbf{x}}, t) + [\vec{\mathbf{v}}(\vec{\mathbf{x}}, t) \cdot \boldsymbol{\nabla}]\theta(\vec{\mathbf{x}}, t) = \kappa \nabla^2 \theta(\vec{\mathbf{x}}, t) + f_\theta(\vec{\mathbf{x}}, t), \tag{1.25}$$

where κ is its molecular diffusivity and f_θ is the external forcing (or source) of the scalar. Similar to the NS equation, the forcing is assumed to be stochastic with Gaussian statistics and concentrated at large scales with covariance:

$$\left\langle f_\theta(\vec{\mathbf{x}}, t) f_\theta(\vec{\mathbf{x}'}, t') \right\rangle = \delta(t - t') N_\theta(|\vec{\mathbf{x}} - \vec{\mathbf{x}'}|). \tag{1.26}$$

Two cases are considered: a scalar passively advected by a velocity field governed by the NS equations (1.1) and a scalar advected by a random velocity field with Gaussian statistics. The principal stages in the FRG analysis are identical to the study of the NS equation in the previous section. First, the stochastic equation (1.25) is reformulated in terms of a path integral with the use of MSRJD procedure and the obtained path integral is modified by a RG filtering term. Next, the symmetries of the equation are explored and the corresponding Ward identities are obtained, which allows to find relations between some vertices or to simplify them. The symmetries for the velocity fields are the same as listed above in the previous section, one has to add the time-dependent Galilean and shift symmetry for the scalar. Then, the limit of large wavenumbers is applied, enabling a closure of the hierarchy of the RG flow equations. Lastly, the flow equations are solved, and the expressions for the scalar correlation functions take simple forms in the limit of small and large time lags. The full details of the derivation can be found in the article of Pagani and Canet, 2021. Here, the principal results are provided, which are tested numerically further in chapter 4.

1.3.1 Flow governed by Navier-Stokes equation

In the case of a passive scalar advected by a velocity field governed by the NS equation (1.1), the field theory is identical to the one discussed in the previous section, one only needs to add terms concerning the scalar in the action (1.5), and to take into consideration the time-dependent shift symmetry of the scalar.

The characteristic length scales of the scalar and forcing are assumed to be comparable, and similarly, the typical length scales of the fluid viscosity and scalar diffusivity are assumed to be comparable. That is to say that there exists a range of wavenumbers between the forcing and dissipation scales, which is referred to as the inertial-convective range, in which both the NS and the scalar equations are dominated by the advection term. In what follows, the universal scalar behavior of the inertial-convective range is considered. This point will be discussed more extensively in the chapter 4 which is dedicated to the passive scalar advection.

The FRG approach allows to obtain a result for the two-point space-time correlation in the Fourier space of the scalar in the Eulerian frame defined as:

$$C_\theta^{(2)}(t, \vec{\mathbf{k}}) \equiv \left\langle \theta\left(t_0, \vec{\mathbf{k}}\right) \theta\left(t_0 + t, -\vec{\mathbf{k}}\right) \right\rangle. \tag{1.27}$$

As it is shown in the work (Pagani and Canet, 2021), the flow equation for the correlation function $C_{\theta,K}^{(2)}$ takes the same form as the flow equation for the velocity correlation function (1.15). Therefore, similarly to the velocity, one can obtain the simplified expression for the scalar correlation function in the limit of small and large time lags:

$$C_\theta^{(2)}(t, \vec{\mathbf{k}}) = \epsilon_\theta \epsilon^{-1/3} k^{-11/3} \begin{cases} C_{\theta S} \exp\left[-\alpha_S \frac{L^2}{\tau_0^2} k^2 t^2 + \mathcal{O}(kL)\right], & t \ll \tau_0, \\ C_{\theta L} \exp\left[-\alpha_L \frac{L^2}{\tau_0} k^2 |t| + \mathcal{O}(kL)\right], & t \gg \tau_0, \end{cases} \tag{1.28}$$

where ϵ and ϵ_θ are the energy dissipation rates of the velocity and scalar fields, respectively. The constants $C_{S,L}$ are not universal, they depend on the form of the scalar and velocity forcing profiles. The parameters $\alpha_{S,L}$ are identical to the ones obtained for the velocity correlation function in Eqs. (1.16), (1.18), as the flow equations for scalar and velocity take the same form. Therefore, the result (1.28) demonstrates that the temporal behavior of the passive scalar correlation function reproduces the one of the correlation function of the velocity of the carrier flow. In addition, the evaluation of the two-point correlation (1.28) at equal times yields a spatial spectrum with the power-law exponent $-5/3$ that corresponds to the well-known Obukhov-Corrsin spectrum for the inertial-convective range of a scalar spectrum (Obukhov, 1949 ; Corrsin, 1951).

The expressions (1.28) have been tested numerically, the results of numerical simulations are provided in the section 4.2. To check the influence of the temporal correlation of velocity on the scalar space-time correlation, the case of the synthetic velocity field with prescribed spatial and temporal statistics is also analyzed, which is discussed in the next section.

1.3.2 Random velocity flow

A simplified scalar advection is considered, in which the velocity is a random Gaussian vector field, characterized by zero mean and prescribed covariance. The covariance of velocity is taken under the following form:

$$\left\langle u_i(t,\vec{\mathbf{x}})u_j\big(t',\vec{\mathbf{y}}\big)\right\rangle = \delta\big(t-t'\big)D_0\int \frac{e^{i\vec{\mathbf{k}}\cdot(\vec{\mathbf{x}}-\vec{\mathbf{y}})}P_{ij}(\vec{\mathbf{k}})}{\big(k^2+m^2\big)^{\frac{d}{2}+\frac{\varepsilon}{2}}}\frac{\mathrm{d}^d\vec{\mathbf{k}}}{(2\pi)^d}, \tag{1.29}$$

where $P_{ij}(\vec{\mathbf{k}}) \equiv \delta_{ij} - \frac{k_i k_j}{k^2}$ is the transverse projector which ensures incompressibility, d - dimensionality of the system. The parameter $0 < \varepsilon/2 < 1$ is the Hölder exponent, describing the roughness of the velocity field. The wavenumber m acts as an infra-red cutoff.

The most essential property of such a velocity flow, enabling simplification, is its white-in-time covariance. This model was proposed by Kraichnan, 1968 and is often referred to in the literature as "Kraichnan's model". This model has been studied extensively (Kraichnan, 1994 ; Falkovich et al., 2001 ; Adzhemyan and S. V. Novikov, 2006 ; Kupiainen and Muratore-Ginanneschi, 2007). Even though the velocity in this model has Gaussian statistics, the passive scalar exhibits anomalous behavior. For this reason, Kraichnan's model is particularly interesting for studying and developing methods for the analysis of intermittency effects. Its simplicity allows to compute some anomalous exponents with analytical methods. However, the assumption of white-in-time velocity covariance, that brings simplifications, also poses problems on the extension of the results obtained in Kraichnan's model to realistic flows, in which the velocity has some nontrivial finite time covariance.

The passive scalar advection in Kraichnan's model has been studied with the FRG approach in the works of Pagani, 2015 ; Pagani and Canet, 2021. The details on the FRG derivation can be found in these works. The general scheme of the FRG analysis is still the same, it is essentially based on the field-theory representation of the stochastic equation of scalar transport, extended symmetries, and the limit of large wavenumbers. A particular feature that arises in Kraichnan's model, thanks to the fact that the velocity temporal covariance is a delta function and thus does not depend on the frequency, is that the flow equation can be simplified, and the integration over the internal frequency can be performed explicitly. The result for the Eulerian two-point spatio-temporal correlation of the scalar takes the form of an exponentially decaying function of the variable tk^2:

$$C_{\mathrm{K}}\left(t,\vec{\mathbf{k}}\right) = F\left(k\right)e^{-\kappa_{\mathrm{ren}}k^2|t|}, \tag{1.30}$$

where the equal-time part is separated as $F(k)$, which is given by a complicated integral. In the inertial range, one finds $F(k) \sim k^{-d-2+\varepsilon}$ while in the inertial-diffusive range, $F(k) \sim k^{-d-2-\varepsilon}$ (Pagani and Canet, 2021). The decorrelation prefactor in the exponential κ_{ren} actually represents the renormalized diffusivity. It is computed exactly and takes the form:

$$\kappa_{\text{ren}} = \kappa + \frac{d-1}{2d} \int \frac{D_0}{(k^2+m^2)^{\frac{d}{2}+\frac{\varepsilon}{2}}} \frac{\mathrm{d}^d \vec{\mathbf{k}}}{(2\pi)^d}. \tag{1.31}$$

This result suggests that if the fluid velocity is zero, the scalar decorrelation is driven purely by its molecular diffusivity κ. In the presence of a randomly moving fluid, the temporal decorrelation is accelerated by the velocity field, and the decorrelation rate is proportional to the variance of the velocity.

It should be noted that the exponential decay in tk^2 can be derived via several approaches, such as standard resummation of the self-energy diagrams and FRG calculation (Pagani and Canet, 2021). A similar expression was obtained in the works (Mitra and Pandit, 2005 ; Sankar Ray et al., 2008) by deriving a differential equation for the two-point correlation function.

In the present thesis, the result for the scalar correlation function (1.30) is tested in the numerical simulation of scalar advection in a synthetic random flow. In addition, the parameter κ_{ren} of the decorrelation extracted from the correlation functions (1.30) is compared to the renormalized viscosity evaluated via (1.31). These results can be found in section 4.3.

It should be noted that the FRG approach can be used in a similar manner in application to any flow with known statistical properties of the velocity field, the limitation to white-in-time velocity covariance is not crucial in the derivation, although it enables simplification. The FRG analysis allows to conclude that as soon as the temporal covariance (1.29) deviates from the delta function and the velocity field possesses some finite correlation time, the two-point space-time correlation function of the scalar develops a short time Gaussian regime, followed by an exponential decay at large time lags, similar to the behavior of the scalar correlation in the NS velocity field (1.28). This conclusion has been also validated numerically in simulations of scalar advected by a random synthetic field with a given typical correlation time (see section 4.3.3).

1.4 Interpretation in terms of single-particle dispersion

Eulerian correlations and Lagrangian displacement. An intuitive interpretation of the short- and large-time regimes of the Eulerian spatio-temporal correlation function can be drawn from the single-particle turbulent dispersion. As the initial point, let us consider the pure advection of a scalar $\partial_t \theta = -\vec{\mathbf{u}} \cdot \nabla \theta$. Kraichnan, 1964b proposed the following approximate relation linking the Eulerian scalar field with the Lagrangian displacement:

$$\theta(t, \vec{\mathbf{x}}) = \exp\left[-\vec{\xi}(t, \vec{\mathbf{x}}|0) \cdot \nabla\right] \theta(0, \vec{\mathbf{x}}), \tag{1.32}$$

where $\vec{\xi}(t, \vec{\mathbf{x}}|s)$ is the Lagrangian displacement during the time interval from s to t of a particle that arrives to the position $\vec{\mathbf{x}}$ at the time instant t. If one assumes that the displacement $\vec{\xi}$ is mainly dominated by the large-scale motions and varies in space much more slowly than the gradient of the scalar, the displacement can be considered as statistically homogeneous in space, and its values are determined by the time difference $t - s$:

$\vec{\xi}(t,\vec{\mathbf{x}}|s) \approx \vec{\xi}_h(t-s)$. Within these assumptions, it is possible to rewrite (1.32) for the Fourier modes of the scalar:

$$\hat{\theta}(t,\vec{\mathbf{k}}) \approx \exp\left[-i\vec{\xi}_h(t)\cdot\vec{\mathbf{k}}\right]\hat{\theta}(0,\vec{\mathbf{k}}). \tag{1.33}$$

By assuming also the statistical independence of the displacement $\vec{\xi}_h(t)$ and the initial distribution of the scalar field at $\theta(0,\vec{\mathbf{x}})$, one can deduce the expression for the space-time correlation function of the scalar:

$$C_\theta^{(2)}(t,\vec{\mathbf{k}}) \approx \left\langle \exp\left[-i\vec{\xi}_h(t)\cdot\vec{\mathbf{k}} - i\cancelto{0}{\vec{\xi}_h(0)\cdot\vec{\mathbf{k}}}\right]\right\rangle \left\langle \hat{\theta}(0,\vec{\mathbf{k}})\hat{\theta}(0,\vec{\mathbf{k}})\right\rangle. \tag{1.34}$$

The statistics of the displacement ξ_h is linked to the statistics of the large-scale velocity field, which can be assumed as having Gaussian distribution. Therefore, one can perform the averaging of the exponential, which leads to:

$$C_\theta^{(2)}(t,\vec{\mathbf{k}}) \approx \exp\left[-\frac{1}{2}\left\langle|\vec{\xi}_h(t)|^2\right\rangle k^2\right] C_\theta^{(2)}(0,\vec{\mathbf{k}}). \tag{1.35}$$

This expression indicates that the temporal decorrelation of the scalar correlation function occurs through statistical averaging of the complex phases of the scalar Fourier modes, which are displaced randomly by the large-scale velocity field.

Single particle dispersion problem. The averaged variance of the Lagrangian displacement vector has been studied in the classical work of Taylor, 1922, where it is shown that the mean squared displacement varies with time as :

$$\left\langle|\vec{\xi}_h(t)|^2\right\rangle \sim \begin{cases} U_{RMS}^2 t^2, & |t| \ll \tau_0, \\ 2D|t|, & |t| \gg \tau_0, \end{cases} \tag{1.36}$$

where $D \approx U_{RMS}^2\tau_0$ is the eddy viscosity.

The result of Taylor, 1922 comes from the consideration of the displacement as the integral of Lagrangian velocity $\vec{\xi}(t,\vec{\mathbf{x}}|0) = \int_0^t \vec{\mathbf{u}}^L(t,\vec{\mathbf{x}}|s)\,\mathrm{d}s$. The average of the square of the displacement can be written as:

$$\begin{aligned}\left\langle|\vec{\xi}_h(t)|^2\right\rangle = \int_0^t\int_0^t \left\langle \vec{\mathbf{u}}^L(t,\vec{\mathbf{x}}|s)\cdot\vec{\mathbf{u}}^L(t,\vec{\mathbf{x}}|s')\right\rangle \mathrm{d}s\,\mathrm{d}s' &= U_{rms}^2\int_0^t\int_0^t R(s-s')\,\mathrm{d}s\,\mathrm{d}s' \\ &= 2U_{rms}^2\int_0^t (t-s)R(s)\,\mathrm{d}s\,,\end{aligned} \tag{1.37}$$

where $R(s-s') = \left\langle \vec{\mathbf{u}}^L(t,\vec{\mathbf{x}}|s)\cdot\vec{\mathbf{u}}^L(t,\vec{\mathbf{x}}|s')\right\rangle / U_{rms}^2$ is the correlation function of the Lagrangian velocity, which is the correlation between velocities at time instants s and s' of a fluid particle that passed the point $\vec{\mathbf{x}}$ at time moment t. At small time delays $s-s'$ the Lagrangian velocity does not change significantly, and the correlation function is $R \approx 1$, so at small t the integral in the right-hand side of (1.37) behaves as t^2. On the contrary, if the time t is much larger than the integral correlation time, defined as $\tau_{corr} = \int_0^\infty R(s)ds$, the integral behaves as $\tau_{corr}t$. In other words, the result (1.36) is just a consequence of the finite correlation time of the velocity field. The scaling (1.36) has been validated by the measurements of the Lagrangian displacement in grid turbulence in the experimental work of Sato and Yamamoto, 1987.

Ballistic and diffusive dispersion. The result (1.36) of Taylor, 1922 can be understood intuitively in the following way (Majda and Kramer, 1999, section 3.1.3). At small times $t \ll \tau_0$, the averaged square displacement $\left\langle \vec{\xi}_h(t)^2 \right\rangle$ grows quadratically in time, which corresponds to the ballistic regime of the dispersion. The velocity field is felt by a fluid particle as a coherent movement pushing it in a certain direction. At times $t > \tau_0$ the large-scale velocity field decorrelates, and it pushes the particle incoherently. If one observes the fluid particle over large times $t \gg \tau_0$ so that many renewals of the large-scale velocity field have passed, the particle is moved in different directions by independent pushes, so the movement of the particle resembles the Brownian motion, and in average exhibits the diffusive dispersion with the mean square displacement growing linearly in time.

The relation (1.35) allows to project this Lagrangian-displacement picture on the Eulerian correlation function of the scalar and link it with the FRG result (1.28). Indeed, the ballistic dispersion at the small time lag results in the Gaussian decay in the variable tk of the Eulerian correlation function, while the diffusive dispersion at the large time delays results in the exponential decay of the variable tk^2, which is totally consistent with the FRG result. Moreover, it also gives a simple explanation of a purely exponential behavior of the scalar correlation in white-in-time velocity field (1.30). Since the velocity field does not possess any correlation in time, the ballistic regime of the dispersion vanishes, and one observes only the Brownian-like dispersion with the linear growth of the mean squared displacement.

These arguments can also be extended to the statistical moments of higher orders, such as multipoint correlation functions, under the assumption that the scales are much smaller than the integral scale of the system L, which is also the limitation of the FRG result.

From Eulerian correlation to particle dispersion. In the work of Majda and Kramer, 1999, section 3.3 the inverse problem is studied. The statistical properties of the single particle dispersion in a random velocity field are considered in two dimensions. It is shown that the regime of the one-particle dispersion depends on the scaling of the typical decorrelation time $\tau_0(k) \sim k^{-z}$ and on the spatial spectrum $E(k) \sim k^{1-\epsilon}$ of the random velocity field. Depending on the assumed values of z and ϵ one can obtain a diffusive or superdiffusive regime of the single-particle dispersion.

Correlation of velocity. Similar arguments can be used to explain the small- and large-time regimes in the Eulerian velocity correlation function resulting from the FRG (1.16), (1.18). However, it is a little less intuitive for the reason of self-advection of velocity. Such an interpretation has been proposed by G. Eyink and is provided in the article (Gorbunova et al., 2021a, section IIB). It can be shown (under certain assumptions) that the Eulerian velocity correlation can be linked to the Lagrangian displacement in the same way as (1.35), so the concept of ballistic and diffusive dispersion can be applied for the velocity correlations as well.

1.5 Summary

This chapter introduces the theoretical framework of functional renormalization group (FRG) in application to the NS equations and its principal results. The presented results are studied numerically in the following chapters of the present thesis. The FRG approach is a powerful method for the analytical study of strongly correlated systems and opens

promising ways in the development of statistical description of hydrodynamic turbulence. The main feature of the FRG approach is that it gives access to the multipoint correlation functions of the fields. The functional formulation also allows to obtain the closure of the RG flow equation without perturbative expansion, by exploiting the symmetries of the principal equations (Navier-Stokes and advection-diffusion equations) and considering the limit of large wavenumbers.

The correlation functions resulting from the FRG are consistent with the known behavior of the velocity and scalar fields, such as the 5/3 power law in the spatial and frequency spectra in Eulerian frame, as well as the dominance of the random sweeping effect in the space-time correlation function at small time lags. Additionally, the FRG provides new results, in particular on the large-time behavior of the correlation functions, as well as on the multipoint correlations, and on the form of the kinetic energy spectrum in the near-dissipative range. These new results are tested numerically in the chapters 3 and 4 of this manuscript.

The last chapter 5 of the manuscript also considers the FRG framework in application to turbulence. In particular, the shell version of Kraichnan's random advection model is studied within this approach. In the case of this particular shell model, the derivations are simplified, and different steps of the FRG analysis are presented in a more detailed manner.

Résumé en français

Ce chapitre introduit le cadre théorique du groupe de renormalisation fonctionnelle (FRG) en application aux équations de Navier-Stokes et ses principaux résultats. Les résultats présentés seront étudiés numériquement dans les chapitres suivants de la thèse. L'approche FRG est une méthode puissante pour l'étude analytique des systèmes fortement corrélés et ouvre des voies prometteuses dans le développement de la description statistique de la turbulence hydrodynamique. La principale caractéristique de l'approche FRG est qu'elle donne accès aux fonctions de corrélation multipoint des champs. La formulation fonctionnelle permet également d'obtenir la fermeture de l'équation du flot RG sans développement perturbatif, en exploitant les symétries des équations principales (Navier-Stokes et équations d'advection-diffusion) et en considérant la limite des grands nombres d'onde.

Les fonctions de corrélation résultant du FRG sont cohérentes avec le comportement connu des champs de vitesse et scalaires, comme la loi de puissance 5/3 dans les spectres spatial et fréquentiel dans le cadre eulérien, ainsi que la dominance de l'effet du balayage aléatoire dans la fonction de corrélation spatio-temporelle à petits décalages temporels. Par ailleurs, le FRG apporte de nouveaux résultats, notamment sur le comportement en temps long des fonctions de corrélation, ainsi que sur les corrélations multipoints, et sur la forme du spectre d'énergie cinétique dans le domaine dissipatif-proche. Ces nouveaux résultats sont testés numériquement dans les chapitres 3 et 4 de ce manuscrit.

Le dernier chapitre, numéro 5, du manuscrit considère également le cadre FRG en application à la turbulence. En particulier, la version en couches du modèle d'advection aléatoire de Kraichnan est étudiée dans cette approche. Dans le cas particulier de ce modèle en couches, les dérivations sont simplifiées et différentes étapes de l'analyse FRG sont présentées de manière plus détaillée.

2

Direct numerical simulation method

This chapter provides a brief description of the Direct Numerical Simulation (DNS) method for turbulent flows and the pseudo-spectral solver. It also describes the method of computation of space-time correlation of the Fourier modes of velocity, which allows to evaluate and average the correlation function progressively during the simulation. This approach allows to combine the simulation with postprocessing and avoid storing large volumes of data. The computational methods described in this chapter are used to obtain the numerical results for the velocity correlations (Chapter 3) and passive scalar correlations (Chapter 4).

Contents

Résumé en français

Ce chapitre fournit une brève description de la méthode de simulation numérique directe (DNS) pour les écoulements turbulents et du solveur pseudo-spectral. Il décrit également la méthode de calcul de la corrélation spatio-temporelle des modes de Fourier de la vitesse, qui permet d'évaluer et de moyenner la fonction de corrélation au fur et à mesure de la simulation. Cette approche permet de combiner la simulation avec le post-traitement et d'éviter le stockage de gros volumes de données. Le solveur et la procédure de calcul de corrélation décrits dans ce chapitre sont utilisés pour obtenir les résultats numériques pour les corrélations de vitesse (Chapitre 3) et les corrélations des scalaires passifs (Chapitre 4).

2.1 Background

Direct numerical simulation (DNS). The main numerical method in the present study is direct numerical simulation (DNS). It is called "direct" since it is based on the solution of the Navier-Stokes equation on a large span of scales, ranging from large scales, at which the energy is injected, to small scales, at which the dissipation occurs. The main advantage of this approach is its high accuracy, since it resolves directly all scales relevant to the dynamics of the flow and does not rely on any model parametrizing small scales. The main limitations of this approach are its high computational cost and restriction to simple geometries (Pope, 2000). One of the simplest models, accessible by DNS, is a homogeneous isotropic turbulent flow in a three-dimensional periodic box governed by incompressible Navier-Stokes equations. For the study of homogeneous isotropic turbulent flows, the main method of simulation is the pseudo-spectral DNS, pioneered by Orszag and Patterson, 1972 and Rogallo, 1981, and which is used in the present study.

Despite the apparent simplicity of a homogeneous isotropic turbulent flow in a 3D periodic box, such a flow retains the intrinsic and universal features of turbulence. For these reasons, the DNS method is mainly applied for the study of the universal statistical properties of small scales in turbulence, such as spectra of energy and energy fluxes, scaling exponents of velocity increments and gradients, intermittency effects and others (Ishihara et al., 2009).

A high computational cost of DNS has been the major limiting factor for performing DNS at large Reynolds numbers for a long time, but nowadays thanks to the tremendous development of supercomputers, it is possible to reach Reynolds numbers comparable to the ones in laboratory experiments. The first pseudo-spectral DNSs in the 1970s were run on spatial grids with $N^3 = 32^3$ points with the Taylor-scale Reynolds number around $R_\lambda \approx 20$. Nowadays, the largest DNS has been performed on a grid with $N^3 = 12288^3$ points which allows to reach $R_\lambda \approx 2000$ (Ishihara et al., 2016; Buaria and Sreenivasan, 2020). For comparison, the Taylor-scale Reynolds number in the largest sonic wind tunnel in the world in Modane is $R_\lambda \approx 500$ (Bourgoin et al., 2018).

Numerical test of FRG results. The main purpose of the present study is to test the FRG results with the use of numerical simulations of homogeneous isotropic turbulence, and the pseudo-spectral DNS appears to be the most appropriate tool. Indeed, the spectral representation of the numerical method enables a simple bridge with FRG results, for instance, for the simple computation of the space-time correlation functions in Fourier space. In addition, the limit of large wavenumbers, on which the FRG results rely, can be easily accessed in DNS by considering the relevant scales and applying spectral filters to

the fields. Another important feature of this method is that the modern implementations of pseudo-spectral DNS can be parallelized, which allows to perform simulations on large computational grids and reach high Reynolds numbers. The parallelization is possible since the core of the solver actually represents a sequence of fast Fourier transforms, for which parallel and efficient algorithms are available in standard libraries. Finally, another important particularity of DNS is the relative simplicity of the solver, since it incorporates only Navier-Stokes equations, which makes possible an easy and quick implementation of the postprocessing routines adapted for individual research tasks.

However, simulations on fine numerical grids produce a large amount of data which is not easy to process, and the problem of data storage and treatment becomes especially sharp when the temporal properties of turbulence are studied. Nowadays, the spatial properties of turbulence can be accessed with the use of the DNS databases, such as Johns Hopkins University Turbulence Database (Li et al., 2008). It provides high-quality datasets for various cases; however, the available datasets containing a long time evolution of the flow fields are less numerous. In addition, the volume of these datasets requires a lot of storage space and elaborated techniques for data treatment. For this reason, in the present study, it was decided to run new DNS simulations, in which space-time correlations and spectra are computed and averaged during the run, instead of using available databases. Such an approach allows to benefit from the parallel implementation of the solver for the data treatment and optimize the data storage.

Structure of the chapter. This chapter provides a brief description of the pseudo-spectral DNS solver used to obtain the main results of this thesis. The particular features of the solver configuration are discussed in section 2.2, such as choice of parameters, time advancement scheme, forcing scheme, and parallel data distribution. Additionally, the implemented method of the computation of space-time correlations is described in section 2.3, which is adapted to parallel execution. The chapter is concluded by a short summary in section 2.4.

2.2 Description of the the pseudo-spectral DNS solver

Pseudospectral method. All DNSs in this thesis were performed with the use of the SCALES software, developed in LEGI. It provides a pseudo-spectral solver with explicit time advancement of the incompressible Navier-Stokes equation (1.1) in three dimensions. The code SCALES represents an implementation of the canonical DNS method (Orszag and Patterson, 1972; Rogallo, 1981; Canuto, 1988) adapted to parallel execution on high performance computational clusters. The method is called "pseudo-spectral" as the equation is solved in the spectral space, except for the treatment of the nonlinear term of the NS equation. Here, the most essential details on the implementation of the solver are provided.

The computational domain represents a periodic cubic box of side length 2π with N^3 discretization points. Since the domain is periodic, it is simple to rewrite the Navier-Stokes equations (1.1),(1.2) for the velocity Fourier modes $\hat{\vec{\mathbf{u}}}(t,\vec{\mathbf{x}}) \equiv \mathrm{FT}\left[\vec{\mathbf{u}}(t,\vec{\mathbf{x}})\right]$:

$$\partial_t \hat{\vec{\mathbf{u}}}(t,\vec{\mathbf{x}}) = \hat{\vec{\mathbf{N}}}(t,\vec{\mathbf{x}}) - \nu k^2 \hat{\vec{\mathbf{u}}}(t,\vec{\mathbf{x}}) + \hat{\vec{\mathbf{f}}}(t,\vec{\mathbf{x}}), \tag{2.1}$$

$$\vec{\mathbf{k}} \cdot \hat{\vec{\mathbf{u}}}(t,\vec{\mathbf{x}}) = 0, \tag{2.2}$$

where $\hat{\vec{\mathbf{N}}} \equiv \mathrm{FT}\left[-(\vec{\mathbf{u}}\cdot\nabla)\vec{\mathbf{u}} - \frac{1}{\rho}\nabla p\right]$ is the Fourier transform of the pressure gradient and the advection terms. The pressure can be eliminated from NS equation in Fourier representation

in case of incompressibility, since its gradient coincides with the projection of the advection term on the direction parallel to $\vec{\mathbf{k}}$ (Pope, 2000, Chapter 6). The Fourier transform of the non-linear term $\hat{\vec{\mathbf{N}}}$ contains a convolution of velocity:

$$\hat{N}_l(t,\vec{\mathbf{k}}) = -ik_n P_{lm}(\vec{\mathbf{k}}) \sum_{\vec{\mathbf{k}}'} \hat{u}_m(t,\vec{\mathbf{k}})\hat{u}_n(t,\vec{\mathbf{k}}-\vec{\mathbf{k}}'), \tag{2.3}$$

where $P_{lm}(\vec{\mathbf{k}}) \equiv \delta_{lm} - \frac{k_l k_m}{k^2}$ is the operator of projection onto the plane normal to $\vec{\mathbf{k}}$.

Thanks to the incompressibility condition $\nabla \cdot \vec{\mathbf{u}} = 0$, the non-linear term $\hat{N}_l(\vec{\mathbf{k}},t)$ can be taken in its skew-symmetric form, which improves the stability and convergence of the numerical scheme:

$$\hat{N}_l(t,\vec{\mathbf{k}}) = P_{lm}(\vec{\mathbf{k}})\ \mathrm{FT}\left[\frac{1}{2}u_n(t,\vec{\mathbf{x}})\frac{\partial u_m(t,\vec{\mathbf{x}})}{\partial x_n} + \frac{1}{2}\frac{\partial [u_n(t,\vec{\mathbf{x}})u_m(t,\vec{\mathbf{x}})]}{\partial x_n}\right]. \tag{2.4}$$

In the pseudo-spectral method, the spatial derivatives $\partial/\partial x_n$ are computed in the spectral domain, where it is equivalent to a multiplication by a wavenumber k_n, while the products $u_n u_m$ and $u_n \partial_{x_n} u_m$ are computed in the physical domain, to avoid the direct computation of the convolution sums.

Dealiasing. The finite spatial resolution of the discretized computational domain gives rise to the aliasing error in the estimation of the convolutional sums used in the pseudo-spectral method. The aliasing error is reduced with the use of the polyhedral truncation method (Orszag, 1971), (Canuto, 1988, Chapter 7). In this method, the spectral representations of all fields (velocity and its derivatives) are nullified for all $\vec{\mathbf{k}}$ outside the region:

$$\begin{cases} |k_\alpha| \le N/2, & \alpha = 1,2,3, \\ |k_\alpha \pm k_\beta| \le 2N/3, & \alpha,\beta = 1,2,3, \alpha \ne \beta. \end{cases} \tag{2.5}$$

This region corresponds to a 18-sided polyhedron. The polyhedral truncation allows to keep more active (not truncated) modes comparing to the spherical truncation, as it takes into account the discreteness and cubic shape of the computational domain. All fields are truncated before the computation of the nonlinear term.

Time advancement. The linear term in Eq. (2.2) representing the molecular viscosity can be treated with the *integrating-factor technique* (Canuto, 1988, Chapter 4). The equation for a component j of a velocity Fourier mode can be rewritten in the following form:

$$\frac{d\hat{u}_j}{dt} = \hat{N}_j - \nu k^2 \hat{u}_j + \hat{f}_j, \tag{2.6}$$

$$\frac{d}{dt}\left[e^{\nu k^2 t}\hat{u}_j\right] = e^{\nu k^2 t}\left[\hat{N}_j + \hat{f}_j\right]. \tag{2.7}$$

Then, the forward Euler time advancement scheme takes the form:

$$\hat{u}_j^{n+1} = e^{-\nu k^2 \Delta t}\left[\hat{u}_j^n + \Delta t \hat{N}_j(\hat{u}^n) + \Delta t \hat{f}_j^{n+1}\right], \tag{2.8}$$

where n is the time iteration, Δt - time step, $\hat{N}_j$ is the nonlinear term evaluated with the solution $\hat{u}_j^n$ obtained at the iteration n.

The integrating-factor technique allows an unconditionally stable and exact treatment of the viscous term, and the restrictions on the time advancement step and method are determined only by the nonlinear and forcing terms.

In this work, the time derivative is approximated with the use of second-order Runge-Kutta method (RK2) for the spectral velocity fields. Taking into account the integrating factor for the viscosity term, the RK2 scheme takes form:

$$\hat{u}_j^{n+\frac{1}{2}} = e^{-\nu k^2 \Delta t/2}\left[\hat{u}_j^n + \frac{\Delta t}{2}\hat{N}_j(\hat{u}^n) + \frac{\Delta t}{2}\hat{f}_j^{n+\frac{1}{2}}\right], \tag{2.9}$$

$$\hat{u}_j^{n+1} = e^{-\nu k^2 \Delta t}\left[\hat{u}_j^n + \Delta t e^{\nu k^2 \Delta t/2}\left(\hat{N}_j(\hat{u}^{n+\frac{1}{2}}) + \hat{f}_j^{n+1}\right)\right]. \tag{2.10}$$

The second-order Runge-Kutta scheme requires only one subiteration and one level of storage of an intermediate result. It was chosen as the most appropriate for the study of time correlation, which requires the collection of data at high temporal resolution, and thus, at a sufficiently small time step. The RK2 scheme is stable at the required time steps, so it provides an optimal balance between accuracy and performance.

The time step is computed based on the Courant-Friedrichs-Lewy (CFL) condition (Ferziger and Perić, 2002):

$$\Delta t \leq C\frac{\Delta x}{\max(|u_x| + |u_y| + |u_z|)}, \tag{2.11}$$

where $\Delta x = L/N$ - spatial discretization size, C is the Courant number, taken at $C = 0.5$.

Forcing. To achieve a statistically stationary state, the velocity field is randomly forced at large scales. The forcing field is randomly renewed at each time step (and subiteration of RK2 time advancement scheme) of the simulation, and it is uncorrelated with the velocity field. The detailed description of the forcing scheme can be found in the article of Alvelius, 1999. The forcing vector field is generated in the spectral domain according to

$$\hat{\vec{\mathbf{f}}}(t, \vec{\mathbf{k}}) = A_{\text{ran}}(t, \vec{\mathbf{k}})\ \vec{\mathbf{e}}_1(\vec{\mathbf{k}}) + B_{\text{ran}}(t, \vec{\mathbf{k}})\ \vec{\mathbf{e}}_2(\vec{\mathbf{k}}), \tag{2.12}$$

where $\vec{\mathbf{e}}_1, \vec{\mathbf{e}}_2$ are orthogonal unit vectors (in order to ensure zero divergence of $\vec{\mathbf{f}}$), and the random coefficients are

$$A_{\text{ran}}(t, \vec{\mathbf{k}}) = \left(\frac{F(k)}{2\pi k^2}\right)^{1/2} \exp(i\theta_1)\sin(\phi), \tag{2.13}$$

$$B_{\text{ran}}(t, \vec{\mathbf{k}}) = \left(\frac{F(k)}{2\pi k^2}\right)^{1/2} \exp(i\theta_2)\cos(\phi), \tag{2.14}$$

with θ_1, θ_2, ϕ - uniformly distributed random real numbers $\in [0, 2\pi]$ generated at each time iteration (or sub-iteration) for each Fourier mode $\vec{\mathbf{k}}$. The function $F(k)$ is the force power spectrum, chosen in the form of a Gaussian centered at a forcing wavenumber k_f:

$$F(k) = \begin{cases} K\exp\left[-c(k-k_f)^2\right], & k_a < k < k_b, \\ 0, & \text{elsewhere}, \end{cases} \tag{2.15}$$

with the prefactor $K = \dfrac{P}{\Delta t}\dfrac{1}{\sum_{k=k_a}^{k_b}\exp\left[-c(k-k_f)^2\right]}$, where Δt is the time step and P is the power input, and the parameter c determines the width of the Gaussian function, it is taken as $c = 2$. The forcing spectrum $F(k)$ is limited to the wavenumber band between $k_a = k_f - 2$ and $k_b = k_f + 1$.

The random forcing scheme enables an approximation of the stochastic Gaussian forcing used in the theoretical framework. In addition, it does not impose any characteristic time scale arising from the correlation of the forcing, and therefore it is the best option to avoid any influence of the forcing on temporal statistics.

Parameters of forcing. The forcing power input P and the wavenumber k_f are determined by the predefined parameters of the simulation: spatial resolution N^3, Taylor-scale Reynolds number R_λ and the product of the maximal wavenumber $k_{max} = N/2$ with the Kolmogorov length scale: $H = k_{max}\eta$.

It is considered that spatial resolution given by $H = 1.5$ is sufficient for DNS (Pope, 2000, Chapter 9), and this value was taken for most numerical simulations in the present work (apart from the study of the dissipative range). The parameter H fixes the value of the Kolmogorov length scale as:

$$\eta = \frac{H}{k_{max}} = \frac{H}{N/2}.$$

Fixing the length scale η allows to calculate the power input:

$$P = \frac{\nu^3}{\eta^4}, \tag{2.16}$$

as well as the forcing wavenumber for the given Taylor-scale Reynolds number R_λ (Pope, 2000):

$$k_f = \frac{2\pi/\eta}{\left(\frac{3}{20}R_\lambda^2\right)^{3/4}} = \frac{\pi N}{H\left(\frac{3}{20}R_\lambda^2\right)^{3/4}}. \tag{2.17}$$

If $k_f < 1$, the forcing wavenumber is outside the numerical domain and the simulation is impossible. Therefore, the last expression shows that for a fixed H and the number of points N^3 there exists a maximal allowed Reynolds number R_λ to simulate a turbulent flow in the given configuration. It also shows that the required size of the numerical grid grows very fast with the Taylor-scale Reynolds number as $N^3 \sim R_\lambda^{9/2}$, demonstrating that the needed spatial resolution grows drastically with the Reynolds number, which is the major limitation of the DNS method.

Initial conditions. At the beginning of each simulation, the velocity field is initialized in the Fourier space as a random vector field with Gaussian statistics and with the wavenumber spectrum:

$$E_{init}(k) = \frac{3}{10}R_\lambda^2\nu^2\left(\frac{k}{k_f}\right)^4 \exp\left[-2\left(\frac{k}{k_f}\right)^2\right]. \tag{2.18}$$

It should be noted that the forcing scheme described above allows to start a simulation with zero velocity field, but a random filling of large scales with kinetic energy at the initialization reduces the number of iterations needed to reach the stationary state.

The computation of statics of the turbulent flow is turned on only once the stationary state is achieved. It is checked by tracing the values of the total kinetic energy (or the total variance of the scalar) in the computational domain. When the kinetic energy becomes stable, making small fluctuations around a constant value, the stationary state is considered reached. All statistical measurements from the numerical simulation presented in this thesis, such as spectra or correlation functions, are collected in the stationary regime

Parallel implementation. For simulations on large numerical grids, the pseudo-spectral solver in SCALES can be used in parallel by means of the MPI tools (Lagaert et al., 2012). In case of parallel execution, the three-dimensional computational grid is divided into partitions along 2 directions: along Y and Z in real space and along X and Y in the spectral space. Each MPI process treats a partition of the computational domain. The 3D fast Fourier transform (FFT) is performed as a sequence of one-dimensional FFTs. The 1D

FFTs do not require any communication between MPI processes and are performed with the use of FFTW library. The communications are necessary only between the consecutive 1D FFTs to reorganize the data for the Fourier transform in another direction. The same approach is applied to compute the inverse Fourier transform. It should be noted that in the described implementation of the pseudo-spectral solver, the MPI communications are invoked only for FFT, the solver algorithm itself requires only local computations that do not require any communications. However, additional communications can be needed for some data analysis operations, such as spatial averaging.

The parallelization of the code allows to run the simulation on high performance computing clusters, which is necessary in case of simulations at high Reynolds numbers on high-resolution grids. The described data organization is optimized for computations on large grids, for this reason it was used not only for the solver, but also for the data treatment. In particular, for the computation of space-time correlation functions, which are the main statistical properties of interest in the present thesis. The adopted method of computation of the space-time correlation is described in the next section.

2.3 Computation of spatio-temporal correlations

The traditional method of computation of time correlation functions consists in the evaluation of the autocorrelation functions of the time series. In application to the 3D simulations of a velocity field, it would mean that one has to gather the time series of complete Fourier velocity fields (or any other field of interest) containing $N^3/2$ points. In addition, the fields have to be recorded at sufficiently high frequency to study the correlation function at small time delays, and the total observation time must be large enough, covering at least a few typical integral times $\tau_0 = L/U_{rms}$ (with L - integral length scale, U_{rms} - root-mean-squared velocity). Although this method can be used in a straightforward manner in the case of small grid sizes (N =64 or 128), at high spatial resolutions, the treatment of the time series of all grid points imposes significant technical difficulties. At $N = 1024$ a single snapshot of one velocity field component at double precision reaches approximately 10 GB. In this case, the volume of time series including 1000 field snapshots would be above 10 TB. Writing, storing, and post-processing such volumes of data requires a lot of resources and elaborated programming techniques.

Computation method. To avoid the storage of large amounts of data and heavy post-processing, the time correlations of the Fourier fields are evaluated and averaged during the simulation once the stationary state is reached. Each snapshot of the time evolution of a flow field is treated immediately once the solver time advancement step is accomplished. To compute the time correlation without the complete time series, the spectral 3D vector velocity field at a chosen time t_0 is saved in the memory. At the next iteration, all Fourier modes of the updated velocity field at time instant $t_0 + i\Delta t$ are multiplied by the corresponding modes of the velocity field at time t_0, giving the non-averaged two-point correlation function for all $\vec{\mathbf{k}}$ at time lag Δt. The computation is entirely performed in the spectral space. Since the velocity field is statistically isotropic, the obtained two-point velocity correlation function can be averaged over spherical spectral shells. The wave vectors $\vec{\mathbf{k}}$ are divided into the shells S_n of thickness $\Delta k = 1$, so that $\vec{\mathbf{k}} \in S_n$ if $n - 1 < \left|\vec{\mathbf{k}}\right| < n$, where $n = 1, .., N/2$.

The same computation is repeated on the consequent time iterations, providing an instantaneous correlation between the current state of the field and the one saved in the

memory. After a certain number of time iterations, corresponding to a predefined period T_w, the reference time instant t_0 is reset to the current time, and the reference velocity field saved in the memory is updated. The necessary duration of the time window T_w is estimated as the time lag, at which the magnitude of the correlations at all scales of interest have already decayed close to zero. Ideally, T_w should be of duration of a few integral time scales of the flow τ_0, but to study the temporal correlation at small time lags $T_w \sim \tau_0$ appears to be enough. The resulting correlation function is averaged over time windows with different reference times t_0, and the real part is taken:

$$\bar{C}^{(2)}(t, \vec{\mathbf{k}}) = \frac{1}{N_t} \sum_{j=1}^{N_t} \frac{1}{M_n} \sum_{\vec{\mathbf{k}} \in S_n} \mathrm{Re}\left[\hat{u}_i(t_{0j}, \vec{\mathbf{k}}) \hat{u}_i^*(t_{0j} + t, \vec{\mathbf{k}})\right], \tag{2.19}$$

where N_t is the number of time windows in the simulation, M_n is the number of modes in the spectral spherical shell S_n, and $k = n\Delta k, n \in \mathbb{Z}$. It allows to obtain a numerical estimation of the two-point spatio-temporal correlation function $C^{(2)}$ defined in Eq. (1.14) with averaging in space (over spectral spherical shells) and time (over observation time windows).

Data storage. Clearly, this approach provides less data for time averaging compared to the autocorrelation function extracted from the time series. If one has a complete time series of a field, it is possible to compute the correlation of all field snapshots between each other and to average the resulting correlations obtained at the same time lag. The method proposed here evaluates the correlation between the snapshot at time instant t_0 and following N_t iterations only, and time average is performed by changing the reference time t_0. However, this approach can be easily applied to the computational grid of any size, since the evaluation of the correlation function is parallelized in the same way as the solver, and it does not require any additional significant amount of storage volume. The computed spatio-temporal correlation function is stored in memory simply as a two-dimensional table containing $T_w/\Delta t$ lines (number of iterations in a time window) and $N/2$ columns (number of spectral wave vector shells). The time average is also performed during the simulation by accumulating the values of the spatially averaged correlations in the table and dividing it by the number of time windows N_t before writing the result.

Averaging. The numerical result obtained from Eq. (2.19) depends on the amount of data collected for spatial and temporal averaging, that is, on the total number of time windows N_t and the number of Fourier modes in each individual spectral shell S_n. As a consequence, this method allows to obtain significantly better averages for high wave numbers compared to small wavenumbers, since the number of modes in a spherical shell grows quadratically with the wavenumber $M_n \propto k^2$. In addition, it is easier to access the correct statistical averages for the correlation function at small time lags, since they require shorter observation windows T_w, and therefore it is possible to collect more time windows N_t.

Testing. One of the simplest ways to test the numerical result of $C^{(2)}(t, k)$ obtained by the described method is to check its behavior at equal times. The integration of the correlation function $C^{(2)}$ over a spherical shell in Eq. (1.14) gives the spectrum of kinetic energy:

$$E(k) = 4\pi k^2 C^{(2)}(t = 0, k) = C_K \epsilon^{2/3} k^{-5/3}. \tag{2.20}$$

Some examples of the spatial spectra extracted from the numerical evaluation of $C^{(2)}(t, k)$ are provided in Fig. 3.1 (p. 49). The spectra compensated by $k^{5/3}$, corresponding to the

Kolmogorov power law of the inertial range, exhibit an emerging plateau at intermediate wavenumbers, extending with increase in R_λ. The vertical scaling by $\epsilon^{2/3}$ and horizontal by η makes the curves for various R_λ collapse, and the estimated Kolmogorov constant C_K is close to 2, which is consistent with the available data for turbulent kinetic energy spectra from experiments and numerical simulations.

The same approach is used for the computation of space-time correlations between the Fourier transforms of the velocity and advection fields in Sec. 3.3 and for the passive scalar correlation function discussed in Chapter 4.

2.4 Summary

The present chapter contains a brief description of the DNS method used in this thesis. DNS is a powerful tool in modern turbulence research, as it provides an accurate description of a turbulent flow and gives access to its various statistical properties. With the development of high-performance computing facilities and parallel computation techniques, nowadays it is possible to perform DNS at Reynolds numbers comparable to experimental values.

In the present study, the DNSs are performed for the case of three-dimensional incompressible homogeneous isotropic flow with periodic boundaries under random external forcing. The used method represents a pseudo-spectral solver in space and the Runge-Kutta scheme for time advancement. The velocity field forcing is random in space and time and is limited to large scales. The power of the forcing is adjusted to obtain the predefined value of the Taylor-microscale Reynolds number in the stationary state of the flow.

To study the statistical properties of the stationary turbulence, the correlation functions are evaluated once the stationary state is reached. The space-time correlation functions are computed and averaged "on-the-fly" during the simulation. This approach allows avoiding saving large amounts of data and to benefit from the parallelized computation of DNS for part of the postprocessing. In addition, the presented method of computation of spatio-temporal correlation functions scales easily to any grid size and can be used in general for the analysis of any statistical property containing time-delayed quantities. The results of the numerical simulations and computed space-time correlation functions are provided and discussed in the following two chapters.

Résumé en français

Le présent chapitre contient une brève description de la méthode DNS utilisée dans cette thèse. Le DNS est un outil puissant dans la recherche moderne sur la turbulence, car il fournit une description précise d'un écoulement turbulent et donne accès à ses diverses propriétés statistiques. Avec le développement des machines de calcul hautes performances et de techniques de calcul parallèle, il est aujourd'hui possible d'effectuer des DNS à des nombres de Reynolds comparables à ces valeurs expérimentales.

Dans les études présentées dans ce manuscrit, les DNS sont réalisés pour le cas d'un écoulement isotrope homogène tridimensionnel incompressible avec des conditions aux bords périodiques sous forçage externe aléatoire. La méthode utilisée représente un solveur pseudo-spectral dans l'espace et un schéma de Runge-Kutta pour l'avancement temporel. Le forçage du champ de vitesse est aléatoire dans l'espace et dans le temps et limité aux grandes échelles. La puissance du forçage est ajustée pour obtenir la valeur prédéfinie du nombre de Reynolds à l'échelle de Taylor à l'état stationnaire de l'écoulement.

Pour étudier les propriétés statistiques de la turbulence stationnaire, les fonctions de corrélations sont évaluées une fois l'état stationnaire atteint. Les fonctions de corrélation espace-temps sont calculées et moyennées "à la volée" pendant la simulation. Cette approche permet d'éviter de sauvegarder de grandes quantités de données et également de bénéficier du parallélisme de l'implémention de DNS pour une partie du post-traitement. De plus, la méthode de calcul des fonctions de corrélation spatio-temporelle présentée s'adapte facilement à n'importe quelle taille de grille et peut être utilisée en général pour l'analyse de toute propriété statistique contenant des quantités retardées. Les résultats des simulations numériques et des fonctions de corrélation espace-temps calculées sont fournis et discutés dans les deux chapitres suivants.

3

Spatio-temporal correlations of velocity

This chapter is dedicated to the study of spatio-temporal correlation functions of velocity in 3D homogeneous isotropic turbulence in Eulerian frame of reference. The conducted numerical simulations of two-point correlation function at small time lags are in total agreement with the theoretical FRG prediction. Similar results were obtained for the triple velocity correlations. In addition, the theoretically predicted kinetic energy spectrum in the near-dissipation range is observed in numerical simulations at high Reynolds numbers.

Contents

Abstract

The present chapter is devoted to the comparison of the FRG results with the direct numerical simulations of 3D homogeneous isotropic turbulent flow. It is organized as follows: first, an overview of the existing theoretical prediction for spatio-temporal correlation functions in turbulence is provided, as well as its experimental and numerical measurements. Next, the results of the numerical simulations are presented. In particular, the two-point correlation function of the velocity field at small and large time lags is studied, resulting in good agreement with the FRG prediction. In addition, a triple velocity correlation function is computed. The link between the triple correlation and the spectral energy transfer function is discussed. Moreover, the correlations of the velocity norms are considered, although this type of correlation is not covered by the theory yet. A part of these results have been published in *Physics of Fluids* (Gorbunova et al., 2021a). The last section of the chapter is dedicated to the study of the spectrum of velocity in near-dissipative range and its comparison with the FRG prediction. This result has been published in *Physical Review Fluids* (Gorbunova et al., 2020).

Résumé en français

Le présent chapitre est consacré à la comparaison des résultats FRG avec les simulations numériques directes d'écoulement turbulent isotrope homogène tridimensionnel. Il est organisé de la manière suivante : tout d'abord, un aperçu de la prédiction théorique existante de la fonction de corrélation spatio-temporelle en turbulence est fourni, ainsi que ses mesures expérimentales et numériques. Ensuite, les résultats des simulations numériques sont présentés, notamment, la fonction de corrélation à deux points du champ de vitesse à petits et grands décalages temporels. Ces résultats sont en un bon accord avec la prédiction FRG. De plus, une fonction de corrélation à trois vitesses est calculée et mise en relation avec la fonction spectrale de transfert d'énergie. En outre, les corrélations des normes de vitesse sont considérées, bien que ce type de corrélation ne soit pas couvert par la théorie. Une partie de ces résultats a été publiée dans *Physics of Fluids* (Gorbunova et al., 2021a). L'analyse du spectre de vitesse dans la zone dissipative et sa comparaison avec la prédiction FRG sont abordés en fin de chapitre. Ces résultats ont été publiés dans *Physical Review Fluids* (Gorbunova et al., 2020).

3.1 Background

This section provides an overview of the previous works dedicated to the study of spatio-temporal correlation functions in turbulence. Firstly, the differences in temporal decorrelation in Eulerian and Lagrangian frames of reference are discussed on phenomenological grounds, and in particular, the presence of the sweeping effect in the Eulerian frame. The principal works proposing the theoretical explanation of the sweeping effect, including FRG, are presented, as well as numerical studies related to this problem. The application of the sweeping hypothesis for models of various usage in fluid mechanics is also discussed. In addition, previous studies concerning correlation function at large time delays and multipoint correlations are discussed.

Role of the space-time correlations. Understanding the multipoint spatio-temporal correlations of velocity is essential for many axes of turbulence research and its applications.

To begin with, assumptions of the behavior of spatio-temporal correlations lie in the basis of some statistical theories of turbulence, such as direct-interaction approximation (Kraichnan, 1964a), models based on quasi-normal hypothesis, in particular Eddy-Damped-Quasi-Normal-Markovian (EDQNM) model (Lesieur, 2008), as well as the local-energy-transfer (LET) model (McComb and Yoffe, 2017). In addition, the advanced comprehension of the spatio-temporal correlations is crucial for studying and modeling the phenomena of wave propagation in turbulent media, for instance, sound waves (Zhou and Rubinstein, 1996). Also, the particle-laden turbulence and turbulent particle diffusion represent a complicated problem and are often studied by means of simplified kinematic models with "synthetic" turbulent flows, including certain assumptions on spatio-temporal behavior of the velocities (Fung et al., 1992). Furthermore, many numerical studies in application to geophysical and industrial problems rely on the turbulent models, such as large eddy simulation (LES) models, whose setting also requires physical understanding of spatio-temporal correlations to make time-accurate predictions (Guo et al., 2012). Apart from that, the knowledge of the spatio-temporal correlation functions in Eulerian frame of reference is necessary for experimental data treatment, for instance, in case of mapping between the spatial and temporal signals of the turbulent flows (G. He et al., 2017).

Lagrangian frame of reference. In the Lagrangian frame, the typical time of velocity correlation is determined by the evolution of individual turbulent eddies of various scales. The eddies deform and break down, creating smaller eddies, and these processes form an energy cascade from large-scale energy injection towards small scales at which the viscous dissipation occurs. The K41 theory (Kolmogorov, 1941 ; Frisch, 1995) assumes a constant energy flux throughout the scales in the inertial range. A dimensional analysis based on K41 arguments leads to a power-law form of the spatial spectrum of the turbulent kinetic energy $E(k) \sim k^{-5/3}$. A similar dimensional analysis based on the argument of energy cascade can be applied to the time scales. The estimation of a typical time of energy transfer from an eddy of size k^{-1} to smaller eddies suggest that is should scale as $\sim k^{-2/3}$, which is also known as local eddy-turnover characteristic time τ_{eddy} (Frisch, 1995). While studying the flow in the Lagrangian frame, the observer follows an individual eddy in the flow and will observe the velocity decorrelation of this fluid particle when the eddy breaks down after the typical time $\tau_{eddy} \sim k^{-2/3}$. This time scaling was observed in numerical studies (Matsumoto et al., 2021).

Eulerian frame of reference. However, in the Eulerian frame the picture is different. In addition to the individual evolution of eddies, one has to take into account the advection of the small eddies by the large-scale flow that was first suggested by Heisenberg in 1948. This effect of the large-scale advection is present even in the absence of a mean flow, and is determined by the velocity fluctuations of large-scale eddies. The large-scale velocity has a zero mean, but varies randomly in time, in the approximate range $[-U_{rms}, +U_{rms}]$. The characteristic time of variation of the large-scale velocity field is much larger than the eddy-turnover time at small scales, or in other words, large-scale eddies evolve slowly comparing to the small eddies. That is to say, the small eddies are all simultaneously advected by this slowly varying random large-scale field without any distortion. Therefore, for an observer in the Eulerian frame of reference attached to a fixed point, an eddy of size k^{-1} will be swept away from this point by a large-scale eddy in a typical time $\tau_s \sim (U_{rms}k)^{-1}$.

Sweeping and straining time scales. The question that naturally arises is which time scale will be dominant for the Eulerian time correlations: the eddy turn-over $\tau_{eddy} \sim k^{-2/3}$ (also referred as straining) or the random advection time $\tau_s \sim k^{-1}$ (also referred as sweeping). In the work of Tennekes, 1975 these two time scales are estimated and

compared on the basis of dimensional analysis, and it is concluded that for the Eulerian time correlation the sweeping effect is dominant. In other words, the eddies are swept faster than they evolve and get distorted due to the turbulent energy cascade. This conclusion was also supported by experimental and numerical evidences of the velocity frequency spectrum in Eulerian frame that takes the form of $E(\omega) \sim \omega^{-5/3}$ (Kit et al., 1995 ; Lévêque et al., 2007), the power law that arises from the sweeping time scaling. Besides, there are experimental and numerical evidences of $E_L(\omega) \sim \omega^{-2}$ for the Lagrangian frequency spectrum (Chevillard et al., 2005 ; Lévêque et al., 2007), which is also consistent with the straining time scaling $\tau \sim k^{-2/3}$.

Kraichnan's sweeping model. A simple kinematic model to describe the sweeping effect was proposed by Kraichnan (1964a). It considers a velocity field that can be decomposed into a large-scale field $\vec{\mathbf{U}}$ and the weak small-scale fluctuation $\vec{\mathbf{u}}$. The velocity $\vec{\mathbf{U}}$ is assumed to be constant (or slowly varying) in space and time and has a Gaussian and isotropic distribution, while $\vec{\mathbf{u}}$ is varying and is small in comparison with $\vec{\mathbf{U}}$. The fields $\vec{\mathbf{U}}$ and $\vec{\mathbf{u}}$ are statistically independent. Then, in the inertial range, where there is no external forcing and the viscous dissipation can be neglected, the evolution of a velocity Fourier mode is given by the following equation:

$$\frac{\partial \vec{\mathbf{u}}(\vec{\mathbf{k}}, t)}{\partial t} = -i(\vec{\mathbf{k}} \cdot \vec{\mathbf{U}})\vec{\mathbf{u}}(\vec{\mathbf{k}}, t). \tag{3.1}$$

The solution of the equation is $\vec{\mathbf{u}}(\vec{\mathbf{k}}, t) = \vec{\mathbf{u}}(\vec{\mathbf{k}}, 0)e^{-i\vec{\mathbf{k}} \cdot \vec{\mathbf{U}}t}$, and the Eulerian two-point spatio-temporal correlation function is then:

$$C^{(2)}(\vec{\mathbf{k}}, t) \equiv \left\langle \vec{\mathbf{u}}(\vec{\mathbf{k}}, t_0) \cdot \vec{\mathbf{u}}(-\vec{\mathbf{k}}, t_0 + t) \right\rangle = C^{(2)}(\vec{\mathbf{k}}, 0) \left\langle e^{-i\vec{\mathbf{k}} \cdot \vec{\mathbf{U}}t} \right\rangle = C^{(2)}(\vec{\mathbf{k}}, 0) \exp\left\{ -\frac{1}{2} U_{rms}^2 k^2 t^2 \right\}, \tag{3.2}$$

where U_{rms} is the root-mean-square of $\vec{\mathbf{U}}$. This result follows from the assumption that the large-scale velocity component $\vec{\mathbf{U}}$ has a Gaussian distribution. Therefore, this simple model leads to a correlation function in the form of a Gaussian function of a variable kt with a characteristic decorrelation time $\tau_D = \sqrt{2}/(U_{rms}k)$, and thus $\tau_D \sim k^{-1}$, which is very close to the FRG prediction for the velocity correlation function at small time lags provided by the expression (1.16).

Surely, this result is based on very strong assumptions. The theoretical grounds and limits of the application of this simplified model are not clear, since it is not evident when this sort of decomposition into $\vec{\mathbf{U}}$ and $\vec{\mathbf{u}}$ can be valid for real turbulent flows, and to which extension statistical independence of $\vec{\mathbf{U}}$ and $\vec{\mathbf{u}}$ can be assumed. However, more elaborated theoretical approaches (see below), as well as the FRG, lead to similar results: the velocity correlation function decays as a Gaussian of the variable tk, which indicates that the mechanism of random sweeping described by Kraichnan, 1964a remains dominant in more complicated models.

Besides, this simplified model puts forward an essential point that should be taken into account in numerical studies: the Gaussian in the correlation function arises from averaging of the complex phases of correlation over an ensemble of random realizations of the large-scale velocity field. Relating it to numerical simulations means that the measured correlation function has to be properly averaged. The ensemble averaging can be replaced by the temporal average, but the duration of the observation has then to be larger than the characteristic time of the velocity field variation.

Theoretical confirmation of the sweeping effect. Although the physical idea behind the sweeping effect is quite simple, the rigorous derivation of this time scaling on the basis of the Navier-Stokes equation is not straightforward. The recent article of Zhou, 2021 provides a large overview on the random sweeping effect in statistical models of turbulence.

The Eulerian spatio-temporal correlation functions were analyzed in the works of Kaneda, 1993; Kaneda et al., 1999 with the use of the Taylor expansion in powers of time. It shows that the leading-order term of the expansion of the two-point correlation function at small time delays is equivalent to (3.2). In addition, these works provide an analysis of the correlation function in Lagrangian frame of reference, resulting in $\tau \sim k^{-2/3}$ scaling for the correlation function. In the work of Kaneda et al., 1999, this approach is developed further and supported by direct numerical simulations.

On the other hand, the results obtained with the use of the perturbative renormalization group (RNG) approach (Yakhot and Orszag, 1986) suggest that the sweeping effect results in having a minor effect (Yakhot et al., 1989). However, as discussed in the works (Kraichnan, 1987; Chen and Kraichnan, 1989; Nelkin and Tabor, 1990), the model used in the perturbative RG approach developed by Yakhot and Orszag, 1986 actually discards the sweeping effect in the premises, and its results are physically valid only in a quasi-Lagrangian sense, apriori free of sweeping.

In a more recent work of Drivas et al., 2017, the Eulerian space-time correlations were analyzed in a more rigorous way on the basis of a band-pass filtering technique applied to the Navier-Stokes equation. The results confirm the dominant contribution of the large-scale sweeping to the Eulerian correlation function at small scales.

The Eulerian space-time correlations were also analyzed within the stretched-spiral vortex model (O'Gorman and Pullin, 2004), where the turbulent flow is modeled as an ensemble of tube-like vortices. The sweeping time scale arises in this framework as well, if the centers of the vortex structures are considered as moving with random velocities.

FRG result. As presented earlier in the Chapter 1, dedicated to the description of the FRG approach to the NS turbulence, the leading order term in the two-point space-time Eulerian correlation function of velocity at small time lags (1.16) takes the form of a Gaussian in the variable tk, which is similar to the Eq. (3.2) obtained within the simplified model of random sweeping. In other words, it validates the sweeping scaling at small time lags in a rigorous and systematic way, since it is based only on the NS equation and its symmetries. Moreover, it allows to expand the results to multipoint spatio-temporal correlations and to the large-time-lag regime.

Numerical confirmation of sweeping effect. The typical decorrelation time scaling $\tau_D \sim k^{-1}$ has been observed in DNS of homogeneous isotropic turbulence through the computation of the space-time correlation function of Fourier modes (Orszag and Patterson, 1972; Sanada and Shanmugasundaram, 1992; Gotoh et al., 1993; Kaneda et al., 1999; O'Gorman and Pullin, 2004; G.-W. He et al., 2004; Favier et al., 2010). In addition, numerically computed space-time spectrum of the kinetic energy in 3D homogeneous isotropic turbulence (Clark di Leoni et al., 2015) demonstrates that the energy is concentrated near and below the line $\omega = U_{\text{rms}}k$, where ω is the angular frequency, which also corresponds to the sweeping time scaling.

The numerical results for the Eulerian two-point space-time correlation function of velocity presented in this thesis in section 3.2 also confirm the scaling corresponding to the random sweeping effect in the space-time correlation function of velocity at small time lags.

Sweeping hypothesis in models. An *ad hoc* assumption of the sweeping hypothesis appears to be useful in phenomenological models. For instance, it was used to obtain a *model of wavenumber-frequency spectrum* of a turbulent flow (Wilczek and Narita, 2012), resulting in:

$$R(\vec{\mathbf{k}},\omega) = \frac{E(\vec{\mathbf{k}})}{\sqrt{2\pi k^2 U_{rms}^2}} \exp\left[-\frac{(\omega - \vec{\mathbf{k}}\cdot\vec{\mathbf{U}}_0)^2}{2k^2U_{rms}^2}\right], \tag{3.3}$$

which implies that the mean velocity $\vec{\mathbf{U}}_0$ leads to a Doppler shift in frequency, while the sweeping, characterized by the fluctuation velocity U_{rms}, leads to a broadening in the frequency spectrum. This model spectrum was used to improve the modeling of wall turbulence (Wilczek et al., 2015) and atmospheric boundary layers (Wilczek et al., 2014), and also to predict power fluctuations of wind farms (Liu et al., 2017; Lukassen et al., 2018). Apart from that, this spectrum model appears to be applicable to the case of strong magnetohydrodynamic turbulence (Perez and Bourouaine, 2020).

The approximated inverse Fourier transform of Eq. (3.3) leads to the *elliptic approximation* (G.-W. He and Zhang, 2006) for Eulerian space-time correlation in physical space. This model suggests a relation between the space-time correlation function $R(\vec{\mathbf{r}},\tau)$ and the purely spatial correlations $R(r,0)$ in the following form:

$$R(\vec{\mathbf{r}},t) \equiv \langle \vec{\mathbf{u}}(\vec{\mathbf{x}},t_0)\vec{\mathbf{u}}(\vec{\mathbf{x}}+\vec{\mathbf{r}},t_0+t)\rangle = R\left(\sqrt{(r-U_0t)^2 + U_{rms}^2t^2}, 0\right). \tag{3.4}$$

One can see that the isolines of the correlation function $R(\vec{\mathbf{r}},t)$ (3.4) on $t-r$ plane represent ellipses. This model provides an inclusion of the sweeping decorrelation effect in the "frozen flow" model (Taylor, 1938), which is largely used for the mapping between experimentally measured temporal and spatial signals in turbulent flows with constant convection velocity U_0. The elliptic model provides a reliable method for the time-space signal mapping in cases when the turbulent fluctuations are large and Taylor's frozen flow hypothesis is not valid. It has been tested in numerical simulations (Zhao and G.-W. He, 2009), as well as in the experimental measurements in turbulent Rayleigh-Bénard convection (X. He and Tong, 2011). It has also been applied for improving near-wall numerical turbulence models (T. Wu and G. He, 2021). Details on validation and application of the elliptic model can be found in the reviews (Wallace, 2014; G. He et al., 2017).

Sweeping-free models. It should be mentioned that there are a number of works focused on the study of temporal correlations "cleaned" from the sweeping effect to understand the nontrivial temporal dynamics determined by the energy cascade. It can be performed, for instance, by means of Lagrangian history closure (Kraichnan, 1965), the Lagrangian renormalized approximation method (Kaneda et al., 1999) or within the quasi-Lagrangian framework introduced in the work of Belinicher and V. S. L'vov, 1987. The multitime-multiscale correlation functions within the quasi-Lagrangian framework were studied in works (V. S. L'vov et al., 1997; Biferale et al., 1999; Daems et al., 1999; Biferale et al., 2011). In addition, the shell models of turbulence, which are apriori free of sweeping, can also provide an insight into time correlations in the presence of energy cascade (Kadanoff et al., 1995; Biferale et al., 1999; Biferale, 2003; Pandit et al., 2008).

However, physical interpretation of results obtained from models without sweeping is not an easy task. The necessary assumptions and consequences of the elimination of the sweeping effect are discussed in the work of Gkioulekas, 2007.

Large time delays. It is important to highlight that the aforementioned behavior of the correlation function as a Gaussian of tk-variable is expected only for small time lags. At larger time lags (comparable with the integral typical time τ_0), the FRG predicts a

crossover to a new regime in the temporal behavior of the velocity correlation function: from the Gaussian in time at small time delays it changes to an exponential decay at large time delays. As it was discussed in section 1.4, the two regimes of temporal decay in the velocity Eulerian correlation function can be linked to the ballistic and diffusive regimes of the single-particle dispersion in turbulent flows. However, such a crossover in the temporal behavior of the Eulerian correlation function has not been reported before the FRG results.

The importance of understanding of the large-time statistics in turbulence has been discussed previously, in particular regarding the velocity increments in the Lagrangian frame of reference (Mordant et al., 2002; Chevillard et al., 2005; Lévêque et al., 2007). A crossover to another regime at large time lags was reported in the experimental study of the modal correlation of the amplitudes of vorticity (Poulain et al., 2006). However, the correlation of the amplitudes represents completely different type of the correlation function, which is beyond the scope of the FRG result presented here, but it will be discussed more in section 3.4.

Multi-point multi-time spatio-temporal correlations. As turbulence does not have Gaussian statistics at small scales, the knowledge of two-point correlations is not sufficient to obtain a reliable description. However, much less research has been conducted for multi-time multipoint statistics of turbulence. In the quasi-Lagrangian framework, the multipoint correlation functions (V. L'vov and Procaccia, 1996) and multi-time correlation functions (V. S. L'vov et al., 1997; Biferale et al., 2011) were studied. In the work of Biferale et al., 1999, the multi-point multi-scale correlations are analyzed within the multi-fractal approach, and in the work of Eyink, 2000 with use of fluctuation-response relations. At the same time, assumptions on the behavior of the three- and four-point correlations lie in the core of some closure approximations, such as DIA (Kraichnan, 1964a) or LET (McComb and Yoffe, 2017).

The FRG approach provides a statistical description of the turbulent flow in terms of n-point n-time correlation functions as it is discussed in Chapter 1. In section 3.3 of the present chapter, the three-point space-time correlation function of velocity is estimated numerically and compared with the FRG result.

Summary. The fact that the sweeping effect is dominant in the Eulerian space-time correlations of the velocity field is known from numerical and experimental studies. It also lies in the core of some models, such as frequency-wavenumber spectrum or the elliptic model of space-time correlations, which are largely applied in various fields. Despite this, the theoretical validation of the sweeping effect appears not to be straightforward and even controversial, although the mechanism behind it is rather trivial.

The validity of the random sweeping hypothesis for Eulerian correlations is supported by recent results obtained with the FRG approach in application to NS equations. It allows to conclude that the sweeping contribution to Eulerian velocity decorrelation is dominant, and this result is based on the NS equation itself and its symmetries and does not require an additional hypothesis. In addition, it allows to conclude that the dominance of the sweeping effect extends to n-point n-time correlation functions at small time lags. Apart from that, the FRG indicates a transition to the exponential form of the correlation decay at large time lags.

In the present thesis, the dominance of the sweeping effect is confirmed for the two- and three-point correlation functions in Eulerian frame of reference. These results are provided in the following sections.

Structure of the chapter. In the present chapter, the results of numerical simulation testing the FRG prediction are provided. In particular, the two-point Eulerian correlation of

velocity (sec. 3.2) is measured in DNS at various Reynolds numbers, and it is shown that at small time lags the correlation functions are indeed dominated by the sweeping scaling. The section (sec. 3.3) is dedicated to the numerical computation of a triple velocity correlation function, which also has the sweeping scaling at small times as predicted by the FRG. The results presented here do not allow to capture the behavior of the correlation functions at large time lags, as the signal becomes too weak and is sensitive to numerical noise. However, it is possible to observe a transition between short- and large-time regimes in the correlation function of the velocity norms (sec. 3.4), though this type of correlation function is not covered by the theoretical prediction. Lastly, the FRG prediction for the spectrum of kinetic energy in the near-dissipation range (sec. 3.5) has been tested, which results from taking an appropriate time limit of the two-point space-time correlation function of velocity. The numerically computed spectra approach the theoretically predicted form with increasing Reynolds number. The chapter finishes with a list of conclusions coming from the main results.

3.2 Two-point space-time velocity correlation function

3.2.1 Numerical set-up

The simulations were performed with the use of the direct numerical simulation (DNS) method. The essential details of the solver are provided in chapter 2. The spatio-temporal correlations of velocity were studied in simulations at 5 values of the Taylor-scale Reynolds number: $R_\lambda = 40, 60, 90, 160, 250$. The corresponding spatial grid sizes are $N^3 = 64^3, 128^3, 256^3, 512^3, 1024^3$. The spatial resolution of all simulations fulfills the condition $k_{max}\eta \simeq 1.5$, where $k_{max} = N/2$ is the maximal wavenumber in the simulation and η is the Kolmogorov length scale. Other parameters of the simulations are provided in the Table 3.1.

R_λ	N	ν	U_{rms}	τ_0	Δt	ΔT_w	N_t	K_cL
40	64	10^{-4}	0.0059	245	0.9	400	1008	14.6
60	128	10^{-4}	0.0147	134	0.1	75	665	23.7
90	256	10^{-4}	0.0375	45.3	0.03	10.0	624	42.5
160	512	10^{-4}	0.0974	19.0	0.005	1.0	322	74.4
250	1024	10^{-4}	0.2482	7.24	0.001	0.2	33	144

TABLE *3.1 – Parameters of simulations for the analysis of two-point and three-point correlations at small time delays. R_λ - Taylor-scale Reynolds number, N - spatial grid resolution, ν - kinematic viscosity, U_{rms} - root-mean-square velocity, τ_0 - eddy-turnover time at the integral scale, Δt - simulation time step, ΔT_w - width of a time window of correlation observation, N_t - number of recorded time windows, K_cL- nondimensional cut-off wavenumber of the scale decomposition.*

3.2.2 Results of DNS

Once the stationary state is reached, the spatio-temporal correlations of velocity were computed following the method described in Sec. 2.3. The compensated spatial spectra

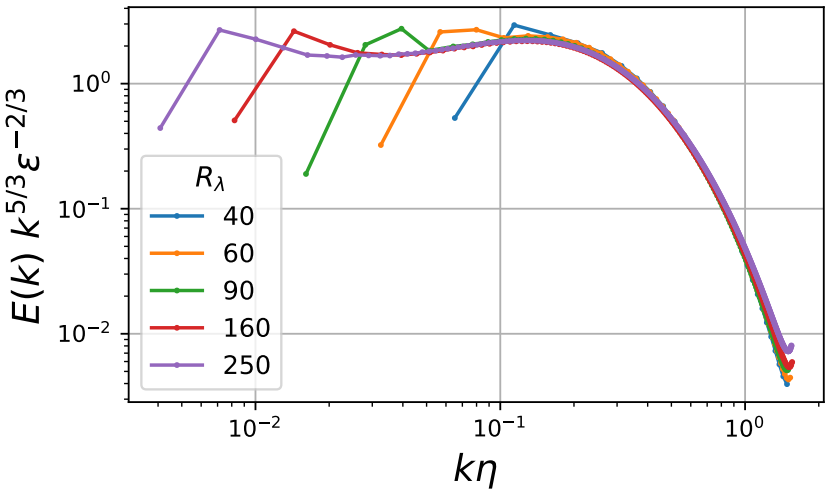

FIGURE *3.1 – Compensated spatial spectrum of the kinetic energy obtained from the averaged two-point spatio-temporal correlation function* $C^{(2)}$ *at zero time delay according to Eq. (2.20). Here,* ϵ *is the average energy dissipation rate.*

obtained from the averaged two-point spatio-temporal correlation function at zero time delay are shown in Fig. 3.1. The inertial ranges of these spectra match the Kolmogorov 5/3 power-law decay and are followed by the dissipation range. At the lowest $R_\lambda = 40$, there is no visible inertial range, while at the largest $R_\lambda = 250$ it extends over about one decade of wavenumbers. In addition to kinetic energy spectra, the spectra of dissipation, energy transfer, and energy flux were computed, they are provided in Appendix A.

To test the FRG prediction (1.16), the numerically computed two-point correlation functions are averaged in space and time, and their dependence on the time lag t, wavenumber k and Taylor-scale Reynolds number R_λ is analyzed.

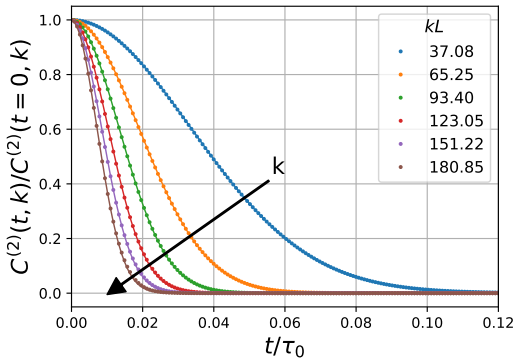

(a) Data from the numerical simulation denoted with dots and its Gaussian fits denoted with continuous lines.

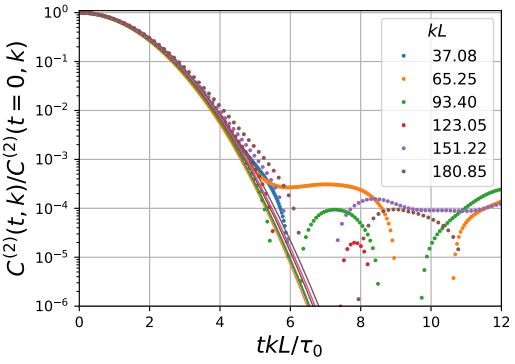

(b) Same data plotted as a function of the variable tk which results in the collapse of all the curves

FIGURE *3.2 – Time dependence of the normalized two-point correlation function* $C^{(2)}(t,k)$ *at different wavenumbers* k *in the simulation at* $R_\lambda = 90$*. Here* L *is the integral length scale,* τ_0 *is the integral eddy-turnover time scale.*

Dependence on time lag. According to the theoretical expression (1.16), a Gaussian dependence in t for small time delays is expected, and it is precisely observed in all simulations. An example of the numerical results for temporal dependence $C^{(2)}$ at various

wavenumbers is provided in Fig. 3.2. All data is normalized by the correlation function for coincident times $C^{(2)}(t=0,k)$. One can see that all curves display a Gaussian behavior, as the data matches perfectly the Gaussian fit. Moreover, when plotted as a function of the variable tk, as it can be observed in Fig. 3.2b, all the curves collapse into a single Gaussian, as expected from Eq. (1.16). The collapse is observed for curves at all wavenumbers that are sufficiently separated from the forcing range. The influence of the forcing on the temporal decorrelation will be discussed in the following section 3.2.3. As it was shown earlier, the tk scaling originates in the random sweeping of the small-scale eddies by slowly fluctuating large-scale velocity fields. At larger time lags, the data points start deviating from the Gaussian fit and oscillating around zero, taking negative values. This large-time behavior is discussed in the end of the present section.

Dependence on wavenumber. The scaling tk that appears in the correlation function can be observed more precisely by analyzing the Gaussian fits. The time correlation curves at various wavenumbers and various Reynolds numbers were fitted using the non-linear least-squares method (Levenberg–Marquardt algorithm), with the Gaussian fitting function: $f_s(t) = ce^{-(t/\tau_s)^2}$ where τ_s and c are the fitting parameters. The fitting range for all data sets corresponds to the range of non-dimensional variable $(tkL/\tau_0) \in [0, 2.5]$. Within this range, all correlation functions are accurately modeled by the Gaussian $f_s(t)$. Performing a non-dimensionalization with parameter $L/\tau_0 \approx U_{rms}$ renders the correlation function plots at various Reynolds numbers comparable. It indicates again that the decorrelation is determined by the random sweeping effect, which is characterized by large-scale velocity fluctuations. The fitting parameter τ_s is the characteristic time scale of the cor-

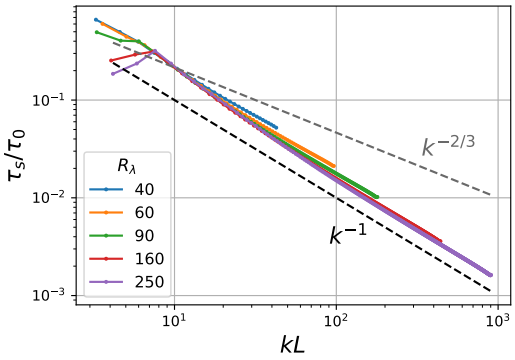

(a) Dependence of the characteristic decorrelation time τ_s on the wavenumber.

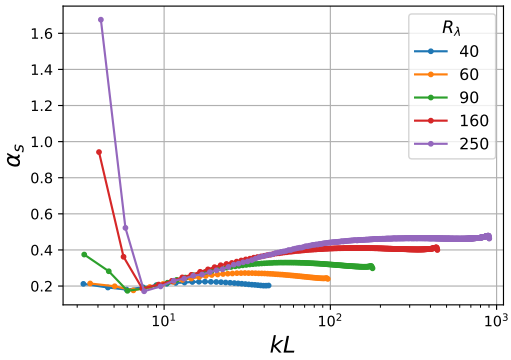

(b) Dependence of the decorrelation parameter α_S in the Eq. (1.16) on the wavenumber.

FIGURE *3.3 – Dependence of the correlation parameters on the wavenumber. The values of the parameters are obtained with the Gaussian fit.*

relation function, its dependence on the wavenumber k is shown in Fig. 3.3a for various R_λ. While for small wavenumbers the dependence is not regular, at intermediate and large wavenumbers, the decorrelation time clearly decays as k^{-1}. This result concurs with the collapse in the Fig. 3.2 occurring for the tk-scaling.

Similarly, one can estimate the coefficient α_S in the theoretical expression Eq. (1.16) from the fits: $\alpha_S \approx (\tau_0/\tau_s kL)^2$. The parameter α_S is expected to be a constant in the limit of large wavenumbers. Plotting α_S versus k as in Fig. 3.3b shows that the numerical estimation of α_S reaches a plateau at large wavenumbers. One can see that the value of kL at which α_S settles to this plateau appears to be dependent on R_λ. It should be highlighted that although the theoretically expected constant value of the prefactor α_S is established only at sufficiently high wavenumbers, the Gaussian shape of the correlation function is

clearly observed in the whole range of spectral modes, including the forcing range.

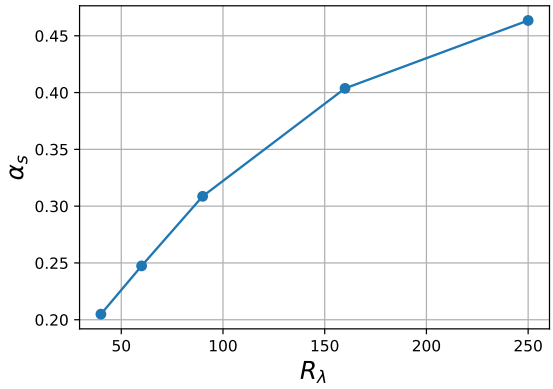

FIGURE *3.4 – Dependence of the plateau value of the decorrelation parameter α_S on Taylor-scale Reynolds number R_λ.*

Dependence on the Reynolds number. The plateau values of α_S in the Fig. 3.3b appear to be dependent on the Reynolds number. This dependence is displayed in Fig. 3.4, showing that α_S grows non-linearly with the Taylor-microscale Reynolds number. At the same time, the FRG result presented in Sec. 1.2.2 suggests that α_S is independent from the Reynolds number at the fixed point of the RG flow equations, which corresponds to the state of the fully developed stationary turbulence, i.e. at high Reynolds numbers. The observed dependence of the prefactor α_S on R_λ can be a consequence of the moderate values of Reynolds number used in DNS in this work. Based on the results of FRG, it is expected that with R_λ increasing further, the parameter α_S will vary weakly and eventually reach a constant value at sufficiently high R_λ.

It is also important to mention that in the FRG result the prefactor α_S is not universal, as it depends on the particular choice of the velocity forcing profile. The influence of the form of forcing profile on the decorrelation parameter α_S has not been investigated in the present work.

In all simulations, the forcing location and its width have the same values, although the spatial resolution of the numerical grid and the amplitude of forcing vary with the Reynolds number. In addition, the finite size of the computational domain and the proximity of the forcing length scale to the size of the box can also affect the numerically obtained values of the decorrelation parameter α_S, which can imply an additional difference with the theoretical model.

Deviation from the Gaussian at larger time delays. Although the analysis of the correlation functions at small time lags allows to see clearly the Gaussian decay and the sweeping time scale, the analysis of the correlation curves at larger time lags is a much more difficult problem. As it was shown in the Fig. 3.2b, with increasing time lags, the correlation curves start deviating from the Gaussian fits and oscillate around zero. These oscillations impede a straightforward analysis of the correlation behavior at large time lags. The presence of oscillations can be related to the low level of the signal of the correlation functions at large time lags, which makes the results more sensitive to numerical errors and the averaging procedure.

The Fig. 3.5 displays the same data points as Fig. 3.2, with thin continuous lines representing the numerical data and thick lines highlighting a portion of the curve where the relative deviation from the Gaussian fit is more than 10% and the magnitude of the

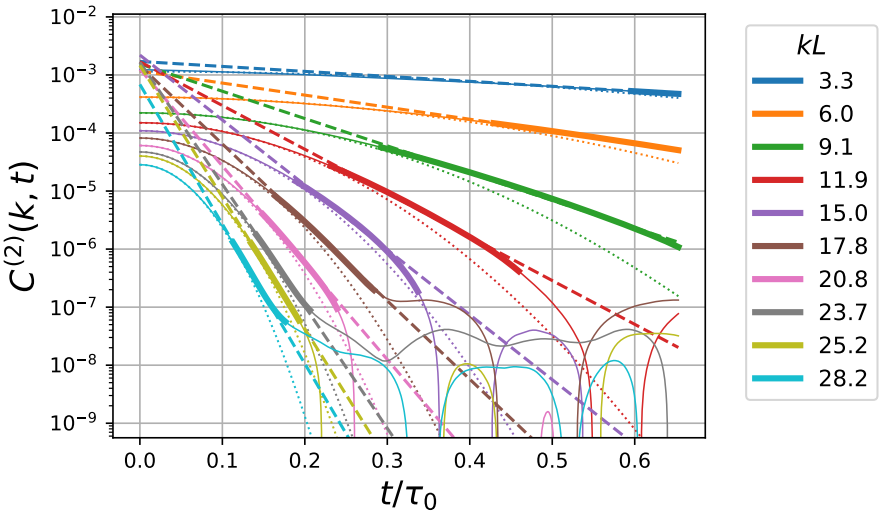

FIGURE *3.5 – Illustration of the deviation from the Gaussian fit at larger time lags. The thin continuous lines represent the numerically computed* $C^{(2)}$ *from the simulation at* $R_\lambda = 90$. *The thick lines indicate the portion of the curves where the deviation from the Gaussian fit becomes larger than 10%. The dotted lines correspond to the Gaussian fit, the dashed lines to the exponential fit of the highlighted portions of the curves.*

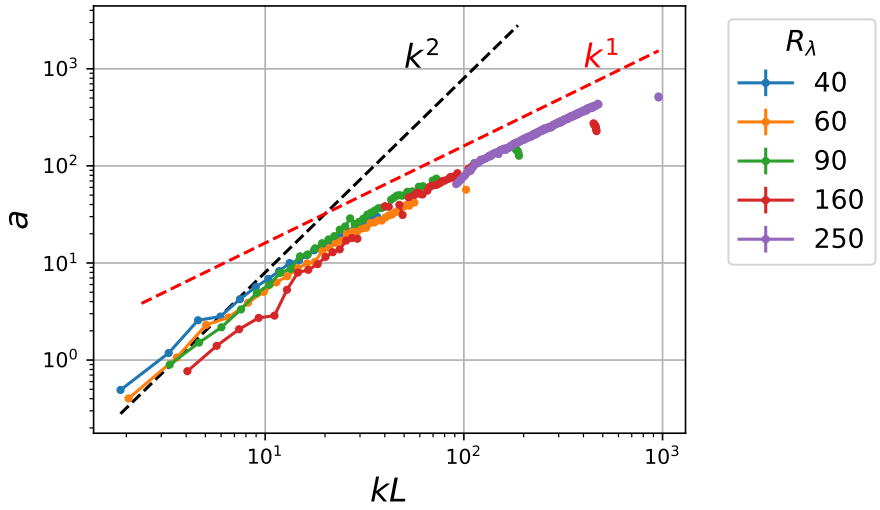

FIGURE *3.6 – Dependence of the parameter* a *of the exponential fit* $f(t) = c\exp^{-at}$ *on wavenumber for different Reynolds number. The straight dashed lines corresponding to* k^1 *and* k^2 *are shown as guide lines.*

correlation function is larger than 0.5% the initial magnitude at $t = 0$ (the second cut-off is needed to exclude the oscillating part from the analysis). This portion of the data points, where the curves start deviating from the Gaussian, can be fitted with a linear function in the y-logarithmic scaling, therefore, the correlation function decays approximately as an exponential in this range. It is important to mention that such a portion of data points in the correlation function is not found for some wavenumbers k, as some correlation curves switch to oscillations right after the Gaussian part.

The exponential fits in the form $f(t) = c\exp^{-at}$ of these data portions are shown in Fig. 3.5 with dashed lines. According to the FRG prediction in Eq. (1.16), one expects that the Gaussian decay changes to an exponential $\exp\left\{-\alpha_L k^2 t\right\}$. Thus, the dependence of the fit parameter on the wavenumber is expected to be of the form $a \sim k^2$. However, as it is shown in the Fig. 3.6, the resulting dependence does not demonstrate a clear power law in k. At small k the dependence is closer to $a \sim k^2$, while at large R_λ and large k at is rather $a \sim k^1$, with a large transitional part in between. One can also see that there are a lot of missing points in the plot, because the used method did not capture any portion of the correlation time curve corresponding to the given criteria (deviation from Gaussian more than 10% and amplitude larger than 0.5% of $C^{(2)}(k, t = 0)$). The fragmented results do not allow one to draw any clear conclusion on the available data. It should be also noted that these fits require additional tests on their sensitivity to the fitting range, and the criteria of the choice of the range for fitting probably have to be reconsidered. For instance, the dependence of the fitting parameter $a \sim k$ can result from the exponential fitting of a data portion, where the correlation function actually still continues the Gaussian decay, so the fitting procedure should be improved to exclude such a bias.

Clearly, analysis of the large-time-lag behavior of the correlation function poses much more stringent requirements on the observation time and amount of data for time averaging. Collecting more data would allow to average out the oscillations progressively to a certain degree; however, the adopted method of computation of correlation functions does not allow to access the large time-lag regime.

3.2.3 Discussion

Influence of forcing on the decorrelation parameter α_S. The deflection of the decorrelation parameter α_S from the plateau value at low wavenumbers k in Fig. 3.3b can be attributed to the effect of the forcing in the numerical scheme. This effect can be observed from the analysis of the direct energy transfer to the modes of the forcing range. Fig. 3.7 shows the rate of energy transfer that occurs between the modes in the forcing range and the modes in the shell corresponding to the wavenumber k. These energy transfers were obtained from shell-to-shell energy transfer computation (Verma, 2019), with the use of a filtered velocity field; this method will be discussed further in Sec. 3.3.2 and is described in detail in Appendix B.

The "ideal" numerical simulation would exhibit in Fig. 3.7 a single peak of energy transfer near the forcing range itself, indicating that all modal exchanges are local, that is to say that the smaller scales receive energy only from the neighboring scales through the turbulent energy cascade. However, Fig. 3.7 shows that energy exchanges with the participation of the forcing modes occur not only in the closest vicinity of the forcing range, but they are present also at a significant level over a band of wavenumbers, the width of which depends on R_λ. This means that the wavenumbers in this band are subjected not only to energy exchange due to the turbulent cascade involving neighboring scales only, but also to direct energy transfer from the forcing range. The occurrence of this type of energy transfer in DNS can be a consequence of the velocity forcing concentrated in a narrow spectral band at large scales, as discussed in the work of Kuczaj et al., 2006. The

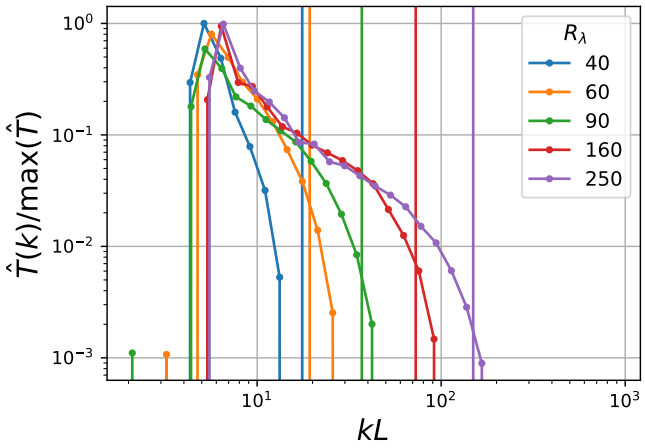

FIGURE *3.7 – Rate of the direct energy transfer from the forcing range to the wavenumbers k normalized by the maximal value at various Reynolds numbers. The vertical colored lines correspond to the cut-off wavenumber K_c of the filter introduced in Sec. 3.3.2.*

intensity and spread of these energy transfers apparently depend on the particular choice of the forcing amplitude and its spectral profile, therefore, one would expect to observe some non-universal features in the range of wavenumbers affected by these interactions. Remarkably, these energy transfers are also present in the simulations at very low Reynolds number, corresponding to the laminar flows, where the energy cascade is absent (Verma et al., 2018).

The mentioned direct energy exchanges with the forcing modes slow down the velocity decorrelation and result in lower values of α_S at small k. Matching the horizontal axes of the figures 3.3b and 3.7 shows that the parameter α_S reaches a constant value at wavenumbers where the direct energy exchanges with the forcing modes become negligible. One can conclude from these observations that the "large wavenumber" regime of the FRG can be here identified as the values of kL such that direct energy transfers from the forcing range are negligible.

Comparison with other works. The analysis presented in this section concurs with results from the work of Kaneda, 1993, in which the Eulerian velocity correlation function is studied by means of a Taylor expansion in powers of time. It is shown that the sweeping time scaling arises from interactions with modes at much smaller wavenumbers (which corresponds to the "sweeping" by a large-scale mode). These interactions are predominant for $kL \gg 1$, while for small wavenumbers there is no scale separation for the interacting modes, and the characteristic decorrelation time is estimated to be smaller. Similar deviations from the sweeping time scaling at small kL were observed in other DNS studies of the velocity correlation function, although the typical decorrelation time scale can be measured with different methods. For instance, in the works of Sanada and Shanmugasundaram, 1992; Favier et al., 2010 the characteristic decorrelation time was estimated by integrating the correlation function, while in the work Kaneda et al., 1999 the characteristic decorrelation time is measured through the second time derivative of the correlation function.

Role of statistical averaging. As discussed in Sec. 3.1, the simple kinematic model of sweeping (Kraichnan, 1964a) suggests that the Gaussian form of the time dependence of the correlation function arises from averaging over rapid oscillations of phases of the velocity Fourier modes. This implies that in numerical simulations, the correlation function should be averaged over a large number of realizations of the large-scale field, or in other words,

the simulation should run much longer than the large-scale eddy-turnover time τ_0 in order to average out the oscillations correctly. In the present work, in addition to time averaging, the isotropy of the flow is exploited by averaging the correlation functions in space over spectral shells, according to Eq. (2.19), which allows to accumulate more statistics for the results.

It should be mentioned that in the numerical study of Verma et al., 2020 another averaging procedure has been implemented, without spatial averaging. Clearly, if one observes the temporal evolution and autocorrelation of a single Fourier mode, the observation time for averaging needs to be very long to achieve the correct averaging. In the mentioned work, the resulting correlation curves exhibit more oscillatory behavior, and the measured scaling of the characteristic correlation time differs from the results presented in this chapter. It highlights the importance of the averaging method for the sweeping effect.

Oscillations in correlation functions. As it was shown in Fig. 3.5, the numerically obtained space-time correlation functions exhibit oscillations at large time lags. The question of the oscillations in Eulerian space-time correlations is discussed in the work of Rubinstein and G.-W. He, 2003. In particular, it is shown that even in a simple kinematic sweeping model proposed by Kraichnan, 1964a and mentioned in Sec. 3.1, changing from the assumption of a purely Gaussian probability density function for the large-scale velocity to a sub-Gaussian (truncated Gaussian) distribution leads to oscillatory solutions for the two-point Eulerian correlation function. Certainly, in numerical simulations, even in the case of a very large amount of statistics in averages, the Gaussian distribution of the large-scale velocity is always truncated. To reduce the influence of this truncation, it is necessary to extend the tail of the velocity probability distribution by counting more rare events, thus, to collect more data. Clearly, the influence of these oscillations becomes more significant for the large-time part of the correlation function, where the magnitudes of the correlations are low.

Large time lags. Although the amount of data collected in the simulations to obtain the statistical averages is enough to study the correlation function at small time lags, the behavior of the correlation function at large time lags appears to be still oscillatory. After the small-time Gaussian decay, the temporal correlation curves mainly demonstrate strong oscillations around zero. The analysis of the fragments of the correlation function which deviate from the Gaussian fit at large time lags does not allow to determine the form of the curve and the dependence of its behavior on the wavenumber, since a significant number of curves turn to oscillations right after the short-time Gaussian part.

The magnitudes of the correlations at large time lags are weak and they are more subjected to numerical and statistical errors compared to the part of the correlation function at small time lags. A qualitative analysis of the variance of the correlation function at large time lags demonstrates that the amplitudes of the oscillations tend to decrease when augmenting the number of temporal observation windows. However, in the data obtained during the current study, the oscillations are still present and impede the observation and analysis of the correlation function at large time lags. At the moment, the DNS data available in the presented study does not allow to draw any solid conclusion about large-time regime of the correlation function.

To improve the quality of data at large time lags, one needs to run longer simulations, which then would cost more computational hours. Another possible way is to improve the method of computation of correlation functions by adding, for example, more referential time instants. However, it would require significantly more memory. Another way to improve the large-time correlation data, which appears to be more promising, is to increase the size of the computational domain. It can be achieved by shifting the peak wavenumber

of the velocity forcing k_f to larger values. It would allow to decrease the integral time scale τ_0 and thus to accelerate the time averaging. Switching to a larger box would also augment the amount of spatial statistics for large scales, which in turn would certainly improve the results of their temporal statistics. However, it also requires more computational resources, since larger computational grids are needed.

It is worth to mention that the passive scalar in the turbulent flow exhibits the same behavior in its Eulerian correlation function. As it will be presented in Chapter 4, for passive scalars, the large-time part of the correlation function remains oscillatory. However, it is possible to observe the large-time regime and transition to it in case of scalar advection in a synthetic velocity field, as it will be shown further in Sec. 4.3.

Summary. The two-point spatio-temporal correlation function in the Eulerian frame of reference has been studied with the use of DNS. The data accurately confirms the theoretical expression (1.16) for the two-point spatio-temporal correlations of the turbulent velocity field for various scales and Reynolds numbers at small time delays. In particular, the numerical data show that the theoretical parameter α_S reaches a plateau at large wavenumbers, in agreement with the theoretical result. The analysis of the modal interactions in the forcing range shows that one can consider that the "large-wavenumber" regime in the DNS, observed as the plateau in α_S, is reached at wavenumbers which do not receive energy directly from the forcing modes. The time-correlations at the intermediate wavenumbers are "polluted" by the additional direct interaction with the forcing, which results in the slowing down the decorrelation in velocities. This results are also consistent with previous studies of the Eulerian two-point space-time correlations. Regarding the form of the space-time correlation function, at large time lags, the presented DNS data does not allow to draw any firm conclusion. The correlation functions at large times become oscillatory and sensitive to numerical and statistical errors. Apparently, another DNS set-up is required for the study of the large-time regime.

3.3 Triple velocity correlation

This section is dedicated to numerical validation of the form of the three-point spatio-temporal correlations $C^{(3)}$ resulting from FRG analysis in DNS. As it was mentioned in Sec. 3.1, due to the fact that turbulence exhibits non-Gaussian behavior, a two-point statistical description is not sufficient. For this reason, the multipoint statistical moments are essential for the statistical study of turbulence. The FRG approach gives a prediction for a generic n-point space-time correlation function of velocity, and in this section the three-point correlation function is studied.

To begin with, one needs to recall the definition of $C^{(3)}$ that is used many times in this section:

$$C^{(3)}_{\alpha\beta\gamma}(t_1,\vec{\mathbf{k}}_1,t_2,\vec{\mathbf{k}}_2) \equiv \left\langle \hat{u}_\alpha(t_0+t_1,\vec{\mathbf{k}}_1)\hat{u}_\beta(t_0+t_2,\vec{\mathbf{k}}_2)\hat{u}^*_\gamma(t_0,\vec{\mathbf{k}}_1+\vec{\mathbf{k}}_2)\right\rangle . \tag{3.5}$$

In contrast to the two-point correlation function $C^{(2)}$, the product in the expression (3.5) is not local in the spectral domain, as it includes the velocity field taken at three different wavevectors. When parallel computation and parallel memory distribution are used, the access to such non-local quantities requires the implementation of additional communication operations between the processors during the simulation. This implies a great increase of computation time and memory.

To avoid these additional implementation difficulties and computational costs, a local triple velocity statistical moment is studied, which naturally arises from the Navier-Stokes equation as the correlation between its nonlinear term (advection) and the velocity. A similar quantity was already introduced in earlier works (Kraichnan, 1959). It will be shown in the following section that it corresponds to a specific configuration of space-time arguments of the general three-point correlation function (3.5).

3.3.1 Advection-velocity correlation function

Definition. The Navier-Stokes equation in the spectral space can be written as:

$$\partial_t \hat{u}_j(t,\vec{\mathbf{k}}) = \hat{N}_j(t,\vec{\mathbf{k}}) - \nu k^2 \hat{u}_j(t,\vec{\mathbf{k}}) + \hat{f}_j(t,\vec{\mathbf{k}}), \tag{3.6}$$

where $\hat{N}_j(t,\vec{\mathbf{k}}) = -ik_n P_{jm} \sum_{k'} \hat{u}_m(t,\vec{\mathbf{k}}')\hat{u}_n(t,\vec{\mathbf{k}}-\vec{\mathbf{k}}')$ is the Fourier transform of the advection and pressure gradient terms of the Navier-Stokes equation, $P_{ij} = \delta_{ij} - k_i k_j/k^2$ is the projection tensor and $\hat{f}_\ell$ is the spectral forcing. Writing Eq. (3.6) at time $t+t_0$, multiplying it by the conjugated velocity $\hat{u}^*_\ell(t_0,\vec{\mathbf{k}})$ at a fixed time t_0 and performing an ensemble average lead to the following equation for the two-point spatio-temporal correlation function:

$$(\partial_t + \nu k^2) C^{(2)}(t,\vec{\mathbf{k}}) = \hat{T}(t,\vec{\mathbf{k}}) + \hat{F}(t,\vec{\mathbf{k}}), \tag{3.7}$$

with

$$\hat{T}(t,\vec{\mathbf{k}}) \equiv \left\langle \hat{N}_i(t+t_0,\vec{\mathbf{k}})\hat{u}^*_i(t_0,\vec{\mathbf{k}}) \right\rangle, \tag{3.8}$$

$$\hat{F}(t,\vec{\mathbf{k}}) \equiv \left\langle \hat{f}_i(t+t_0,\vec{\mathbf{k}})\hat{u}^*_i(t_0,\vec{\mathbf{k}}) \right\rangle, \tag{3.9}$$

where $\hat{T}(t,\vec{\mathbf{k}})$ is the spatio-temporal correlation of the advection and velocity, and $\hat{F}(t,\vec{\mathbf{k}})$ is the spatio-temporal correlation of the spectral forcing and velocity. Note that if the time delay is set to zero ($t = 0$), then Eq. (3.7) simplifies to the well-known equation (Pope, 2000, Chapter 6) of the evolution of the average kinetic energy of a single spectral mode (after summing together with the complex conjugated equation), which is referred to as the energy transfer relation (Frisch, 1995, Chapter 6):

$$\partial_t E_{kin}(\vec{\mathbf{k}}) = \frac{1}{2}\mathrm{Re}\left[\hat{T}(0,\vec{\mathbf{k}})\right] - \hat{D}(\vec{\mathbf{k}}) + \frac{1}{2}\mathrm{Re}\left[\hat{F}(0,\vec{\mathbf{k}})\right], \tag{3.10}$$

with $E_{kin}(\vec{\mathbf{k}}) \equiv \frac{1}{2}\left\langle \hat{u}(t,\vec{\mathbf{k}})\hat{u}^*(t,\vec{\mathbf{k}}) \right\rangle = \frac{1}{2}C^{(2)}(0,\vec{\mathbf{k}})$ - kinetic energy of a Fourier mode and $\hat{D}(\vec{\mathbf{k}}) \equiv 2\nu k^2 E_{kin}(\vec{\mathbf{k}})$ - spectrum of the viscous dissipation rate. The term $\frac{1}{2}\mathrm{Re}\left[\hat{T}(0,\vec{\mathbf{k}})\right]$ thus corresponds to the nonlinear energy tranfers from all modes in the system to the mode $\hat{u}(\vec{\mathbf{k}})$, and the last term corresponds to the forcing power input, which is zero outside the forcing range.

Link with the three-point correlation function. The advection-velocity correlation function $\hat{T}$ is a triple correlation, and its link with the three-point correlation function $C^{(3)}$ becomes clear if one develops the nonlinear term in the definition of $\hat{T}(t,\vec{\mathbf{k}})$:

$$\begin{aligned}\hat{T}(t,\vec{\mathbf{k}}) &\equiv \left\langle \hat{N}_\ell(t_0+t,\vec{\mathbf{k}})\hat{u}^*_\ell(t_0,\vec{\mathbf{k}}) \right\rangle \\ &= -ik_n P_{\ell m} \sum_{k'} \left\langle \hat{u}_m(t+t_0,\vec{\mathbf{k}}')\hat{u}_n(t+t_0,\vec{\mathbf{k}}-\vec{\mathbf{k}}')\hat{u}^*_\ell(t_0,\vec{\mathbf{k}}) \right\rangle \\ &= -ik_n P_{\ell m} \sum_{k'} C^{(3)}_{mn\ell}(t,\vec{\mathbf{k}}',t,\vec{\mathbf{k}}-\vec{\mathbf{k}}').\end{aligned} \tag{3.11}$$

Hence, the correlation function $\hat{T}$ actually provides a linear combination of three-point correlation functions. Since the theoretical prediction (1.24) suggests that all correlation functions $C^{(3)}(t,\vec{\mathbf{k}}',t,\vec{\mathbf{k}}-\vec{\mathbf{k}}')$ take the form of a Gaussian of the variable tk (at small times and large wavenumbers), the advection-velocity correlation function $\hat{T}(t,\vec{\mathbf{k}})$ that includes the sum over $C^{(3)}$, is expected also to have the same Gaussian dependence in tk:

$$\hat{T}(t,\vec{\mathbf{k}}) \sim \sum_{k'} C^{(3)}_{mn\ell}(t,\vec{\mathbf{k}}',t,\vec{\mathbf{k}}-\vec{\mathbf{k}}') \sim \exp\left\{-\alpha_S (L/\tau_0)^2 k^2 t^2\right\}, \tag{3.12}$$

with $k = |\vec{\mathbf{k}}|$.

Link with the variation of the two-point correlation function. Another useful property of the correlation function $\hat{T}$ is its link with the two-point correlation function $C^{(2)}$. Considering a small time delay t, one can use the expression for the two-point correlation function $C^{(2)}_S(t,\vec{\mathbf{k}})$ from Eq. (1.16), which also takes the form of a Gaussian in tk. Inserting this result into Eq. (3.7) leads to an explicit expression for the function $\hat{T}$ at small time delays (and for wavenumbers outside the forcing range):

$$\begin{aligned}\hat{T}(t,\vec{\mathbf{k}}) = \nu k^2 C^{(2)}(0,\vec{\mathbf{k}}) \left(1 - \frac{2\alpha_S L^2}{\tau_0^2 \nu} t\right) \exp\left\{ -\alpha_S (L/\tau_0)^2 k^2 t^2 \right\} = \\ = \hat{D}(\vec{\mathbf{k}}) \left(1 - 2\alpha_S Re \frac{t}{\tau_0}\right) \exp\left\{ -\alpha_S (L/\tau_0)^2 k^2 t^2 \right\},\end{aligned} \tag{3.13}$$

where $\hat{D}(\vec{\mathbf{k}}) = \nu k^2 C^{(2)}(0,\vec{\mathbf{k}})$ is the spectrum of dissipation and $Re = \frac{U_{rms} L}{\nu}$ is the Reynolds number. Eq. (3.13) indicates that the function $\hat{T}$ is in general not symmetric with respect to the origin of the t-axis, and that it can have a minimum and maximum at non-zero time delays. At the same time, at zero time delay $t = 0$ this expression turns into the simple equality $\hat{T} = \hat{D}$ meaning that the energy transfer of a Fourier mode is balanced by the viscous dissipation, which is expected in the case of the stationary flow at scales beyond the forcing range.

Numerical computation of $\hat{T}$. In the numerical simulations, the computation of the correlation function $\hat{T}(t,\vec{\mathbf{k}})$ is performed as the multiplication of each Fourier mode of the nonlinear term $\hat{N}(t_0+t,\vec{\mathbf{k}})$ by the corresponding modes of the complex conjugated velocity field $\hat{u}^*(t_0,\vec{\mathbf{k}})$. The nonlinear term $\hat{N}$ is evaluated at each time iteration of the pseudo-spectral solver, and therefore, it is easily accessible. This quantity $\hat{T}$ is local in the spectral space and the computation does not require significantly more computational resources.

The velocity-advection correlation functions $\hat{T}$ are collected and averaged during the run-time of the simulation with the use of the same method as for the two-point correlation function, as described in in the Sec. 2.3. However, in this case, since the two quantities in the correlation function are different, the correlation function is not expected to be symmetrical relative to the axis $t = 0$ in the general case, so it becomes necessary to take into account the sign of the time delay: the negative time delays t correspond to time instants before the reference time t_0, while the positive ones to the time instants after t_0. The advection-velocity correlation function $\hat{T}$ at negative time delays can be computed just by switching the time instants of the fields in the following way:

$$\hat{T}(t,\vec{\mathbf{k}}) = \begin{cases} \left\langle \hat{N}_i(t_0+|t|,\vec{\mathbf{k}}) \hat{u}_i^*(t_0,\vec{\mathbf{k}}) \right\rangle, & t > 0, \\ \left\langle \hat{N}_i(t_0,\vec{\mathbf{k}}) \hat{u}_i^*(t_0+|t|,\vec{\mathbf{k}}) \right\rangle, & t < 0. \end{cases} \tag{3.14}$$

Hence, to compute the correlation $\hat{T}(t,\vec{\mathbf{k}})$ at negative time delays during the simulation one only needs to store the spectral advection field at one reference time t_0.

Summary. The advection-velocity correlation function $\hat{T}$ is a local triple statistical quantity in spectral space, as it implies the multiplication of the advection and velocity fields at the same wave vector $\vec{\mathbf{k}}$, and it represents a linear combination of three-point velocity correlation functions in a particular configuration. The equivalence of the function $\hat{T}$ at zero time delay with the spectral energy transfer function and its link with the two-point spatio-temporal correlation function Eq. (3.7) facilitate the testing of the numerical method and the interpretation of the results in the following.

Note that an equation similar to Eq. (3.7) is also used in the Direct Interaction Approximation scheme (DIA) (Kraichnan, 1959), where a time dependent triple statistical quantity similar to $\hat{T}$ is introduced. Moreover, the equation Eq. (3.7) lies in the core of the local energy transfer (LET) closure. The recent work (McComb and Yoffe, 2017) extends the LET approach to two-time statistics and investigates a two-time triple statistical moment, equivalent to $\hat{T}$.

3.3.2 Scale decomposition and link to spectral energy transfer function

Although the advection-velocity correlation function $\hat{T}$ provides a triple statistical quantity that can be easily accessed in numerical simulations, it contains a summation coming from the convolution in the advection term Eq. (3.11). Contributions from all possible wavevector triads $\{\vec{\mathbf{k}}', \vec{\mathbf{k}}-\vec{\mathbf{k}}', \vec{\mathbf{k}}\}$ of any scale are thus summed up. However, the FRG prediction Eq. (1.23) is valid in the limit where all three wavenumbers are large. One hence needs to refine this sum to eliminate contributions from the triads containing small wavenumbers.

Velocity filtering. The simplest way to solve this issue is to perform a scale decomposition of the velocity fields. A threshold wavenumber K_c is set, so that all wavevectors of smaller norm $|\vec{\mathbf{k}}| < K_c$ are considered as "large" scales and are denoted with a superscript L, whereas the modes with higher wavenumbers are considered as "small scales" and denoted with S. The velocity field is decomposed into small- and large-scale parts $\vec{\mathbf{u}} = \vec{\mathbf{u}}^L + \vec{\mathbf{u}}^S$. In the spectral domain, the decomposition is performed by a simple box-filtering operation:

$$\hat{u}_i^L(\vec{\mathbf{k}},t) = \begin{cases} \hat{u}_i(\vec{\mathbf{k}},t), & |\vec{\mathbf{k}}| < K_c \\ 0, & |\vec{\mathbf{k}}| \geq K_c \end{cases} \qquad \hat{u}_i^S(\vec{\mathbf{k}},t) = \begin{cases} 0, & |\vec{\mathbf{k}}| < K_c \\ \hat{u}_i(\vec{\mathbf{k}},t), & |\vec{\mathbf{k}}| \geq K_c \end{cases} \tag{3.15}$$

The velocity field scale decomposition leads to a decomposition of the advection-velocity correlation function $\hat{T}$ into four terms. (the derivation of this decomposition from the NS equations is provided in Appendix C). Here, the energy transfer function is written for a wavevector $\vec{\mathbf{k}}$ belonging to the small-scale range:

$$\hat{T}(\vec{\mathbf{k}},t) = \left[\hat{T}^{SSS} + \hat{T}^{SLS} + \hat{T}^{SSL} + \hat{T}^{SLL}\right](\vec{\mathbf{k}},t), \tag{3.16}$$

with $\hat{T}^{XYZ}(\vec{\mathbf{k}},t,t_0) = -[\hat{u}_i^X]^*(\vec{\mathbf{k}},t_0)\ \mathrm{FT}[u_j^Y \partial_j u_i^Z](\vec{\mathbf{k}},t_0+t)$ where X,Y,Z stand for S or L. A similar decomposition at equal times has been used in studies of the energy transfer function (Frisch, 1995; Verma, 2019). The complete expressions for the various terms of the scale decomposition are provided in Appendix C.

Notations. Using the terminology of the book of Verma, 2019, the energy transfer terms are written as $\hat{T}^{XYZ}$. Each superscript X,Y,Z can be either S ("small" scale) or L ("large"

scale). The first superscript X is related to the mode that receives energy in a triadic interaction process (it is actually the mode $\vec{\mathbf{k}}$ for which the equation (3.16) is written), the intermediate superscript Y denotes the mediator mode and the last superscript Z is related to the giver mode that sends the energy to the receiver mode $\vec{\mathbf{k}}$. The mediator mode does not loose nor receive energy in the interaction, it corresponds to the velocity field which comes as a prefactor of the operator nabla in the nonlinear term of the Navier-Stokes equation, so one can term it the "advecting" field.

Interpretation. The term $\hat{T}^{SSS}$ gathers all triadic interactions where the three modes belong to the small scale. The term $\hat{T}^{SLS}$ contains the energy transfers between two small scales mediated by large-scale modes, which thus represent the triads involved in the sweeping. Both energy exchanges $\hat{T}^{SSS}$ and $\hat{T}^{SLS}$ occur between small scales, and are thus local in spectral space, so they form the turbulent energy cascade. The terms $\hat{T}^{SSL}$ and $\hat{T}^{SLL}$ denote the energy transfers from large-scale modes to small-scale ones, thus they are nonlocal and are expected to be small compared to the local ones. In what follows, only the results concerning the all-small-scale term $\hat{T}^{SSS}$ are presented and discussed, as this term corresponds to the limit of large wavenumbers on which the theoretical prediction relies. It is also compared with the total non-filtered correlation $\hat{T}$ to highlight the role of filtering in the result. The other terms of decomposition $\hat{T}^{SLS}$ and $\hat{T}^{SSL} + \hat{T}^{SLL}$ were also analyzed, these results are provided in Appendix C, where one can find in particular the comparison of the contribution of each term of the decomposition to the total energy transfer (see Fig. C.1).

Choice of the filter cut-off wavenumber. The cut-off wavenumber K_c of the filter in the Eq. (3.15) is chosen in such a way that at $k \gtrsim K_c$ the direct energy transfer between the forcing range and small-scale modes becomes negligible. The rate of energy exchange with the forcing range is computed with the method of shell-to-shell energy transfer, based on the method described in the book of Verma, 2019 and briefly summarized in Appendix B, where also the full matrices of shell-to-shell energy transfers computed in DNS are presented (see. Fig.B.2). The direct energy exchanges with the forcing range correspond to a single line of the energy transfer matrix at a fixed wavenumber of the giver mode, located in the forcing range (see Fig. B.3). The dependence of these energy transfers on the wavenumber of the receiving mode for different Reynolds numbers are shown in the Fig. 3.7 (p. 54). The chosen filtering wavenumber K_c is indicated as a vertical line of the corresponding color. It is expected that the dynamics of the modes at $k \gtrsim K_c$ does not depend directly on the forcing mechanism and the correlation functions approach the universal behavior predicted by the theory. The numerical value of $K_c L$ used for each simulation is provided in Table 3.1 (p. 48). As discussed in Sec. 3.2.3, the wavenumbers $k \gtrsim K_c$ approximately correspond to the range of validity of the theoretical prediction for the two-point correlation function at large wavenumbers (see Fig. 3.3).

3.3.3 Results of DNS

The data presented in this section is obtained from the same set of simulations used for the analysis of the two-point correlation function at small time delays in Sec. 3.2 and described in Table 3.1.

Difference between filtered and non-filtered $\hat{T}$. The results for the time dependence of $\hat{T}$ at different wavenumbers $k \gtrsim K_c$ are shown in Fig. 3.8. One observes that the total (non-filtered) advection-velocity correlation function $\hat{T}$ (Fig. 3.8a) is not symmetric with respect to the time origin and takes negative values. This form is in qualitative agreement

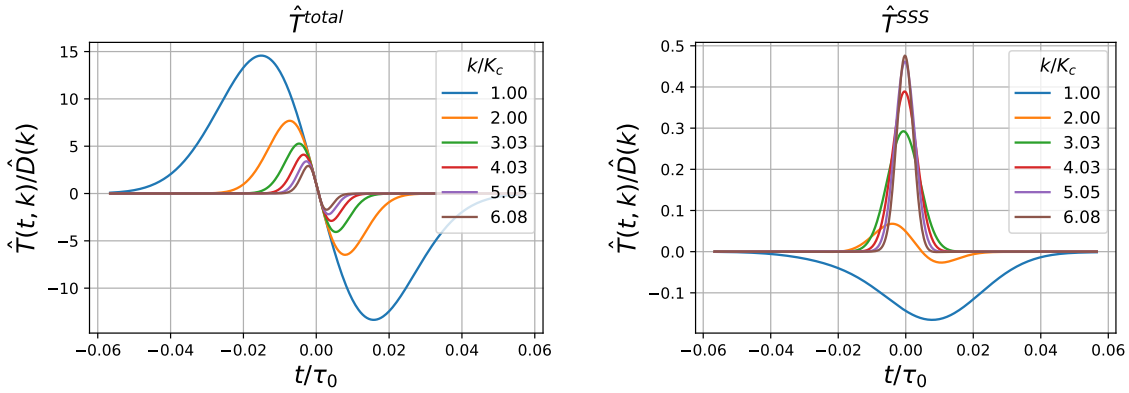

(a) Total (non-filtered) function $\hat{T}$

(b) Small-scale-only filtered function $\hat{T}$

FIGURE *3.8 – The non-filtered and filtered advection-velocity spatio-temporal correlation functions $\hat{T}(t,k)$ versus time at selected values of wavenumbers k/K_c from simulation $R_\lambda = 160$, $N = 512$. The curves are normalized by the spectrum of dissipation $\hat{D}(k) = \nu k^2 C^{(2)}(0,k)$.*

with the form of the Eq. (3.13). In contrast, the filtered term $\hat{T}^{SSS}$, which only contains contributions from small scale modes to the correlation function $\hat{T}$, significantly changes shape (Fig. 3.8b).

For the wavenumbers close to the cut-off wavenumber K_c, the curves are affected by the filter. To explain this, one should recall that at zero time delay $\hat{T}^{SSS}(t=0,\vec{\mathbf{k}})$ is equal to the local nonlinear energy transfer between small-scale modes. At wavenumbers close to the filter cut-off K_c, some spectral modes participating in local energy transfers are suppressed by the filter. Thus, the modes close to the filter cut-off transmit the energy to smaller scales, but they do not receive energy from the nullified larger scales, which results in a negative energy balance.

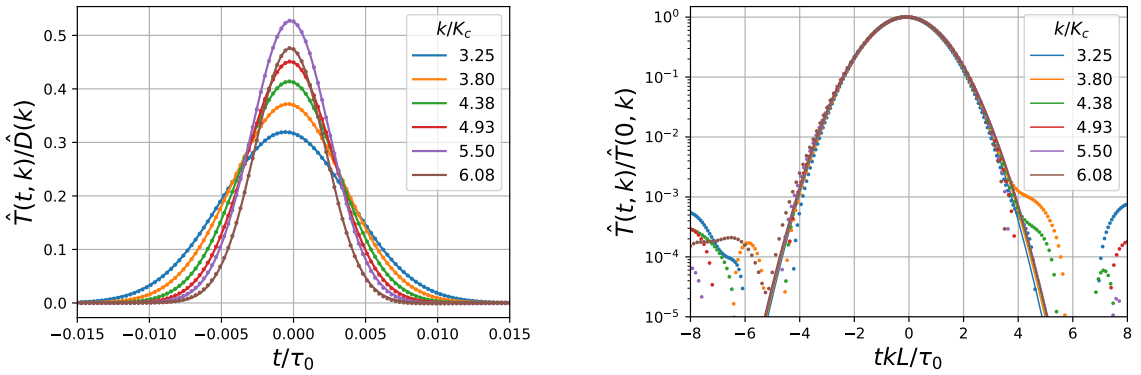

(a) Normalization by dissipation spectrum $\hat{D}(k)$

(b) Normalization by $\hat{T}(0,k)$ and in horizontal scaling $\sim tk$.

FIGURE *3.9 – The small-scale-only advection-velocity correlation function $\hat{T}^{SSS}$ versus tk at large wavenumbers $k \gtrsim 2K_c$, for $R_\lambda = 160$, $N = 512$. The same data is presented in two different scalings. The numerical data is denoted with dots, the continuous lines correspond to fit with the function $f(t)$ from the Eq. (3.17).*

For the larger wavenumbers $k \gtrsim 2K_c$, the curves of the filtered correlation $\hat{T}^{SSS}$ deform towards the expected Gaussian and the negative part becomes indiscernible, as it can be seen in Fig. 3.9a. Moreover, when plotting $\hat{T}^{SSS}$ versus the scaling variable tk in semi

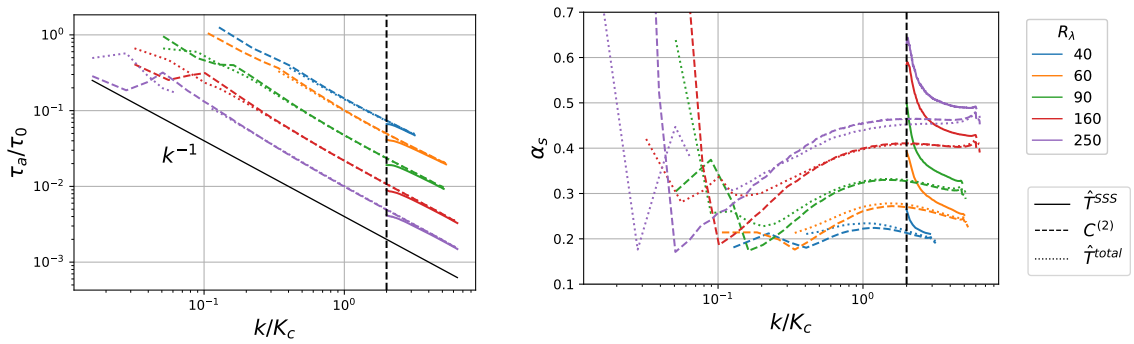

(a) Characteristic decorrelation time τ_a *(b) Decorrelation parameter α_S*

FIGURE *3.10 – Numerical estimation of the decorrelation parameters τ_a and α_S obtained from the small scale advection-velocity correlation $\hat{T}^{SSS}$ (continuous lines), compared with the result for the two-point correlation function $C^{(2)}$ (dashed lines). Both estimations converge to a similar value, as expected from the theory. The result of the fitting for the total advection-velocity correlation $\hat{T}^{total}$ is also indicated with dotted lines for completeness.*

logarithmic scale as in Fig. 3.9b, all the curves collapse into a single Gaussian. This is in plain agreement with the theoretical result (1.23) for the three-point correlation function. This behavior is very similar to the one for the two-point correlation function presented in Fig. 3.2.

All curves for various advection-correlation functions $\hat{T}$ were fitted with a function representing the product of a linear function and a Gaussian, similar to the expression (3.13), corresponding to the expected behavior of the non-filtered $\hat{T}$:

$$f(t) = c \underbrace{\left(1 - \frac{t}{\tau_b}\right)}_{\text{linear part}} \underbrace{e^{-(t/\tau_a)^2}}_{\text{Gaussian part}}, \tag{3.17}$$

where τ_a, τ_b and c are the parameters. Both correlation functions $\hat{T}$ and $\hat{T}^{SSS}$ accurately match the fitting function (3.17). It can be seen in the Fig. 3.9 where the resulting fits are shown as continuous lines together with the numerical data points. The dependence of the parameter τ_a, corresponding to the Gaussian part of the fitting function, and of the the parameter τ_b, corresponding to the linear part, on the wavenumber k are discussed in the following paragraphs. Note that both parameters τ_a and τ_b have units of time, which simplifies the interpretation.

Gaussian part. The fitting parameter τ_a for both functions is proportional to k^{-1} in simulations at various Reynolds numbers, as displayed in Fig. 3.10a. This result is in agreement with the theoretical prediction Eq. (1.23) and corresponds to the sweeping time scale. The fit allows as well to estimate the decorrelation parameter α_S introduced in Eq. (1.24) as $\alpha_S = \tau_0/(\tau_a k^2 L^2)$. The result is shown in Fig. 3.10b which allows to compare the correlation parameter of the Gaussian part extracted from fits of the filtered small-scale-only function $\hat{T}^{SSS}$ and the non-filtered $\hat{T}^{total}$, as well as the one from the fit of the two-point correlation function that has been already presented in Fig. 3.3b. One can see that at sufficiently large wavenumbers, the values of α_S extracted from both filtered function $\hat{T}^{SSS}$ and from total $\hat{T}$ are comparable. Furthermore, they match the values obtained from $C^{(2)}$, presented in the previous section. This result is in agreement with the theoretical prediction, which indicates that the decorrelation parameter α_S is the same for the two- and three-point correlation functions. The small discrepancy between the values

of α_S from $C^{(2)}$ and from $\hat{T}^{SSS}$ could be attributed to the influence of the filter cut-off. In addition, the filtered quantity suffers from a loss of accuracy, since the magnitude of the filtered signal is much weaker, so it is more sensitive to the noise in numerical results.

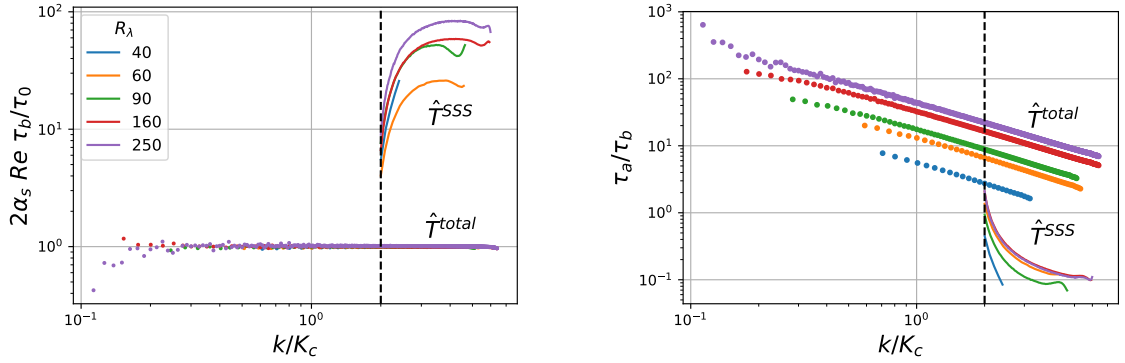

(a) Characteristic decorrelation time τ_b, normalized by $\tau_0/2\alpha_S Re$.

(b) Relation between the decorrelation time scales τ_a and τ_b.

FIGURE *3.11 – Dependence of the parameter τ_b of the fitting function Eq. (3.17) on the wavenumber for the small scale advection-velocity correlation $\hat{T}^{SSS}$ (continuous) and for the total $\hat{T}$ (dotted lines).*

Linear part. The fit (3.17) provides also an estimation of the parameter τ_b that characterizes the time scale of the linear part of the function. For the non-filtered $\hat{T}^{total}$ the time scale τ_b can be also estimated through Eq. (3.13), which was obtained from the Navier-Stokes equation assuming that the two-point correlation function $C^{(2)}$ is a Gaussian function, bringing the following expression:

$$\tau_b = \frac{\tau_0}{2\alpha_S Re}. \tag{3.18}$$

Fig. 3.11a shows the dependence of the non-dimensional parameter $2\alpha_S Re\tau_b/\tau_0$ on the wavenumber. The values of α_S are taken from the fit of the two-point correlation function $C^{(2)}$ analyzed in Sec. 3.2. As expected, for the total (non-filtered) advection-velocity correlation function $\hat{T}$ the values from all simulations are close to one independently of the wavenumber, which is consistent with Eq. (3.18). At the same time, the points corresponding to the filtered function $\hat{T}^{SSS}$ deviate significantly from unity.

This fact can be also observed from the Fig. 3.11b showing the ratio between the two time scales τ_a and τ_b. For $\hat{T}^{SSS}$ the relation time scale τ_a/τ_b is at least one order of magnitude smaller than for the total $\hat{T}$. This means that for $\hat{T}^{SSS}$ the time scale of the linear part τ_b of the function (3.17) becomes much larger than the time scale τ_a of the Gaussian part. In other words, the Gaussian part decays fast and the correlation function already approaches zero before the slower linear part comes into play, which results in the Gaussian-like shapes of $\hat{T}^{SSS}$ in the figures 3.8 and 3.9b. On the contrary, for the total (non-filtered) function $\hat{T}$ the time scale τ_b is smaller than τ_a and the shape of the total $\hat{T}$ is dominated by the linear part at short times, resulting in a non-symmetric shape.

3.3.4 Discussion

Link with the energy transfer. An interpretation of these results can be proposed based on the identification of the advection-velocity correlation function $\hat{T}$ at $t = 0$ as the spectral energy transfer function. The simulations show that a significant part of the

energy exchanges between the small scales in 3D turbulence occurs in spectral triads with the participation of a large-scale mode as a mediator (the term $\hat{T}^{SLS}$ in the decomposition (3.16) - see Appendix C). The same conclusion can be found in other studies (Verma, 2019 ; Domaradzki and Rogallo, 1990 ; Ohkitani and Kida, 1992). However, as discussed in the work of Aluie and Eyink, 2009, although the triads of this type have significant individual contributions to energy transfer, they are much less numerous than the fully local triads formed of small-scale modes (the term $\hat{T}^{SSS}$ in the decomposition), because there are fewer large-scale modes. In the limit of large Reynolds number and large wavenumbers, the fully local triads become numerous and dominate in the turbulent energy cascade.

Non-filtered $\hat{T}$. The detailed analysis of the contributions in the decomposition (3.16) shows that the nonsymmetric behavior in time of the total correlation $\hat{T}$ is also inherited from the contribution of $\hat{T}^{SLS}$ (See Fig. C.2b). The occurrence of the maximal and minimal values of the non-filtered advection-velocity correlation $\hat{T}$ at non-zero time delays (see the top panel of the Fig. 3.8) implies that there is some coherence between two small-scale vortices simultaneously advected by a large slowly varying vortex. The origin of this coherence can be through an alignment of turbulent stress and large-scale strain rate. The dynamics of the alignment between time-delayed filtered strain rate and the stress tensor, as well as its link with the energy flux between scales, has been recently analyzed in the work of Ballouz et al., 2020, where the alignment also displays an asymmetrical behavior in time and is peaked at scale-dependent time delays. The product of stress and strain rate also represents a triple statistical quantity of velocity, as well as the energy transfer, so it would be natural to expect that it exhibits a temporal behavior similar to the advection-velocity correlation $\hat{T}$.

Small-scale-only $\hat{T}^{SSS}$. In the case of the purely small-scale correlation function $\hat{T}^{SSS}$, the characteristic time scales of all modes in the triad are comparable, and the mediator mode cannot impose any coherence on the interacting modes, as all three modes decorrelate fast before any alignment can occur. This results in a symmetric, close to Gaussian form of the small-scale correlation functions $\hat{T}^{SSS}$. Note that all three modes in $\hat{T}^{SSS}$ are still transported simultaneously by the random large-scale velocity field. This mechanism that is responsible for the Gaussian time dependence of $\hat{T}^{SSS}$ and of $C^{(2)}$ is the same random sweeping effect as for the two-point correlation function.

Summary. Spatio-temporal correlation function between the velocity and advection fields constitutes a triple statistical quantity easily accessible in numerical simulations. The application of the scale decomposition to this correlation is a necessary refinement to approach the regime of large wavenumbers of the FRG result. The refined advection-velocity correlation gives an insight into the statistics of the three-point spatio-temporal correlation function with a particular configuration of wave vectors. One observes a Gaussian with the same time and wavenumber dependence as in the theoretical result (1.23). Moreover, this analysis provides a further nontrivial quantitative validation, since the correlation parameter α_S is found to be the same for the two-point and three-point correlations. Therefore, the numerical results confirm with good accuracy the FRG prediction for Eulerian three-point space-time correlation function of velocity.

3.4 Spatio-temporal correlation function of velocity norms

As it has been shown, at large time delays, the numerical analysis of the two-point correlation function of the velocity represents a challenging task since its values become very low and are drowned in the oscillations. However, it is possible to analyze another type of correlation function, in particular the correlation function of the velocity modulus. By definition, this correlation function is different from the real part of the complex correlation function that was discussed previously in section 3.2. It is important to note that the correlation function of velocity norms cannot be interpreted through the averaging of the complex phases of the velocity perturbed randomly by the large-scale motions, as all information about the complex phase is wiped out when the modulus is computed, so the interpretation proposed in section 1.4 is not applicable in this case. The correlations of this kind are not covered by the FRG either; however, their numerical computation does not represent any difficulty. In this section it is shown that for this quantity, the large time regime turns out to be observable. The data treatment of the signal of velocity moduli appears to be simpler, since the magnitudes of the correlation function at large time lags are not as low as in the previous case, and the moduli do not take negative values.

Definition. The connected two-point correlation function of the velocity modulus in spectral space is defined as:

$$\bar{C}_n^{(2)}(t,\vec{\mathbf{k}}) = \left\langle \left|\hat{\vec{\mathbf{u}}}(t_0,\vec{\mathbf{k}})\right| \left|\hat{\vec{\mathbf{u}}}(t_0+t,\vec{\mathbf{k}})\right| \right\rangle - \left\langle \left|\hat{\vec{\mathbf{u}}}(t_0,\vec{\mathbf{k}})\right| \right\rangle \left\langle \left|\hat{\vec{\mathbf{u}}}(t_0+t,\vec{\mathbf{k}})\right| \right\rangle, \tag{3.19}$$

with spatial and time averaging identical to Eq. (2.19) $\langle ... \rangle = \frac{1}{N_t}\frac{1}{M_n}\sum_{j=1}^{N_t}\sum_{\vec{\mathbf{k}}\in S_n}(...)$.

As it was mentioned, the complex phases of velocity are eliminated from the computation by definition. The modulus of the velocity can be related to the kinetic energy $\left|\hat{\vec{\mathbf{u}}}(t_0,\vec{\mathbf{k}})\right| = \sqrt{2E_k(t_0,\vec{\mathbf{k}})}$, so the measured correlation function of the velocity moduli is physically related to the autocorrelation of the kinetic energy of a Fourier mode.

During the simulations, the first term in (3.19) is calculated with the use of the method described in section 2.3. Simultaneously, the average of the moduli is computed $\left\langle \left|\hat{\vec{\mathbf{u}}}(t_0+t,\vec{\mathbf{k}})\right| \right\rangle$. It is averaged in the same manner as the correlation function: over spherical spectral shells and over time windows. The average modulus is kept in memory under the same form: as a table where columns correspond to the spectral shells k, and rows to various discrete time lags t_0+t. The first row of this table then corresponds to $\left\langle \left|\hat{\vec{\mathbf{u}}}(t_0,\vec{\mathbf{k}})\right| \right\rangle$. Therefore, the multiplication of each row of the table with the first one gives the second term of the expression (3.19). The subtraction of the two terms is performed during the post-processing of the data obtained in simulations.

Parameters of the simulations. To access large time lags, another set of simulations with a larger width of the time window has been performed. The simulation parameters are detailed in Table 3.2. Only the time window for the computation of the correlation functions has been modified, the rest of the parameters are identical to the ones used for the simulations presented in section 3.2.

Results of DNS. An example of the correlation function computed according to Eq. (3.19) for $R_\lambda = 60$ is presented in Fig. 3.12. Similarly to the two-point correlation studied in Sec. 3.2, one observes at short time delays the Gaussian decay in time and the curves at different wavenumbers collapse in the tk-scaling. However, Fig. 3.12 reveals a crossover to another regime at larger time delays: a slower decorrelation in time that can visually be

R_λ	N	ν	U_{rms}	τ_0	Δt	ΔT_w	N_t
40	64	10^{-4}	0.0059	245	0.9	500	1219
60	128	10^{-4}	0.0147	134	0.2	300	907
90	256	10^{-4}	0.0375	45.3	0.03	49	477
160	512	10^{-4}	0.0974	19.0	0.005	12	133

TABLE *3.2 – Parameters of simulations for analysis of correlations of velocity norms: R_λ - Taylor-scale Reynolds number, N - spatial grid resolution, ν - kinematic viscosity, U_{rms} - root mean square velocity, τ_0 - eddy turnover time scale at the integral scale, Δt - time step, ΔT_w- width of a time window of correlation observation, N_t - number of recorded time windows.*

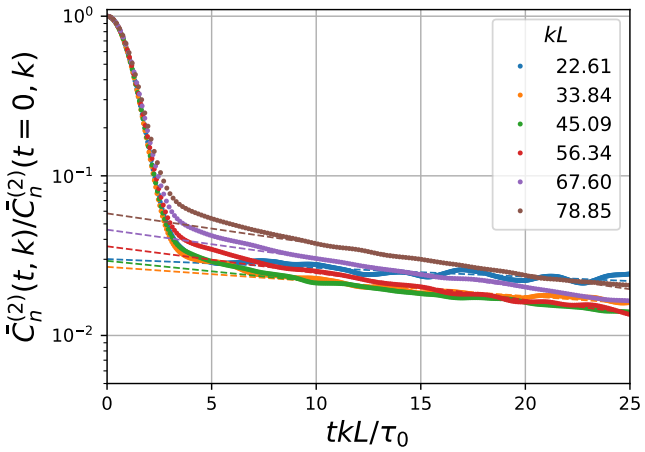

FIGURE *3.12 – Time dependence of the normalized two-point correlation function of the velocity norms $\bar{C}_n^{(2)}(t,k)$ at $R_\lambda = 60$ for different wavenumbers k in semi-logarithmic scales. The numerical data is denoted with dots, the exponential fit is denoted with the dashed lines.*

estimated as exponential. The curves at various wavenumbers no longer collapse in the horizontal scaling tk, and the slope of this decay appears to be steeper for larger wavenumbers.

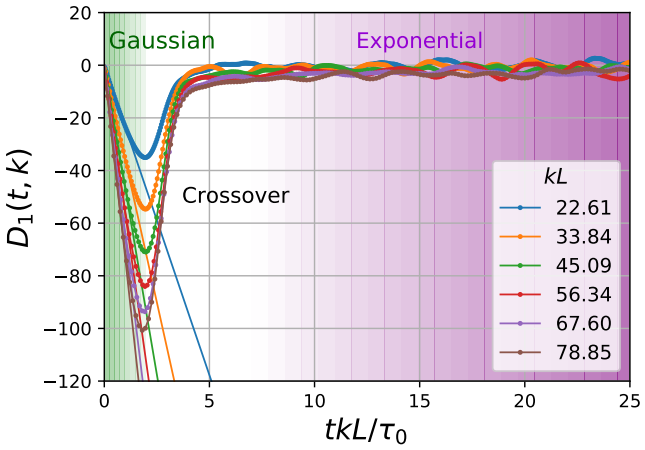

FIGURE *3.13 – The normalized time derivative D_1 defined in Eq. (3.20) calculated numerically with the data from the simulation at $R_\lambda = 60$. The linear part of D_1, highlighted by green shades, corresponds to the Gaussian decay at small time delays, and the approximately constant part of D_1, highlighted by purple shades, corresponds to the exponential time correlation at large time delays.*

Crossover. The transition between these two temporal regimes of the correlation function can be identified more clearly through the time derivative of the logarithm of $\bar{C}_n^{(2)}(t,k)$:

$$D_1(t,k) = \frac{\partial \log\left[\bar{C}_n^{(2)}(t,k)\right]}{\partial t}. \tag{3.20}$$

If the correlation function $\bar{C}_n^{(2)}$ is a Gaussian, the time derivative D_1 is linear with a slope equal to $-2/\tau_s^2$, and if the correlation function is an exponential function, the function D_1 becomes a constant. The derivative D_1 is represented in Fig. 3.13 for $R_\lambda = 60$. At small time delays, D_1 is a linear function with a negative slope. It then displays a non-monotonous transition before approximately reaching a constant value at large time delays. The crossover time delay t can be defined as the location of the minimum of the derivative D_1. This crossover time at different Reynolds numbers is shown in the Fig. 3.14. It depends on the wavenumber as $\tau_c \sim k^{-1}$. The crossover time can be also defined through the second derivative of the correlation function. It was also checked that this k^{-1} behavior does not depend on the precise definition chosen for the crossover time.

Discussion. It is important to emphasize that the correlation function of the velocity norms introduced in Eq. (3.19) is not related in any simple way to the standard real part of the correlation function (1.14) computed theoretically in the FRG approach. Moreover, as the phases play no role in these correlations, the sweeping argument based on phase averaging cannot explain this behavior. The decorrelation must ensue a priori from another physical mechanism, yet to be identified. However, the results of the numerical simulation show that the correlation of the velocity modulus and the real part of the complex velocity correlation function at small time delays (the Gaussian decay) are similar, and exhibit close values for the characteristic decorrelation time. In addition, at large time delays the

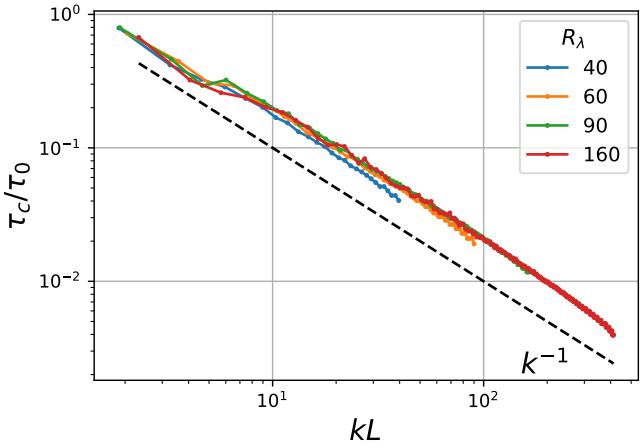

FIGURE *3.14 – Typical crossover time scale for the two-point correlations of the velocity norms* $\bar{C}_n^{(2)}$ *between the small time and large time regimes as a function of the wavenumber* k*, estimated from the minimum of* D_1*.*

correlations of the velocity modulus exhibit a crossover to an exponential decay in time, analogous to the one expected for the real part of the correlation function.

A very similar picture is observed in the work of Biferale et al., 1999 in numerical simulations of a shell model of turbulence. The single-scale two-time correlation function is considered in two definitions: as the correlation of velocity norms equivalent to Eq. (3.19), but also as the real part of the complex velocity modes. The correlation of velocity norms shows a fast decay at small time lags and a much slower decay at large time lags, while the real part of the correlation of complex velocities has only small-time decay and at larger time lags oscillates around zero. Interestingly, the shell models are free from the sweeping effect discussed in the beginning of this chapter, so the mechanism of the decorrelation of velocity fields in shell models is completely different. Probably, a similar mechanism is the reason of the observed behavior of the correlation function of the velocity norms in Navier-Stokes turbulence.

Additionally, the results of the experimental work of Poulain et al., 2006 can be relevant to the problem. Extracted from the measurements of an air jet, the temporal decay of the two-point correlation function of the amplitude of the vorticity field exhibits a crossover from a tk Gaussian decay to a slower exponential one. The crossover time between these two regimes is found to scale as k^{-1} as observed in our simulations.

The correlation of the velocity norms could be linked to the correlation of the energy of Fourier modes. In a recent work of Khurshid et al., 2021 the time-delayed statistics of the spectral energy and energy transfer was studied numerically, with a focus on the crossed correlation between large and small scales. In particular, the difference is highlighted between the behaviors of the correlations of slow and fast components of energy fluctuations, which could also be relevant to the observed regimes in the correlation of velocity norms.

Summary. In this section, the temporal behavior of the correlation function of velocity norms is discussed. The correlation functions demonstrate a Gaussian decorrelation at small time lags and switch to a slow exponential-like decorrelation at large time lags. The typical time of crossover between these two regimes scales as $\tau_c \sim k^{-1}$. The correlation function of the velocity norms defined in Eq. (3.19) is completely different from the real part of the correlation of the complex velocities discussed in Sec. 3.2. A straightforward interpretation through the sweeping mechanism based on the random phase averaging cannot be applied to velocity norms, since all information about the phases is wiped out in this quantity.

This type of correlation function has not been calculated within the FRG approach, and to our knowledge there is no theoretical explanation regarding these correlations in the existing literature. Interpretation and theoretical explanation of these results require more investigation.

3.5 Kinetic energy spectrum in the near-dissipative range

One of the remarkable consequences of the FRG result for the two-point space-time correlation function of velocity is the computation of the form of the kinetic energy spatial spectrum in the near-dissipative range. In the work of Canet et al., 2017, it was shown that taking an appropriate limit $t \to 0$ in the expression for the two-point correlation function leads to a spatial spectrum decaying as a power law multiplied by a stretched exponential at large wavenumbers, and the value of the stretched exponent is $\alpha = 2/3$. This result concerns only the near-dissipative range, since the far-dissipative range is dominated by the viscosity term and is not controlled by the same RG fixed point. Although the turbulent kinetic energy spectrum has been measured in numerous experiments and numerical simulations, there is no agreement on the form of its decay in the dissipation range. To compare the numerical spectra with the FRG prediction, a set of DNS with well-resolved near-dissipation range has been performed.

This section provides firstly an overview of the previous studies on the form of the spectrum in the dissipation range, followed by the section containing the description of the simulations, numerical results, and their treatment. Lastly, the obtained results are discussed and compared with the FRG prediction, as well as with other studies and experimental data. Part of the results presented in this section has been published in *Physical Review Fluids* (Gorbunova et al., 2020).

3.5.1 Background

According to Kolmogorov's first hypothesis of similarity (Kolmogorov, 1941) at high Reynolds numbers the small-scale statistics of turbulence is determined by the scale k^{-1}, the mean dissipation rate $\langle\varepsilon\rangle$ and the viscosity ν. By dimensional argument, one can obtain a universal form for the energy spectrum of the turbulent fluctuations (Frisch, 1995):

$$E(k) = \varepsilon^{2/3} k^{-5/3} F(\eta k), \tag{3.21}$$

with $F(\eta k)$ - a universal dimensionless function of a dimensionless argument.

In the inertial range (at $k\eta \ll 1$) according to K41, the spectrum depends only on k and ϵ, but not on η, thus, the function $F(k\eta)$ tends to a positive constant (Kolmogorov constant). The power law $k^{-5/3}$ is supported by experimental and numerical data. At the same time, there is no agreement on the universal form of the spectrum, or in other words, the form of $F(k\eta)$ at high wavenumbers $k \sim \eta^{-1}$ (in the dissipation range).

Theoretical models. The first attempts to find a form of the equation for $E(k)$ at small scales are summarized in the book of Monin and Yaglom, 2007, Chapter 7, Sec 17 (see also Ref. Davidson, 2004, Chapter 8). They are mainly based on dimensional arguments making a link between the energy spectrum function and the spectral energy flux, or in other words, finding a closure hypothesis allowing to integrate the equations for the variation of the spectrum function $E(k)$. Within this approach, a dimensionally consistent functional relation between the energy spectrum and the energy flux has to be found,

ensuring the 5/3 law in the inertial range. The main point is to extend the found result to the dissipation range, thus, the method consists in extrapolating the results obtained for the inertial range to the dissipation range. These closure models are also called algebraic. They include, among others, hypotheses of Kovasznay, Obukhov, Heisenberg, and Karman. However, these models lead to some non-physical results, such as modes with zero energy and only twice differentiable velocity (Monin and Yaglom, 2007, Chapter 7, Sec 17).

Additionally, there are a number of works suggesting that the spectrum function is a power law multiplied by a (stretched) exponential:

$$E(k) = const \cdot k^{-\beta} \exp(-\mu k^{\alpha}). \tag{3.22}$$

Different values for α have been proposed, for instance $\alpha = 1/2$ (Tatarskii, 1967), $\alpha = 3/2$ (Uberoi and Wallis, 1969), $\alpha = 4/3$ (Pao, 1965) or $\alpha = 2$ (Townsend and Taylor, 1951; E. A. Novikov, 1961; Gurvich and Yaglom, 1967), $\alpha = 3/5$ (Bershadskii, 2016). These results are obtained within simplified analytical models, based on physical considerations, or approximate fits of experimental data (Uberoi and Wallis, 1969). For instance, one of the most referred models is the Pao's closure, which is based on two assumptions: locality of the energy transfer in spectral space and a power-law dependence of the energy flux on the energy spectrum function. Only dimensionally consistent closure leads to $\alpha = 4/3$ (Pao, 1965).

In other works, a purely exponential spectrum decay $\alpha = 1$ on the limit of large k is suggested, based on different theoretical approaches, such as the Direct Interaction Approximation (Kraichnan, 1959), asymptotic expansions (Foias et al., 1990; Sirovich et al., 1994; Bershadskii, 2008). This result can be understood as a consequence of regularity at very small spatial scales for small but finite viscosity, which can be assumed in the limit $k \to \infty$, that is in the far-dissipative range. Besides, a purely exponential decay is also shown to characterize the spectra at very low Reynolds numbers, corresponding to laminar flows (Verma et al., 2018).

Experimental studies. The behavior of the spectrum in the dissipative range has been extensively studied in experiments. However, accurate experimental measurements of the spectrum at small scales are difficult to obtain, because of the limitations of the measuring instruments. Several fits of the spectrum in the dissipative range have been proposed, for instance, pure exponential functions with $\alpha = 1$ but on two successive separate ranges (Sreenivasan, 1985), or a single pure exponential but with different coefficients μ (Saddoughi and Veeravalli, 1994; Manley, 1992). Conversely, the analysis of Smith and Reynolds, 1991 concluded that an exponential with $\alpha = 2$ was the best fit for the existing experimental data. In the book of Pope, 2000, section 6.5.3 another fitting function with a more complicated exponential function is proposed, which is in better agreement with the available experimental data compared to the pure exponential or Pao's spectrum.

Numerical simulations. On the other hand, numerical simulations can provide more accurate data for the kinetic energy spectrum. However, as discussed in 2.2, because of the high computational cost, the DNS studies of the dissipation range are limited to low Reynolds numbers (Chen et al., 1993; Martínez et al., 1997; Schumacher, 2007; Verma et al., 2018), or to low spectral resolution, which do not allow to get an extended dissipation range (Sanada, 1992; Ishihara et al., 2003; Ishihara et al., 2005). Most of these works lead to the conclusion that the purely exponential form with $\alpha = 1$ does not describe accurately the entire dissipative range, and is valid rather for the far-dissipation range (Chen et al., 1993; Domaradzki, 1992; Martínez et al., 1997; Schumacher, 2007). In the work of Verma et al., 2018, it is demonstrated that neither Pao's nor Pope's model of spectra match the results of DNS, while the purely exponential decay is observed only in

spectra of laminar flows. In the work of Ishihara et al., 2005, it is shown that the results of fitting the numerical spectra with a function in the form of (3.22) depend significantly on the range of wavenumbers chosen for fitting. Another difficulty of the analysis of the spectra is the strongly nonlinear functional dependence, which makes the fitting procedure very sensitive to the input data and its accuracy (Schumacher, 2007).

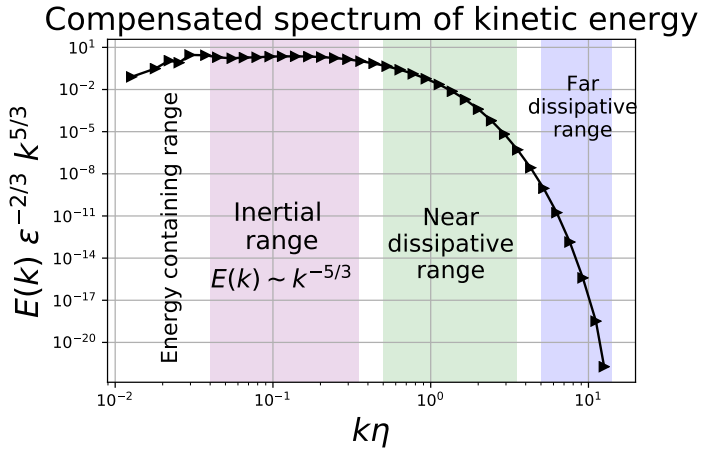

FIGURE *3.15 – Schematic representation of the inertial, near- and far-dissipative ranges in the spectrum of kinetic energy.*

Near- and far-dissipation ranges. Although different behaviors were predicted in earlier studies, the work of Khurshid et al., 2018 based on high-resolution DNS delimits the two ranges in the energy spectrum: the near-dissipative range for $0.2 \lesssim k\eta \lesssim 4$ and the far-dissipative range for $k\eta \gtrsim 4$ (see a sketch of a spectrum in Fig. 3.15). In the near-dissipative range, the numerical spectra have $\alpha < 1$, while in the far-dissipative range, the decay of the spectrum is well described by a pure exponential ($\alpha = 1$). This finding may explain the failure of previous attempts to describe the whole dissipative range as a pure exponential with various power laws.

FRG result. It is shown in the work of Canet et al., 2017 that the behavior of the energy spectrum in the dissipative range can also be probed in the FRG framework, by taking the appropriate $t \to 0$ limit, accounting for the existence of the Kolmogorov scale, or equivalently of the Kolmogorov time-scale τ_K. Under the additional assumption that the scaling variable $tk^{2/3}$ saturates in this limit, that is $\epsilon^{1/3} tk^{2/3} \to \epsilon \tau_K L^{-2/3} = (\eta/L)^{2/3}$ when $t \to 0$, one obtains

$$E(k) \equiv \lim_{t \to 0} 4\pi k^2 C(t,k) = A' \, \epsilon^{2/3} (k\eta)^{-\beta} \exp\left(-\mu (k\eta)^{\alpha}\right), \tag{3.23}$$

with $\beta = 5/3$ and $\alpha = 2/3$ and where $\mu = \gamma(\eta/L)^{2/3}$ is a (positive) non-universal constant and $A' = 4\pi A \eta^{5/3}$. It is important to highlight that this behavior is valid at large wavenumbers, but which are still controlled by the RG fixed point. That is to say that this result is expected to describe correctly the near-dissipative range, since the far-dissipative range, totally dominated by the viscosity, is controlled by another fixed point.

This value for the stretched exponent $\alpha = 2/3$ in the near-dissipative range was then shown to match the spectra obtained in DNS (Canet et al., 2017), and also in experiments of von Kármán turbulent swirling flow (Debue et al., 2018). The presence of the portion of spectrum with $\alpha = 2/3$ in the near-dissipation range was also shown in numerical study of Buaria and Sreenivasan, 2020.

Applications. Despite the fact that the kinetic energy spectrum is measured in numerous numerical and experimental studies of turbulence, the results regarding the form of the dissipative range of the spectrum are controversial. Yet the knowledge of the form of the turbulent kinetic energy spectrum is essential for many problems, such the generation of turbulent-like fields (X. Wu, 2017) or large-eddy-scale (LES) models. For instance, early LES approaches were based on integrating Pao's spectrum (Piomelli and Balaras, 2002), although recent experimental and DNS results demonstrate that the Pao's hypothesis is not consistent (Pope, 2000; Verma et al., 2018). Better understanding of universal features and a more accurate description of the dissipative range would allow to improve the existing numerical models of turbulence.

Objective. The goal of the study presented in this section is to analyze the kinetic energy spectra in the dissipative range using the DNS data and compare it with the FRG prediction (3.23). The spectra obtained from DNS are treated by computing three consecutive numerical logarithmic derivatives, allowing to extract the local exponent α without the contribution of other parameters. Tracing the local stretched exponent with the proposed method provides a more precise estimation of the form of the spectrum and the limits of the near- and far- dissipation ranges than in the previous works on this subject. This approach allows as well to evaluate the range of wavenumbers corresponding to the near-dissipative range where the FRG result is expected to be valid. These results were published in *Physical Review Fluids* (Gorbunova et al., 2020). The article provides in addition the results for the form of spectra in the dissipative range from experimental data of grid turbulence in Modane wind tunnel.

3.5.2 Description and results of DNS

Challenges. The principal challenge of the numerical study of the dissipative range by means of DNS is its high computational cost. As discussed in Sec. 2.2, increasing the Reynolds number requires higher spatial resolution. Moreover, one also needs to extend the resolved velocity spectrum to larger wavenumbers to study the spectrum further into the dissipative range, in comparison with the traditional DNS configurations. In the solver, it is regulated by the choice of the parameter $H = k_{max}\eta$. Here, it is important to increase the parameter H as high as possible, which requires higher spatial resolution as well. The choice of parameters is a compromise between the necessity of high Reynolds numbers, spectrum extension, and computational cost.

Another issue is the necessity of computation of time averages of the spectra. The simulations have to be sufficiently long to acquire enough data for correct averaging, which increases again the computational costs. Lastly, the strongly nonlinear functional form of the spectra in the dissipation range complicates data treatment and requires adapted techniques for post-processing.

Parameters of the simulations. The simulation parameters are determined by the Taylor-scale Reynolds number R_λ and the value of $H = k_{\max}\eta$. To obtain accurate spectra in the dissipation range, a sequence of simulations with fixed R_λ and increasing grid resolution was performed. In the first run, the computational grid size is chosen to ensure at least $H = 1.5$ which is commonly accepted as an adequate spatial resolution for DNS (Pope, 2000, Chapter 9). In the following runs, the solution obtained in the previous simulations is transferred to a finer computational grid with resolution $N \to 2N$, while R_λ and the forcing scales are unchanged. By doing so, the value of H can be increased twofold, and therefore one gets access to smaller scales in the dissipative range of the turbulence

spectrum. The values of the Taylor-scale Reynolds number, size of the computational grid, and the associated value of H used in the simulations are presented in the Table 3.3.

N \ R_λ	60	90	160	240
256	3.0	1.5	-	-
512	6.0	3.0	1.5	-
1024	12.0	6.0	3.0	1.5
2048	-	12.0	6.0	3.0

TABLE *3.3 – Parameters of the simulations for analysis of the dissipation range of spectra: Maximal wave-number $H = k_{\max}\eta$ as a function of the Taylor microscale Reynolds number R_λ and the grid resolution N.*

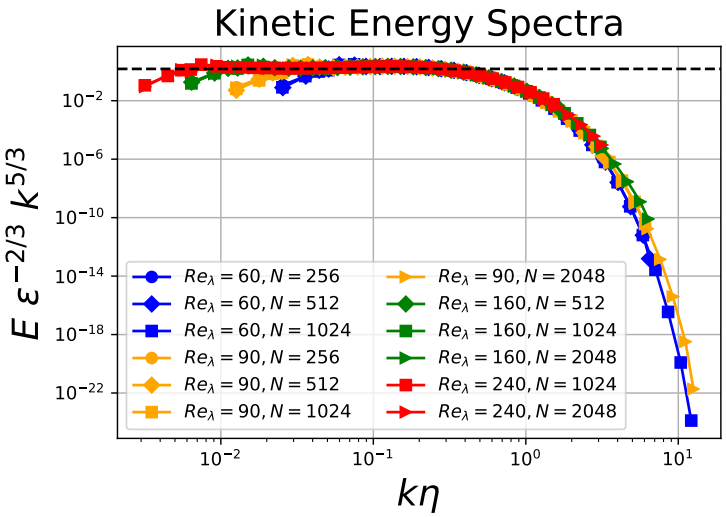

FIGURE *3.16 – Kinetic energy spectra for dissipation range analysis, obtained from the set of simulations with the Taylor-scale Reynolds numbers R_λ and resolutions N given in Table 3.3.*

Kinetic energy spectra. Once the stationary state is reached, the spectra of the kinetic energy spectra are computed. The spectra are averaged over spectral spherical shells and in time:

$$E(k) = \frac{1}{N_t}\sum_{j=1}^{N_t}\frac{1}{M_n}\sum_{\vec{\mathbf{k}}\in S_n}\frac{1}{2}\hat{u}_i(\vec{\mathbf{k}},t_j)\hat{u}_i^*(\vec{\mathbf{k}},t_j), \tag{3.24}$$

where N_t is the number of time snapshots at which the spectra are computed, and M_n is the number of modes in a shell.

In this study, the spherical shells for averaging have logarithmic spacing so that the n-th shell is defined as $S_n^\lambda = \left\{\vec{\mathbf{k}}\in\mathbb{R}^3 \,\middle|\, \lambda^n \le |\vec{\mathbf{k}}| < \lambda^{n+1}\right\}$. The value of the basis of the exponential function is set to $\lambda = 1.21$, as it is estimated as the minimal value that does not lead to the appearance of shells with no modes (Stepanov et al., 2014). The use of the exponentially spaced shells allows to avoid some biases in the spectra, like kinks,

that appear because of the cubical discretization of the computational grid, and it gives significantly better results while computing the log-log derivatives of the spectra.

The spectra obtained for each R_λ and resolution, averaged over space and time, are displayed in Fig. 3.16. The spectra are compensated by $\varepsilon^{-2/3}k^{5/3}$, so that in the inertial range there is a plateau with approximate value 1.5 (the dashed black line), which corresponds to the Kolmogorov constant for the three-dimensional energy-spectrum function (Sreenivasan, 1995; Pope, 2000). It shows that in the inertial range, the spectra decay as power-laws with K41 exponent $-5/3$ approximately up to $k\eta \approx 0.4$. In the following section, the near-dissipation zone of the spectra at $k\eta \gtrsim 0.4$ is analyzed.

3.5.3 Analysis of the numerical spectra in the near-dissipative range

The detection of the stretched exponential form of the kinetic energy spectrum in the near-dissipation range predicted by the FRG given in Eq. (3.23) is not a trivial task, as the function is strongly nonlinear. The attempts to perform a 4-parameter nonlinear fit with the given form did not lead to any conclusive result. Parameters resulting from the fitting procedure appear to be extremely sensitive to small variations in the input data. Moreover, in certain cases, the Jacobian matrix calculated within the nonlinear fitting procedure becomes poorly conditioned, leading to numerical instabilities.

Another approach, more suitable for strongly nonlinear functions, consists in the consecutive analysis of the first, second, and third derivatives. Since the function in Eq. (3.23) contains a power law, it is more convenient to use the log-log derivatives. The derivatives are computed from the DNS averaged spectra with the use of a central second-order difference scheme. Note that the use of exponentially spaced shells for spatial averaging provides relatively smooth numerical log-log derivatives, which is not the case if linearly distanced shells are used.

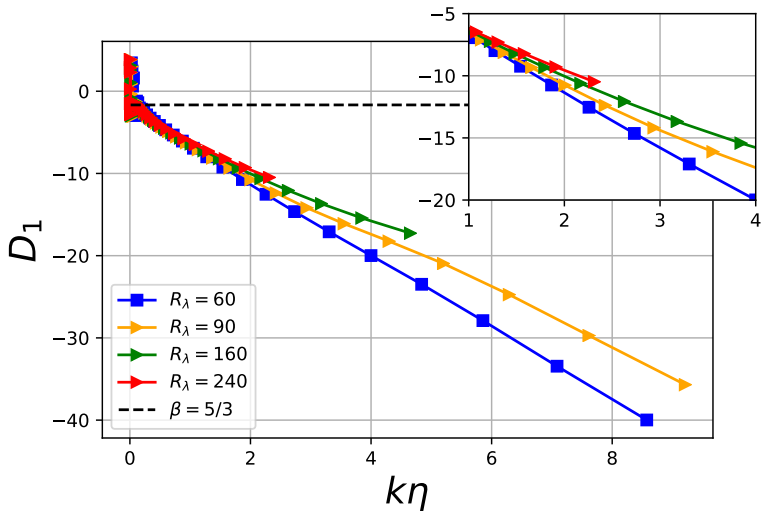

FIGURE *3.17 – First logarithmic derivative D_1 of the kinetic energy spectra, defined by Eq. (3.25). The inset shows a zoom in the near-dissipative range to illustrate the curvature increasing with R_λ. For the sake of clarity, only the curves for the highest resolution N for each R_λ are shown.*

First derivative. The first logarithmic derivative of the spectrum is defined as:

$$D_1(k\eta) = \frac{d\ln(E)}{d\ln(k\eta)} = -\beta - \mu\alpha(k\eta)^{\alpha}, \tag{3.25}$$

where the general form (3.23) for $E(k)$ is used in the second equality. This function is still nonlinear and contains 3 unknown parameters, so it is still not easy to apply a fitting procedure. However, the visual evaluation of the form of D_1 can already provide some information. For instance, if the exponent $\alpha = 1$, the function D_1 becomes linear, and the behavior of the spectrum according to (3.23) is purely exponential in the dissipative range (multiplied by the power law $k^{-\beta}$). Thus, the nonlinear form of D_1 can at least indicate that the spectrum deviates from a purely exponential function.

The result of numerical estimation of the first derivative is shown in the Fig. 3.17. Firstly, one can notice that only the curve corresponding to the smallest $R_\lambda = 60$ visually appears to be linear, while other curves exhibit a slight curvature, and this curvature is getting more visible as R_λ increases. The curvature can be seen a little more clearly from the inset of the Fig. 3.17. The fact that the curvature is convex indicates that $\alpha < 1$ in this region. Moreover, the curves do not collapse at very large wavenumbers, suggesting that this behavior is not universal and depends on the Reynolds number. Secondly, although there are not many points for high $k\eta > 4$, one can distinguish two qualitatively different regimes: the near-dissipative range up to $k\eta \approx 4$, and the far-dissipative range extending beyond this value. It appears that in the far dissipative range, the curves of D_1 have a linear form in log-log scale, indicating a pure exponential decay $\alpha \simeq 1$.

The first logarithmic derivative D_1 has been used for analysis of the dissipation range in other works as well (Martínez et al., 1997 ; Ishihara et al., 2005 ; Khurshid et al., 2018 ; Buaria and Sreenivasan, 2020). The results presented here are consistent with the mentioned studies.

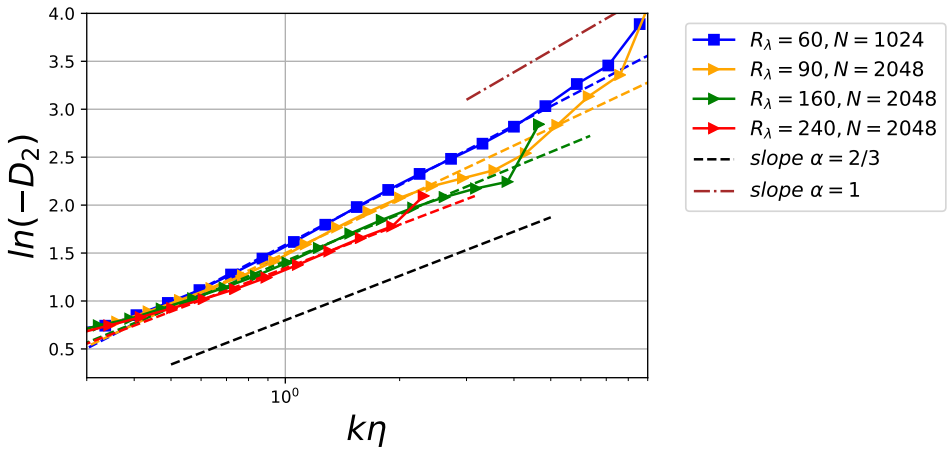

FIGURE *3.18 – Second logarithmic derivative of the kinetic energy spectra, defined by Eq. (3.26). Only the curves for the highest resolution for each R_λ are shown for clarity. The colored dashed lines denote the linear fits of the data points. The lines with slope 2/3 (dashed black) and 1 (purple dotted-dashed) are provided for a visual comparison of the slope.*

Second derivative. Since the first derivative D_1 does not provide a straightforward way to estimate the exponent α, one can go further and evaluate the second logarithmic

derivative:

$$D_2(k\eta) = \frac{d(-D_1)}{d\ln(k\eta)} = \mu\alpha^2(k\eta)^\alpha. \tag{3.26}$$

When plotting D_2 in log-log scale, it is expected to be a straight line with a slope α and intercept $\ln\left[\mu\alpha^2\right]$ in the dissipative range.

The derivative D_2 extracted from the numerical spectra is presented in Fig. 3.18. It is clear that the linear fit matches well the data for the points $k\eta < 3$ (the near-dissipation range). The slope of the lines varies from $\alpha \approx 1$ to $\alpha \approx 2/3$ with increasing R_λ.

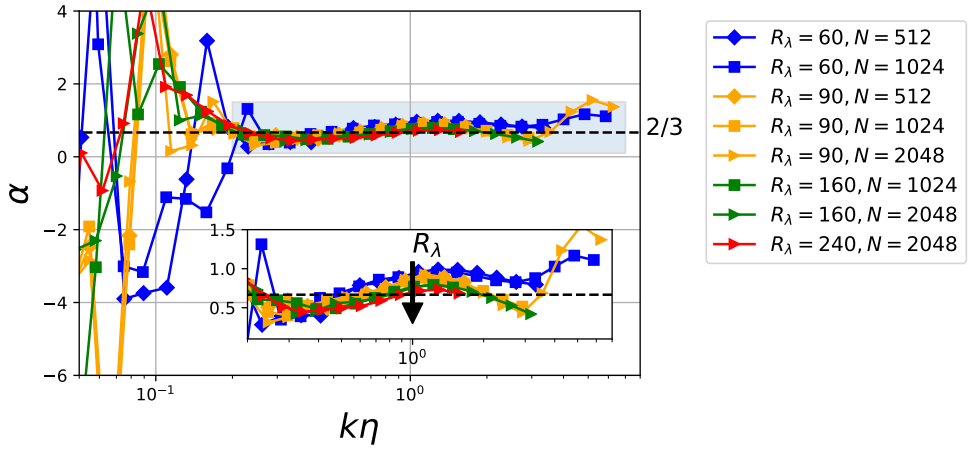

FIGURE *3.19 – The exponent α calculated as the third logarithmic derivative D_3, defined by Eq. (3.27). The inset shows a zoom in the dissipative range (corresponding to the area highlighted in blue in the main figure).*

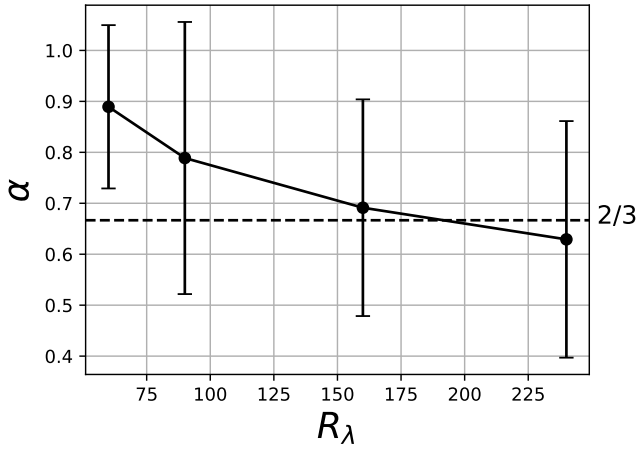

FIGURE *3.20 – Dependence of the near-dissipation range exponent α on Reynolds number. The values are estimated as the plateau values from Fig. 3.19. The error bars correspond to the standard deviation between the data and the plateau value. Only points for the simulations at the best resolution are shown.*

Third derivative. Taking another log-log derivative gives D_3, one expects to find a constant in the dissipative range with value α:

$$D_3(k\eta) = \frac{d\ln(D_2)}{d\ln(k\eta)} = \alpha. \tag{3.27}$$

The result for the third derivative is displayed in Fig. 3.19. The derivative D_3 appears to be noisy in the inertial range, but clearly exhibits a plateau in the near-dissipative range for wavenumbers $0.2 \lesssim k\eta \lesssim 2.5$. The range of wavenumbers corresponding to the plateau of α appears independent of the R_λ.

The inset gives a zoomed view of the dissipative range (the area highlighted in blue in the main plot), which allows to see that α is close to 1 at the smallest $R_\lambda = 60$ and approaches the value $\alpha \approx 2/3$ as R_λ increases. The dependence of the plateau values of α on the Reynolds number is shown in Fig. 3.20.

One can also observe in Fig. 3.19 that at large wavenumbers $k\eta > 3.5$ the curves for $R_\lambda = 60, 90$ deviate and start growing, which can be an indication of the transition to the far-dissipation range, where the purely exponential behavior with $\alpha = 1$ is expected. However, the provided spectra do not allow to draw any solid conclusion regarding the far-dissipative range, as the data is not sufficient.

3.5.4 Discussion

Near-dissipative range. To our knowledge, there is no rigorous definition of the threshold wavenumbers delimiting the near- and far-dissipative ranges. In the present work, the near-dissipation range of the kinetic energy spectrum is identified as the zone of a plateau of the third log-log derivative, which is equal to the exponent α. The near-dissipation range approximately spans from $k\eta = 0.2$ to 2.5, which is in agreement with the work of Khurshid et al., 2018, where the near-dissipation range is estimated as $k\eta \lesssim 3$. The work of Khurshid et al., 2018 does not provide an exact evaluation of α; however, it concludes that $\alpha < 1$ in the near-dissipative range from the form of curvature of D_1.

It is important to mention that the stretched exponential form of the kinetic energy spectrum was independently studied in the work of Buaria and Sreenivasan, 2020, where higher Reynolds numbers were reached in DNS. Remarkably, the exponent $\alpha = 2/3$, predicted by the FRG, is also observed in the near-dissipation range. The spectra are analyzed with the use of the first logarithmic derivative D_1. However, the range of wavenumbers corresponding to the stretched exponential with $\alpha = 2/3$ is estimated to be much shorter (only until $k\eta < 1$) than in the present study. This range is evaluated simply as a range where the derivative D_1 plotted in log-log scale behaves as a straight line with a slope 2/3. However, as one can see from the equation (3.25), such an evaluation based on D_1 only can be contaminated by the power-law exponent β, which can make D_1 deviate from the straight line in log-log scale, even if $\alpha = 2/3$. The dependence of β on wavenumber and the Reynolds number is not known. According to FRG, in the leading order term, the power-law exponent is $\beta = 5/3$; however, it can be modified by sub-leading terms and change its value in the dissipative range. In contrast, the method of estimation of α from the derivatives D_2 and D_3, proposed in this Section, allows to get rid of the unknown contribution of β and provides a more accurate estimation of α.

Averaging. Another important remark concerns the role of statistical averaging in the analysis of spectra. The FRG prediction is applicable for the kinetic energy spectra computed in the sense of ensemble average. In DNS, the spectra for averaging are collected when a stationary state of the flow is reached. Spectra are saved every 100 iterations and averaged in the phase of post-processing. Clearly, sufficiently long simulations are needed for correct averaging.

However, going "deeper" into the dissipation range requires much more temporal statistics for averaging. In the beginning of data acquisition, the tails of the spectra strongly fluctuate. This is due to non-Gaussianity of the fluctuations at small scales. The time series of modal kinetic energy at large wavenumbers show the presence of intermittent high

peaks, the same behavior is reported in the work of Khurshid et al., 2018. The amplitude of extreme peaks in the kinetic energy time series increases with wavenumber and Reynolds number. The spectra must be computed by averaging over a sufficiently long time series, such that enough extreme events are taken into account in the averages to build correct statistics.

Comparison with experimental data. Unfortunately, it was impossible to reach higher Reynolds numbers in this DNS study due to high computational costs. However, it is possible to access higher Reynolds numbers in experiments of grid turbulence. The size of the S1MA wind tunnel of ONERA in Modane allows to reach high Reynolds number and still obtain data with the dissipation scales resolved enough for the analysis of the spectra in dissipation range (Bourgoin et al., 2018). The comparison of the experimental spectra with the theoretical prediction (3.23) is provided in the paper (Gorbunova et al., 2020), it states $\alpha \simeq 0.68 \pm 0.19$, which is consistent with the value obtained for α in DNS for high Reynolds number.

Summary. In this section, a numerical study of the kinetic energy spectrum in the dissipative range is presented. The form of the averaged spectra is analyzed by computing numerical log-log derivatives. The results show that the dependence of the spectra on the wavenumber in the dissipative range can be described by a power law multiplied by a stretched exponential. The value of the stretched exponent is estimated through the third derivative, which reaches a plateau in the near-dissipative range. The plateau spans approximately $0.2 \lesssim k\eta \lesssim 2.5$, which estimates the near-dissipation range limits. The value of α appears to be dependent on Reynolds number. It is $\alpha \approx 1$ at the smallest $R_\lambda = 60$, and $\alpha \approx 2/3$ for the highest $R_\lambda = 240$, approaching the value predicted by FRG. These results are also in agreement with the experimental data obtained in grid turbulence in Modane wind tunnel.

3.6 Conclusions

In this chapter, results of the numerical study of the spatio-temporal correlation function of velocity in Eulerian frame of reference are presented. It is shown that the two-point space-time correlation function takes the form of a Gaussian function of the variable tk, where t is the time lag and k is the wavenumber. This behavior is in agreement with the FRG prediction for small time lags. This observation thus allows to confirm the dominance of the sweeping time scaling in the Eulerian frame, which is in agreement with the existing experimental and numerical studies.

In addition, the dominance of the sweeping effect is demonstrated for the filtered triple correlation function, computed as space-time correlation between the advection and velocity fields. Applying a filtering procedure that nullifies all large-scale modes makes it possible to link the numerically computed triple correlation with the FRG prediction for the three-point velocity correlation function. The triple correlation behaves also as a Gaussian of tk variable, its temporal behavior is identical to the one of the two-point correlation, which is also in agreement with FRG.

Unfortunately, the transition to another form of the decay in the correlation function at large time lags, predicted by FRG, was not captured in DNS. The analysis of the correlation functions at large time lags represents a challenging task due to the low magnitude of the

correlation function and strong sensitivity to the amount of data collected for averaging. However, two different regimes are observed for another type of correlation function - correlation of the velocity vector norms. The FRG approach does not cover this type of correlation function. The observed behavior of the correlation of velocity norms requires further theoretical and numerical investigation.

Lastly, the form of the kinetic energy spectrum in the dissipative range is analyzed. According to FRG, taking an appropriate limit $t \to 0$ in the two-point correlation function leads to a result for the spectrum in the near-dissipative range in the form of a power law multiplied by a stretched exponential function with an exponent $\alpha = 2/3$. The analysis of the spectra by means of logarithmic derivatives demonstrates that the stretching exponent indeed approaches the theoretically predicted value at high Reynolds numbers. Moreover, this approach allows to estimate the wavenumbers delimiting the near-dissipative range. These results are in agreement with the stretched exponents extracted from experimental data collected in grid turbulence. Parts of the results presented in this chapter are published in articles (Gorbunova et al., 2020 ; Gorbunova et al., 2021a).

At this point, the part of the thesis dedicated to the correlation of velocity is over. The remaining two chapters concern the statistical properties of the passive scalar. The next chapter 4 continues the numerical study presented in this section by including into the analysis the space-time correlation of an advected scalar. The influence of the temporal covariance of the velocity field on the scalar correlation function is studied in simulations of a scalar advected by a random synthetic flow, as well as by a homogeneous isotropic turbulent flow governed by the Navier-Stokes equations.

Conclusions en français

Ce chapitre présente les résultats de l'étude numérique de la fonction de corrélation spatio-temporelle de la vitesse dans le cadre de référence eulérien. On montre que la fonction de corrélation spatio-temporelle à deux points prend la forme d'une fonction gaussienne de la variable tk, où t est le décalage temporel et k est le nombre d'onde. Ce comportement est en accord avec la prédiction FRG pour les petits décalages temporels. Cette observation permet ainsi de confirmer la dominance de la loi d'échelle de balayage dans le cadre eulérien, ce qui est en accord avec les études expérimentales et numériques existantes.

De plus, la dominance de l'effet de balayage est démontrée pour la fonction de triple corrélation basée sur les champs filtrés, calculée comme corrélation spatio-temporelle entre les champs d'advection et de vitesse. L'application d'une procédure de filtrage qui annule tous les modes à grande échelle permet de lier la triple corrélation calculée numériquement avec la prédiction FRG pour la fonction de corrélation de vitesse à trois points. La triple corrélation se comporte également comme une gaussienne de variable tk, son comportement temporel est identique à celui de la corrélation à deux points, qui est également en accord avec FRG.

Malheureusement, la transition vers l'autre forme de décroissance de la fonction de corrélation avec des décalages temporels larges, prédite par FRG, n'a pas été observée dans les simulations. L'analyse des fonctions de corrélation avec des décalages temporels importants représente une tâche difficile en raison des faibles amplitudes de la fonction de corrélation et de la forte sensibilité à la quantité de données collectées pour le calcul de la moyenne. Cependant, deux régimes différents sont observés pour un autre type de fonction de corrélation - la corrélation des normes du vecteur vitesse. Pour le moment, l'approche FRG ne couvre pas ce type de fonction de corrélation. Le comportement observé de la corrélation des normes de vitesse nécessite une étude théorique et numérique plus approfondie.

Enfin, la forme du spectre d'énergie cinétique dans le domaine dissipatif est analysée.

Selon FRG, prendre une limite appropriée $t \to 0$ dans la fonction de corrélation à deux points conduit à un résultat pour le spectre dans la zone dissipative-proche sous la forme d'une loi de puissance multipliée par une fonction exponentielle étirée avec un exposant $\alpha = 2/3$. L'analyse des spectres au moyen de dérivées logarithmiques démontre que l'exposant d'étirement se rapproche bien de la valeur théoriquement prédite à des nombres de Reynolds élevés. De plus, cette approche permet d'estimer les nombres d'onde délimitant la zone dissipative-proche. Ces résultats sont en accord avec les exposants étirés extraits des données expérimentales recueillies dans la turbulence de grille. Une partie des résultats présentés dans ce chapitre est publiée dans les articles (Gorbunova et al., 2020 ; Gorbunova et al., 2021a).

Ce chapitre conclut la partie de la thèse consacrée à la corrélation des vitesses. Les deux chapitres restants concernent les propriétés statistiques du scalaire passif. Le chapitre suivant 4 poursuit l'étude numérique présentée dans cette section en incluant dans l'analyse la corrélation spatio-temporelle d'un scalaire advecté passivement. L'influence de la covariance temporelle du champ de vitesse sur la fonction de corrélation d'un scalaire est étudiée dans des simulations d'un scalaire advecté par un écoulement synthétique aléatoire, ainsi que par un écoulement turbulent isotrope homogène régi par les équations de Navier-Stokes.

4

Spatio-temporal correlations of passive scalar

In this chapter, the two-point spatio-temporal correlation function of a passive scalar in Eulerian frame of reference is studied. The results are obtained from numerical simulations of the advection-diffusion equation of a scalar in Navier-Stokes and synthetic velocity fields. The influence of the temporal covariance of the random velocity field on scalar correlations is studied numerically in a white-in-time velocity field and a time-correlated one. In the last case, the crossover between Gaussian and exponential decays in the scalar correlation is observed.

Contents

Abstract

This chapter is dedicated to the numerical study of the correlation functions of a passive scalar in a turbulent flow. The term "passive scalar" means a scalar quantity, which can be modeled as a continuous field and does not have any back-reaction on the carrier flow. The passive scalar approximation is used in many applications, for instance, transport of a non-reacting admixture, small fluctuations of temperature, humidity, or salinity (Monin and Yaglom, 2007).

In particular, the Eulerian two-point space-time correlation functions of a passive scalar are discussed. Firstly, in section 4.1 a general background and literature overview on scalar correlation functions is provided. Next, two cases of flow are considered: a scalar advected by a turbulent flow governed by Navier-Stokes equation (Sec. 4.2) and scalar advected in a synthetic random velocity field (Sec. 4.3) with a prescribed covariance in space and time. The results of the numerical simulations for the two cases are presented and compared with the FRG results presented previously in Sec. 1.3 (page 23). Lastly, in Sec. 4.4, the main conclusions of the chapter are listed. A part of the results presented in this chapter is also published in *Physical Review Fluids* (Gorbunova et al., 2021b).

Résumé en français

Ce chapitre est consacré à l'étude numérique des fonctions de corrélation d'un scalaire passif dans un écoulement turbulent. Le terme "scalaire passif" désigne une quantité scalaire qui peut être modélisée comme un champ continu et qui n'a aucune réaction en retour sur le champs de vitesse porteur. L'approximation scalaire passive est utilisée dans de nombreuses applications, par exemple, le transport d'un mélange non réactif, de petites fluctuations de température, d'humidité ou de salinité (Monin and Yaglom, 2007).

En particulier, les fonctions de corrélation espace-temps eulériennes à deux points d'un scalaire passif sont discutées. Tout d'abord, la section 4.1 donne un aperçu général de l'historique et de la littérature sur les fonctions de corrélation scalaire. Ensuite, deux cas d'écoulement sont considérés : un scalaire advecté par un écoulement turbulent régi par les équations de Navier-Stokes (Sec. 4.2) et un scalaire advecté dans un champ de vitesse aléatoire synthétique (Sec. 4.3) avec une covariance prescrite dans l'espace et le temps. Les résultats des simulations numériques pour les deux cas sont présentés et comparés aux résultats FRG présentés précédemment dans la section 1.3 (page 23). Enfin, dans la section 4.4, les principales conclusions du chapitre sont répertoriées. Une partie des résultats présentés dans ce chapitre est également publiée dans *Physical Review Fluids* (Gorbunova et al., 2021b).

4.1 Background

The statistics of a scalar advected by a turbulent flow has been extensively studied in various works, summarized in reviews (Warhaft, 2000; Shraiman and Siggia, 2000; Falkovich et al., 2001; Sreenivasan, 2019). In this section, a brief summary of the known results on the scalar correlation function is provided.

Two-point equal-time statistics of the scalar. The wavenumber spectrum of scalar variance is a two-point equal-time statistical property of the scalar field, and it is essential to discuss it before moving to the two-time two-point correlation function.

Let us consider a turbulent velocity flow of a fluid with viscosity ν, governed by Navier-Stokes equation (1.1), and a passive scalar field with diffusivity κ, governed by the diffusion-advection equation (1.25). The ratio between the viscosity of the fluid and diffusivity of the scalar gives a non-dimensional parameter called Schmidt number $Sc \equiv \nu/\kappa$. This number is also referred to as Prandl number if the passive scalar represents temperature, and κ is thermal conductivity. The velocity field is characterized by the Kolmogorov length scale, at which the viscous dissipation becomes dominant over the advection: $\eta = (\nu^3/\varepsilon)^{1/4}$, with ε the average dissipation rate of velocity. Similarly, for the passive scalar, there exists a characteristic length scale r_d, at which the molecular diffusion process becomes faster than the advection. Depending on the value of the Schmidt number, which is also linked with the ratio between the two length scales η and r_d, one can distinguish different regimes of dynamics of the passive scalar (Lesieur, 2008 ; Sreenivasan, 2019).

In the case where viscosity and diffusivity are comparable, so the Schmidt number is $Sc \sim 1$, the dissipative length scales are comparable $\eta \approx r_d$. The range of wavenumbers $1/L \ll k \ll 1/\eta \approx 1/r_d$, where neither scalar diffusivity nor viscosity play a role, is called *inertial-convective*. For this range, the phenomenology of Kolmogorov (1941) is applicable, and the velocity spectrum exhibits the power-law decay $E(k) = C_K \epsilon^{2/3} k^{-5/3}$. An extension of Kolmogorov's theory to passive scalar turbulence was first proposed by Obukhov (1949) and Corrsin (1951). The dimensional argument behind is similar to K41: far from the forcing and dissipative scales, the scalar dynamics solely determined by the constant spectral flux of scalar variance, which leads to the same $5/3$ power-law spatial spectrum:

$$E_\theta(k) = C_{OC} \varepsilon_\theta \epsilon^{-1/3} k^{-5/3} \tag{4.1}$$

with $\varepsilon_\theta = 2\kappa \langle \nabla\theta \cdot \nabla\theta \rangle$ - average dissipation rate of scalar, and C_{OC} - the Obukhov-Corrsin constant.

The situation changes if the fluid viscosity is considerably larger than the scalar diffusivity, in other words, when $Sc \gg 1$, which also implies that $r_d \ll \eta$. In this case, the diffusive length scale r_d is also referred to as the Batchelor length scale η_B, and it is related to the Kolmogorov length scale as $\eta_B = r_d = Sc^{-1/2}\eta$. There exists a range of wavenumbers $1/\eta \ll k \ll 1/\eta_B$ at which the viscosity becomes important while the diffusivity effects are still negligible, called *viscous-convective* range. The scalar exhibits in this range the Batchelor spectrum with the power law $E_\theta(k) \sim k^{-1}$. In the opposite case, when $Sc \ll 1$ and thus $r_d \gg \eta$, the scalar diffusivity starts acting at scales which are not sensitive to viscosity, which brings to emergence of an *inertial-diffusive* (or *inertial-conductive*) range which is expected to have the Batchelor-Howells-Townsend spectrum with the power law $k^{-17/3}$.

In the present work, the advection of a scalar is considered in the inertial-convective regime with $Sc \sim 1$. In this regime, for both velocity and scalar, the advection term is dominant for the range of wavenumbers $1/L \ll k \ll 1/\eta \approx 1/r_d$. Therefore, one expects to observe the Obukhov-Corrsin power law $k^{-5/3}$ in the scalar spectrum in the mentioned subrange.

Two-point space-time correlation function of the scalar. In certain problems, it is necessary to know not only the spatial statistics of the scalar field, but also its temporal correlations, in particular space-time Eulerian correlation functions. Its comprehension is essential, for instance, for the development of time-accurate numerical models parametrizing small-scale motions (G. He et al., 2017), or experimental data treatment (X. He and Tong, 2011) for space-time mapping of signals. In addition, the assumptions on space-time scalar correlation functions lie at the basis of certain approaches used in turbulent diffusion problems (Mazzino, 1997 ; Majda and Kramer, 1999).

Since we consider the inertial-convective range, where the advection term is dominating, one may intuitively suppose that the temporal properties of Eulerian correlation functions of the scalar in a turbulent flow are determined by the large-scale velocity field where most of the kinetic energy is concentrated, by analogy with the velocity correlation discussed in Chapter 3. Therefore, one should expect the appearance of the random sweeping effect in the temporal behavior of the correlation functions of scalars, with the typical time of decorrelation scaling as $\tau_D \sim k^{-1}$. The analogy between the sweeping effect in velocity and scalar fields is discussed in the work of Chen and Kraichnan (1989), where the straining of scalar threads is compared to the straining of thin vortical tubes, so that both are determined by the large-scale velocity and thus sweeping.

The dominance of the sweeping effect in two-time statistics of passive scalars has been observed in numerical simulations. In work of P. K. Yeung and Sawford (2002) it is shown through measuring the frequency spectrum of the passive scalar, which results to be $E(\omega) \sim \omega^{-5/3}$. Moreover, in the work of O'Gorman and Pullin (2004), the scalar space-time correlations are computed in DNS for scalar at $Sc = 0.7$ and compared with results of the stretched-spiral vortex model. The resulting temporal correlations of the scalar Fourier modes collapse when plotted against tk variable, which validates the sweeping scaling. In addition, it is shown that the characteristic times of decorrelation for the velocity and scalar fields are very close.

Apart from that, the evidence supporting the dominance of sweeping in scalar correlations were obtained from the experimentally measured space-time correlation of temperature in turbulent Rayleigh-Bénard convection (X. He and Tong, 2011 ; X. He and Tong, 2014). The sweeping hypothesis appears to be applicable as well for magnetic field in strong magnetohydrodynamic turbulence (Perez and Bourouaine, 2020) and in solar wind (Matthaeus et al., 2016 ; Perschke et al., 2016). However, despite the existing evidence, a rigorous theoretical justification was missing.

Model of scalar advection in random velocity field. A lot of important results were obtained by means of the analysis of simplified models of scalar turbulence, such as the model proposed by Kraichnan (1968). The simplification consists in replacing the velocity field by a random vector field with a white-in-time Gaussian statistics and a prescribed power law for the spatial covariance. This model represents a particular interest as it shows the emergence of an anomalous scaling in the scalar structure functions even when the velocity field has Gaussian statistics and therefore provides a simplified framework for the study of intermittency. Additionally, thanks to the simplification of velocity covariance, it allows to obtain closed equations for the scalar structure functions. Explicit analytical calculations of the anomalous scaling exponents of the structure functions were obtained by means of different approaches (Chertkov et al., 1996 ; Kraichnan, 1994 ; Frisch and Wirth, 1997 ; Adzhemyan and S. V. Novikov, 2006 ; Kupiainen and Muratore-Ginanneschi, 2007 ; Pagani, 2015). Furthermore, the temporal dependence of the scalar correlation function has been also studied, see the works of Mitra and Pandit (2005) and Sankar Ray et al. (2008). However, the assumption of white-in-time velocity prevents one from relating the model to real scalar turbulence in Navier-Stokes field, which has a non-trivial space-time dependent velocity covariance.

FRG results. Within the FRG framework, one can derive an approximated form of the spatio-temporal Eulerian two-point correlation function of the scalar field advected by NS flows and in Kraichnan's model (Pagani and Canet, 2021). These results were discussed in the section 1.3. According to FRG, the spatio-temporal dependence of the Eulerian two-point correlation function of the scalar exhibits two distinct time regimes in the stationary state depending on the time lag. If one considers the time lags smaller or comparable

to the typical correlation time of the velocity field, the correlation function of the scalar takes the form of a Gaussian function in the variable tk, which justifies the dominance of the sweeping effect. At time lags larger than the velocity correlation time scale, the correlation function of the scalar switches to an exponential decay in the variable tk^2. In the case of the Kraichnan's random advection model, the characteristic time of the velocity correlation vanishes, and according to the FRG, only the exponential part of the correlation function decay remains. Therefore, the FRG result demonstrates the crucial role of the temporal correlation of velocity on Eulerian space-time correlations of passive scalars. These results can be tested in numerical simulations of scalars in NS velocity field and in random synthetic fields.

Objective. The present work aims to study the Eulerian space-time correlations of a passive scalar by means of DNS and compare it with the FRG results. In particular, to test the influence of the velocity field temporal correlation, three cases of velocity fields are studied: a turbulent flow governed by the Navier-Stokes equation, a random velocity flow with white-in-time covariance and a random velocity flow with a finite correlation time. For the white-in-time velocity one expects to observe a purely exponential decay in scalar correlation functions, while for the case of Navier-Stokes velocity field and the synthetic velocity with finite correlation time, the two-regime decay is expected: a Gaussian at small time lags and the exponential at large time lags. The results for the scalar correlation function from the DNS in these three cases are presented in the following two sections.

4.2 Passive scalar advection in Navier-Stokes turbulent velocity field

4.2.1 Configuration of simulations.

In the simulations described in this section, in addition to the Navier-Stokes equation (1.1), the advection-diffusion for a passive scalar (1.25) is solved numerically with the use of the pseudo-spectral method. The solver for the scalar is totally identical to the velocity solver presented in Sec. 2.2 (p. 33). Since the scalar is passive, there is no need of two-way coupling between velocity and scalar, and the scalar is simply computed at each iteration once the computation of the velocity field is finished.

Parameters of simulations. The direct numerical simulations of the Navier-Stokes equation for the turbulent velocity field and the advection-diffusion equation for the passive scalar are performed at various resolutions, Reynolds numbers, and diffusivities (see Table 4.1). Schmidt number is the ratio between the fluid viscosity and scalar diffusivity: $Sc = \nu/\kappa$; the Péclet number is the ratio between the typical advection and diffusive times of the scalar and is thus high for an advection-dominant flow:

$$Pe = \frac{L\, U_{rms}}{\kappa} = Re\; Sc \tag{4.2}$$

In the present work, two velocity fields with different Taylor-scale Reynolds numbers $R_\lambda = 70$ and 90 are considered. For the case with the lower $R_\lambda = 70$ the scalars were simulated at 5 different values of Schmidt numbers from $Sc = 1$ to 64. In all cases, the Péclet numbers are $Pe \gg 1$, in order to reach regimes where the advection dominates over the diffusion in scalar dynamics.

Simulation	R_λ	N_v	Sc	N_s	Pe	$\Delta t/\tau_0$	$\Delta T_w/\tau_0$	N_w
1	70	160	1	160	426	5.0×10^{-4}	0.60	82
2	70	160	4	320	1706	2.5×10^{-4}	0.30	24
3	70	160	9	480	3840	1.2×10^{-4}	0.30	12
4	70	160	16	640	6827	1.0×10^{-5}	0.03	72
5	70	160	36	960	15362	4.1×10^{-5}	0.03	9
6	90	256	0.7	256	484	6.2×10^{-4}	1.7	50

TABLE *4.1 – Parameters of DNS of scalar advection in Navier-Stokes velocity field. R_λ - Taylor-scale Reynolds number, N_s - spatial grid resolution for velocity, Sc - Schmidt number, N_s - spatial grid resolution for scalar, Pe - Péclet number, τ_0 - integral eddy-turnover time, Δt - simulation time step, ΔT_w - width of a time window of correlation measurement, N_w - number of recorded time windows for time correlation.*

At $Sc = 1$ the spatial resolutions for scalar and velocity are equivalent, since the corresponding typical dissipation scales are close $\eta \approx \eta_B$. When switching to higher Schmidt numbers, the scalars are simulated on finer computational grids, while the velocity resolution is kept the same. The necessary spatial resolution for the scalar is evaluated as $N_s = N_v\sqrt{Sc}$, which follows from the ratio between the Kolomogov and Batchelor length scales η and η_B (Gotoh and P. Yeung, 2012). When computing the advection term of the scalar on a finer grid, the velocity field is rediscretized to the scalar grid size in spectral space by padding the velocity field at large wavenumbers $N_v/2 < k < N_s/2$ with zeros.

Scalar forcing. To reach a stationary state of the scalar evolution, the scalar field has to be forced. In the present study, the forcing (or source) term for the scalar f_θ in Eq. (1.25) is chosen to be a random field peaked at large scales, homogeneous and isotropic. This forcing ensures the symmetries assumed in the theoretical model. The forcing field is updated at every iteration, each new realization is uncorrelated with the previous one. The peak wavenumber of scalar forcing is close to the one of velocity.

4.2.2 Results of DNS.

The section presents the data collected in simulations of scalars advected by Navier-Stokes velocity field. The results for spatial spectra and two-point space-time correlation functions for both velocity and scalar are presented and discussed.

Fields and spectra of scalar and velocity. Examples of instantaneous 2D cuts of the velocity and scalar fields are displayed in Fig. 4.1, for the spatial resolution $N^3 = 256^3$, the Taylor-scale Reynolds number $R_\lambda = 90$ and the Schmidt number $Sc = 0.7$. The view of the scalar field shows the presence of intense mixing due to advection.

The figure 4.2 shows the kinetic energy spectrum of the velocity and variance of the scalar fields. The spatial spectra correspond to the same case as the fields presented in Fig. 4.1. One can see that both spectra exhibit approximately one decade of the inertial-convective range with the power law $k^{-5/3}$, before switching to rapid decay in the dissipation range.

Space-time correlation function. The correlation function of the scalar field is computed in the stationary state and is averaged in time and in space, over spherical spectral shells S_n of thickness $\Delta k = 1$. The method is completely identical to the computation

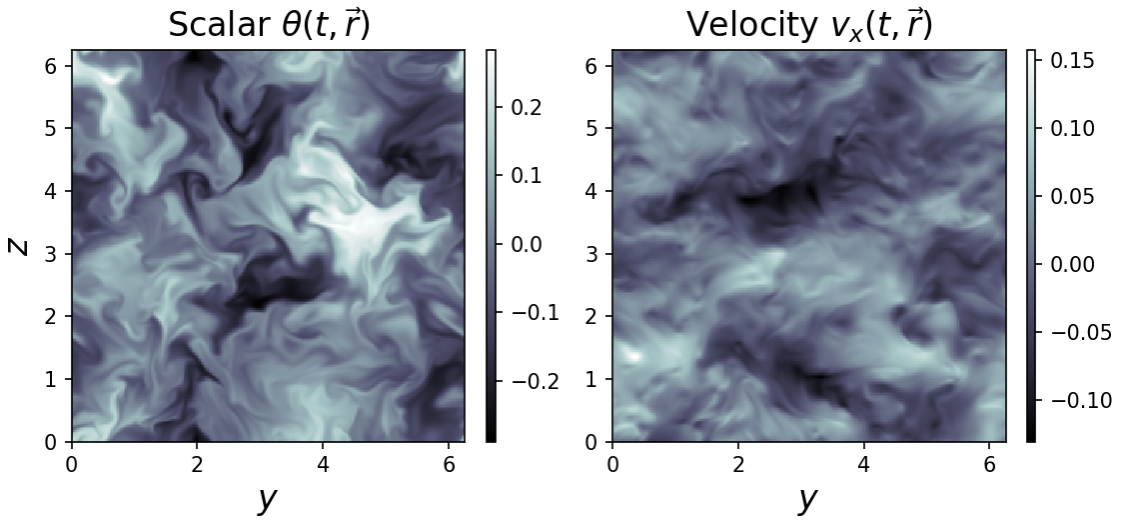

FIGURE *4.1 – Instantaneous 2D snapshots of the scalar field and of the x-component of the velocity field, obtained from the DNS of the Navier-Stokes equation at Taylor-scale Reynolds number* $R_\lambda = 90$ *on a grid of size* $N^3 = 256^3$*, with the Schmidt number of the scalar* $Sc = 0.7$.

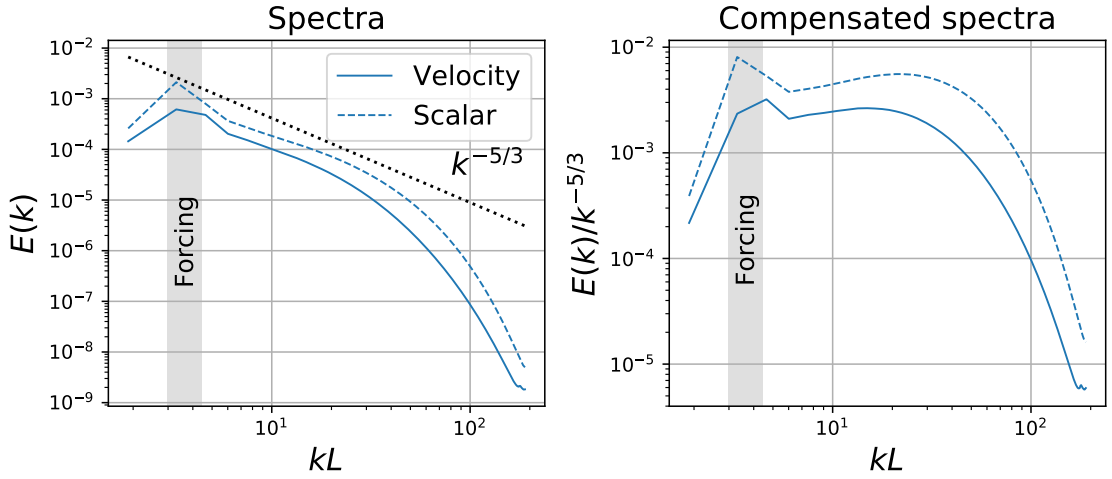

FIGURE *4.2 – Spectra and compensated spectra of the velocity kinetic energy and scalar variance from DNS at Taylor-scale Reynolds number* $R_\lambda = 90$ *on a grid of size* $N^3 = 256^3$*, with the Schmidt number of the scalar* $Sc = 0.7$.

of the velocity correlation function described in Sec. 2.3 (page 37). For the scalar, the computation formula is written as:

$$C(t,\vec{\mathbf{k}}) = \frac{1}{N_w}\sum_{j=1}^{N_w}\frac{1}{M_n}\sum_{\vec{\mathbf{k}}\in S_n}\mathrm{Re}\left[\hat{\theta}(t_{0j},\vec{\mathbf{k}})\hat{\theta}^*(t_{0j}+t,\vec{\mathbf{k}})\right], \tag{4.3}$$

where N_w is the number of time windows in the simulation, and M_n is the number of modes in the spectral spherical shell S_n. During the simulations, both scalar and velocity correlations are computed simultaneously.

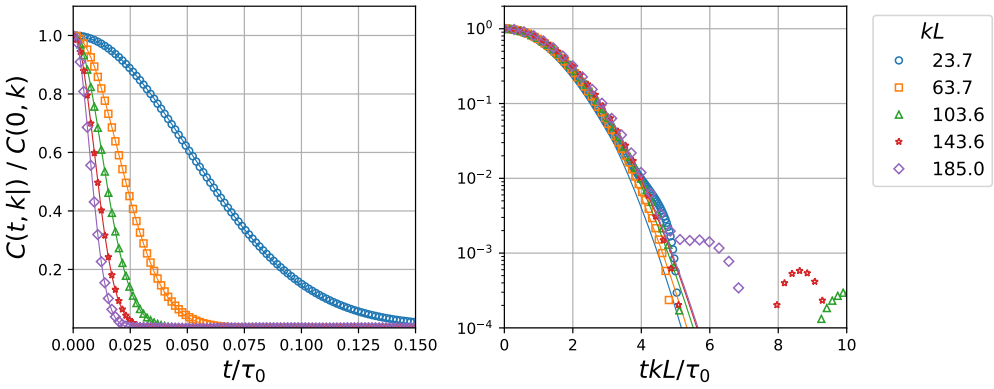

FIGURE *4.3 – Normalized averaged two-point correlation function* $C(t,\vec{\mathbf{k}})$ *of a scalar in the NS velocity field at various wavenumbers* k *from simulation at* $R_\lambda = 90$ *and* $Sc = 0.7$. *Points correspond to the numerical data and continuous lines represent the Gaussian fits. On the right panel: the same data in* tk *horizontal scaling to demonstrate the collapse of the curves.*

The Fig. 4.3 gives an example of the typical behavior in time of the correlation function of a passive scalar at various wavenumbers. Note that the picture is similar to the correlation function of velocity shown in Fig. 3.2 (page 49). When plotted against the tk variable (right panel of Fig. 4.3), all curves collapse into a single one, indicating the sweeping scaling predicted by FRG. The data points also accurately follow the Gaussian fit (denoted with continuous lines), calculated in the form $g(t) = C\exp\{-at^2\}$ with two parameters: a and C. In all figures, the wavenumbers are non-dimensionalized by the integral length scale L, and the times by the integral turn-over time $\tau_0 = L/U_{\mathrm{rms}}$ with U_{rms} the root mean square velocity.

Typical decorrelation time of the scalar. The typical decorrelation time is estimated through the fitting parameter a as $\tau_D = 1/\sqrt{a}$. The dependence of the decorrelation time on the wavenumber is shown in Fig. 4.4a. One can see that all curves exhibit a decay $\tau_D \sim k^{-1}$ corresponding to the sweeping scaling. In addition, the decorrelation times of the scalar and velocity are very close. The decorrelation time at the two considered Reynolds numbers $R_\lambda = 70$ and 90 also almost coincide.

The value of the fitting parameter a can also provide a numerical estimation of the decorrelation parameter α_S in the theoretical expression (1.28) as $\alpha_S = a\,(\tau_0/Lk)^2$. The dependence of the estimated parameter α_S on the wavenumber is displayed in Fig. 4.4b, showing that both the velocity and scalar reach a plateau beyond the forcing range. This observation is in agreement with the theoretical short-time expression in Eq. (1.28). Moreover, the numerical values of α_S for the scalar and velocity fields are very close, which is also in agreement with the theoretical result, according to which the parameter α_S is solely

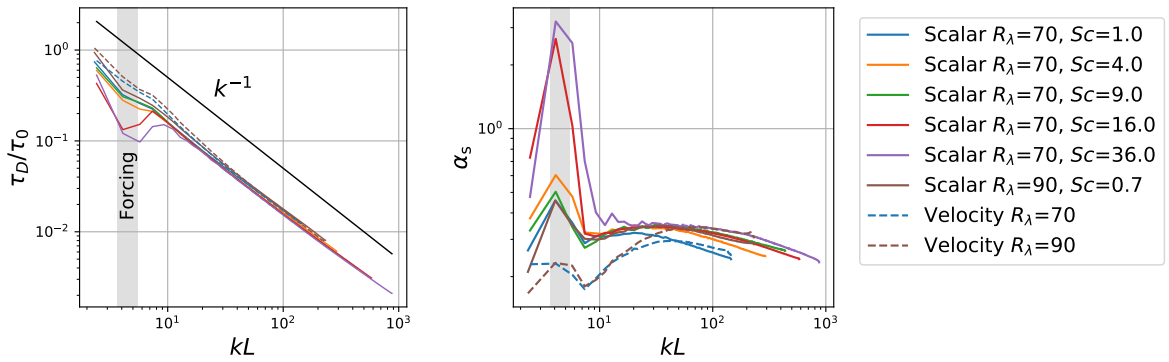

(a) Decorrelation time scale $\tau_D = 1/\sqrt{a}$

(b) Decorrelation parameter $\alpha_S = a\,(\tau_0/Lk)^2$

FIGURE *4.4 – Dependence of the decorrelation time scale* τ_D *and the decorrelation parameter* α_S *on the wavenumber* k *for the scalar and velocity fields.* τ_D *and* α_S *are estimated with the use of the parameter* a *of the Gaussian fitting of numerical data in the form* $g(t) = Ce^{-at^2}$.

determined by the properties of the velocity statistics and is the same for the velocity and for the scalar.

Dependence on the Schmidt number. As one can see from the Fig. 4.4a, the change of Schmidt number from $Sc = 1$ to $Sc = 36$ does not lead to significant changes in the typical decorrelation time. However, one can notice that the decorrelation time slightly tends to decrease with growing Schmidt numbers. It can also be seen from Fig. 4.4b, where the parameter α_S for the larger Schmidt numbers appears to be a little higher. However, to draw a solid conclusion, a larger span of Schmidt numbers is needed. It should also be noticed that a similar decrease in the typical decorrelation time with Schmidt number was observed in the numerical study of P. K. Yeung and Sawford, 2002, although this time scale was evaluated as the one characterizing the rate of change of the scalar at Taylor microscale.

Scalar correlation at large time lags. The behavior of the scalar correlation function at large time lags is hindered by oscillations around zero after the Gaussian decay. This effect is identical to the oscillations in the correlations of velocity, discussed in Sec. 3.2.2. For this reason, the presented numerical data does not allow to observe the transition from the Gaussian to the exponential decay in the scalar correlation function at large time lags, predicted by FRG.

Summary. In this section, we report the numerically computed Eulerian two-point spatio-temporal correlation function of a passive scalar advected by a velocity field governed by NS equation. At small time lags, the correlation function behaves as a Gaussian function in the variable tk, similar to the correlation function of velocity discussed in the previous chapter. This time scaling is related to the process of sweeping of the passive scalar by the random large-scale velocity field. Moreover, it is shown that the typical decorrelation times for velocity and scalar almost coincide, which is in agreement with the FRG result. Unfortunately, at large time lags, the correlation function is too oscillatory and does not enable analysis. However, both regimes appear clearly in the case of scalars advected by synthetic velocity fields. It is shown in the following section.

4.3 Scalar advection in synthetic velocity field

As it was discussed in Sec. 1.3, the FRG approach shows that in the case of the random white-in-time velocity field (corresponding to Kraichnan's model), the temporal dependence of the two-point space-time correlation function of the scalar takes the form of an exponentially decaying function of the variable tk^2. In the present section, we aim to test this dependence on the time lag t and the wavenumber k. In addition, the FRG provides an exact form for the prefactor of the exponential, which is equal to the renormalized diffusivity κ_{ren}, given in Eq. (1.31). The theoretical renormalized diffusivity κ_{ren} depends on the microscopic molecular diffusivity of the scalar κ and parameters of the synthetic velocity field (amplitude of its variance, its Hölder exponent, spectral cut-off). In addition, the integral defining κ_{ren} in Eq. (1.31) can be estimated numerically, and thus by varying the parameters of the synthetic velocity field, one can numerically validate the theoretical prediction for the prefactor in the exponential of the correlation function. For this reason, 4 sets of simulations have been performed to test the dependence on various parameters.

In the case of a velocity field which is correlated in time, the FRG predicts that for time lags smaller than the velocity correlation time, the scalar correlation function behaves as a Gaussian (equivalent to the behavior in NS field discussed above), and then switches to the exponential decay, equivalent to the one characterizing the scalar correlation functions in Kraichnan's model. This result is also tested in DNS by generating a velocity field that is kept as constant over a certain number of temporal iterations of the solver. Slowing down the velocity field update allows to get the velocity fields correlated in time. The number of iterations between the updates imposes the typical correlation time of the velocity field. Moreover, since this correlation time is controlled by the parameters of a simulation, it is relatively easy to adjust the parameters to observe the two regimes in the correlation function of the scalar.

This section is organized in the following way. Firstly, details about the method of velocity field generation and the choice of parameters are provided. Next, the results obtained from simulations with random velocity fields are presented. The cases of white-in-time velocity field and a velocity correlated over a certain time span are discussed. The scalar two-point spatio-temporal correlations are computed in both cases and compared with the FRG results.

4.3.1 Description of simulations

Since the velocity field is generated as a random vector field, there is no need to solve the Navier-Stokes equation. The solver for velocity is replaced by the random field generator. Only the equation for the scalar dynamics (1.25) is solved with the use of the pseudo-spectral solver. It makes the computation significantly less expensive.

Random velocity field generation. To approximate the stochastic white-in-time self-similar velocity field of Kraichnan's model (1.29), a synthetic velocity field generator has been implemented. The generated velocity field must ensure the following variance:

$$\left\langle \hat{u}_i(t_0,\vec{\mathbf{k}})\hat{u}_j^*(t_0+t,\vec{\mathbf{k}})\right\rangle = \begin{cases} \dfrac{D_0}{T_e}\left(k^2+m^2\right)^{\frac{-3-\varepsilon}{2}} P_{ij}(\vec{\mathbf{k}}), & t<T_e, \\ 0, & t>T_e, \end{cases}$$

where T_e is the existence time of an individual realization of the velocity field, which is calculated as $T_e = n\Delta t$, where n is the number of time iterations before a new velocity field is generated. The wavenumber m is set to 1 in all simulations.

The velocity field is generated in Fourier space as a random vector field:

$$\hat{\vec{u}}(t,\vec{\mathbf{k}}) = \sqrt{\frac{2D_0(k^2+m^2)^{\frac{-3-\varepsilon}{2}}}{T_e}}\vec{\eta}(t,\vec{\mathbf{k}}), \tag{4.4}$$

where $\vec{\eta}$ is a unit random complex vector fulfilling the requirements of zero-divergence and isotropy. The velocity field is characterized by the root-mean-square velocity $U_{rms} = \sqrt{2E_k/3}$, with E_k the total kinetic energy. The RMS velocity is linked to the parameter D_0 through $U_{rms} = \sqrt{A\frac{D_0}{2T_e}}$, where $A = \frac{1}{3}\sum_{\vec{\mathbf{k}}}\left(k^2+m^2\right)^{\frac{-3-\varepsilon}{2}}$ is the constant coming from the numerical estimation of the integral of the power law in the spatial velocity spectrum. The velocity field in the simulation is thus determined by the four principal parameters: the Hölder exponent $\varepsilon/2$, the variance amplitude D_0, the renewal period T_e and the infra-red cut-off m (set everywhere to 1).

Update frequency of velocity field. The random velocity field is generated in the spectral space every n iterations and is totally uncorrelated with the previous realizations. If T_e is small compared to the dynamical time scales of the flow (advection time scale $\tau_A \sim \Delta x/U_{\text{rms}}$ and diffusion time scale $\tau_\kappa \sim (\Delta x)^2/\kappa$, with Δx spatial grid cell), the velocity field can be considered as approximately white-in-time. Note also that the update time T_e is limited also by the step of time discretization of the numerical scheme $T_e \geq \Delta t$.

The parameter T_e is varied in the present study. Firstly, a numerical approximation of white-in-time velocity field is considered, so the update period is set to be small $T_e \ll \tau_A$. This case corresponds to the numerical approximation of the Kraichnan's random advection model. In the following subsection, the update period T_e is increased to $T_e \sim \tau_A$, allowing to switch to velocity fields correlated in time. It will be shown that this parameter controls the form of the scalar time correlation function.

Roughness of velocity field. The spatial properties of the velocity field are controlled by its roughness, which is determined by the parameter ε. Its half value $\varepsilon/2$ gives the Hölder exponent of the velocity field. In other words, the small values $\varepsilon \to 0$ correspond to rough velocity fields, while the large values $\varepsilon \to 2$ correspond to smooth fields. To illustrate this, instantaneous snapshots of the velocity fields at various ε are shown in the first row of Fig. 4.5 (p. 95). Also, the parameter ε coincides with the power-law exponent of the second-order structure function of velocity. The physical value of the parameter is $\epsilon = 4/3$, at which the prefactor D_0 has dimensional units of the energy power (Adzhemyan and S. V. Novikov, 2006).

In the present work, five values of this parameter are used: $\varepsilon = 0.1, 0.5, 1.0, 1.5, 2.0$. It should be noted that the case with $\varepsilon = 2$ is not trivial. This limiting case corresponds to the Batchelor regime of Kraichnan's model, where the velocity gradients are constant (Falkovich et al., 2001). In this case, the integral of the kinetic energy diverges in the analytical model. However, numerically there is no divergence due to the finite size of the computational domain, so the simulations at $\varepsilon = 2$ do not correspond to a completely smooth velocity field, but allow at least to approach this regime.

Forcing of scalar. The scalar field is subjected to a large-scale random forcing. The forcing term f_θ is generated at each iteration in spectral space within a narrow wavenumber band $3 < k_f < 4$ corresponding to large scales. The amplitude of the forcing is the same in all simulations. Spectral forcing has been chosen to ensure the isotropy of the scalar fields.

set	N	$\kappa \cdot 10^3$	ε	$D_0 \cdot 10^3$	n	$\frac{T_e}{\tau_0} \cdot 10^3$	$\Delta t \cdot 10^3$	U_{rms}	τ_0	Pe	A	N_w	$\kappa_{\text{ren}} \cdot 10^3$
1	256	6	0.1	0.418	6	2.35	0.24	2.87	0.62	1.45	14.56	8	12.2
	256	1.70	0.5	2.09	6	3.46	0.24	4.22	0.42	6.54	6.28	10	14.8
	384	0.17	1.0	4.18	9	2.9	0.16	3.54	0.51	85.7	2.96	17	12.5
	384	0.025	1.5	6.27	9	2.7	0.16	3.32	0.54	793	1.72	17	10.8
	256	0.014	2.0	16.7	6		2.53	3.09	0.58	1836	1.12	9	1.08
2	192	100	0.1	0.418	6	2.65	0.32	2.42	0.74	0.09	13.81	26	105.8
	192	100	0.5	2.09	6	3.39	0.32	3.62	0.49	0.11	6.16	5	112.9
	192	100	1.0	4.18	6	3.88	0.32	3.55	0.50	0.15	2.96	5	112.3
	192	100	1.5	6.27	6	3.63	0.32	3.32	0.54	0.20	1.72	5	110.8
	192	100	2.0	16.7	6	3.38	0.32	3.09	0.58	0.26	1.12	9	110.8
3	64	2	1.0	0.0	-	-	0.98	0.0	-	0.0	-	440	2
	64	2	1.0	2.09	2	3.1	0.98	2.86	0.62	2.5	2.86	440	8
	96	2	1.0	3.14	3	3.3	0.65	3.05	0.58	3.76	2.91	318	11
	128	2	1.0	4.18	4	3.8	0.49	3.23	0.50	5.02	2.93	266	14
	192	2	1.0	6.28	6	4.7	0.32	4.34	0.41	7.52	2.95	95	20
	256	2	1.0	8.37	8	5.5	0.24	5.03	0.35	10.04	2.97	49	26
	384	2	1.0	12.55	12	6.7	0.16	6.16	0.29	22.52	2.97	35	39
	512	2	1.0	16.75	16	7.7	0.12	7.12	0.25	30.03	2.98	35	51
	768	2	1.0	25.10	32	9.5	0.06	8.74	0.20	45.05	2.98	39	76
4	128	0.05	1.0	8.36	4	6.7	0.49	3.23	0.29	0.30	2.93	34	62
		20								0.75			32
		13								1.12			25
		10								1.50			22
		5								3.00			17
		3.3								4.50			15
		2								7.51			14
5	384	2	1.0	12.55	24	13.4	0.16	4.36	0.29	22.52	2.97	258	39

TABLE *4.2 – Parameters of simulations of scalars in synthetic velocity fields. N - spatial resolution of the computational grid, κ - scalar diffusivity, $\varepsilon/2$ - Hölder exponent of the velocity field, D_0 - amplitude of the velocity covariance, n - number of iterations between velocity field updates, T_e/τ_0 - velocity update period normalized by the typical large-scale time τ_0, Δt - simulation time step, U_{rms} - root-mean-square velocity, τ_0 - large-scale time defined as $\tau_0 = L/U_{rms}$, Pe - Péclet number, A - sum of the velocity spectrum, N_w - numbers of time windows for correlations averaging, κ_{ren} - numerical estimation of the renormalized diffusivity estimated according to Eq. (4.5).*

Parameters of simulations. The dynamics of the scalar can be characterized by a non-dimensional parameter analogous to the Péclet number $Pe = D_0' L^{\varepsilon}/\kappa$, where $D_0' = D_0/\varepsilon$, and L corresponds to the scalar integral length scale $L = 2\pi/k_f$. The Péclet number is defined as the ratio between the advective and diffusive terms at the forcing length scale (Falkovich et al., 2001).

The main parameters to be determined for the initialization of a simulation are: scalar diffusivity κ, velocity field Hölder exponent $\varepsilon/2$, the prefactor of velocity covariance D_0 and the number of iteration between velocity fields renewals n. The time step Δt is dictated by the numerical stability of the solver, in particular by the choice of the time advancement scheme and CFL number.

In the present study, the parameters are chosen based on consideration of the separation between time scales. Firstly, to approach the white-in-time velocity field, the period of velocity generation $T_e = n\Delta t$ must be much smaller compared to the typical advection time scale τ_A. Secondly, if one is interested in the turbulent regime dominated by advection, the typical advection time τ_A must be considerably smaller in comparison with the characteristic diffusion time scale τ_κ. This is to say, the separation between the three time scales $T_e \ll \tau_A \ll \tau_\kappa$ needs to be respected.

The initial estimation of the parameters of the simulation was done on the basis of the parameters used in the numerical study of Chen and Kraichnan (1998). Although that study covers only 2D flows, and the method of velocity field generation is different, the proposed parameters appear to be useful as a starting point. The parameters of all simulations are provided in Table 4.2 (p. 92).

Simulation sets. As one can see in Table 4.2, the simulations are divided into four sets. Sets 1 and 2 contain simulations at various ε with the parameter $D_0' = D_0\varepsilon$ kept constant. In set 1, the diffusivities κ were chosen small to reach the inertial regime, dominated by the advection ($Pe > 1$). In set 2, the diffusivity is fixed at a higher value, so that $Pe \sim 0.1$. In this case, the scalar transport is dominated by diffusion but is still strongly affected by the advection. For this reason we refer to this regime as inertial-diffusive. The snapshots of the scalar fields for data sets 1 and 2 are provided in Fig. 4.5 in second and third rows, respectively.

Set 3 aims to test the dependence of the scalar correlation on the velocity covariance amplitude D_0. It consists of simulations with a fixed value of diffusivity κ and $\varepsilon = 1$ and gradually increasing parameter D_0. The first simulation at $D_0 = 0$ corresponds to the purely diffusive case.

The dependence on the scalar molecular diffusivity κ is tested in set 4. It consists of a single simulation in which 7 scalars with various diffusivities are transported simultaneously by the same velocity field, so the velocity field is identical for all scalars with $\varepsilon = 1$ and fixed D_0.

The last set 5 consists of only one simulation with a larger velocity update, this case is discussed in subsection 4.3.3.

Renormalized diffusivity. According to the FRG, the prefactor in the correlation function coincides with the renormalized diffusivity κ_{ren}, which is given in Eq. (1.31). For numerical estimation, the integration in the theoretical result can be replaced by a summation over the discrete computational grid, so the renormalized scalar diffusivity is evaluated according to:

$$\kappa_{\text{ren}} = \kappa + \frac{1}{3}\sum_{\vec{\mathbf{k}}} \frac{D_0}{(k^2+m^2)^{\frac{3+\varepsilon}{2}}} = \kappa + AD_0. \tag{4.5}$$

It should be noted that the expression in (4.5) depends only on the scalar diffusivity and properties of the velocity field. It can be computed just on the basis of the initialization parameters, it does not require solving the equation of the scalar transport. The numerical estimations of κ_{ren} for each simulation are provided in the last column of the Table 4.2.

Summary. A generator of synthetic velocity field has been implemented. The obtained velocity fields fulfill the conditions of homogeneity and isotropy. The intensity of the velocity field is defined by the amplitude of the covariance D_0, its roughness in space is determined by the Hölder exponent $\varepsilon/2$, and its temporal covariance is regulated by the update period T_e. These three parameters are the input parameters for the velocity field generator. They are chosen based on the consideration of the separation between the time scales.

The simulations are divided in 4 data sets, in which the parameters D_0, ε and κ are varied, which allows to check the influence of these parameters on the decorrelation of the scalar and compare it with the FRG prediction.

In addition, the proposed implementation of the random field generator allows to easily change the renewal period of the velocity field. Therefore, one can study the scalar correlation function in quickly changing velocity fields, which corresponds to a numerical approximation of Kraichnan's model, as well as in slowly changing velocity fields. It allows determining the influence of the temporal covariance of velocity on scalar correlations.

4.3.2 Scalar two-point spatio-temporal correlation function in white-in-time velocity field

Firstly, the results of DNS of scalar advection in synthetic flows with fast velocity renewal are presented. The period of velocity field generation is much smaller than the advection and diffusive time scales of the flow. We expect in this case to obtain a numerical approximation of the Kraichnan random advection model with corresponding power laws in scalar spatial spectra and with scalar correlations matching the FRG prediction presented in section 1.3.2 (p. 25).

Snapshots of the scalar and velocity fields. Two-dimensional cuts on the instantaneous three-dimensional synthetic velocity fields at various exponents ε are shown in the first row of Fig. 4.5. One can see that the velocity field looks rough at smaller ε and rather smooth at $\varepsilon = 2$. On the contrary, the field of the passive scalar in the inertial regime is smooth at small ε and becomes rough with growing ε (see the second row Fig. 4.5). It is in agreement with the known fact for the Kraichnan model: the degrees of roughness for scalar and velocity are complementary (Falkovich et al., 2001).

The fields of the scalar in the inertial-diffusive regime are shown in the last row of Fig. 4.5, corresponding to higher values of the molecular diffusivity κ. One can see that the fields are smoothed by the effect of diffusivity, and one cannot distinguish between various ε just by visual inspection of scalar fields.

Spatial spectra of the passive scalar. Figure 4.6 displays the spectra, i.e., the equal-time correlation functions for the velocity and the scalar field in set 1, which is the inertial (turbulent) regime, and in set 2, which is the inertial-diffusive (or weakly nonlinear) regime. The curves corresponding to set 1 (the second column in Fig. 4.6) match quite accurately the power-law $k^{-5+\varepsilon}$. This power law corresponds to the inertial range and can be deduced from dimensional arguments (Falkovich et al., 2001). This power law has been also obtained in numerical simulations of 2D random scalar advection in works of Chen and Kraichnan (1998) and Fairhall et al. (1997).

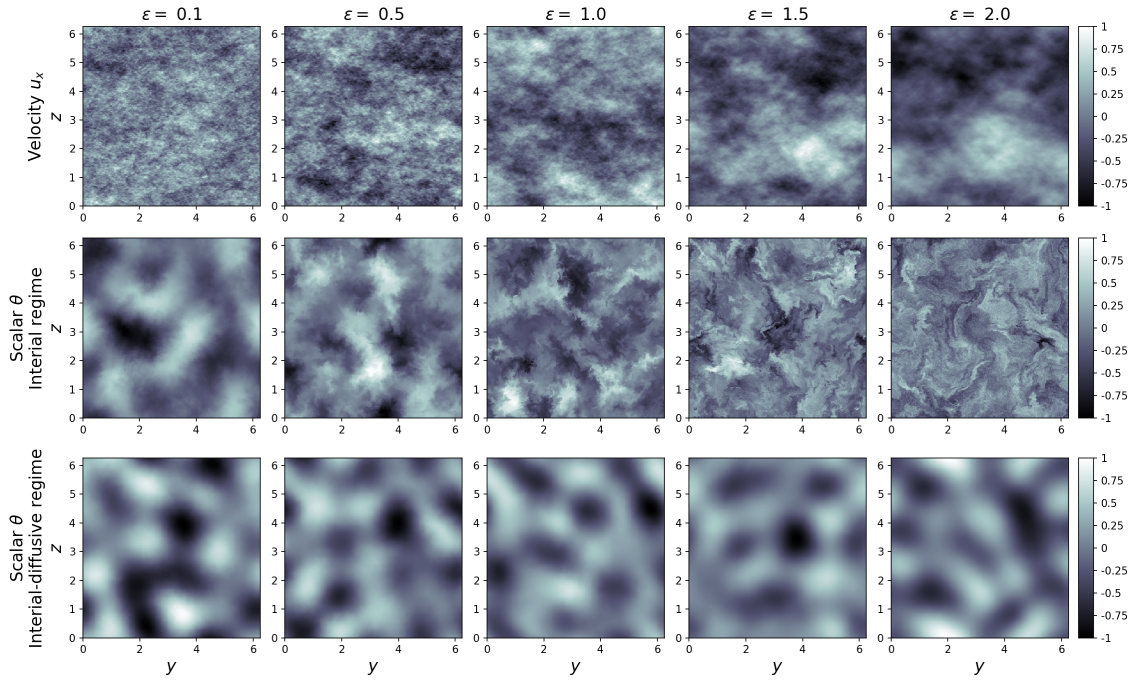

FIGURE *4.5 – Two-dimensional instantaneous cuts at various ϵ of the x-component of the synthetic velocity (first row), and the passive scalar field in the inertial (second row) and inertial-diffusive (third row) regimes. The inertial regime corresponds to the set 1, and the inertial-diffusive to set 2 of Table 4.2.*

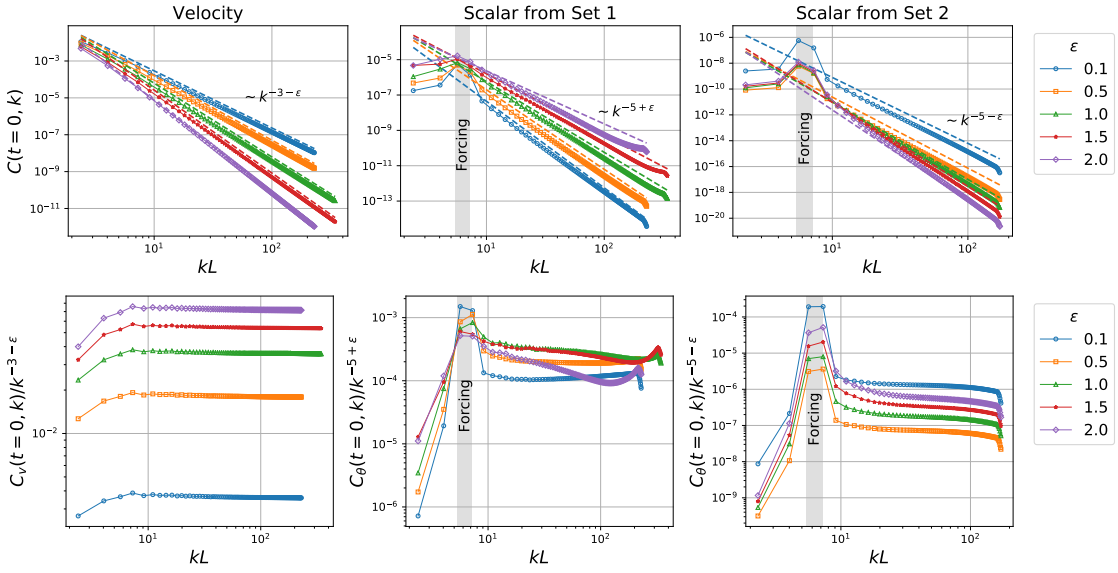

FIGURE *4.6 – Upper row: equal-time two-point correlation functions of the velocity and scalars from data set 1 (inertial regime) and set 2 (inertial-diffusive regime). The points correspond to the numerical data, the dashed lines to the theoretical power law. The bottom row shows the same data but compensated by the theoretically predicted power law.*

Note, that the curve $\varepsilon = 2$ does not follow the expected power law. This deviation can be attributed to the finite-size effect of the computational domain. The corrections due to finite size become more significant at $\varepsilon \to 0$ and $\varepsilon \to 2$, since these cases limit the integral convergence. In other words, putting $\varepsilon = 2$ in numerical simulations actually corresponds to a $\varepsilon \lesssim 2$ analytical model, which explains why the exponent of the power law observed numerically is less than $-5 + \varepsilon$.

The plots in the second column present spectra obtained from simulations of set 2 corresponding to the inertial-diffusive regime, in which the diffusivity becomes dominant. The numerically obtained spectra accurately match the power law $k^{-5-\varepsilon}$ for all values of ε. It is in agreement with previous works (Frisch and Wirth, 1996; Frisch and Wirth, 1997), where this power law for Kraichnan's model is shown to be analog of the Batchelor-Howells-Townsend scalar spectrum with $k^{-17/3}$ law in Navier-Stokes turbulence. In the recent work of Pagani and Canet, 2021, it is also demonstrated that by considering the advection term as a perturbation, this power law can be obtained within different approaches.

Therefore, the obtained spatial spectra of the scalars presented in Fig. 4.6 are in agreement with known theoretical results for Kraichnan's model. It allows to conclude that the implemented numerical model captures correctly the equal-time statistics of the scalar in random velocity fields.

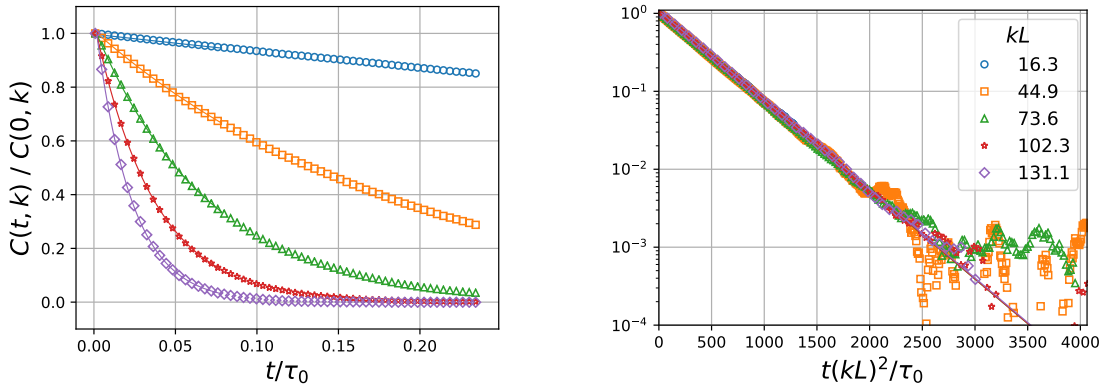

(a) Linear scaling

(b) Horizontal variable tk^2 and y-logarithmic scaling.

FIGURE *4.7 – Two-point correlation function $C_\theta(t, \vec{\mathbf{k}})$ at various wavenumbers k of a passive scalar in 3D of Kraichnan's random advection model for $\varepsilon = 1$ (simulation at $N = 92$ of set 3). All curves collapse onto a single exponential when plotted against the variable tk^2. The continuous lines correspond to the exponential fit in the form $g_K(t) = C_0 \exp\{-bt\}$.*

The two-point two-time correlation function of the scalar The spatio-temporal correlation function of the scalar has been measured numerically for all sets. The time dependence of the normalized correlation function $C_\mathrm{K}(t, \vec{\mathbf{k}})/C_\mathrm{K}(0, \vec{\mathbf{k}})$ at fixed wavenumbers is always exponential, as illustrated in Fig. 4.7. Moreover, when plotted as a function of tk^2, all the curves collapse onto a single exponential, which confirms the theoretically predicted form (1.30). For a more detailed analysis, all curves were fitted with the two-parameter exponential function $g_K(t) = C_0 \exp[-bt]$. The obtained fitting exponential functions are shown in Fig. 4.7 as continuous lines.

As one can see from Fig. 4.8a, the fitting parameter b is proportional to k^2, and this behavior is independent of the parameter D_0. For the sake of clarity, only the results from simulations of set 3 are shown, but similar results were obtained for all data sets. It can be seen more clearly in Fig. 4.8b showing that the fitting parameter b compensated by

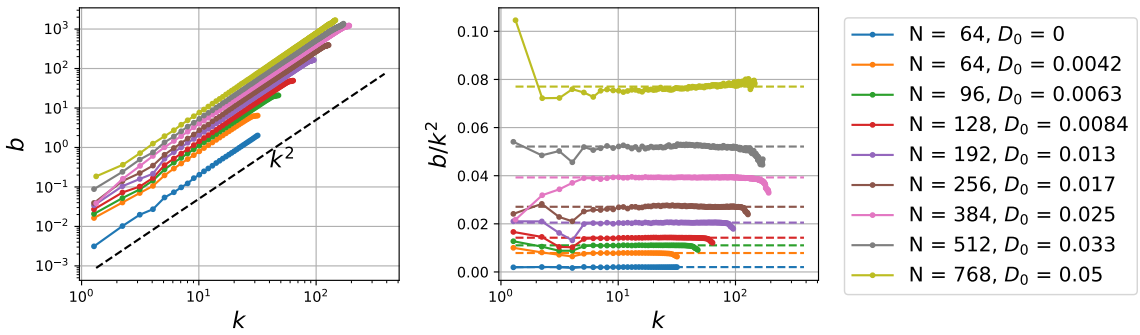

(a) Fitting parameter b versus k. *(b) Dependence of the ratio b/k^2 on the wavenumber.*

FIGURE *4.8 – Dependence of the fitting parameter b on the wavenumber k of the fitting function $g_K(t) = C_0 \exp\{-bt\}$ for simulations of the Set 3. The parameter b appears to depend on the wavenumber as k^2, so the compensated value b/k^2 gives a constant over a large span of wavenumbers. The colored dashed lines in figure b) correspond to the plateau values used for the subsequent data analysis.*

k^2 takes an approximately constant value in a large range of wavenumbers. These results demonstrate that the correlation functions $C_{\mathrm{K}}(t, \vec{\mathbf{k}})$ indeed take the expected form (1.30) of an exponential in time with the rate of decay proportional to k^2. One can also observe that the plateau value of b/k^2 appears to grow monotonously with D_0.

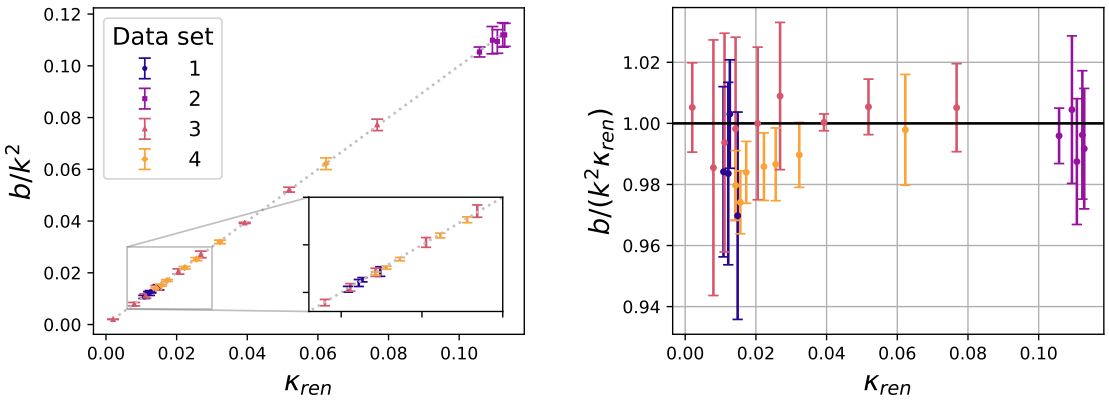

(a) Parameter b/k^2 versus κ_{ren}. *(b) Dependence of the ratio $b/(k^2\kappa_{\mathrm{ren}})$ on the κ_{ren}.*

FIGURE *4.9 – Decorrelation parameter b/k^2 of the exponential fit of the scalar correlation function versus its theoretical estimate κ_{ren} based on the Eq. (1.31) for 4 data sets. The error bars correspond to doubled standard deviation of b/k^2 from the estimated plateau value, shown in Fig. 4.8b with dashed lines.*

Prefactor in the exponential. The theoretical prediction (1.30) gives the exact form for the prefactor in the exponent of the correlation function, it coincides with the renormalized diffusivity κ_{ren}. The renormalized diffusivity is defined in Eq. (1.31): it depends on the scalar molecular diffusivity κ and the details of velocity statistics (in particular, on the amplitude D_0, Hölder exponent $\varepsilon/2$ and the spectral cut-offs). In DNS, κ_{ren} has been evaluated at the initialization of each simulation using the approximated form (4.5) where the integral is replaced by a numerical summation over the discrete modes of the computational grid. Its values are provided in Table 4.2.

One can also estimate the prefactor of the exponential of the scalar correlation function on the basis of the fit by taking simply the plateau value of b/k^2 (indicated with dashed lines in Fig. 4.8b). Moreover, it is possible to compare it with the theoretically predicted prefactor, which is equal to the renormalized diffusivity κ_{ren}. This comparison is shown in Fig. 4.9a. It shows that the two quantities are equal for all data sets. It can be seen more clearly from Fig. 4.9b showing the ratio between the parameter $b/(k^2\ \kappa_{\text{ren}})$ versus κ_{ren}. Results are close to 1 with good accuracy for simulations of all data sets.

It brings us to the conclusion that the prefactor in the exponential of the scalar correlation function extracted from the fit of the numerical data as b/k^2 is equal to the renormalized diffusivity κ_{ren} evaluated with the use of expression (4.5). The computation of these two quantities is totally independent. Therefore, we obtain a numerical confirmation of the FRG results for the temporal dependence of the scalar correlation function (1.30) up to the precise form of the prefactor in the exponential.

It is worth mentioning that Fig. 4.9 demonstrates that the temporal dependence predicted by FRG is valid for all data sets. It means that the time dependence of the scalar correlation function is identical for the inertial (set 1) and inertial-diffusive regimes (set 2), as for sets 3 and 4 containing mixed regimes, while its equal-time correlation function has different power laws as it is shown in Fig. 4.6.

Another important remark: the obtained results are tested for values of ε spanning from 0.1 up to 2.0. It indicates that the obtained results are valid for different degrees of roughness of the velocity field, and thus the FRG approach is also applicable for high ε, which is not the case of the perturbative approaches limited by the assumption of smallness of ε (Adzhemyan et al., 1998).

Summary. Simulations of scalar advection in a random velocity field were performed. The numerical model represents an approximation of a white-in-time velocity field, which is referred to in the literature as Kraichnan's random advection model. The spatial spectra of scalar variance in the inertial and inertial-diffusive regimes match the theoretically predicted power laws, which allows to conclude that the applied numerical method provides correct results for two-point equal-time statistics of the scalar.

The analysis of the scalar two-point space-time correlation function shows that it behaves as an exponential function of the variable tk^2, in total agreement with the FRG prediction. Moreover, even the prefactor in the exponential, which depends on details on the velocity statistics, is in quantitative agreement with the theoretical expression. The obtained exponential time dependence of the scalar correlation function appears to be universal and is recovered in different regimes of scalar advection.

4.3.3 Scalar two-point spatio-temporal correlation function in correlated-in-time velocity field.

Simulation configuration. To study the scalar dynamics in the case of a random velocity field with non-delta-in-time covariance, a simulation with a larger renewal period T_e of the velocity field has been performed. Extending the update period T_e means that we increase the number of time iterations during which the scalar is evolving in a "frozen" velocity field, before a new velocity field is generated. For this purpose, the configuration of the simulation from set 5 of Table 4.2 is taken. This configuration is similar to the one with $N = 384$ from set 3, but the number of iterations between two velocity updates is increased twofold up to $n = 24$. This number is taken as it makes the update period T_e comparable to the typical decorrelation time of the scalar, computed in the previous subsection for the case of the white-in-time velocity.

However, larger values of T_e impose a temporal periodicity on the flow related to this

time scale, and therefore on the scalar correlation. To avoid the impact of this periodicity on the measured scalar time statistics, the method of computation of temporal correlations was slightly modified by adding a random delay between the records of consecutive time windows of the correlation curves. After the record of one temporal correlation curve is finished, the algorithm waits a random number of iterations before starting the next record. The randomization of the initial time instants of correlation recording allows to avoid the overlapping of the periodical velocity field generation with periodical scalar correlation computation. At the same time, the duration T_e should be kept not very large, so that more time statistics can be collected during the simulation.

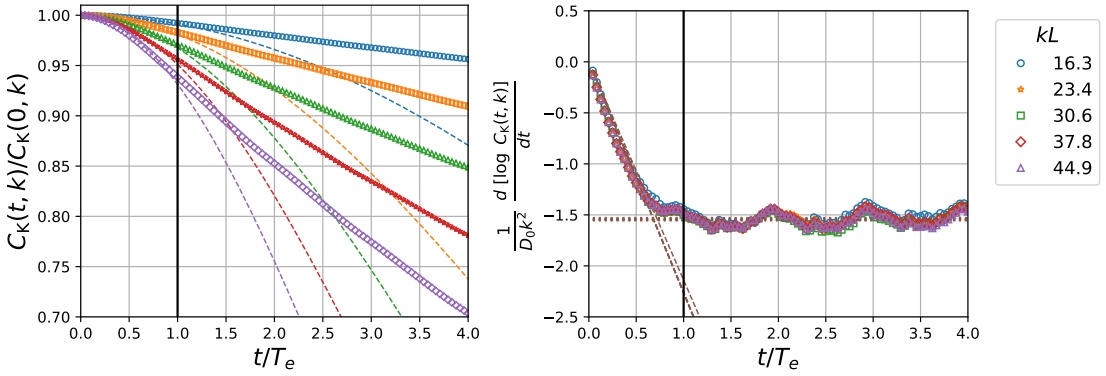

(a) Scalar correlation function $C_K(t,k)$ *(b) Time derivative of $\log C_K(t,k)$*

FIGURE *4.10 – Crossover in the correlation function of the scalar: Scalar correlation $C_K(t,k)$ and time derivative of its logarithm at time scales comparable to the velocity field renewal period T_e for various wavenumbers k. The dashed lines correspond to the Gaussian fit fit of C_K at $t < T_e$, while the dotted lines correspond to the exponential fit at $t > T_e$. The curves at various wavenumbers are rescaled vertically by k^2 which leads to their collapse. The black vertical line corresponds to $t = T_e$ which also matches to the crossover time.*

Crossover from Gaussian to exponential decay in scalar correlations. According to FRG results, in this case, since the velocity field is not white-in-time anymore, the scalar correlation function is expected to decay as a Gaussian in tk variable at small time lags, similarly to the scalar in the NS flow discussed in the sec. 4.2, and to switch to the exponential decay at large time lags, as in the case of white-in-time velocity field.

Indeed, this is the picture observed in the numerically computed correlations of the scalar as it is shown in Fig. 4.10a. At small times $t < T_e$, the correlation function $C_K(t,\vec{\mathbf{k}})$ behaves as a Gaussian. To demonstrate this, the Gaussian fits of this portion of the data are shown in Fig. 4.10a with continuous lines. Then, at larger time lags $t > T_e$, the correlation curves significantly deviate from the Gaussian and take an exponential form, similar to the ones obtained in the case of white-in-time velocity and presented before in Fig. 4.7.

The transition between the small- and large-time decays can also be visualized through the time derivative of $\log C_K(t,\vec{\mathbf{k}})$. According to the FRG result (1.28) for the two-point scalar correlation function, this derivative takes the form:

$$\frac{1}{k^2}\frac{\partial \log C_K(t,\vec{\mathbf{k}})}{\partial t} = \begin{cases} -2\alpha_S \frac{L^2}{\tau_0^2} t, & t \ll \tau_0, \\ -\alpha_L \frac{L^2}{\tau_0}, & t \gg \tau_0. \end{cases} \tag{4.6}$$

In other words, when the correlation function of the scalar $C_K(t,\vec{\mathbf{k}})$ is a Gaussian, this derivative decreases linearly, whereas when $C_K(t,\vec{\mathbf{k}})$ is an exponential, the derivative of its logarithm is a negative constant.

The derivative of $\log C_{\mathrm{K}}(t, \vec{\mathbf{k}})$ is displayed in Fig. 4.10b. One can see that it indeed exhibits the expected crossover from a linear decay to a constant. Moreover, the vertical rescaling of the derivatives by a factor proportional to $1/k^2$ leads to a collapse of all curves. It demonstrates that the Gaussian and the exponential parts of the decorrelation both possess a k^2-dependence on the wavenumber, as expected from Eq. (1.28). It also demonstrates clearly that the typical time of crossover is approximately equal to T_e, thus, to the correlation time of the velocity field, which is in agreement with the FRG result.

Comparison with NS flows. At high wavenumbers, the scalar in the time-correlated velocity field decorrelates significantly faster due to the $\sim k^2$ dependence in the Gaussian, and the correlation function $C_{\mathrm{K}}(t, \vec{\mathbf{k}})$ falls down to near-zero values at relatively small time lags t. In these cases, the correlation curves turn to be oscillatory after the Gaussian decay, and the large-time regime becomes indiscernible. The constant portion of the derivative of $\log C_{\mathrm{K}}(t, \vec{\mathbf{k}})$, corresponding to the exponential decay, exhibits random oscillations, spoiling the detection of the crossover and the analysis of the decay. A similar effect hinders the large-time regime in scalar correlations in NS flows. In the case of a synthetic velocity field, its correlation time scale can be chosen arbitrarily, so the crossover time between the small- and large-time behaviors in scalar correlations can be adjusted to make both types of decays observable. However, in NS flows, the decorrelation time of the velocity field cannot be adjusted so simply. In addition, the decorrelation time of velocity in real turbulent flows is scale-dependent.

Summary. A small modification in the simulation configuration consisting in an increase of the period of the velocity update leads to the emergence of a portion of Gaussian temporal decay in scalar correlations at small time lags. The observed scalar correlation function with a Gaussian decay at small time lags and an exponential at large time lags is in agreement with the FRG prediction. The crossover time between these two regimes of correlation decay matches the velocity correlation time scale. The behavior of the correlation function at high wavenumbers becomes oscillatory, similarly to the scalar correlations in NS velocity field.

4.4 Conclusions

The work presented in this chapter is dedicated to the numerical study of the two-point Eulerian spatio-temporal correlation function of a passive scalar in a 3D homogeneous isotropic turbulent flow. The numerical methods of computation of the scalar correlation function and generation of synthetic velocity field with prescribed spatial and temporal covariance are implemented. The main conclusions are:

1. In the case of the velocity field governed by the Navier-Stokes equation for inertial-convective regime:
   (a) The correlation function of the scalar at small time lags takes the form of a Gaussian function of variable tk, where t is the time lag and k is the wavenumber, as predicted by FRG approach. This scaling also corresponds to the large-scale random sweeping effect, known phenomenologically from previous works.
   (b) The coefficient characterizing the Gaussian temporal decay rate of the passive scalar field is approximately the same as the one of the velocity field. In other words, the correlation function of scalar repeats the one of the velocity field.

(c) The increase of Schmidt number from $Sc = 1$ to 36 does not lead to significant changes in the decorrelation time of the scalar, although there is a slight tendency towards its decrease.

(d) At large time lags, the numerically computed correlation functions of passive scalars are oscillatory. The large-time-lag exponential decay predicted by FRG is indiscernible in DNS of the proposed configuration because of the oscillations.

2. In the case of the random synthetic velocity field with white-in-time covariance (Kraichnan's random advection model):

   (a) The equal-time two-point correlation function of the scalar exhibits a power law matching the analytical results for Kraichnan's model in inertial and inertial-diffusive regimes.

   (b) The two-time two-point correlation function of the scalar behaves as an exponential function of the variable tk^2 for simulations at various parameters, in total agreement with the FRG prediction.

   (c) The constant prefactor of the exponential in the scalar correlation function coincides with good accuracy with the renormalized diffusivity, also confirming the validity of the FRG results.

3. In the case of the random synthetic velocity field with a finite-time correlation:

   (a) Switching to a random synthetic velocity field, which is kept constant over a time period of duration T_e, reveals a crossover between the Gaussian and the exponential temporal decay in the scalar correlation function.

   (b) At small time lags $t < T_e$ the scalar correlation takes the form of a Gaussian function of tk variable, similar to its behavior in Navier-Stokes velocity field. At large-time lags $t > T_e$ the correlation function turns purely exponential identical to the one in the white-in-time velocity field. This result is in agreement with the FRG prediction.

   (c) The crossover between the two regimes occurs at time T_e which is actually the imposed characteristic time of the velocity field correlation. In other words, at small time lags when the velocity field can be considered as correlated with itself at $t = 0$, the scalar exhibits a Gaussian decay, while at large time lags, when the velocity field becomes uncorrelated, the scalar correlation switches to an exponential decay.

   (d) According to the FRG, a similar crossover should also be present in the case of scalar fields advected by Navier-Stokes flows, although it could not be detected in our simulations. Contrarily to the synthetic velocity field, it is impossible to easily manipulate the velocity correlation time, so it is more challenging to find a DNS configuration in which the large-time part of the scalar correlation would be appreciable.

These results are totally consistent with the interpretation of the two regimes in the scalar Eulerian space-time correlation function with the single-particle dispersion (sec. 1.4). Indeed, in the case of white-in-time synthetic velocity field, a fluid particle is rapidly displaced by the velocity in random directions, which results in Brownian-type dispersion, in which the mean squared displacement grows linearly in time, and the Eulerian correlation function decays exponentially. Modifying the synthetic velocity field by increasing the time of its update implies that during the period between two velocity updates, a fluid particle is moved by the velocity field coherently. Averaging over many particles results in a ballistic regime of the particle dispersion with the mean squared displacement growing quadratically in time, and the scalar Eulerian correlation function decays as a Gaussian function in time.

Clearly, the last case is also valid for the scalars advected in the Navier-Stokes velocity field, since the large-scale velocity in a real turbulent flow also possesses a finite correlation time. The large-time regime of the Eulerian correlation function of the scalar is not accessible in DNS in the described configurations.

The main conclusion of this chapter is that the behavior of the Eulerian spatio-temporal correlation function of a passive scalar is determined by the temporal covariance of the velocity field, as it is demonstrated by the FRG approach. Therefore, for studies of passive scalar dynamics, the choice of assumptions on the temporal correlations of velocity plays a crucial role. It is essential, for instance, for designing physically valid models of the synthetic velocity field, which are largely used in studies of turbulent particle dispersion and mixing, or for developing time-accurate numerical models of parametrization of small-scale dynamics.

Conclusions en français

Le travail présenté dans ce chapitre est consacré à l'étude numérique de la fonction de corrélation spatio-temporelle eulérienne à deux points d'un scalaire passif dans un écoulement turbulent isotrope homogène 3D. Les méthodes numériques de calcul de la fonction de corrélation scalaire et de génération de champ de vitesse synthétique avec une covariance spatiale et temporelle prescrite sont mises en œuvre. Les principales conclusions sont :

1. Dans le cas du champ de vitesse régi par l'équation de Navier-Stokes pour le régime inertiel-convectif :
   (a) La fonction de corrélation du scalaire aux petits décalages prend la forme d'une fonction gaussienne de variable tk, où t est le décalage temporel et k est le nombre d'onde, comme prédit par l'approche FRG. Cette loi d'échelle correspond également à l'effet de balayage aléatoire à grande échelle, connu phénoménologiquement à partir de travaux antérieurs.
   (b) Le coefficient caractérisant le taux de décroissance temporelle gaussien du champ scalaire passif est approximativement le même que celui du champ de vitesse. En d'autres termes, la fonction de corrélation du scalaire reproduit celle du champ de vitesse.
   (c) L'augmentation du nombre de Schmidt de $Sc = 1$ à 36 n'entraîne pas de changements significatifs dans le temps de décorrélation du scalaire, bien qu'il y ait une légère tendance à sa diminution.
   (d) Aux grands décalages temporels, les fonctions de corrélation calculées numériquement des scalaires passifs sont oscillatoires. La décroissance exponentielle à retard important prédite par FRG est indiscernable dans le DNS de la configuration proposée en raison des oscillations.
2. Dans le cas du champ de vitesse synthétique aléatoire avec covariance blanche dans le temps (modèle d'advection aléatoire de Kraichnan) :
   (a) La fonction de corrélation à deux points à temps égal du scalaire présente une loi de puissance correspondant aux résultats analytiques du modèle de Kraichnan en régimes inertiel et inertiel-diffusif.
   (b) La fonction de corrélation à deux temps et à deux points du scalaire se comporte comme une fonction exponentielle de la variable tk^2 pour les simulations à divers paramètres, en accord total avec la prédiction FRG.
   (c) Le préfacteur constant de l'exponentielle dans la fonction de corrélation scalaire coïncide avec une bonne précision avec la diffusivité renormalisée, confirmant également la validité des résultats FRG.

3. Dans le cas du champ de vitesse synthétique aléatoire avec une corrélation en temps fini :
   (a) Le passage à un champ de vitesse synthétique aléatoire, qui est maintenu constant sur une période de temps de durée T_e, fait apparaître une transition entre la décroissance temporelle gaussienne et exponentielle dans la fonction de corrélation scalaire.
   (b) Aux petits décalages $t < T_e$ la corrélation scalaire prend la forme d'une fonction gaussienne de la variable tk, similaire à son comportement dans le champ de vitesse de Navier-Stokes. Aux grands décalages temporels $t > T_e$, la fonction de corrélation devient purement exponentielle, identique à celle du champ de vitesse aléatoire sans corrélations temporelles. Ce résultat est en accord avec la prédiction FRG.
   (c) La transition entre les deux régimes se produit approximativement au temps T_e qui est en fait le temps caractéristique imposé par la corrélation du champ de vitesse. En d'autres termes, aux petits décalages, lorsque le champ de vitesse est corrélé à lui-même à $t = 0$, le scalaire présente une décroissance gaussienne, tandis qu'aux grands décalages, lorsque le champ de vitesse n'est plus corrélé, la corrélation scalaire bascule à une décroissance exponentielle.
   (d) Selon le FRG, une transition similaire devrait également être présente dans le cas de champs scalaires advectés par les écoulements Navier-Stokes, bien qu'il n'ait pas pu être détecté dans nos simulations. Contrairement au champ de vitesse synthétique, il est impossible de manipuler facilement le temps de corrélation de la vitesse, il est donc plus difficile de trouver une configuration DNS dans laquelle la partie exponentielle de la corrélation scalaire serait visible.

Ces résultats sont tout à fait cohérents avec l'interprétation des deux régimes de fonction de corrélation espace-temps scalaire eulérienne par la dispersion des particules uniques (sec. 1.4). En effet, dans le cas d'un champ de vitesse synthétique avec bruit blanc en temps, une particule fluide est rapidement déplacée par le champ de vitesse dans des directions aléatoires, ce qui entraîne une dispersion de type diffusif, dans laquelle le déplacement quadratique moyen croît comme la racine carrée avec le temps, et la fonction de corrélation eulérienne décroît de façon exponentielle. Modifier le champ de vitesse synthétique en augmentant le temps de sa mise à jour implique que pendant la période entre deux mises à jour de vitesse, une particule de fluide est déplacée par le champ de vitesse de manière cohérente. Le calcul de la moyenne sur de nombreuses particules donne un régime balistique de la dispersion des particules avec le déplacement quadratique moyen croissant linéairement avec le temps, et la fonction de corrélation eulérienne du scalaire décroît comme une fonction gaussienne du temps. Clairement, le dernier cas est aussi valable pour les scalaires advectés dans le champ de vitesse de Navier-Stokes, puisque la vitesse à grande échelle dans un écoulement turbulent réel possède également un temps de corrélation fini. Le régime à grand temps dans la fonction de corrélation eulérienne du scalaire n'est pas accessible en DNS dans les configurations décrites.

La principale conclusion de ce chapitre est que le comportement de la fonction de corrélation spatio-temporelle eulérienne d'un scalaire passif est déterminé par la covariance temporelle du champ de vitesse, comme cela est démontré par l'approche FRG. Par conséquent, pour les études de dynamique scalaire passive, le choix des hypothèses sur les corrélations temporelles des vitesses joue un rôle crucial. Il est essentiel, par exemple, pour concevoir des modèles physiquement valides du champ de vitesse synthétique, qui sont largement utilisés dans les études de dispersion et de mélange turbulent des particules, ou pour développer des modèles numériques précis dans le temps des paramétrisations de la dynamique à petite échelle.

5

Shell model of scalar random advection

This chapter is dedicated to the analytical study of the shell model of random advection of a passive scalar by means of the FRG approach. The main idea is to illustrate the main steps of a FRG calculation on the basis of simple model. A simplest ansatz is constructed, which allows to obtain the second-order structure function of the scalar.

Contents

Abstract

This chapter provides a preliminary analytical study of the shell model of random advection of a passive scalar by means of the FRG approach. It contains a detailed description of the principal steps of FRG derivation: from formulation of the shell model equations in terms of path integral to the solution of the flow equations and the computation of structure functions. A simplest ansatz for truncation of the flow equations is considered. The obtained flow equations were solved numerically. Numerical solution shows that the system reaches a fixed point, and at this fixed point the scalar structure functions exhibit a power law corresponding to the normal scaling known from previous studies.

The considered problem serves as a good illustration of the application of FRG method to turbulence thanks to its simplicity. However, the presented analysis also represents the initial step in the study of anomalous scaling within the FRG approach, which possibly can be done with the use of a more elaborated ansatz.

Résumé en français

Ce chapitre propose une étude analytique préliminaire du modèle en couches d'advection aléatoire d'un scalaire passif au moyen de l'approche FRG. Il contient une description détaillée des principales étapes de la dérivation FRG : à partir de la formulation des équations du modèle en couches en termes d'intégrales de chemin jusqu'à la résolution des équations du flot et au calcul des fonctions de structure. L'ansatz le plus simple pour la troncature des équations du flot est considéré. La solution numérique des équations du flot montre que le système atteint un point fixe, et à ce point fixe les fonctions de structure scalaire présentent une loi de puissance correspondant à la loi d'échelle normale connue des études précédentes.

Le problème considéré illustre bien l'application de la méthode FRG à la turbulence grâce à sa simplicité. Cependant, l'analyse présentée représente également la première étape de l'étude des lois d'échelle anormales dans l'approche FRG, ce qui peut éventuellement être fait avec l'utilisation d'un ansatz plus élaboré.

5.1 Background

The shell models are largely used in turbulence research as they provide significant simplification while keeping some important features of the turbulent dynamics. The main idea of shell models is to represent a flow field as a set of complex amplitudes $u_n(t)$ labeled by an index $n = 0, 1, 2, ..., N$. Each amplitude $u_n(t)$ corresponds to an integrated velocity in a shell characterized by the wavenumber $k_n = k_0\lambda^n$ where λ is usually set equal to 2. That is to say that the wavenumber space is discretized into N spherical shells with a power-law spacing, and the velocity field of each shell is characterized by a single complex number $u_n(t)$. The evolution of the system is thus given by a set of N coupled nonlinear ordinary differential equations describing the dynamics of each individual shell. Replacing partial differential equations such as NS or advection-diffusion equations by a set of coupled ordinary differential equations allows a significant simplification of the problem.

In this chapter, the shell model of a randomly advected scalar is considered. This model represents a shell version of Kraichnan's model for the scalar advection (see Sec. 1.3.2 and sec. 4.3), as it is also based on the assumption of a random Gaussian velocity field. The specific simplification implemented in this shell model consists in the limitation of the advection term to local interactions. However, even in such a simplified case, this model

leads to anomalous scaling in the scalar structure function.

The first version of this model was introduced in the work of Jensen et al., 1992, and developed further in the work of Wirth and Biferale, 1996. The work of Benzi et al., 1997 provides a modified version of Kraichnan's shell model with fewer interaction terms which still gives rise to the anomalous behavior. In the article of Biferale and Wirth, 1997 it is referred to as "minimal intermittency model of a passive scalar". In these works, it is shown analytically and numerically that the second-order structure function of the scalar is non-anomalous as it behaves according to the dimensional analysis, while starting from the fourth-order structure function the intermittent deviation of the scaling exponent is already observed.

For this reason, Kraichnan's shell model appears to be a good candidate for a toy model to study intermittency effects by means of the FRG method, as it contains all essential ingredients for intermittency, while its simplicity allows to explore various approaches.

Structure of the chapter. The present chapter provides a preliminary analytical study of Kraichnan's shell model with the use of the FRG approach, already introduced in the Chapter 1, but giving more details on the application of the method. Firstly, the stochastic differential equation of the passive scalar shell model is introduced and reformulated in terms of a path integral. Next, the FRG method is applied to the problem. A simple ansatz for the scale-dependent effective average action is proposed, and the RG flow equation for the two-point functions is obtained. Solving the flow equations allows to obtain the scalar structure functions in the first approximation. The results for the second-order structure function are compared with the previous studies and with the behavior of the structure function in continuous Kraichnan's model, already discussed in Sections 1.3.2 and 4.3.

5.2 Problem statement

Following the work of Benzi et al., 1997, the equation of the dynamics of the Fourier amplitude of a passive scalar θ in a shell with index $n = 1, ..., N$ is given by the following differential equation:

$$\left[\frac{d}{dt} + \kappa k_n^2\right] \theta_n(t) = i \underbrace{\left[k_{n+1}\theta^*_{n+1}(t)u^*_n(t) - k_n\theta^*_{n-1}(t)u^*_{n-1}(t)\right]}_{B_n(\theta,\theta^*,u,u^*)} + f_n(t), \tag{5.1}$$

in which κ denotes the molecular diffusivity of the scalar and $f_n(t)$ is the external forcing of the scalar in the shell n. The star symbol * denotes complex conjugation. One can see that the shell model (5.1) share some similarities with the advection-diffusion partial differential equation (1.25). In particular, it is linear in θ, the diffusion term has a prefactor proportional to k^2, and the advection is modeled by a term bilinear in θ and u. It should be noted that the choice of prefactors in the advection term is not unique. The prefactors k_{n+1} and k_n used in (5.1) give one of the possible configurations ensuring the scalar energy conservation. As there are no diagonal terms proportional to $u_n\theta_n$, the phase space volume is conserved.

As it has been mentioned before, the shell model is constructed with the assumption of the locality of nonlinear interactions in the wavenumber space. In Eq. (5.1) the locality of the interactions is manifested by the dependence of the amplitude of shell n on the amplitudes of the nearest shells $n-1$ and $n+1$ only.

Velocity field. Similarly to the continuous version of Kraichnan's behavior of random advection, the velocity in (5.1) is a random field with delta-in-time correlation and a spatial spectrum with power-law decay:

$$\left\langle u_m(t)u_n^*(t')\right\rangle = 2\delta(t-t')\delta_{mn}D_m^v, \tag{5.2}$$

$$D_m^v = D_0^v k_m^{-\varepsilon}, \tag{5.3}$$

where the parameter D_0^v is linked to the kinetic energy of the flow, and ε is the parameter defining the power law of the spatial covariance of velocity. The probability distribution of the velocity is assumed to be Gaussian:

$$P_u\left[u,u^*\right] = N_u \exp\left\{-\frac{1}{2}\int \mathrm{d}t \sum_n (D_n^v)^{-1}|u_n(t)|^2\right\}. \tag{5.4}$$

Forcing. The forcing term $f_n(t)$ in Eq. (5.1) is also assumed to be white-in-time with Gaussian distribution:

$$\left\langle f_m(t)f_n^*(t')\right\rangle = 2\delta(t-t')\delta_{mn}D_n^f, \tag{5.5}$$

$$P_f[f,f^*] = N_f \exp\left\{-\frac{1}{2}\int \mathrm{d}t \sum_n (D_n^f)^{-1}|f_n(t)|^2\right\}. \tag{5.6}$$

In the original model (Benzi et al., 1997) the forcing term is set to be nonzero in the first shell to model a large-scale forcing. However, for this work this limitation is not necessary, a more general forcing can be considered, with some arbitrary dependence of the forcing power D_n^f on the shell index.

Initial and boundary conditions. Since the scalar evolution equation is forced, one can take as the initial condition a uniform scalar amplitude $\theta_n(t=0)=0$. As the boundary condition, one can set that the scalar amplitudes in the boundary shells with indices $n=0$ and $n=N+1$ to zero.

Structure functions. The main quantities of interest in Kraichnan's shell model are the scalar structure functions S_p and their scaling exponents ζ_p, defined as:

$$S_p(k_m) = \left\langle (\theta_m\theta_m^*)^{p/2}\right\rangle \propto k_m^{-\zeta_p}. \tag{5.7}$$

The normal scaling, resulting from a dimensional analysis, corresponds to the linear dependence of the exponent ζ_p on the order p, that is $\zeta_{2p} = p\zeta_2$, while deviations from it correspond to anomalous scaling. In previous works, it has been shown that the second-order structure function S_2 exhibits normal scaling with the exponent $\zeta_2 = 2-\varepsilon$, while the structure functions of the fourth-order and higher have anomalous scaling (Wirth and Biferale, 1996 ; Benzi et al., 1997).

Arbitrary correlation functions, including structure functions, can be accessed through the Martin-Siggia-Rose-Janssen-de Dominicis (MSRJD) approach. As discussed in section 1.2.1, this method provides the generating functional of the correlation functions. The idea is to reformulate the original stochastic differential equation (5.1) in terms of a path integral and to construct a generating functional, whose functional derivatives give the correlation functions of the scalar field. The MSRJD procedure in application to the shell version of Kraichnan's model is described in the next section.

5.3 Action and correlation functions

The aim is to compute the average of an observable O depending on the scalar θ over a history of realizations of the random velocity u and forcing f:

$$\langle O(\theta_m, \theta_m^*)\rangle_{u,f} = \int \mathcal{D}[f] P_f[f, f^*] \mathcal{D}[u] \mathcal{D}[u^*] P_u[u, u^*] O(\theta_m, \theta_m^*). \tag{5.8}$$

The condition that the scalar dynamics is governed by the Eq. (5.1) is imposed through integrating a functional delta:

$$1 = \int \mathcal{D}[\theta] \mathcal{D}[\theta^*] \prod_m \prod_t \delta^{(2)}\left[(\partial_t + \kappa k_m^2)\theta_m - iB_m(\theta, \theta^*, u, u^*) - f_m\right], \tag{5.9}$$

where the symbol $\delta^{(2)}$ serves to distinguish the complex delta functional. The next step consists in replacing the δ-functional by its functional integral representation $\delta^{(2)}[z(x)] = \int \mathrm{d}[\bar{z}] \exp\{-i\bar{z}(x)z(x)\}$, or, for $z \in \mathbb{C}$ the following representation is adopted:

$$\delta^{(2)}[z(x)] = \delta[\mathrm{Re}\, z]\delta[\mathrm{Im}\, z] = \int \mathrm{d}[\mathrm{Re}\, \bar{z}]\mathrm{d}[\mathrm{Im}\, \bar{z}] \exp\{-i\mathrm{Re}\, \bar{z}\ \mathrm{Re}\, z - i\mathrm{Im}\, \bar{z}\ \mathrm{Im}\, z\}. \tag{5.10}$$

Similar replacement of the δ-functional can be made in Eq. (5.9), by introducing Martin-Siggia-Rose auxiliary fields (Täuber, 2014, Chapter 4), or also referred to as the response fields $\bar{\theta}$ and $\bar{\theta^*}$, or equivalently $\mathrm{Re}\,\bar{\theta}$ and $\mathrm{Im}\,\bar{\theta}$.

$$\begin{aligned}
&\delta^{(2)}\left[(\partial_t + \kappa k_m^2)\theta_m - iB_m(\theta, \theta^*, u, u^*) - f_m\right] = \\
&\quad = \int \mathcal{D}\left[\mathrm{Re}\,\bar{\theta}\right] \mathcal{D}\left[\mathrm{Im}\,\bar{\theta}\right] \exp\left\{-i\mathrm{Re}\,\bar{\theta}_m\ \mathrm{Re}\left[(\partial_t + \kappa k_m^2)\theta_m - iB_m(\theta, \theta^*, u, u^*) - f_m\right]\right. \\
&\qquad\qquad \left. - i\mathrm{Im}\,\bar{\theta}_m\ \mathrm{Im}\left[(\partial_t + \kappa k_m^2)\theta_m - iB_m(\theta, \theta^*, u, u^*) - f_m\right]\right\}.
\end{aligned} \tag{5.11}$$

Inserting the integral from (5.11) into (5.9) and then into (5.8) leads to:

$$\begin{aligned}
\langle O(\theta_m, \theta_m^*)\rangle_{u,f} = &\int \mathcal{D}f P_f[f, f^*] \mathcal{D}u \mathcal{D}u^* P_u[u, u^*] O(\theta_m, \theta_m^*) \mathcal{D}\theta \mathcal{D}\theta^* \mathcal{D}\left[\mathrm{Re}\,\bar{\theta}\right] \mathcal{D}\left[\mathrm{Im}\,\bar{\theta}\right] \\
&\times \exp\left\{-i\sum_m \int \mathrm{d}t\, \mathrm{Re}\,\bar{\theta}_m\ \mathrm{Re}\left[(\partial_t + \kappa k_m^2)\theta_m - iB_m(\theta, \theta^*, u, u^*) - f_m\right]\right. \\
&\left. - i\sum_m \int \mathrm{d}t\, \mathrm{Im}\,\bar{\theta}_m\ \mathrm{Im}\left[(\partial_t + \kappa k_m^2)\theta_m - iB_m(\theta, \theta^*, u, u^*) - f_m\right]\right\},
\end{aligned} \tag{5.12}$$

where the integration over the random forcing can be done explicitly, as the probability distribution of forcing $P_f[f, f^*]$ is given in (5.6):

$$\begin{aligned}
&\int \mathcal{D}f P_f[f, f^*] \exp\left\{i\sum_m \int \mathrm{d}t \left[\mathrm{Re}\,\bar{\theta}_m\ \mathrm{Re}\, f_m + \mathrm{Im}\,\bar{\theta}_m\ \mathrm{Im}\, f_m\right]\right\} \\
&\quad = \int \mathcal{D}[\mathrm{Re}\, f] \mathcal{D}[\mathrm{Im}\, f] N_f \exp\left\{-\frac{1}{2}\int \mathrm{d}t \sum_m (D_m^f)^{-1}\left[(\mathrm{Re}\, f_m)^2 + (\mathrm{Im}\, f_m)^2\right]\right\} \\
&\times \exp\left\{i\sum_m \int \mathrm{d}t \left[\mathrm{Re}\,\bar{\theta}_m\ \mathrm{Re}\, f_m + \mathrm{Im}\,\bar{\theta}_m\ \mathrm{Im}\, f_m\right]\right\} = \exp\left\{-\int \mathrm{d}t \sum_m \frac{D_m^f |\bar{\theta}_m|^2}{2}\right\}.
\end{aligned} \tag{5.13}$$

The simplification is obtained by separating and integrating the Gaussian part of the expression:

$$\int N_f \mathcal{D}[\mathrm{Re}\, f] \exp\left\{ \int \mathrm{d}t \sum_m -\frac{1}{2D_m^f} \left(\mathrm{Re}\, f_m - iD_m^f \mathrm{Re}\, \bar{\theta}_m \right)^2 \right\} \times \mathcal{D}[\mathrm{Im}\, f] \exp\left\{ \int \mathrm{d}t \sum_m -\frac{1}{2D_m^f} \left(\mathrm{Im}\, f_m - iD_m^f \mathrm{Im}\, \bar{\theta}_m \right)^2 \right\} = 1. \quad (5.14)$$

The expression for the observable in Eq. (5.12) takes then the form:

$$\langle O(\theta_m, \theta_m^*) \rangle_{u,f} = \int \mathcal{D}u \mathcal{D}u^* O(\theta_m, \theta_m^*) \mathcal{D}\theta \mathcal{D}\theta^* \mathcal{D}\bar{\theta} \mathcal{D}\bar{\theta}^* \times \exp\left\{ \int \mathrm{d}t \sum_m -i\mathrm{Re}\, \bar{\theta}_m\ \mathrm{Re}\left[(\partial_t + \kappa k_m^2)\theta_m - iB_m(\theta, \theta^*, u, u^*) \right] -i\mathrm{Im}\, \bar{\theta}_m\ \mathrm{Im}\left[(\partial_t + \kappa k_m^2)\theta_m - iB_m(\theta, \theta^*, u, u^*) \right] - \frac{D_m^f |\bar{\theta}_m|^2}{2} - \frac{|u_m|^2}{2D_m^v} \right\}.$$

To eliminate the imaginary unit and create a prefactor 2 in the exponential, the real and imaginary parts of the response scalar field can be redefined as $\mathrm{Re}\, \bar{\theta} \to \frac{2}{i} \mathrm{Re}\, \bar{\theta}$ and $\mathrm{Im}\, \bar{\theta} \to \frac{2}{i} \mathrm{Im}\, \bar{\theta}$. In addition, the combination of real and imaginary parts can be rewritten using the property $\mathrm{Re}\, A\ \mathrm{Re}\, B + \mathrm{Im}\, A\ \mathrm{Im}\, B = \frac{1}{2}[A^* B + A B^*] = \mathrm{Re}\, [A^* B]$. Then, by inserting the expression for the velocity distribution $P_u[u, u^*]$ from (5.4), one gets an equivalent expression for the observable:

$$\langle O(\theta_m, \theta_m^*) \rangle_{u,f} = \int \mathcal{D}u \mathcal{D}u^* O(\theta_m, \theta_m^*) \mathcal{D}\theta \mathcal{D}\theta^* \mathcal{D}\bar{\theta} \mathcal{D}\bar{\theta}^* \times \exp\left\{ \int \mathrm{d}t \sum_m -2\mathrm{Re}\, [\bar{\theta}_m^* \left(\left[\partial_t + \kappa k_m^2 \right] \theta_m - iB_m \right)] + 2D_m^f |\bar{\theta}_m|^2 - \frac{|u_m|^2}{2D_m^v} \right\}. \quad (5.15)$$

The probability distribution of the passive scalar is then:

$$P_\theta[\theta, \theta^*] = C^{-1} \int \mathcal{D}u \mathcal{D}u^* \mathcal{D}\bar{\theta} \mathcal{D}\bar{\theta}^* \exp\{ -\mathcal{S}\left[\theta, \theta^*, \bar{\theta}, \bar{\theta}^*, u, u^* \right] \}, \quad (5.16)$$

where the functional $\mathcal{S}$ is the action. The normalization C^{-1} can be absorbed in the functional measure of the response fields $\mathcal{D}\bar{\theta}$, $\mathcal{D}\bar{\theta}^*$. The resulting action takes the form:

$$\mathcal{S}\left[\theta, \theta^*, \bar{\theta}, \bar{\theta}^*, u, u^* \right] = \int \mathrm{d}t \sum_m 2\mathrm{Re} \left[\bar{\theta}_m^* \left(\left[\partial_t + \kappa k_m^2 \right] \theta_m - i[k_{m+1} \theta_{m+1}^* u_m^* - k_m \theta_{m-1}^* u_{m-1}^*] \right) \right] - 2D_m^f |\bar{\theta}_m|^2 + \frac{|u_m|^2}{2D_m^v}. \quad (5.17)$$

Generating functional of correlation functions. From (5.16) one can construct the generating functional of the correlation functions (analogue of the partition function) by introducing source terms J for each field $\phi \in \{\theta, \bar{\theta}^*, \theta^*, \bar{\theta}, u, u^*\}$:

$$Z[J] = \int \mathcal{D}u \mathcal{D}u^* \mathcal{D}\theta \mathcal{D}\theta^* \mathcal{D}\bar{\theta} \mathcal{D}\bar{\theta}^* \exp\{ -\mathcal{S}[\phi] \} \times \exp\left\{ \int \mathrm{d}t \sum_m J_{\theta_m} \theta_m + J_{\theta_m^*} \theta_m^* + J_{\bar{\theta}_m} \bar{\theta}_m + J_{\bar{\theta}_m^*} \bar{\theta}_m^* + J_{u_m} u_m + J_{u_m^*} u_m^* \right\}. \quad (5.18)$$

The expression $\mathcal{S}[\phi]$ denotes the action provided in Eq. (5.17). The first functional derivative of Z with respect to a source $J_\phi(t)$ give the average of the field ϕ.

The functional derivatives of the generating functional $Z[J]$ with respect to the sources J give the expressions for the statistical moments of the fields. For instance, the average of the scalar can be computed through the first functional derivative:

$$\langle \theta_m(t) \rangle = \frac{\delta Z[J]}{\delta J_{\theta_m}(t)}. \tag{5.19}$$

As it was already introduced in the chapter 1, the two-time correlation function of the scalar is computed by taking two functional derivatives of Z:

$$\left\langle \theta_m(t)\theta_n^*(t') \right\rangle = \frac{1}{Z} \frac{\delta^2 Z[J]}{\delta J_{\theta_m}(t)\, \delta J_{\theta_n^*}(t')} \tag{5.20}$$

The higher-order statistical moments are obtained in a similar way by taking appropriate higher order functional derivatives of Z.

Taking a logarithm of $Z[J]$ gives the generating functional $W[J] = \log Z[J]$ of the connected correlation functions. The connected two-time correlation function of the scalar is then computed as:

$$\left\langle \theta_m(t)\theta_n^*(t') \right\rangle - \langle \theta_m(t) \rangle \left\langle \theta_n^*(t') \right\rangle = \frac{\delta^2 W[J]}{\delta J_{\theta_m}(t)\, \delta J_{\theta_n^*}(t')} \tag{5.21}$$

Therefore, reformulating the problem in terms of a path integral with the use of the MSRJD method provides a framework for a systematic computation of Eulerian correlation functions. In the next section, the implementation of the functional renormalization group approach in this framework is presented.

5.4 Functional renormalization group formalism

The main idea of the renormalization group approach is to achieve a progressive integration of the small-scale fluctuations in the system. In such a way, a set of scale-dependent models for varying wavenumber K is constructed, by progressive averaging of the fluctuations at wavenumbers larger than K. It is done by adding to the action of the system $\mathcal{S}$ a scale-dependent term $\Delta\mathcal{S}_K[\phi]$. This term aims to filter out the modes with wavenumbers $k < K$ from the integration (Delamotte, 2012). The modified (scale-dependent) generating functionals of the correlation functions Z_K and W_K then take the form:

$$Z_K[J] = e^{W_K[J]} = \int \mathcal{D}\phi \exp\left\{ -\mathcal{S}[\phi] - \Delta\mathcal{S}_K[\phi] + \int \mathrm{d}t \sum_m \sum_\phi J_\phi \phi \right\}. \tag{5.22}$$

Here, the summation $\sum_\phi$ occurs over all fields $\phi \in \left\{\theta, \bar{\theta}^*, \theta^*, \bar{\theta}, u, u^*\right\}$, as it is written in a full form in Eq. 5.18.

5.4.1 Effective average action

As it was introduced in the first chapter, the scale-dependent models are described by a single functional, called the effective average action functional $\Gamma_K[\langle\phi\rangle]$, which is defined

as the Legendre transform of the generating functional $W_K[\langle\phi\rangle]$ (Delamotte, 2012):

$$\Gamma_K[\psi] = -W_K[J_\psi] + \int \mathrm{d}t \sum_m \sum_\psi J_\psi \psi - \Delta\mathcal{S}_K[\psi], \tag{5.23}$$

where the average fields are denoted with $\psi = \langle\phi\rangle = \left\{\langle\theta\rangle, \langle\bar{\theta^*}\rangle, \langle\theta^*\rangle, \langle\bar{\theta}\rangle, \langle u\rangle, \langle u^*\rangle\right\}$.

The term $\Delta\mathcal{S}_K[\psi]$ has to ensure the following properties of the effective average action: If the microscale of the problem is characterized by a wavenumber Λ, the effective average action at $K = \Lambda$ coincides with the microscopic action $\Gamma_{K=\Lambda}[\psi] = \mathcal{S}[\psi]$, as no fluctuation is averaged yet. At large scales $K \to 0$ all fluctuations need to be integrated, so $\Delta\mathcal{S}_K[\psi] = 0$, and one restores the true properties of the initial model. To satisfy these conditions, the filtering term $\Delta\mathcal{S}_K[\psi]$ can be chosen as quadratic in fields:

$$\Delta\mathcal{S}_K[\psi] = \frac{1}{2}\int \mathrm{d}t \sum_{m_1,m_2} \langle\psi_{m_1}|\, \mathcal{R}_{K,m_1,m_2}\, |\psi_{m_2}\rangle, \tag{5.24}$$

where $|\psi_m\rangle$ denotes a vector-column containing 6 fields $\left(\theta_m, \bar{\theta^*}_m, \theta^*_m, \bar{\theta}_m, u_m, u^*_m\right)$, while $\langle\psi_m|$ denotes the same vector-row. $\mathcal{R}_{K,m_1,m_2}$ represents a matrix consisting of the corresponding regulator functions. All elements of the matrix $R_K \in \mathcal{R}_{K,m}$ have to be suitable cut-off functions, which means that they have to keep the small scales unaffected so that $R_K(k_m > K) \simeq 0$, vanish at $K \to 0$ and also "freeze" all fluctuations at $K \to \Lambda$ so that $R_{K=0} = 0$, $R_{K=\Lambda} \sim \Lambda^2\ \forall k_m$.

Notations. The following notation for functional derivatives is used:

$$\Gamma^{(\psi_1,\psi_2,..,\psi_n)}_{K,m_1,m_2,...,m_n}(\omega_1,\omega_2,...,\omega_n) = \left.\frac{\delta^n\Gamma_K[\psi]}{\delta\psi_{1,m_1}(\omega_1)\,\delta\psi_{2,m_2}(\omega_2)\,...\,\delta\psi_{n,m_n}(\omega_n)}\right|_{\psi=0}. \tag{5.25}$$

The superscript of Γ denotes the field relative to which the functional derivative is taken. All derivatives are evaluated at zero average field $\psi = 0$. Note that the effective average action is a functional of the averaged fields $\Gamma_K[\psi] = \Gamma_K[\langle\theta\rangle, \langle\bar{\theta^*}\rangle, \langle\theta^*\rangle, \langle\bar{\theta}\rangle, \langle u\rangle, \langle u^*\rangle]$, but to shorten the notations, the averaging brackets $\langle\,\cdot\,\rangle$ are omitted in the following.

RG flow equations. The dependence of the effective average action on the scale K is governed by the exact RG flow equation (Wetterich, 1993). This equation has been already given in (1.10), and with the notations introduced in this chapter it takes the form:

$$\partial_s\Gamma_K[\psi] = \frac{1}{2}\,\mathrm{Tr}\int\frac{\mathrm{d}\omega}{2\pi}\sum_{m_i}\left[\partial_s\mathcal{R}_{K,m_1,m_2}\left(\Gamma^{(2)}_{K,m_2,m_1}[\psi] + \mathcal{R}_{K,m_2,m_1}\right)^{-1}\right], \tag{5.26}$$

where the differentiation variable is $s \equiv \log(K/\Lambda)$. Note that the flow equation is written for the Fourier transforms of $\Gamma^{(2)}_K$ and $\mathcal{R}$. The same notation is kept for the Fourier transforms for simplicity.

From the definition (5.23) of the Legendre transform, the connected two-point correlation functions $W^{(2)}$ are obtained as the inverse of the sum of the second functional derivative of the effective average action Γ and the regulator $\mathcal{R}$. The correlation functions $W^{(2)}$ are also referred to as the propagators and are denoted with G:

$$G^{(\psi_1,\psi_2)}_{K,m_1,m_2}(\omega_1,\omega_2) = \left(\Gamma^{(\psi_1,\psi_2)}_{K,m_1,m_2}(\omega_1,\omega_2) + \mathcal{R}^{(\psi_1,\psi_2)}_{K,m_1,m_2}\right)^{-1}. \tag{5.27}$$

The flow equations can be obtained for higher order functional derivatives of the effective average action Γ. Taking two functional derivatives of the flow equation (5.26) with respect to the fields ψ_a and ψ_b leads to the following equation:

$$\begin{aligned}\partial_s \Gamma^{(\psi_a,\psi_b)}_{K,m_a,m_b}(\Omega,-\Omega) = \partial_s \frac{\delta^2 \Gamma_K[\psi]}{\delta\psi_{a,m_a}(\Omega)\delta\psi_{b,m_b}(-\Omega)} = \sum_{\varphi_i}\int \frac{\mathrm{d}\omega}{2\pi}\sum_{m_i}\partial_s \mathcal{R}^{(\varphi_1,\varphi_2)}_{K,m_1,m_2}\times \\ G^{(\varphi_2,\varphi_3)}_{K,m_2,m_3}(\omega,-\omega)\Gamma^{(\psi_a,\varphi_3,\varphi_4)}_{K,m_a,m_3,m_4}(\Omega,\omega,-\Omega-\omega)G^{(\varphi_4,\varphi_5)}_{K,m_4,m_5}(\Omega+\omega,-\Omega-\omega)\times \\ \Gamma^{(\psi_b,\varphi_5,\varphi_6)}_{K,m_b,m_5,m_6}(-\Omega,\omega+\Omega,-\omega)G^{(\varphi_6,\varphi_1)}_{K,m_6,m_1}(\omega,-\omega) - \frac{1}{2}\sum_{\varphi_i}\int \frac{\mathrm{d}\omega}{2\pi}\sum_{m_i}\partial\mathcal{R}^{(\varphi_1,\varphi_2)}_{K,m_1,m_2}\times \\ G^{(\varphi_2,\varphi_3)}_{K,m_2,m_3}(\omega,-\omega)\Gamma^{(\psi_a,\psi_b,\varphi_3,\varphi_4)}_{K,m_a,m_b,m_3,m_4}(\Omega,-\Omega,\omega,-\omega)G^{(\varphi_4,\varphi_1)}_{K,m_4,m_1}(\omega,-\omega), \quad (5.28)\end{aligned}$$

where the translational invariance in time has been used. To simplify the reading of the flow equation, the letter ψ denotes the external fields, while φ denotes the internal fields upon which the summation in the right-hand side occurs. Similarly, the capital Ω always corresponds to the external frequency, and the small ω to the integration frequency.

Note that at this stage the flow equation (5.28) is exact. However, its right-hand side contains the vertices $\Gamma^{(3)}$ and $\Gamma^{(4)}$, which in their turn are governed by the next-order flow equations, resulting from the third- and fourth-order derivatives of Eq. (5.26). The flow equations for the vertices $\Gamma^{(3)}$ and $\Gamma^{(4)}$ depend on the higher order vertices. Repeating this procedure for higher-order derivatives thus leads to an infinite hierarchy of equations for $\Gamma^{(n)}$. A standard approximation within the FRG framework consists in truncating the hierarchy of flow equations to a given order n by simply neglecting the higher-order vertices (Dupuis et al., 2021). This strategy is implemented in the following section.

It is important to emphasize that this approach is completely different from the large-wavenumber expansion, which underlies all FRG results on Navier-Stokes and scalar turbulence presented in Chapter 1. Within the large-wavenumber expansion, no truncation is performed, it does not rely on the use of an ansatz, but rather on an expansion of the vertices in the limit of large wavenumbers.

5.4.2 Ansatz

A simple ansatz is chosen in which only the third-order vertices are kept. Within this approximation, only the first term will be considered in Eq. (5.28), as the fourth-order vertices $\Gamma^{(4)}_K$ are neglected. At the same time, the second-order derivatives $\Gamma^{(2)}_K$ are considered in a general form, that is to say, dependent both on the renormalization scale K and the shell index m. In practice, it means that one has to replace the molecular diffusivity κ and the forcing power spectrum D^f_m in the bare action $\mathcal{S}$ in Eq. (5.17) by unknown functions $F^\kappa_{K,m}$ and $d^f_{K,m}$ depending on the renormalization scale K and the shell index m:

$$\begin{aligned}\kappa &\mapsto F^\kappa_{K,m}, \\ D^f_m &\mapsto D^f_0 f^d_{K,m},\end{aligned}$$

where D^f_0 is a constant parameter related to the forcing power. At the microscale, characterized by the wavenumber $K = \Lambda$, the renormalized diffusivity $F^\kappa_{K,m}$ is equal to the molecular diffusivity of the scalar $F^\kappa_{K=\Lambda,m} = \kappa \ \forall\ m$, and there is the renormalized forcing is set to $f^d_{K=\Lambda,m} = 0 \ \forall\ m$, since the forcing is entirely contained in the regulator N_κ (see below).

The ansatz is thus given by the following effective average action:

$$\Gamma[\psi] = \int \mathrm{d}t \sum_m 2\mathrm{Re}\left[\bar{\theta}^*_m\Big(\big[\partial_t + F^\kappa_{K,m}k_m^2\big]\theta_m - i[k_{m+1}\theta^*_{m+1}u^*_m - k_m\theta^*_{m-1}u^*_{m-1}]\Big)\right] - 2D_0^f f^d_{K,m}|\bar{\theta}_m|^2 + \frac{|u_m|^2}{2D^v_m}. \quad (5.29)$$

One can show that the velocity sector is not renormalized, so the velocity amplitude parameter D^v_m is kept in the initial form (5.4) and does not depend on the renormalization scale K.

The flow equation (5.28) can be projected onto this ansatz (5.29) yielding two flow equations for the functions $F^\kappa_{K,m}$ and $f^d_{K,m}$. To compute this flow, one needs to specify the regulator $\mathcal{R}$, and to establish the expression for the propagator G and vertices $\Gamma^{(3)}$, which is done in the following section.

Matrix notations. To simplify the writing of the flow equations (5.28), it is rewritten in the matrix form. The matrix of the second functional derivatives of the effective average action $\Gamma^{(2)}_K$ is written as follows:

$$\Gamma^{(2)}_{K,m_1,m_2}(\omega_1,\omega_2) = \begin{pmatrix} 0 & \Gamma^{(\theta,\bar{\theta}^*)}_{K,m_1,m_2} & 0 & 0 & 0 & 0 \\ \left(\Gamma^{(\theta,\bar{\theta}^*)}_{K,m_1,m_2}\right)^* & 0 & 0 & \Gamma^{(\bar{\theta}^*,\bar{\theta})}_{K,m_1,m_2} & 0 & 0 \\ 0 & 0 & 0 & \Gamma^{(\theta^*,\bar{\theta})}_{K,m_1,m_2} & 0 & 0 \\ 0 & \left(\Gamma^{(\bar{\theta}^*,\bar{\theta})}_{K,m_1,m_2}\right)^* & \left(\Gamma^{(\theta^*,\bar{\theta})}_{K,m_1,m_2}\right)^* & 0 & 0 & 0 \\ 0 & 0 & 0 & 0 & 0 & \Gamma^{(u,u^*)}_{K,m_1,m_2} \\ 0 & 0 & 0 & 0 & \left(\Gamma^{(u,u^*)}_{K,m_1,m_2}\right)^* & 0 \end{pmatrix}. \quad (5.30)$$

The indices in the superscript of a matrix element indicate with respect to which field the derivatives are taken. The rows and columns of the matrix correspond to different fields, and the order of the fields is always $\big(\theta,\bar{\theta}^*,\theta^*,\bar{\theta},u,u^*\big)$. The elements of the matrix $\Gamma^{(2)}$ are computed as the Fourier transform (from time domain t to the frequency domain ω) of the second-order functional derivatives of the ansatz $\Gamma[\psi]$ from Eq. (5.29) evaluated at zero fields $\psi = 0$. The expressions for the matrix elements after the Fourier transform take the following form:

$$\begin{aligned}
\Gamma^{(\theta,\bar{\theta}^*)}_{K,m_1,m_2}(\omega_1,\omega_2) &= \mathrm{FT}\left[\frac{\delta^2\Gamma}{\delta\theta_{m_1}(t_1)\,\delta\bar{\theta}^*_{m_2}(t_2)}\right] &&= 2\pi\delta(\omega_1+\omega_2)\delta_{m_1m_2}\big(i\omega_1 + F^\kappa_{K,m_1}k^2_{m_1}\big),\\
\Gamma^{(\bar{\theta}^*,\bar{\theta})}_{K,m_1,m_2}(\omega_1,\omega_2) &= \mathrm{FT}\left[\frac{\delta^2\Gamma}{\delta\bar{\theta}^*_{m_1}(t_1)\,\delta\bar{\theta}_{m_2}(t_2)}\right] &&= 2\pi\delta(\omega_1+\omega_2)\delta_{m_1m_2}\Big(-2D_0^f f^d_{K,m_1}\Big),\\
\Gamma^{(\theta^*,\bar{\theta})}_{K,m_1,m_2}(\omega_1,\omega_2) &= \mathrm{FT}\left[\frac{\delta^2\Gamma}{\delta\theta^*_{m_1}(t_1)\,\delta\bar{\theta}_{m_2}(t_2)}\right] &&= 2\pi\delta(\omega_1+\omega_2)\delta_{m_1m_2}\big(i\omega_1 + F^\kappa_{K,m_1}k^2_{m_1}\big),\\
\Gamma^{(u,u^*)}_{K,m_1,m_2}(\omega_1,\omega_2) &= \mathrm{FT}\left[\frac{\delta^2\Gamma}{\delta u_{m_1}(t_1)\,\delta u^*_{m_2}(t_2)}\right] &&= 2\pi\delta(\omega_1+\omega_2)\delta_{m_1m_2}\left(\frac{1}{2D^v_{m_1}}\right).
\end{aligned}$$

Since all second derivative terms $\Gamma^{(2)}_{K,m_1,m_2}(\omega_1,\omega_2)$ include the delta function of the frequency sum $\delta(\omega_1+\omega_2)$ and the Kronecker delta $\delta_{m_1m_2}$, it can be represented as a function of a single frequency ω and single shell index m. The second derivatives $\Gamma^{(2)}_K$

simplified by the two deltas and the 2π-prefactor will be denoted as $\bar{\Gamma}^{(2)}_K$, so that:

$$\Gamma^{(2)}_{K,m_1,m_2}(\omega_1,\omega_2) = 2\pi\delta(\omega_1+\omega_2)\delta_{m_1m_2}\bar{\Gamma}^{(2)}_{K,m_1}(\omega_1) = 2\pi\delta(\omega_1+\omega_2)\delta_{m_1m_2}\bar{\Gamma}^{(2)}_{K,m_2}(-\omega_2). \tag{5.31}$$

Therefore, the ansatz (5.29) leads to the following expressions for the two-point functions:

$$\bar{\Gamma}^{(\theta,\bar{\theta}^*)}_{K,m}(\omega) = \bar{\Gamma}^{(\theta^*,\bar{\theta})}_{K,m}(\omega) = i\omega + k_m^2 F^{\kappa}_{K,m}, \tag{5.32}$$

$$\bar{\Gamma}^{(\bar{\theta}^*,\bar{\theta})}_{K,m}(\omega) = -2D_0^f f^d_{K,m}, \tag{5.33}$$

$$\bar{\Gamma}^{(u,u^*)}_{K,m}(\omega) = \frac{1}{2D^v_m} = \frac{k_m^{\varepsilon}}{2D_0^v}. \tag{5.34}$$

The velocity is not renormalized, so the derivative $\bar{\Gamma}^{(u,u^*)}$ does not depend on the renormalization scale K.

5.4.3 Regulator, propagator and vertices

As it was mentioned above, to compute the flow equation of the two-point functions $\Gamma^{(2)}_K$ (5.28), one needs to specify the regulator functions of the matrix $\mathcal{R}_K$, as well as to find the expressions for the propagator G_K and vertices within the chosen ansatz (5.29).

Regulator matrix. Since the two-point functions $\Gamma^{(2)}$ are diagonal in the shell index m_i, the regulator matrix can also be chosen diagonal in the following way:

$$\mathcal{R}_{K,m} = \begin{pmatrix} 0 & R_{K,m} & 0 & 0 & 0 & 0 \\ R_{K,m} & 0 & 0 & -2N_{K,m} & 0 & 0 \\ 0 & 0 & 0 & R_{K,m} & 0 & 0 \\ 0 & -2N_{K,m} & R_{K,m} & 0 & 0 & 0 \\ 0 & 0 & 0 & 0 & 0 & \frac{1}{2}R^v_{K,m} \\ 0 & 0 & 0 & 0 & \frac{1}{2}R^v_{K,m} & 0 \end{pmatrix}. \tag{5.35}$$

with the functions:

$$R_{K,m} = \kappa k_m^2\, r\left(\frac{k_m}{K}\right), \tag{5.36}$$

$$N_{K,m} = D_0^f\, n\left(\frac{k_m}{K}\right), \tag{5.37}$$

$$R^v_{K,m} = \frac{K^{\epsilon}}{D_0^v}. \tag{5.38}$$

The cut-off functions r and n have to provide the filtering properties discussed in Sec. 5.4 in order to decouple the large scales from the small ones. One of the possible choices is the following:

$$r(y) = \frac{1}{e^{y^2}-1}; \quad n(y) = y^2 e^{-y^2}. \tag{5.39}$$

It should be noted here that the resulting solution is expected to be independent of the precise form of the cut-off functions r and n.

Propagator. The propagator $G_{K,m}$ is defined as the inverse of the Hessian $(\Gamma_K^{(2)} + \mathcal{R}_K)$, as it was introduced in Eq. (5.27). Since the matrix $(\Gamma_K^{(2)} + \mathcal{R}_K)$ is diagonal in frequency and shell index, the inverse in the definition of the propagator is simply a matrix inverse. Hence, inverting the sum of the matrix (5.30) of $\Gamma_K^{(2)}$ and the matrix (5.35) for $\mathcal{R}_K$ leads to the propagator matrix:

$$G_{K,m}(\omega) = \left(\bar{\Gamma}^{(2)}_{K,m}(\omega) + \mathcal{R}_{K,m}\right)^{-1} = \begin{pmatrix} 0 & G^{(\theta,\bar{\theta}^*)}_{K,m}(\omega) & G^{(\theta,\theta^*)}_{K,m}(\omega) & 0 & 0 & 0 \\ \left(G^{(\theta,\bar{\theta}^*)}_{K,m}(\omega)\right)^* & 0 & 0 & 0 & 0 & 0 \\ \left(G^{(\theta,\theta^*)}_{K,m}(\omega)\right)^* & 0 & 0 & G^{(\theta^*,\bar{\theta})}_{K,m}(\omega) & 0 & 0 \\ 0 & 0 & \left(G^{(\theta^*,\bar{\theta})}_{K,m}(\omega)\right)^* & 0 & 0 & 0 \\ 0 & 0 & 0 & 0 & 0 & G^{(u,u^*)}_{K,m}(\omega) \\ 0 & 0 & 0 & 0 & \left(G^{(u,u^*)}_{K,m}(\omega)\right)^* & 0 \end{pmatrix}, \tag{5.40}$$

with the resulting expressions for the components of the propagator matrix:

$$G^{(\theta,\bar{\theta}^*)}_{K,m}(\omega) = G^{(\theta^*,\bar{\theta})}_{K,m}(\omega) = \frac{1}{i\omega + k_m^2\left(F^{\kappa}_{K,m} + \kappa\, r(k_m/K)\right)}, \tag{5.41}$$

$$G^{(\theta,\theta^*)}_{K,m}(\omega) = \frac{2D_0^f\left(f^d_{K,m} + n(k_m/K)\right)}{\omega^2 + k_m^4\left(F^{\kappa}_{K,m} + \kappa\, r(k_m/K)\right)^2}, \tag{5.42}$$

$$G^{(u,u^*)}_{K,m}(\omega) = \frac{2D_0^v}{k_m^{\varepsilon} + K^{\varepsilon}}. \tag{5.43}$$

It is important to highlight here that the propagator $G_K^{uu^*}$ is independent of the frequency. This is the consequence of the white-in-time velocity field assumed in the Kraichnan's shell model (5.4).

Vertices $\Gamma_K^{(3)}$. The ansatz Γ_K in (5.29), as well as the microscale action $\mathcal{S}$ given in (5.17), have only two nonzero third-order derivatives: with respect to the fields $\bar{\theta}^*, \theta^*, u^*$ and the corresponding complex conjugated term with respect to the fields $\theta, \bar{\theta}, u$, taking the form:

$$\begin{aligned}\Gamma^{(\bar{\theta}^*,\theta^*,u^*)}_{K,m_1,m_2,m_3}(\omega_1,\omega_2,\omega_3) &= \mathrm{FT}\left[\frac{\delta^3\Gamma_K}{\delta\bar{\theta}^*_{m_1}(t_1)\,\delta\theta^*_{m_2}(t_2)\,\delta u^*_{m_3}(t_3)}\right] \\ &= 2\pi\delta(\omega_1+\omega_2+\omega_3)(-i)(k_{m_1+1}\delta_{m_3,m_1}\delta_{m_2,m_1+1} - k_{m_1}\delta_{m_3,m_1-1}\delta_{m_2,m_1-1}),\end{aligned} \tag{5.44}$$

$$\begin{aligned}\Gamma^{(\theta,\bar{\theta},u)}_{K,m_1,m_2,m_3}(\omega_1,\omega_2,\omega_3) &= \mathrm{FT}\left[\frac{\delta^3\Gamma_K}{\delta\theta_{m_1}(t_1)\,\delta\bar{\theta}_{m_2}(t_2)\,\delta u_{m_3}(t_3)}\right] \\ &= 2\pi\delta(\omega_1+\omega_2+\omega_3)i(k_{m_1}\delta_{m_2,m_1-1}\delta_{m_3,m_1-1} - k_{m_1+1}\delta_{m_2,m_1+1}\delta_{m_3,m_1}).\end{aligned} \tag{5.45}$$

Within the chosen approximation, the third-order derivatives of the effective action do not depend on the renormalization scale K, so $\Gamma_K^{(3)} = \mathcal{S}^{(3)}$.

5.4.4 Flow equations

After choosing an ansatz and establishing the form for the functional derivatives of the effective average action Γ_κ and regulator matrix $\mathcal{R}_K$, there are all ingredients to compute the flow equation (5.28) for $\Gamma_K^{(2)}$. Plugging the vertices $\Gamma_\kappa^{(3)}$ and propagators from Eqs. (5.41)-(5.43) into the flow equation (5.28) for $\Gamma_\kappa^{(2)}$ leads to a set of ordinary differential equations for the two functions $F_{K,m}^\kappa$ and $f_{K,m}^d$ corresponding to different shells. Solving these equations allows to find the form of the two-point functions $\bar{\Gamma}^{(2)}$ in the fixed point limit $K \to 0$, which in turn lead to a solution for the structure function of the scalar.

The truncated flow equation (5.28) for $\bar{\Gamma}^{(2)}$ with respect to the fields ψ_a and ψ_b takes the following form:

$$\partial_s \bar{\Gamma}_{K,m}^{(\psi_a,\psi_b)}(\Omega) = \sum_{\varphi_i} \sum_{m_i} \int \frac{\mathrm{d}\omega}{2\pi} \partial_s \mathcal{R}_{K,m_1}^{(\varphi_1,\varphi_2)} G_{K,m_1}^{(\varphi_2,\varphi_3)}(\omega) \Gamma_{K,m,m_1,m_2}^{(\psi_a,\varphi_3,\varphi_4)}(\Omega,\omega,-\omega-\Omega) \times G_{m_2}^{(\varphi_4,\varphi_5)}(\omega+\Omega) \Gamma_{K,m,m_2,m_1}^{(\psi_b,\varphi_5,\varphi_6)}(-\Omega,\omega+\Omega,-\omega) G_{m_1}^{(\varphi_6,\varphi_1)}(\omega), \quad (5.46)$$

where the summation over the fields φ_i means that each of the fields φ_i with $i = 1,..6$ runs over all possible of six average fields $\varphi_i \in \{\theta, \bar{\theta}^*, \theta^*, \bar{\theta}, u, u^*\}$. That is to say, that one has to compute a product of six matrices in 36 configurations of the set φ_i. However, most of these terms vanish. One can easily find the nonzero configurations with the diagrammatic method. For this purpose, the following notations are introduced: continuous lines correspond to the scalar field θ, dashed lines - to the response field $\bar{\theta}$ and waved lines - to the velocity field u. The doubled lines denote the complex conjugated fields. The diagrammatic representations of the propagators G_K, regulators $\mathcal{R}_K$ and vertices $\Gamma^{(3)}$ are shown in Fig. 5.1.

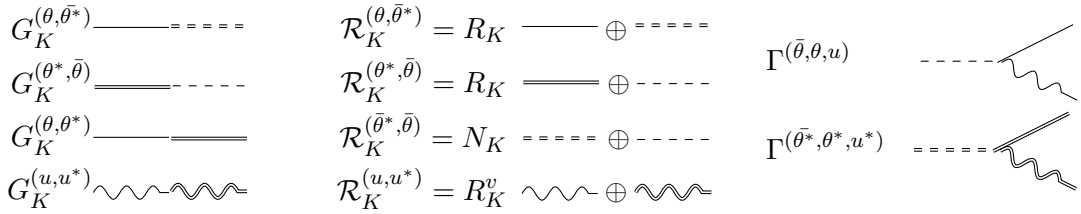

FIGURE *5.1 – Diagrammatic representation of the propagators, regulators and vertices.*

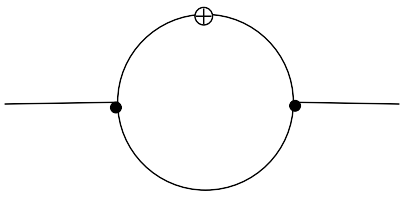

FIGURE *5.2 – General diagrammatic scheme of the right-hand side of the flow equation for the second derivatives of the effective action* $\Gamma^{(2)}$ *in the approximation of Eq.* (5.46).

The diagrammatic representation of the right-hand side of the truncated flow equation (5.46) is shown in the Fig. 5.2. Finding all possible configurations of this loop diagram with elements from the Fig. 5.1 gives the non-vanishing terms remaining after summation over the fields φ_i in Eq. (5.46).

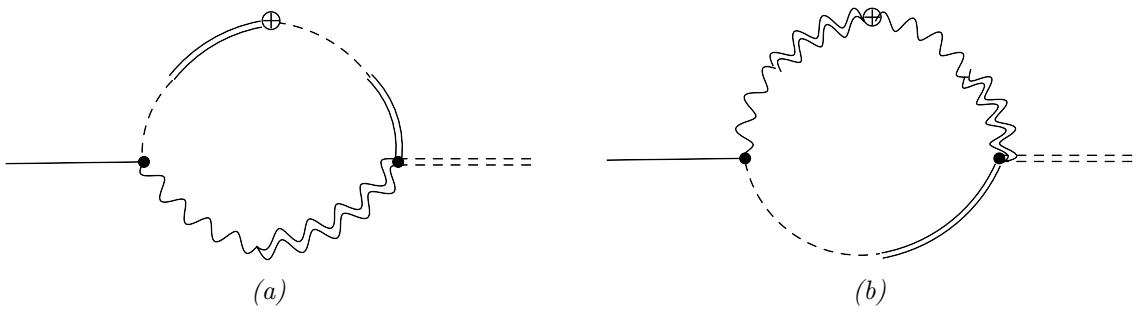

FIGURE 5.3 – *All diagrams for the right-hand side of the flow equation* (5.47) *for* $\Gamma_K^{(\theta,\bar{\theta^*})}$.

Flow equation for $\Gamma_K^{(\theta,\bar{\theta^*})}$

The flow equation (5.28) for the functional derivative $\bar{\Gamma}^{(2)}_{K,m}$ with respect to the fields θ and $\bar{\theta}^*$ has two nonzero terms which can be represented diagrammatically as in Fig. 5.3. The non-vanishing terms in of the Eq. (5.46) for the flow of $\Gamma^{\theta\bar{\theta^*}}$ are thus:

$$\begin{aligned}\partial_s\bar{\Gamma}^{(\theta,\bar{\theta^*})}_{K,m}(\Omega) = \sum_{m_i}\int\frac{\mathrm{d}\omega}{2\pi}\partial_s\mathcal{R}^{(\theta^*,\bar{\theta})}_{K,m_1}G^{(\theta^*,\bar{\theta})}_{K,m_1}(\omega)\Gamma^{(\theta,\bar{\theta},u)}_{K,m,m_1,m_2}(\Omega,\omega,-\omega-\Omega)\\ \times G^{(u,u^*)}_{m_2}(\omega+\Omega)\Gamma^{(\bar{\theta^*},u^*,\theta^*)}_{K,m,m_2,m_1}(-\Omega,\omega+\Omega,-\omega)G^{(\theta^*,\bar{\theta})}_{K,m_1}(\omega)\\ +\sum_{m_i}\int\frac{\mathrm{d}\omega}{2\pi}\partial_s\mathcal{R}^{(u,u^*)}_{K,m_1}G^{(u^*,u)}_{K,m_1}(\omega)\Gamma^{(\theta,u,\bar{\theta})}_{K,m,m_1,m_2}(\Omega,\omega,-\omega-\Omega)\\ \times G^{(\bar{\theta},\theta^*)}_{K,m_2}(\omega+\Omega)\Gamma^{(\bar{\theta^*},\theta^*,u^*)}_{K,m,m_2,m_1}(-\Omega,\omega+\Omega,-\omega)G^{(u^*,u)}_{K,m_1}(\omega).\end{aligned}\tag{5.47}$$

Inserting the expressions for $\mathcal{R}_K$, G_K and $\Gamma^{(3)}_K$ from Eqs. (5.32)-(5.43) into the Eq. (5.47) and subsequent summations over the indices m_1, m_2, m_3 and integration over the frequency ω lead to the following equation for the renormalized diffusivity $F^\kappa K, m$:

$$k_m^2 K\frac{\mathrm{d}F^\kappa_{K,m}}{\mathrm{d}K} = -D_0^v\varepsilon K^\varepsilon\left(\frac{k_m^2}{(K^\varepsilon+k_{m-1}^\varepsilon)^2}+\frac{k_{m+1}^2}{(K^\varepsilon+k_m^\varepsilon)^2}\right).\tag{5.48}$$

The frequency integration of the first term in Eq. (5.47) is zero, so only the integration over the frequency in the second term, corresponding to the second diagram in Fig. 5.3, contributes to the flow of $\Gamma_K^{(\theta,\bar{\theta^*})}$. This integration over the frequency has to be performed in terms of Cauchy principal value.

As it has been mentioned above, at microscale $K=\Lambda$ the renormalized diffusivity $F^\kappa_{K,m}$ coincides with the molecular diffusivity κ of the scalar. It provides the initial conditions $F^\kappa_{K=\Lambda}(k_m)=\kappa\ \forall m$ for the set of ODEs (5.48). Due to the fact that the velocity is not renormalized, this equation appears to be simple enough to be integrated analytically. Integrating the equations with the given initial conditions leads to:

$$F^\kappa_{K,m} = \kappa+\frac{D_0^v}{k_m^2}\left[\frac{k_m^2}{K^\varepsilon+k_{m-1}^\varepsilon}-\frac{k_m^2}{\Lambda^\varepsilon+k_{m-1}^\varepsilon}+\frac{k_{m+1}^2}{K^\varepsilon+k_m^\varepsilon}-\frac{k_{m+1}^2}{\Lambda^\varepsilon+k_m^\varepsilon}\right].\tag{5.49}$$

One can see from this expression that for shells of scales much larger than the microscale $k_m\ll\Lambda$ and with integrating out all fluctuation ($K\to 0$), the approximate expression for the renormalized viscosity takes the form:

$$\lim_{K\to 0}F^\kappa_{K,m}\approx\kappa+\frac{D_0^v}{k_m^\varepsilon}.\tag{5.50}$$

This means that for the wavenumbers $k_m \ll (D_0^v/\kappa)^{1/\varepsilon}$ the renormalized viscosity behaves as a power law $F^{\kappa}_{K,m} \sim D_0^v k_m^{-\varepsilon}$, while at large wavenumbers $k_m \gg (D_0^v/\kappa)^{1/\varepsilon}$ it is mainly determined by the molecular diffusivity $F^{\kappa}_{K,m} \approx \kappa$.

Flow equation for $\Gamma_K^{(\bar\theta,\bar\theta^*)}$

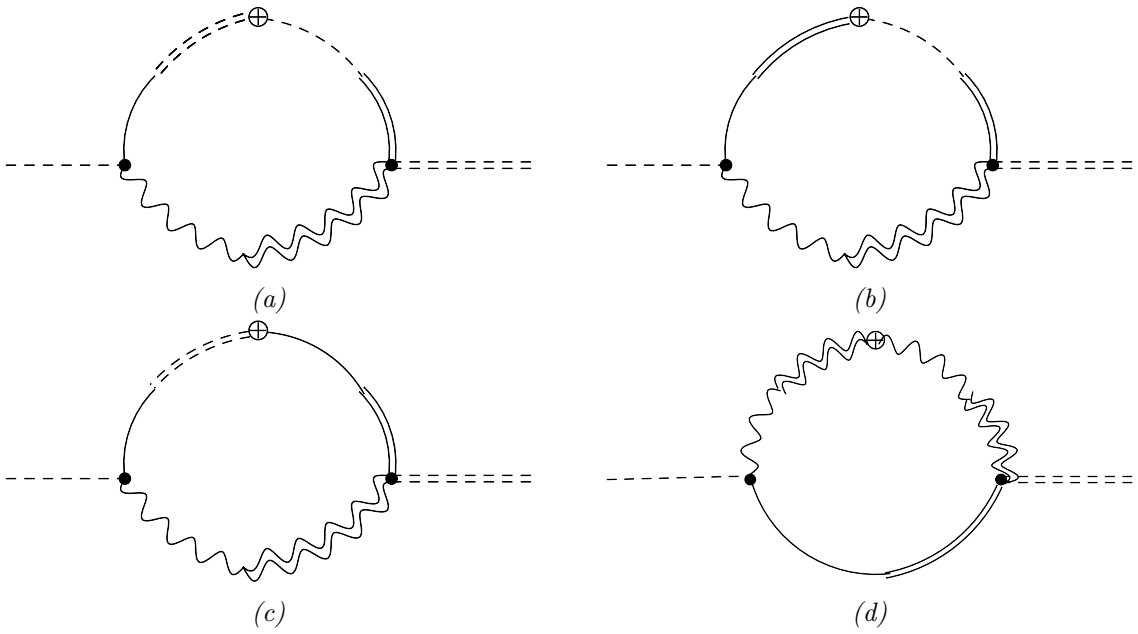

FIGURE 5.4 – *All diagrams of the right-hand side of the flow equation (5.51) for* $\Gamma_K^{(\bar\theta,\bar\theta^*)}$.

A similar analysis can be performed for the flow of the effective action derivative $\Gamma^{(\bar\theta,\bar\theta^*)_K}$. The four diagrams that may contribute to $\partial_s\Gamma^{(\bar\theta,\bar\theta^*)}$ are shown in the Fig. 5.4. The right-hand side of the flow equation thus contains 4 terms:

$$
\begin{aligned}
\partial_s\bar\Gamma^{(\bar\theta,\bar\theta^*)}_{K,m}(\Omega) = \sum_{m_i}\int\frac{\mathrm{d}\omega}{2\pi}\partial_s\mathcal{R}^{(\bar\theta,\bar\theta^*)}_{K,m_1}G^{(\bar\theta^*,\theta)}_{K,m_1}(\omega)\Gamma^{(\bar\theta,\theta,u)}_{K,m,m_1,m_2}(\Omega,\omega,-\omega-\Omega)\\
\times G^{(u,u^*)}_{m_2}(\omega+\Omega)\Gamma^{(\bar\theta^*,u^*,\theta^*)}_{K,m,m_2,m_1}(-\Omega,\omega+\Omega,-\omega)G^{(\theta^*,\bar\theta)}_{K,m_1}(\omega)\\
+\sum_{m_i}\int\frac{\mathrm{d}\omega}{2\pi}\partial_s\mathcal{R}^{(\bar\theta,\theta^*)}_{K,m_1}G^{(\theta^*,\theta)}_{K,m_1}(\omega)\Gamma^{(\bar\theta,\theta,u)}_{K,m,m_1,m_2}(\Omega,\omega,-\omega-\Omega)\\
\times G^{(u,u^*)}_{K,m_2}(\omega+\Omega)\Gamma^{(\bar\theta^*,u^*,\theta^*)}_{K,m,m_2,m_1}(-\Omega,\omega+\Omega,-\omega)G^{(\theta^*,\bar\theta)}_{K,m_1}(\omega)\\
+\sum_{m_i}\int\frac{\mathrm{d}\omega}{2\pi}\partial_s\mathcal{R}^{(\theta,\bar\theta^*)}_{K,m_1}G^{(\bar\theta^*,\theta)}_{K,m_1}(\omega)\Gamma^{(\bar\theta,\theta,u)}_{K,m,m_1,m_2}(\Omega,\omega,-\omega-\Omega)\\
\times G^{(u,u^*)}_{K,m_2}(\omega+\Omega)\Gamma^{(\bar\theta^*,u^*,\theta^*)}_{K,m,m_2,m_1}(-\Omega,\omega+\Omega,-\omega)G^{(\theta^*,\theta)}_{m_1}(\omega)\\
+\sum_{m_i}\int\frac{\mathrm{d}\omega}{2\pi}\partial_s\mathcal{R}^{(u,u^*)}_{K,m}G^{(u^*u)}_{K,m_1}(\omega)\Gamma^{(\bar\theta,u,\theta)}_{K,m,m_1,m_2}(\Omega,\omega,-\omega-\Omega)\\
\times G^{(\theta,\theta^*)}_{K,m_2}(\omega+\Omega)\Gamma^{(\bar\theta^*,\theta^*,u^*)}_{K,m,m_2,m_1}(-\Omega,\omega+\Omega,-\omega)G^{(u^*,u)}_{K,m_1}(\omega).
\end{aligned}
\tag{5.51}
$$

After substitution of the propagators, regulators, and vertices, followed by the summation over indices m and integration over the frequency ω, one obtains the following set of ODEs for the renormalized forcing functions $f^D_{K,m}$ corresponding to different shells with

indices m:

$$\partial_s f^d_{K,m} = -\frac{k_m^2 G^{(u,u^*)}_{K,m-1}}{4D_0^f \rho^2_{K,m-1}}\Big[\rho_{K,m-1}\Big(\Delta_{K,m-1}G^{(u,u^*)}_{K,m-1}\partial_s R^v_{K,m-1} - 2\partial_s N_{K,m-1}\Big) + 2\partial_s R_{K,m-1}\Delta_{K,m-1}\Big] - \frac{k_{m+1}^2 G^{(u,u^*)}_{K,m}}{4D_0^f \rho^2_{K,m+1}}\Big[\rho_{K,m+1}\Big(\Delta_{K,m+1}G^{(u,u^*)}_{K,m}\partial_s R^v_{K,m} - 2\partial_s N_{K,m+1}\Big) + 2\partial_s R_{K,m+1}\Delta_{K,m+1}\Big]. \quad (5.52)$$

Here the following notations are introduced to shorten down the equation and simplify the integration over the frequency:

$$\rho_{K,m} \equiv k_m^2\big(F^\kappa_{K,m} + \kappa\ r(k_m/K)\big), \quad (5.53)$$

$$\Delta_{K,m} \equiv D_0^f\Big(f^d_{K,m} + n(k_m/K)\Big). \quad (5.54)$$

The set of equations for $f^d_{K,m}$ (5.51) is more complicated than the one for F^κ. The equations for different shells are coupled, and this set of equations does not allow for an analytical solution. However, it is rather simple to solve numerically. The results of the numerical solutions are provided in the following section 5.5.

Two-point correlation function of the scalar

As discussed in the Sec. 5.3, the generating functional of the connected correlation function $W[J_\psi]$ can be found as the Legendre transform of the effective average action functional $\Gamma_K[\psi]$ (5.23). When the flow equations are solved and the functions $f^d_{K,m}$, $F^\kappa_{K,m}$ at the fixed point at $K \to 0$ are known, the two-point equal-time correlation function $W^{(2)}$ of the scalar can be found as the propagator $G^{(\theta,\theta^*)}$ integrated over the frequency:

$$S_2(k_m) \equiv \langle\theta(k_m)\theta^*(k_m)\rangle = \lim_{K\to 0}\int G^{(\theta,\theta^*)}_{K,m}(\omega)\frac{\mathrm{d}\omega}{2\pi} = \int \frac{2D_0^f f^d_{K\to 0,m}}{\omega^2 + k_m^4 (F^\kappa_{K\to 0,m})^2}\frac{\mathrm{d}\omega}{2\pi} = \frac{D_0^f f^d_{K\to 0,m}}{k_m^2 F^\kappa_{K\to 0,m}}. \quad (5.55)$$

The expression (5.55) shows that the form of the second-order structure function in this approximation is determined by the behavior of the functions f^d and F^κ at the fixed points $K \to 0$. If both functions appear to be power laws of the shell wavenumber k_m, so is the structure function S_2.

It should be noted that even though the vertices $\Gamma^{(n)}$ of order $n > 4$ are neglected in the adopted ansatz (5.29), the higher-order correlation functions and structure functions S_n with $n > 4$ do not vanish. The fixed-point solution of the flow equations also allows to compute any higher-order structure function S_3, S_4, S_5 and so on, in the similar way through the generating functional of the correlation functions (5.23).

5.5 Numerical solution

Using the exact analytical solution for the functions $F^\kappa_{K,m}$ from Eq. (5.49) one can solve numerically the set of coupled ODEs for $f^d_{K,m}$ from Eq. (5.52).

Parameters. For numerical solution, the following numerical values of the model parameters are used: number of shells $N = 100$, molecular diffusivity $\kappa = 1$, velocity variance amplitude $D_0^v = 1$, velocity spatial covariance exponent $\varepsilon = 0.5, 1.0, 1.5, 2.0$, the wavenumbers of the shells $k_m = k_0\lambda^m$ with $\lambda = 2$, $k_0 = 0.01$, $m = \{m_1, ..., m_N\}$, $m_1 = -70$, $m_N = 29$, the microscale wavenumber $\Lambda = 10^8$, the forcing amplitude $D_0^f = 1$. The set of ODEs (5.52) is integrated over the variable $s = \ln(K/\Lambda)$ from $s = 0$ to $s = -100$, which is equivalent to integrating over K from $K = \Lambda$ to $K = \Lambda e^{-100}$. The initial conditions at $s = 0$ (or $K = \Lambda$) are $f^d_{K=0,m} = 0\ \forall m$. The boundary conditions for the limiting shells are $f^d_{K,m_1-1} = 0$, $f^d_{K,m_N+1} = 0$. The system of equations (5.52) has been solved with the fourth-order Runge-Kutta scheme implemented in `scipy` library (Jones et al., 2001), with the maximal step limited to $\Delta s < 0.1$.

To avoid the over- and underflow errors when computing expressions of the regulators, the functions from Eq. (5.39) are replaced by the following piecewise-defined functions:

$$r(y) = \begin{cases} 0, & y > 10 \\ \frac{1}{e^{y^2}-1}, & 10^{-4} < y < 10 \\ y^{-2}, & y < 10^{-4} \end{cases}; \quad n(y) = \begin{cases} 0, & y > 10 \\ y^2 e^{-y^2}, & y < 10 \end{cases} \tag{5.56}$$

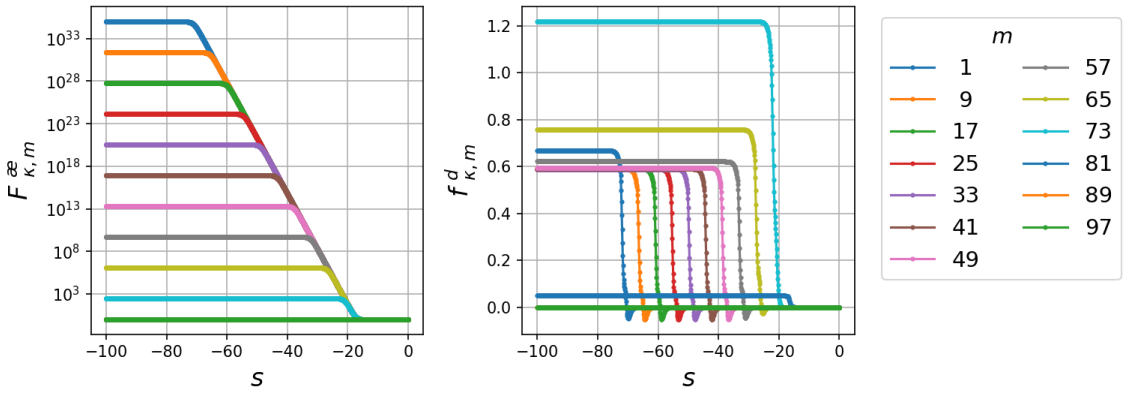

FIGURE 5.5 – *Analytical solution of the flow equation F^κ and the numerical one for f^d evolving with the renormalization scale $s = \ln(K/\Lambda)$ for various shells with indices m for the case with $\varepsilon = 1.5$. The solution of f^d for all shells reaches to a plateau with decreasing s, which indicates that the fixed point of the flow equation is reached in the solution.*

Solution of the flow equations. The flow equations have to be integrated up to a sufficiently large renormalization scale K, which is equivalent to reaching large negative values of the variable s. The evolution of the functions F^κ and f^d with the scale variable s is shown in Fig. 5.5. The solution for F^κ is obtained simply by evaluation of the analytical expression (5.49) at various values of s and shell indices m, while the solution for f^d is obtained numerically with the Runge-Kutta method. The curves in Fig. 5.5 saturate at constant levels at large negative s, indicating that the solutions of the flow equations reach the fixed point when the renormalization wavenumber K is small enough. These plateau values of the functions F^κ and f^d are needed for the computation of the observables, such as structure functions.

The dependence of the solutions at the fixed point on the shell wavenumber k_m is shown in Fig. 5.6. As previously discussed, the renormalized viscosity at the fixed point has a power-law dependence $F^\kappa_{K\to 0,m} \sim k_m^{-\varepsilon}$ at wavenumbers $k_m < (D_0^v/\kappa)^{1/\varepsilon} = 1$ and then switches to a constant value equal to the molecular viscosity κ at $k_m > 1$. The function

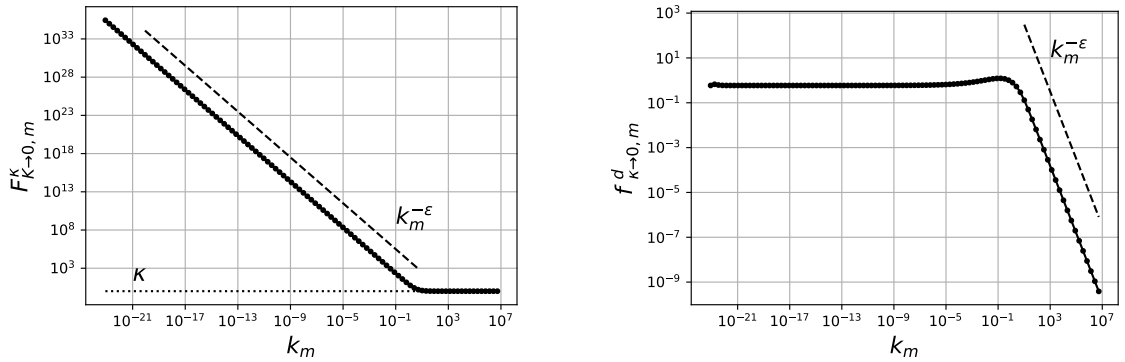

(a) Analytical solution for F^{κ} *(b) Numerical solution for f^{d}*

FIGURE 5.6 – *Dependence of F^{κ} and f^{d} on the shell wavenumber k_m at $s = -100$ corresponding to the fixed point of the flow equations. The dashed lines show the slope of the power law $k_m^{-\varepsilon}$. Both curves change their behavior in the vicinity of $k_m = (D_0^v/\kappa)^{1/\varepsilon} = 1$.*

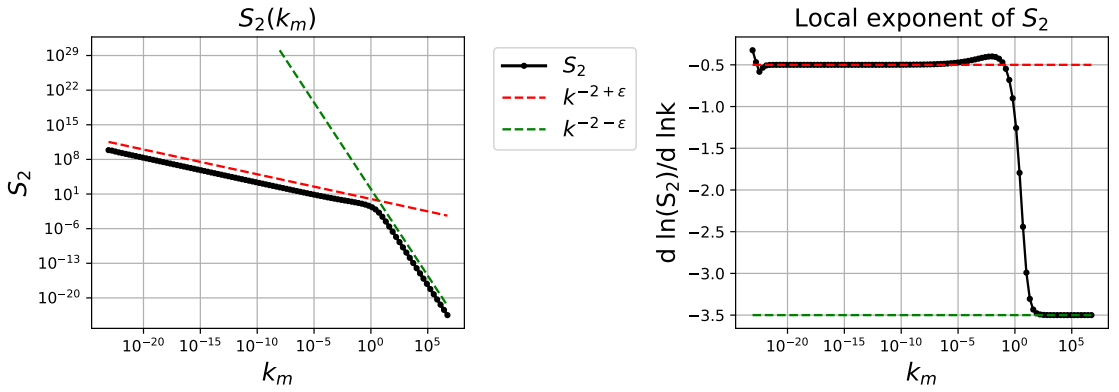

FIGURE 5.7 – *Left-panel: second-order structure functions of the scalar for the case $\varepsilon = 1.5$ computed according to Eq. (5.55) with the functions f^{d} and F^{κ} shown in Fig. 5.6. Right panel: the local power-law exponent of S_2 evaluated through numerical log-log derivative: the structure function S_2 exhibits two zones with distinct power laws.*

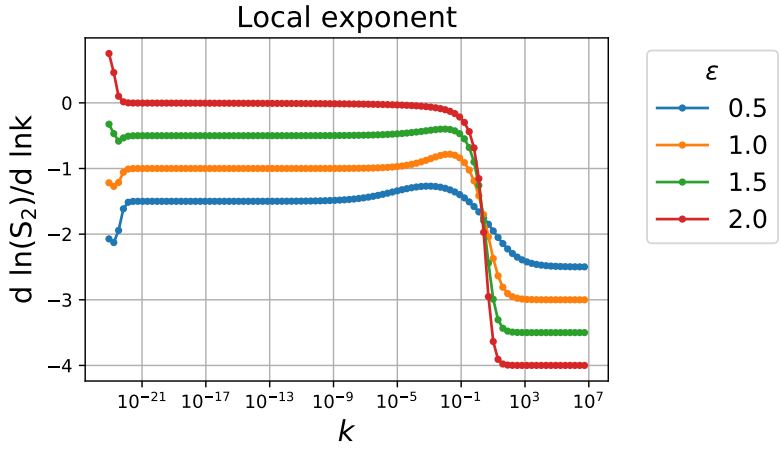

FIGURE 5.8 – *Local power-law exponent of the second order structure function at various ε. In all cases, the exponent of S_2 takes the value $-2+\varepsilon$ at $k_m \lesssim 1$ and $-2-\varepsilon$ at $k_m \gtrsim 1$.*

f^d at the fixed point also changes its shape in the vicinity of $k_m = 1$: from the constant at $k_m < 1$ to the power law $k_m^{-\varepsilon}$ at large wavenumbers.

Structure functions of the scalar. Once the fixed-point solutions of the functions F^κ and f^d are known, one can calculate the second-order structure function of the scalar with the use of the expression (5.55). The resulting dependence of the structure function S_2 on the shell wavenumber k_m is shown in the left panel Fig. 5.7. It shows that the function $S_2(k)$ exhibits two distinct power laws. The right panel of Fig. 5.7 displays the local power-law exponents of S_2 estimated through taking the numerical log-log derivative. The dependence of the power-law exponent on ε was tested in four cases $\varepsilon = 0.5, 1.0, 1.5, 2.0$, the results for $S_2(k)$ in all four cases are shown in Fig. 5.8. One can see that at $k_m \lesssim 1$ the structure function possesses the exponent $-2 + \varepsilon$, while at $k_m \lesssim 1$ the exponent takes the value $-2 - \varepsilon$.

The third-order structure function S_3 results to be zero, as it is expected for any odd-order structure function. The numerical evaluation of the fourth-order structure function S_4 shows that within the chosen ansatz it also takes the form of a power law with respect to k_m. At $k_m \lesssim 1$, its exponent is $-4 + 2\varepsilon$, which is two-fold larger than the one of S_2. At higher wavenumbers $k_m \gtrsim 1$, the power-law exponent of S_4 takes the value $-4 - 3\varepsilon$.

Discussion. Regarding S_2, the power law $k_m^{-2+\varepsilon}$ at wavenumbers $k_m \lesssim 1$ can actually be deduced from the dimensional considerations of the initial shell model equation. It coincides with the power law in the inertial range of the spectrum of the scalar in the continuous Kraichnan's model (see Sec. 1.3.2) in the case of zero dimension $d = 0$. The same power law has been obtained analytically for S_2 and observed in numerical solutions of the initial stochastic differential equation of Kraichnan's shell model (Wirth and Biferale, 1996).

Regarding the large wavenumbers, the power law $k_m^{-2-\varepsilon}$ of the second-order structure function S_2 at large wavenumbers $k_m \gtrsim 1$ is identical to the power law of the intertial-diffusive range of the passive scalar in continuous Kraichnan's model with zero dimension (section 1.3.2). However, this power law has not been reported previously in the works dedicated to the shell model of random passive advection. It can be related to an insufficient number of shells in numerical modeling in previous works. It could also be a consequence of a different implementation of the scalar forcing in the original shell model in the FRG analysis that has been developed in this chapter. This question requires further investigation.

The fixed point solution allows in addition the computation of the higher order structure functions. The numerical solution for S_4 shows that at $k \lesssim 1$ it behaves as a power law with an exponent twofold greater than the one for S_2, which corresponds to the normal scaling in Kraichnan's shell model (5.7). However, it is known from previous works that S_4 power law exhibits a small deviation from the normal scaling, which is the intermittency correction. Therefore, the simplest ansatz, adopted in the present study, contains only the normal scaling of the model. The further study of this model within FRG approach will be focused on developing a more complex ansatz and checking whether it allows observing the intermittency correction for S_4 and higher-order structure functions.

5.6 Conclusions

In this chapter, the initial steps of the FRG study of the shell model of random advection of a passive scalar are provided. As a first step, the stochastic differential equation of the advection-diffusion shell model was transformed to a corresponding path integral with the use of MSRJD procedure. The advantage of switching to the path integral formalism is that it yields multipoint Eulerian correlation functions. Then, a scale-dependent effective average action functional is constructed by adding a regulator functional to the previously found action of the initial stochastic differential equation. This regulator decouples the large-scale modes from the small-scale ones. This approach allows to build a family of scale-dependent models described by the effective average action. The dependence of the effective action on the renormalization scale is governed by an exact flow equation.

Solving the flow equation consists in integrating the fluctuations progressively moving from the known microscale model towards the effective large-scale model. However, since the flow equations are complicated, an appropriate ansatz is needed. In the present chapter, the shell model has been studied within the simplest ansatz: it is assumed that the fourth-order derivatives of the action are negligible and that only the second-order derivatives depend on the renormalization scale. In this assumption, only two flow equations have to be solved: for the renormalized diffusivity $F^{\kappa}_{K,m}$ and the renormalized forcing parameter $f^{d}_{K,m}$, both being functions of the renormalization scale K and the shell index m. Thanks to the white-in-time velocity field, the ordinary differential equation for the renormalized diffusivity $F^{\kappa}_{K,m}$ can be solved analytically within the chosen ansatz. The set of ODEs for the forcing-related function $f^{d}_{K,m}$ can be solved numerically. Both solutions reach a fixed point when the renormalization wavenumber K goes to 0.

The fixed point solutions of the flow equations allow to compute observables such as scalar structure functions. In this chapter, results for the second-order structure function S_2 are provided. In the inertial range, S_2 exhibits a power law $S_2 \sim k^{-2+\varepsilon}$, which matches with the power law resulting from dimensional arguments, and is in agreement with the previous analytical and numerical studies of Kraichnan's shell model. In addition, another power law at high wavenumbers $S_2 \sim k^{-2-\varepsilon}$ is observed, which can be analog to the inertial-diffusive range in the continuous version of Kraichnan's model. However, this result should be tested with different implementations of the forcing in the model.

Regarding the fourth-order structure function S_4, the simplest ansatz used for the analysis in this chapter allows to recover the normal scaling. However, it is known from previous studies that this shell model possesses anomalous scaling for the structure functions of the order higher that 4. It would be interesting to see whether taking a more precise ansatz with the non-vanishing fourth-order derivatives of the action would give rise to the correction terms in S_4, corresponding to anomalous exponents. This problem is particularly interesting since it can give a clue about the minimal ansatz for FRG that allows to observe the anomalous corrections. Furthermore, this result can be useful in the application of FRG to study anomalous scaling in models more complicated than Kraichnan's shell model.

Conclusions en français

Dans ce chapitre, les premières étapes de l'étude FRG du modèle en couches d'advection aléatoire d'un scalaire passif sont présentées. D'abord, l'équation différentielle stochastique du modèle en couches d'advection-diffusion a été transformée en une intégrale de chemin grâce à la procédure MSRJD. L'avantage de passer au formalisme de l'intégrale de chemin est qu'il produit des fonctions de corrélation eulériennes multipoints. Ensuite, une fonctionnelle d'action effective moyenne dépendant de l'échelle est construite en ajoutant une

fonctionnelle de régularisation à l'action de l'équation différentielle stochastique initiale trouvée précédemment. Ce régulateur découple les modes à grande échelle des modes à petite échelle. Cette approche permet de construire une famille de modèles dépendant de l'échelle et décrits par l'action effective moyenne. La dépendance de l'action effective sur l'échelle de renormalisation est régie par une équation de flot exacte.

La résolution de l'équation de flot consiste à intégrer les fluctuations, passant ainsi progressivement du modèle microscopique connu vers le modèle à grande échelle effectif. Cependant, comme les équations de flot sont compliquées, un ansatz approprié est nécessaire. Dans le présent chapitre, le modèle en couches a été étudié au sein de l'ansatz le plus simple : on suppose que les dérivées du quatrième ordre de l'action sont négligeables et que seules les dérivées du second ordre dépendent de l'échelle de renormalisation. Dans cette hypothèse, seules deux équations de flot doivent être résolues : celle de la diffusivité renormalisée $F^{\kappa}_{K,m}$ et celle du paramètre de forçage renormalisé $f^{d}_{K,m}$, les deux étant des fonctions de l'échelle de renormalisation K et de l'indice de couche m. Grâce au champ de vitesse qui a le comportement d'un bruit blanc en temps, l'équation différentielle ordinaire pour la diffusivité renormalisée $F^{\kappa}_{K,m}$ peut être résolue analytiquement dans l'ansatz choisi. L'ensemble des équations differentielles ordinaires pour la fonction liée au forçage $f^{d}_{K,m}$ peut être résolu numériquement. Les deux solutions atteignent un point fixe lorsque le nombre d'onde de renormalisation K tend vers 0.

Les solutions au point fixe des équations de flot permettent de calculer des observables telles que des fonctions de structure scalaire. Dans ce chapitre, les résultats pour la fonction de structure du second ordre S_2 sont fournis. Dans le domaine inertiel, S_2 présente une loi de puissance $S_2 \sim k^{-2+\varepsilon}$, qui correspond à la loi de puissance résultant des arguments dimensionnels, et est en accord avec les études analytiques et numériques précédentes du modèle en couches de Kraichnan. De plus, une autre loi de puissance aux nombres d'onde élevés $S_2 \sim k^{-2-\varepsilon}$ est observée, qui peut être analogue à la gamme inertielle-diffusive dans la version continue du modèle de Kraichnan. Cependant, ce résultat devra être testé avec différentes implémentations du forçage dans le modèle.

Concernant les fonctions de structure de l'ordre quatre S_4, l'ansatz le plus simple utilisé pour l'analyse dans ce chapitre permet de retrouver la loi d'échelle normale. Cependant, il est connu d'après des études antérieures que ce modèle en couches possède une loi d'échelle anormale pour les fonctions de structure d'ordre 4 et supérieur.

Il serait intéressant de voir si un ansatz plus précis avec les dérivées du quatrième ordre non nulles donnerait lieu aux termes de correction en S_4, correspondant aux exposants anormaux. Ce problème est particulièrement intéressant parce qu'il peut donner un indice sur l'ansatz minimal pour FRG permettant d'observer les corrections anormales. De plus, ce résultat peut être utile dans l'application de FRG pour étudier la loi d'échelle anormale dans des modèles plus compliqués que le modèle en couches de Kraichnan.

Conclusions and perspectives

The main objective of the study presented in this thesis is the numerical validation of new theoretical results obtained within the FRG approach for spatio-temporal Eulerian correlation functions in turbulent flows. In particular, the main conclusions regarding the velocity correlation functions are the following:

— The two-point correlation function of velocity at small time lags, measured in the numerical simulations, decays as a Gaussian function of the tk-variable, which is in agreement with the FRG prediction. This result also shows that the typical time of the decorrelation of a velocity Fourier mode scales as $\tau_D \sim k^{-1}$ which can be explained by the dominance of the random sweeping effect in the Eulerian temporal correlation.

— The same Gaussian decay is also observed for the triple velocity correlation function at large wavenumbers, which was evaluated through the advection-velocity correlation of filtered velocity fields. This result can be linked to the FRG result for the three-point correlation function, predicting the same Gaussian form. Moreover, the quantitative results for the decorrelation parameters of the Gaussian decay for two- and three-point correlations are very close, which is also in agreement with the theoretical results. To our knowledge, the temporal behavior of the triple velocity correlation in Fourier space has not been studied before, so these results represent a nontrivial quantitative check of the FRG prediction.

— Besides, the correlation function of the velocity moduli has been measured, although such a correlation is not covered by the FRG analysis. The numerical results show that the correlation function of moduli also decays as a Gaussian in tk at small time lags and switches to a slower decay at large time lags.

— The results from another set of numerical simulations on finer grids allow to conclude that the spectrum of the turbulent kinetic energy takes the form of a stretched exponential in the near-dissipative range, and the value of the stretch exponent approaches the one predicted by the FRG at high Reynolds numbers.

The analysis of the space-time correlations of a passive scalar in the inertial-convective range allows to conclude that they are determined by the temporal covariance of the velocity field. More precisely, the results allow to come to the following conclusions:

— In a turbulent velocity field governed by the Navier-Stokes equations, the space-time correlation function of the scalar reproduces the form of the velocity correlation function, decaying as a Gaussian at small time lags.

— In a random velocity field with approximately white-in-time covariance, the scalar field decorrelates as an exponential of the variable tk^2, which is in agreement with the FRG result for Kraichnan's model of random advection.

— Adding a finite correlation time to the synthetic velocity field leads to the emergence of a Gaussian decay at small time lags in the scalar correlation function, while at time lags larger than the characteristic decorrelation time of velocity, the scalar decorrelates as an exponential, identical to the one observed in the simulations of Kraichnan's model.

— These results can be interpreted from the point of view of a single particle dispersion, or more precisely through the (approximate) link of the Eulerian correlation function with the Lagrangian displacements. The Gaussian decay of the scalar correlation function can be related to the ballistic regime of the particle dispersion, when the mean square displacement of a fluid particle grows quadratically in time. At large time lags, the scalar correlation decays as an exponential, which can be linked to the diffusive regime of the particle dispersion with the mean squared displacement growing linearly in time.

— The analytical study of the shell model of a randomly advected scalar shows that the FRG derivation for the structure functions for this model is considerably simpler compared to the continuous models. The simplest ansatz described in this thesis allows to build a set of renormalization group flow equations which reach a fixed point. The scalar structure functions corresponding to the fixed point solution behave as a power law matching the normal scaling of the model. These results are in agreement with previous studies and represent the initial step for a more advanced FRG analysis of this model.

The presented results demonstrate that the FRG predictions for the space-time correlation functions are consistent with the numerical data. Therefore, the FRG provides reliable results that can be mapped to numerical data, which makes the FRG approach a promising framework for more advanced studies of statistical properties of turbulence. It should be also mentioned that the presented predictions of the spatio-temporal correlation functions can serve for the development of the closure of statistical models of turbulence or to improve the numerical models parametrizing small-scale motions. Another example of a direct application of the presented results for Eulerian space-time correlation is the generation of synthetic velocity fields with realistic temporal behavior, which are largely used for studies of particle dispersion of wave propagation in turbulent media.

However, in the direction of comparison of DNS results with the FRG predictions, there are a lot of questions to explore, for instance:

— Study the large-time regime of the correlation functions. A possible way to reduce the oscillations in the tail of the correlation functions and to improve the data quality at large time lags is to increase the size of the computational domain or, equivalently, to shift the peak wavenumber of velocity forcing to larger values. In such a way, the simulation box fits more spatial integral scales, therefore the spatial large-scale statistics has more realizations over the box, which clearly has an influence on the temporal statistics on the large scales as well. Preliminary data obtained from simulations of the scalar advection in NS velocity field in larger boxes show the presence of a portion of exponential-like data at large time lags, while in the simulation of the same scalar in a small box this range of time lags is already polluted by oscillations. However, the extension of DNS to larger boxes requires more computational resources.

— Another interesting question, partly related to the previous question, is the influence of the form of the forcing profile on the decorrelation parameters of the velocity and scalar space-time correlation functions. The shell-to-shell analysis of the energy transfer mentioned in this manuscript can be also used for a deeper understanding of the influence of forcing on the energy transfers and correlation functions in DNS data.

— The role of forcing in the temporal statistical properties of scalars and velocity can also be analyzed through the numerical computation of the response function. In the most basic approach, it can be evaluated as a correlation between the forcing field with a time-shifted velocity field (or scalar). Moreover, the response functions

have also a representation in the FRG derivation, so it can provide an additional method for comparison with the FRG predictions. Numerically computed response functions can be additionally compared with the linear response theory of turbulence, summarized in the recent review of Kaneda, 2020.

— Concerning the passive scalar turbulence, it would also be interesting to study other ranges in the passive scalar spectrum, for example, the viscous-convective range, which is expected to have the power law k^{-1}. In particular, one can check whether significant changes in the scalar Schmidt numbers lead to modification of the characteristic decorrelation time of the scalar.

— Regarding the shell model of random scalar advection, this model is known to be the simplest one exhibiting intermittency effects. Therefore, the shell version of Kraichnan's passive scalar model is a good toy model for testing and exploring the FRG method to compute the intermittency effects. It would be interesting to see whether a more complicated FRG ansatz could give rise to intermittency corrections. One of the possible ways to check it is to include the next-order (fourth-order) vertices in the ansatz and recalculate structure functions. Finding the minimal order of vertices that contribute to the intermittency effects can serve also for the development of FRG approach in more complicated models.

Acknowledgments The numerical simulations presented in this manuscript were performed using the high-performance computing resources from Grand Instrument National de Calcul Intensif (GENCI) of the Institut du Développement et des Ressources en Informatique Scientifique (IDRIS) (Grant No. 020611) and the *GRICAD* infrastructure, which is supported by Grenoble research communities.

Conclusions et perspectives en français

L'objectif principal de l'étude présentée dans cette thèse est la validation numérique de nouveaux résultats théoriques obtenus dans le cadre de l'approche FRG pour les fonctions de corrélation eulériennes spatio-temporelles dans les écoulements turbulents. En particulier, les principales conclusions concernant les fonctions de corrélation de vitesse sont les suivantes :

— La fonction de corrélation à deux points de la vitesse à de petits décalages temporels, mesurée dans les simulations numériques, se comporte comme une fonction gaussienne de la variable tk, ce qui est en accord avec la prédiction FRG. Ce résultat montre également que le temps typique de la décorrélation d'un mode de Fourier vitesse s'échelonne comme $\tau_D \sim k^{-1}$ ce qui peut s'expliquer par la dominance de l'effet de balayage aléatoire dans la corrélation temporelle eulérienne.

— La même décroissance gaussienne est également observée pour la fonction de corrélation de vitesse triple aux grands nombres d'onde, qui a été évaluée par la corrélation advection-vitesse des champs de vitesse filtrés. Ce résultat peut être lié au résultat FRG pour la fonction de corrélation à trois points, prédisant la même forme gaussienne. De plus, les résultats quantitatifs pour les paramètres de décorrélation de la décroissance gaussienne pour les corrélations à deux et trois points sont très proches, ce qui est également en accord avec les résultats théoriques. A notre connaissance, le comportement temporel de la triple corrélation de vitesse dans l'espace de Fourier n'a pas été étudié auparavant, donc ces résultats représentent une vérification quantitative non triviale de la prédiction FRG.

— Par ailleurs, la fonction de corrélation des modules de vitesse a été mesurée, bien qu'une telle corrélation ne soit pas couverte par l'analyse FRG. Les résultats numériques montrent que la fonction de corrélation des modules décroît également comme

une gaussienne en tk à de petits décalages temporels et passe à une décroissance plus lente à de grands décalages temporels.

— Les résultats d'un autre ensemble de simulations numériques sur des mailles plus fines permettent de conclure que le spectre de l'énergie cinétique turbulente prend la forme d'une exponentielle étirée dans le domaine dissipatif-proche, et la valeur de l'exposant d'étirement se rapproche de celle prédite par le FRG à des nombres de Reynolds élevés.

L'analyse des corrélations spatio-temporelles d'un scalaire passif dans le domaine inertiel-convectif permet de conclure qu'elles sont déterminées par la covariance temporelle du champ de vitesse. Plus précisément, les résultats permettent de tirer les conclusions suivantes :

— Dans un champ de vitesse turbulent gouverné par les équations de Navier-Stokes, la fonction de corrélation espace-temps du scalaire reproduit la forme de la fonction de corrélation de vitesse, décroissant comme une gaussienne à de petits décalages temporels.

— Dans un champ de vitesse aléatoire avec une covariance approximativement blanche en temps, le champ scalaire est décorrélé comme une exponentielle de la variable tk^2, ce qui est en accord avec le résultat FRG pour le modèle d'advection aléatoire de Kraichnan.

— L'ajout d'un temps de corrélation fini au champ de vitesse synthétique conduit à l'émergence d'une décroissance gaussienne à de petits décalages temporels dans la fonction de corrélation scalaire, tandis qu'à des décalages temporels supérieurs au temps de décorrélation caractéristique de la vitesse, le scalaire décorrèle comme une exponentielle, identique à celui observé dans les simulations du modèle de Kraichnan.

— Ces résultats peuvent être interprétés du point de vue de la dispersion d'une seule particule, ou plus précisément à travers le lien (approximatif) de la fonction de corrélation eulérienne avec les déplacements lagrangiens. La décroissance gaussienne de la fonction de corrélation scalaire peut être liée au régime balistique de la dispersion des particules, lorsque le déplacement quadratique moyen d'une particule fluide croît de façon linéaire dans le temps. À de grands décalages temporels, la corrélation scalaire décroît comme une exponentielle, ce qui peut être lié au régime diffusif de la dispersion des particules avec le déplacement quadratique moyen croissant comme la racine carrée du temps.

— L'étude analytique du modèle en couches d'un scalaire à advection aléatoire montre que la dérivation FRG pour les fonctions de structure pour ce modèle est considérablement plus simple que les modèles continus. L'ansatz le plus simple décrit dans cette thèse permet de construire un ensemble d'équations de flux de groupe de renormalisation qui atteignent un point fixe. Les fonctions de structure scalaires correspondant à la solution du point fixe se comportent comme une loi de puissance correspondant à la loi d'échelle normale du modèle. Ces résultats sont en accord avec les études précédentes et représentent la première étape d'une analyse FRG plus avancée de ce modèle.

Les résultats présentés démontrent que les prédictions FRG pour les fonctions de corrélation espace-temps sont cohérentes avec les données numériques. Par conséquent, le FRG fournit des résultats fiables qui correspondent à des données numériques, ce qui fait de l'approche FRG un cadre prometteur pour des études plus avancées des propriétés statistiques de la turbulence. Il convient également de mentionner que les prédictions des fonctions de corrélation spatio-temporelles présentées peuvent servir pour le développement de la fermeture de modèles statistiques de turbulence ou pour améliorer les modèles numériques

paramétrant les mouvements à petite échelle. Un autre exemple d'application directe des résultats présentés pour la corrélation spatio-temporelle eulérienne est la génération de champs de vitesse synthétiques avec un comportement temporel réaliste, qui sont largement utilisés pour les études de dispersion des particules et de propagation des ondes dans les milieux turbulents.

Cependant, il reste de nombreuses questions à explorer dans le cadre de la comparaison des résultats DNS avec les prédictions FRG, par exemple :

— Étudier le régime en temps grand des fonctions de corrélation. Une manière possible de réduire les oscillations dans la queue des fonctions de corrélation consiste à augmenter la taille du domaine de calcul en déplaçant le nombre d'onde du forçage de vitesse vers des valeurs plus grandes. De cette manière, la boîte de simulation contient plusieurs échelles intégrales spatiales, donc les statistiques spatiales à grande échelle ont plus de réalisations sur la boîte, ce qui aurait clairement une influence sur les statistiques temporelles aux grandes échelles également. Les données préliminaires obtenues à partir de simulations de l'advection scalaire dans le champ de vitesse NS dans des boîtes plus grandes montrent la présence d'une partie de données de type exponentielle à de grands décalages temporels, tandis que dans la simulation du même scalaire dans une petite boîte, cette plage de décalages temporels est déjà pollué par les oscillations. Cependant, l'extension du DNS à des boîtes plus grands nécessite plus de ressources de calcul.

— Une autre question intéressante est l'influence de la forme du profil de forçage sur les paramètres de décorrélation des fonctions de vitesse et de corrélation espace-temps scalaire. L'analyse "shell-to-shell" du transfert d'énergie mentionnée dans ce manuscrit peut également être utilisée pour une compréhension plus approfondie de l'influence du forçage sur les transferts d'énergie et les fonctions de corrélation dans les données DNS.

— Le rôle du forçage dans les propriétés statistiques temporelles des scalaires et de la vitesse peut également être analysé par le calcul numérique de la fonction de réponse. Dans l'approche la plus basique, il peut être évalué comme une corrélation entre le champ de forçage avec un champ de vitesse (ou scalaire) décalé dans le temps. De plus, les fonctions de réponse ont également une représentation dans la dérivation FRG, de sorte qu'elles peuvent fournir une méthode supplémentaire de comparaison avec les prédictions FRG. Les fonctions de réponse calculées numériquement peuvent également être comparées aux théories de réponse linéaire de la turbulence, résumées dans la récente revue de Kaneda, 2020.

— Concernant la turbulence scalaire passive, il serait également intéressant d'étudier d'autres domaines du spectre scalaire passif, par exemple le domaine visqueux-convectif, qui devrait avoir la loi de puissance k^{-1}. En particulier, on peut vérifier si des changements significatifs des nombres de Schmidt scalaires conduisent à une modification du temps de décorrélation caractéristique du scalaire.

— En ce qui concerne le modèle en couches d'advection scalaire aléatoire, ce modèle est connu pour être le plus simple présentant des effets d'intermittence. Par conséquent, la version en couches du modèle scalaire passif de Kraichnan est un bon modèle pour tester et explorer la méthode FRG pour calculer les effets d'intermittence. Il serait intéressant de voir si un ansatz FRG plus compliqué pourrait donner lieu à des corrections d'intermittence. L'une des façons possibles de le vérifier est d'inclure les vertex d'ordre supérieur (quatrième ordre) dans l'ansatz et de recalculer les fonctions de structure. Trouver l'ordre minimal des vertex qui contribuent aux effets d'intermittence peut également servir au développement de l'approche FRG dans des modèles plus compliqués.

Appendices

A

Spectra of energy dissipation, transfer and flux

This appendix provides additional spectra obtained within DNS such as spectra of energy dissipation, energy transfer function, and energy flux. These spectra allow to have additional information about the turbulent energy cascade in numerical simulations, and in particular to evaluate the width of the inertial range. The resulting spectra are compared with previous numerical studies with the use of DNS method.

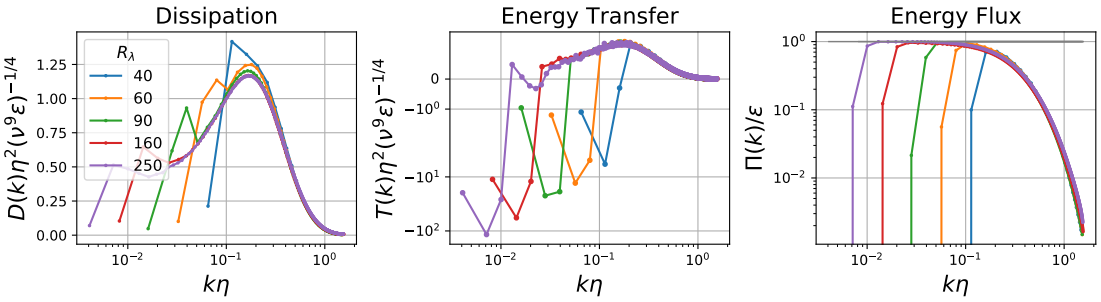

FIGURE *A.1 – Averaged spectra of dissipation, energy transfer function and energy flux from numerical simulations at various Reynolds numbers.*

To complete the spectra of kinetic energy shown in Fig. 3.1, this Appendix provides the spectra of dissipation, nonlinear energy transfer, and energy flux (Fig A.1). The parameters of the simulations are detailed in Table 3.1 (p. 48).

Spectral dissipation. The spectra of $\hat{D}$ is computed as:

$$\hat{D}(\vec{\mathbf{k}}) = 2\nu k^2 E_{kin}(\vec{\mathbf{k}}), \tag{A.1}$$

where ν is the kinematic viscosity and E_{kin} is the kinetic energy spectrum. Note that the use of vertical scaling $(\eta^2\nu^9\epsilon)^{-1/4}$ and horizontal scaling η makes the curves at various Reynolds numbers collapse at wavenumbers beyond the forcing range. The maximum of dissipation occurs in the vicinity of $k\eta \approx 0.2$. The summation of the spectral dissipation

over all Fourier modes gives the total dissipation rate in the flow so that $\epsilon = \sum_{\vec{\mathbf{k}}} \hat{D}(\vec{\mathbf{k}})$. These results are in agreement with previous DNS studies (Wang et al., 1996 ; P. K. Yeung and Zhou, 1997 ; Ishihara et al., 2003).

Spectral energy transfer function. The energy transfer function $\hat{\mathcal{T}}$ is computed as:

$$\hat{\mathcal{T}}(\vec{\mathbf{k}}) = -\left\langle \mathrm{Re}\left[\hat{N}_j(\vec{\mathbf{k}},t)\hat{u}_j^*(\vec{\mathbf{k}},t)\right]\right\rangle, \tag{A.2}$$

where $\hat{N}_j(\vec{\mathbf{k}},t) = ik_i \sum_{k'} \hat{u}_j(\vec{\mathbf{k}}',t)\hat{u}_i(\vec{\mathbf{k}}-\vec{\mathbf{k}}',t) = \mathrm{FT}[(u_i\partial_i)u_j + \nabla p](\vec{\mathbf{k}},t)$ - Fourier transform of the advection and pressure gradient terms. The averaging is performed in spectral space over spherical shells and in time over all iterations in simulation. The energy transfer function gives the amount of energy that a Fourier mode $\vec{\mathbf{k}}$ receives from all other modes in the system. For the modes belonging to the forcing range, the energy transfer function is negative, because these modes only send energy to smaller-scale modes through nonlinear interactions and do not receive any energy. In the present study, it has been checked that the total sum of energy transfers $\sum_{\vec{\mathbf{k}}} \hat{\mathcal{T}}(\vec{\mathbf{k}}) \approx 0$, which is expected since the nonlinear interactions neither add nor drain energy from the system, they only redistribute the energy between scales.

In addition, for the modes outside the forcing range, the energy transfer $\hat{\mathcal{T}}(\vec{\mathbf{k}})$ becomes equal to the spectral dissipation $\hat{D}(\vec{\mathbf{k}})$. It expresses the balance between these two terms of the energy transfer relation (3.10), which is expected in the case of stationary flow. These results are also coherent with other numerical studies (Domaradzki and Rogallo, 1990 ; Aoyama et al., 2005).

Spectral energy flux. The spectral energy flux at a wavenumber k is computed as a sum of the energy transfer function over smaller wavenumbers:

$$\Pi(k) = \sum_{|\vec{\mathbf{k}}'|\leq k} \hat{\mathcal{T}}(\vec{\mathbf{k}}') \tag{A.3}$$

The function $\Pi(k)$ gives the flux of energy passing through the scale k from large scales to the smaller ones. According to K41 theory, for scales which are far enough from both forcing and dissipation scales, the energy flux is constant and approaches the total average dissipation rate ϵ (Frisch, 1995), which in the case of stationary flow is also equal to the forcing power input. That is to say that in the inertial range, relation $\Pi(\vec{\mathbf{k}})/\epsilon \approx 1$, which is indeed observed in DNS, as it can be seen from the last plot of Fig. A.1. In this way, the spectral energy flux allows to estimate the width of the inertial range in each simulation. One can see that the inertial range becomes more pronounced with increasing Reynolds number. At the highest $R_\lambda = 240$, the inertial range extends approximately over one decade.

B

Shell-to-shell energy transfers and filtering threshold

This appendix describes the shell-to-shell energy transfer function and the numerical algorithm of its computation. The matrices of shell-to-shell energy transfers obtained from DNS and their interpretation are provided. These matrices give a more detailed picture of the energy cascade and allow to evaluate, in particular, the influence of the forcing modes on the energy transfer. These considerations served for establishing the threshold wavenumber for the small-scale filter in this thesis.

B.1 Numerical method of computation of shell-to-shell energy transfers

This appendix provides a schematic description of the method of computation of shell-to-shell energy transfers in DNS. It is described and discussed in detail in the book of Verma, 2019. Here only the principal steps are listed. The starting point of the derivation of shell-to-shell energy transfer is the equation of variation of the kinetic energy of a single Fourier mode of velocity, also known as the energy transfer relation (Frisch, 1995):

$$\partial_t \hat{E}(\vec{\mathbf{k}},t) = \underbrace{-\mathrm{Re}\left\langle \hat{N}_j(\vec{\mathbf{k}},t)\hat{u_j}^*(\vec{\mathbf{k}},t)\right\rangle}_{\hat{\mathcal{T}}-\text{energy transfer}} \underbrace{-2\nu k^2 \hat{E}(\vec{\mathbf{k}},t)}_{\hat{D}-\text{dissipation}} + \underbrace{\left\langle \hat{f}_j(\vec{\mathbf{k}},t)\hat{u_j}^*(\vec{\mathbf{k}},t)\right\rangle}_{\hat{P}-\text{forcing power}}. \tag{B.1}$$

The energy transfer can be developed as:

$$\hat{\mathcal{T}}(\vec{\mathbf{k}},t) = -\mathrm{Re}\left\langle \hat{N}_j(\vec{\mathbf{k}},t)\hat{u}_j^*(\vec{\mathbf{k}},t)\right\rangle = -\mathrm{Re}\left\langle \hat{u}_j^*(\vec{\mathbf{k}},t)\; ik_l \sum_{k'} \hat{u}_j(\vec{\mathbf{k}'},t)\hat{u}_l(\vec{\mathbf{k}}-\vec{\mathbf{k}'},t)\right\rangle. \tag{B.2}$$

The energy transfer function $\hat{\mathcal{T}}(\vec{\mathbf{k}},t)$ corresponds to the energy that all other Fourier modes transfer to the mode with wavevector $\vec{\mathbf{k}}$.

To get the energy transfer function related to a single spectral shell, the shell filter is introduced (see Fig. B.1).

$$\hat{u}_i^A(\vec{\mathbf{k}}', t) = \begin{cases} \hat{u}_i(\vec{\mathbf{k}}', t), & \text{if } \vec{\mathbf{k}}' \in \text{shell A}, \\ 0, & \text{otherwise.} \end{cases} \tag{B.3}$$

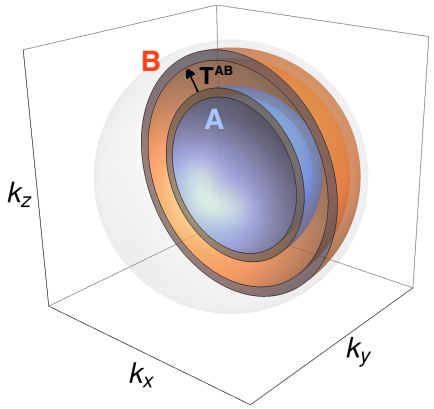

FIGURE *B.1 – Schematic representation of the spectral shells.*

Then, one can deduce that the total amount of energy transfers that all modes of shell B receive from all modes of the shell A has the following expression:

$$\begin{aligned} \hat{T}^{AB}(\vec{\mathbf{k}}, t) &= -\mathrm{Re}\left\langle \sum_{k\in B} i k_l \hat{u}_j{}^*(\vec{\mathbf{k}}, t) \sum_{k'\in A} \hat{u}_j{}^A(\vec{\mathbf{k}}', t) \hat{u}_l(\vec{\mathbf{k}} - \vec{\mathbf{k}}', t) \right\rangle \\ &= -\mathrm{Re}\left\langle \sum_{k\in B} \hat{u}_j{}^*(\vec{\mathbf{k}}, t)\ \mathrm{FT}\ \underbrace{\left[(u_l\partial_l)u_j^A\right]}_{\text{in physical space}}\ (\vec{\mathbf{k}}, t) \right\rangle. \end{aligned} \tag{B.4}$$

Therefore, to compute the matrix of shell-to-shell energy transfers, one needs to perform the following steps:

1. Apply the spectral shell filtering to the velocity field $\hat{u}_i(\vec{\mathbf{k}}', t)$ over the shell A.
2. Compute the advection term $N_j^A = (u_l\partial_l)u_j^A$ in the physical space. Note that only the advected velocity field is filtered, the advecting velocity field is not.
3. Compute the Fourier transform of the filtered advection term N^A.
4. Compute the local product of the filtered advection $\hat{N}_j^A$ with the velocity field $\hat{u}_j$ in the spectral space .
5. Average the resulting product in space over spectral shells, which is also equivalent to applying filtering over shell B (each spectral shell is an individual shell B).
6. Repeat the same for other shells A.

B.2 Results of DNS

The resulting averaged-in-time matrices of shell-to-shell energy transfers are presented in Fig. B.2. It is noticeable that most of the energy transfers are concentrated along the diagonal of the matrix, which indicates the dominance of the local energy exchanges, or

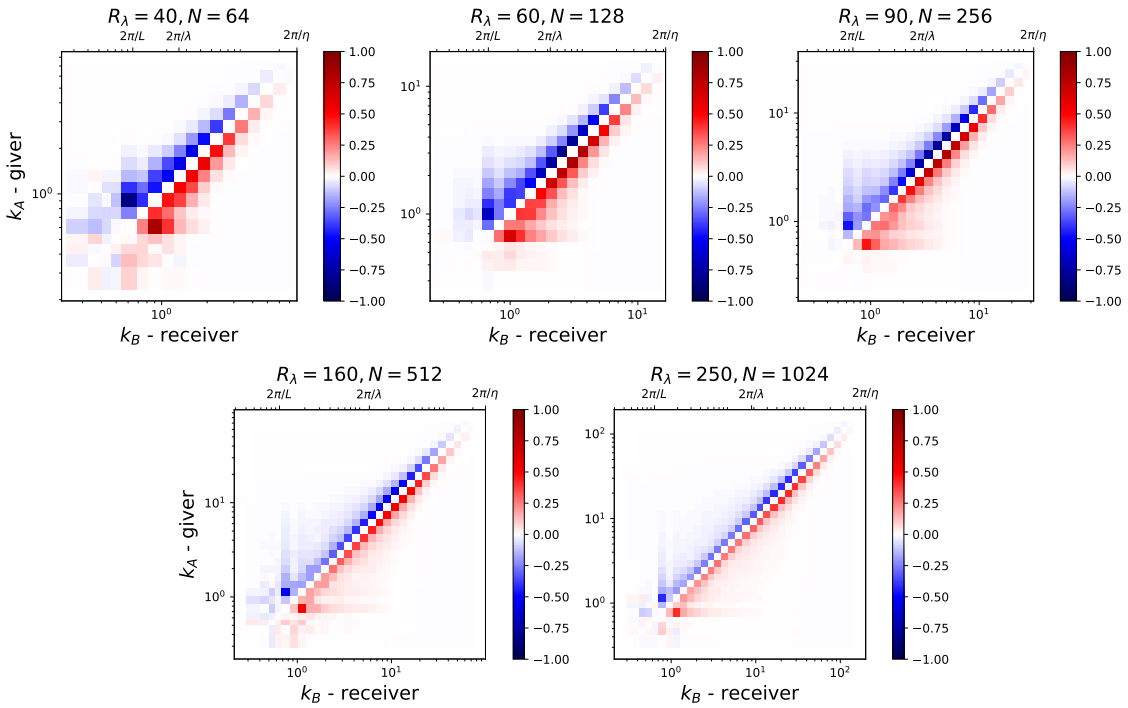

FIGURE *B.2 – Matrices representing shell-to-shell energy transfers for various Reynolds number. The abscissa corresponds to the wavenumber of the receiving mode in the transfer; the ordinate corresponds to the wavenumber of the giving mode.*

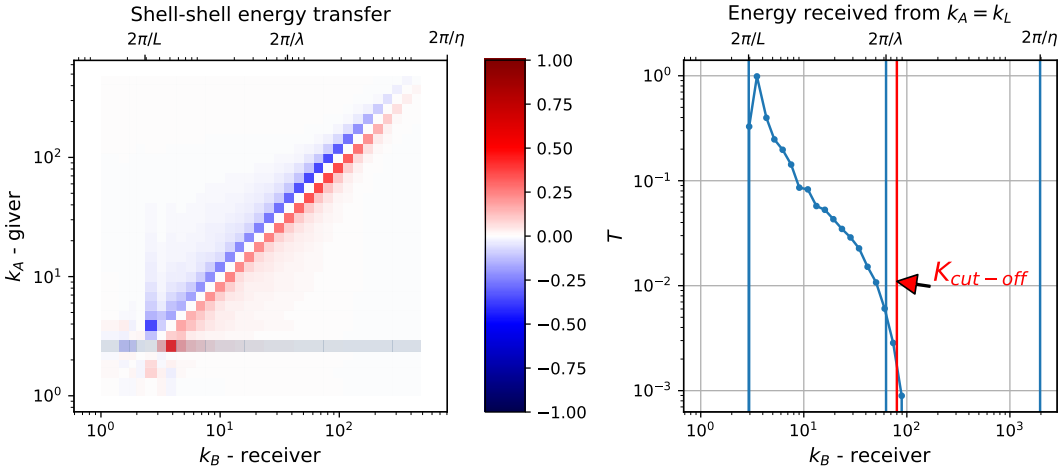

FIGURE *B.3 – Choice of the filter cut-off wavenumber from shell-to-shell energy transfer matrix. The highlighted line on the left corresponds to the energy transfers where the forcing shell is a giver. The plot on the right corresponds to the highlighted line and displays the dependence of the energy transfer between the forcing shell and a shell characterized by the wavenumber k_B. The blue vertical lines on the right plot correspond to typical length scales of the flow: the integral scale L, the Taylor scale λ and the Kolmogorov scale η. The red vertical line shows the cut-off wavenumber $K_{cut-off}$ which is chosen from the considerations that the direct energy transfers from the forcing shell becomes negligible.*

in other words, the most intense energy exchanges occur between the neighboring shells, which is the signature of the turbulent energy cascade. The main diagonal is zero (colored in white), indicating that in average the energy exchanges between the modes within a spectral shell balance each other, which is expected in stationary turbulence. The fact that the negative energy exchanges (blue squares) are above the positive ones (red squares) indicates the main direction of the energy cascade: a shell-receiver with index i gets energy from the shell-giver with index $i-1$ (red square) and sends energy to the shell $i+1$ (blue square). It shows that the energy cascade is direct, meaning that the energy is cascading from large scales to the small ones.

These results are consistent with the matrices of shell-to-shell energy transfers provided in the book of Verma, 2019. This method provides a clear visualization of the energy cascade in turbulence. As one can see from Fig. B.2, the cascade becomes more pronounced at higher Reynolds numbers.

Another important feature that these matrices make clear: at small wavenumbers close to the forcing wavenumber k_f there are non-diagonal cells with non-zero energy transfer. It means that the modes in the shell containing the forcing range interact directly with several following shells, not only with the neighboring ones. In other words, there is a range of shells, whose Fourier modes receive the kinetic energy not only through the turbulent cascade (diagonal lines in the plots), but also through direct interactions with the forcing modes (straight lines in the plots).

B.3 Choice of the filtering wavenumber

The matrices of the shell-to-shell energy transfers allow to evaluate the contribution of the direct, not-cascade energy transfers from the forcing range to a certain shell B (see Fig. B.3). The most useful application of this plot is that it allows to find a minimal wavenumber, at which these direct interactions with the forcing modes become negligible, and the turbulent cascade becomes the main mechanism of the energy transfer from large scales to small ones. In other words, it serves to estimate the range of wavenumbers which are not affected directly by the forcing, and thus which are expected to exhibit universal behavior. This approach was used to find the filtering wavenumber K_c for computing the filtered velocity-advection correlation function in section 3.3.

C

Filtered advection-velocity correlation

This appendix provides Navier-Stokes equations written for the small-scale filtered velocity field in physical and in spectral spaces. It also contains the full expressions for the energy transfer of filtered fields and their interpretation. The numerical results for different terms of the decomposition of the spectral energy transfer function and of the advection-velocity correlation function are provided.

C.1 Scale decomposition and Navier-Stokes equation

In physical space

Navier-Stokes equations in the physical space read as:

$$\partial_t u_i + (u_j \partial_j) u_i = -\partial_i p + \nu \nabla^2 u_i + f_i. \tag{C.1}$$

One can decomposition of the physical velocity field into large-scale and small-scale parts (following the idea from the book of Frisch, 1995, section 2.4) :

$$u_i(\vec{x}, t) = u_i^L(\vec{x}, t) + u_i^S(\vec{x}, t), \tag{C.2}$$

where the components can be determined with the use of the sharp spectral filter:

$$\hat{u}_i^L(\vec{\mathbf{k}}, t) = \begin{cases} \hat{u}_i(\vec{\mathbf{k}}, t), & \text{if } \left|\vec{\mathbf{k}}\right| < K_{cut-off} \\ 0, & \text{if } \left|\vec{\mathbf{k}}\right| \geq K_{cut-off} \end{cases}; \quad \hat{u}_i^S(\vec{\mathbf{k}}, t) = \begin{cases} 0, & \text{if } \left|\vec{\mathbf{k}}\right| < K_{cut-off} \\ \hat{u}_i(\vec{\mathbf{k}}, t), & \text{if } \left|\vec{\mathbf{k}}\right| \geq K_{cut-off} \end{cases}. \tag{C.3}$$

A similar decomposition can be performed for the forcing and pressure fields.

The operator $\mathcal{S}$ denotes the operator of small-scale pass filter : $\mathcal{S}[u_i] = u_i^S$. The application of the operator $\mathcal{S}$ to the NS equation gives (assuming that there is no forcing at

small scales):

$$\partial_t u_i^S + \mathcal{S}[(u_j^L + u_j^S)\partial_j(u_i^L + u_i^S)] = -\partial_i p^S + \nu\nabla^2 u_i^S + \cancel{f_i^S}. \tag{C.4}$$

One can multiply both sides of the equation by u_i^S. Then it is not necessary anymore to put the operator $\mathcal{S}$ in front of the advection term, since the multiplication by u_i^S implies also filtering. One obtains:

$$\partial_t \frac{|u^S|^2}{2} + u_i^S[(u_j^L + u_j^S)\partial_j(u_i^L + u_i^S)] = -u_i^S\partial_i p^S + \nu u_i^S\nabla^2 u_i^S. \tag{C.5}$$

As the next step, one can apply the operator of averaging over the periodic box, which will be denoted as $\langle ... \rangle$. The periodicity implies that $\langle \partial_i f \rangle = 0$ and $\langle (\partial_i f)g \rangle = \langle f\partial_i g \rangle$ for any f, g.

$$\partial_t \left\langle \frac{|u^S|^2}{2} \right\rangle + \underbrace{\left\langle u_i^S[(u_j^L + u_j^S)\partial_j(u_i^L + u_i^S)] \right\rangle}_{-\mathcal{T}^S} = -\left\langle u_i^S\partial_i p^S \right\rangle + \nu \left\langle u_i^S\nabla^2 u_i^S \right\rangle. \tag{C.6}$$

The term containing pressure vanishes on average due to the incompressibility condition. The energy transfer term can be developed into four terms:

$$\begin{aligned}\mathcal{T}^S &= -\left\langle u_i^S[(u_j^L + u_j^S)\partial_j(u_i^L + u_i^S)] \right\rangle = \\ &= -\left[\left\langle u_i^S u_j^L(\partial_j u_i^L) \right\rangle + \left\langle u_i^S u_j^S(\partial_j u_i^L) \right\rangle + \left\langle u_i^S u_j^L(\partial_j u_i^S) \right\rangle + \left\langle u_i^S u_j^S(\partial_j u_i^S) \right\rangle \right].\end{aligned} \tag{C.7}$$

The last two terms can be simplified with the use of the properties of the averaging operator:

$$\left\langle u_i^S u_j^L(\partial_j u_i^S) \right\rangle = \cancel{\left\langle \partial_j(u_i^S u_j^L u_i^S) \right\rangle} - \left\langle (\partial_j u_i^S) u_j^L u_i^S \right\rangle - \cancel{\left\langle u_i^S(\partial_j u_j^L) u_i^S \right\rangle} \Rightarrow \left\langle u_i^S u_j^L(\partial_j u_i^S) \right\rangle = 0.$$

$$\left\langle u_i^S u_j^S(\partial_j u_i^S) \right\rangle = \cancel{\left\langle \partial_j(u_i^S u_j^S u_i^S) \right\rangle} - \left\langle (\partial_j u_i^S) u_j^S u_i^S \right\rangle - \cancel{\left\langle u_i^S(\partial_j u_j^S) u_i^S \right\rangle} \Rightarrow \left\langle u_i^S u_j^S(\partial_j u_i^S) \right\rangle = 0.$$

The vanishing term $\left\langle u_i^S u_j^L(\partial_j u_i^S) \right\rangle$ means that the process of advection of small-scale velocity fields u^S by the large-scale field u_L does not change the average (or total over the box) energy of the small-scale motions. The vanishing term $\left\langle u_i^S u_j^S(\partial_j u_i^S) \right\rangle$ means that the internal energy exchanges between the small scales are in total zero.

The remaining non-zero terms of the average energy transfer can be written as:

$$\mathcal{T}^S = -\left\langle u_i^S u_j^L(\partial_j u_i^L) \right\rangle - \left\langle u_i^S u_j^S(\partial_j u_i^L) \right\rangle = -\left\langle u_i^S u_j(\partial_j u_i^L) \right\rangle. \tag{C.8}$$

This expression signifies that the average non-zero energy transfer towards small scales occurs only due to interactions with the large scale motions. This picture is rather simple and intuitively clear, and it will guide the interpretation in the spectral space.

In spectral space

Equation (C.4) can be rewritten in Fourier space:

$$\partial_t \hat{u}_i^S(\vec{\mathbf{k}}, t) + \mathrm{FT}\left[\mathcal{S}[(u_j^L + u_j^S)\partial_j(u_i^L + u_i^S)]\right](\vec{\mathbf{k}}, t) = -ik_i\hat{p}^S(\vec{\mathbf{k}}, t) - \nu k^2 \hat{u}_i^S(\vec{\mathbf{k}}, t). \tag{C.9}$$

Multiplying both sides of this equation by the velocity field $[\hat{u}_i^S]^*(\vec{\mathbf{k}}, t_0)$ gives:

$$\begin{aligned}[\hat{u}_i^S]^*(\vec{\mathbf{k}}, t_0)\partial_t \hat{u}_i^S(\vec{\mathbf{k}}, t) + [\hat{u}_i^S]^*(\vec{\mathbf{k}}, t_0)\ \mathrm{FT}[(u_j^L + u_j^S)\partial_j(u_i^L + u_i^S)](\vec{\mathbf{k}}, t) = \\ = \cancel{-ik_i\hat{p}^S(\vec{\mathbf{k}}, t)[\hat{u}_i^S]^*(\vec{\mathbf{k}}, t_0)} - \nu k^2 \hat{u}_i^S(\vec{\mathbf{k}}, t)[\hat{u}_i^S]^*(\vec{\mathbf{k}}, t_0).\end{aligned} \tag{C.10}$$

The second term in the left-hand side of this equation represents the energy transfer function for small-scale modes. One can see that it consists of four terms, which actually are the decomposition terms $\hat{T}$ introduced in the main text in Eq. 3.16. Following the notations proposed in the book of of Verma, 2019 for energy transfers, the first superscript of $\hat{T}^{XYZ}$ is related to the receiver mode, the intermediate superscript denotes the mediator mode, and the last superscript is related to the giver mode. The complete definitions of the decomposition terms are:

— $\hat{T}^{SSS}(\vec{\mathbf{k}}, t, t_0)$ - energy transfer with participation of only small-scale modes.

$$\begin{aligned}\hat{T}^{SSS}(\vec{\mathbf{k}}, t, t_0) &= \left\langle -[\hat{u}_i^S]^*(\vec{\mathbf{k}}, t_0)\ \mathrm{FT}[u_j^S \partial_j u_i^S](\vec{\mathbf{k}}, t) \right\rangle \\ &= \left\langle -ik_j[\hat{u}_i^S]^*(\vec{\mathbf{k}}, t_0) \sum_{\vec{\mathbf{k}}'} \hat{u}_j^S(\vec{\mathbf{k}} - \vec{\mathbf{k}}', t)\hat{u}_i^S(\vec{\mathbf{k}}', t) \right\rangle \\ = \left\langle -ik_j[\hat{u}_i^S]^*(\vec{\mathbf{k}}, t_0) \sum_{\substack{|k'| \geq K_c \\ |\vec{\mathbf{k}} - \vec{\mathbf{k}}'| \geq K_c}} \hat{u}_j(\vec{\mathbf{k}} - \vec{\mathbf{k}}', t)\hat{u}_i(\vec{\mathbf{k}}', t) \right\rangle, &\qquad \text{for} \left|\vec{\mathbf{k}}\right| \geq K_{cut-off}.\end{aligned} \tag{C.11}$$

From the previous consideration in the physical space, it is already known that at $t = t_0$ the average over the periodic box nullifies the term $\sum_k \hat{T}^{SSS}(\vec{\mathbf{k}}, t_0, t_0) = 0$.

— $\hat{T}^{SLS}(\vec{\mathbf{k}}, t, t_0)$ - energy transfers between two small-scale modes with a large-scale advecting mode.

$$\begin{aligned}\hat{T}^{SLS}(\vec{\mathbf{k}}, t, t_0) &= -\left\langle [\hat{u}_i^S]^*(\vec{\mathbf{k}}, t_0)\ \mathrm{FT}[u_j^L \partial_j u_i^S](\vec{\mathbf{k}}, t) \right\rangle \\ &= -\left\langle ik_j[\hat{u}_i^S]^*(\vec{\mathbf{k}}, t_0) \sum_{k'} \hat{u}_j^L(\vec{\mathbf{k}} - \vec{\mathbf{k}}', t)\hat{u}_i^S(\vec{\mathbf{k}}', t) \right\rangle \\ = -\left\langle ik_j[\hat{u}_i^S]^*(\vec{\mathbf{k}}, t_0) \sum_{\substack{|k'| \geq K_c \\ |\vec{\mathbf{k}} - \vec{\mathbf{k}}'| < K_c}} \hat{u}_j(\vec{\mathbf{k}} - \vec{\mathbf{k}}', t)\hat{u}_i(\vec{\mathbf{k}}', t) \right\rangle, &\qquad \text{for} \left|\vec{\mathbf{k}}\right| \geq K_{cut-off}.\end{aligned} \tag{C.12}$$

The average of this term over the periodic box is also zero: $\sum_k \hat{T}^{SLS}(\vec{\mathbf{k}}, t_0, t_0) = 0$, meaning that the advection (or sweeping) of small scales by large scales does not change the total energy of small-scale field. It should be also noted that if one writes the same equation for the large-scale velocity field $\hat{u}_i^L$, it does not contain explicitly the term $\hat{T}^{SLS}$, which means that the large scales do not lose nor gain energy directly in this type of interaction, the large-scale mode acts only as a mediator in the energy exchange between two small-scale modes, with:

— $\hat{T}^{SL}(\vec{\mathbf{k}}, t, t_0) = \hat{T}^{SSL}(\vec{\mathbf{k}}, t, t_0) + \hat{T}^{SLL}(\vec{\mathbf{k}}, t, t_0)$ - energy transfers between the small and large scales.

$$\begin{aligned}\hat{T}^{SSL}(\vec{\mathbf{k}}, t, t_0) &= -\left\langle [\hat{u}_i^S]^*(\vec{\mathbf{k}}, t_0)\ \mathrm{FT}[u_j^S \partial_j u_i^L](\vec{\mathbf{k}}, t) \right\rangle = \\ &-\left\langle ik_j[\hat{u}_i^S]^*(\vec{\mathbf{k}}, t_0) \sum_{k'} \hat{u}_j^S(\vec{\mathbf{k}} - \vec{\mathbf{k}}', t)\hat{u}_i^L(\vec{\mathbf{k}}', t) \right\rangle = \\ -\left\langle ik_j[\hat{u}_i^S]^*(\vec{\mathbf{k}}, t_0) \sum_{\substack{|k'| < K_c \\ |\vec{\mathbf{k}} - \vec{\mathbf{k}}'| \geq K_c}} \hat{u}_j(\vec{\mathbf{k}} - \vec{\mathbf{k}}', t)\hat{u}_i(\vec{\mathbf{k}}', t) \right\rangle, &\qquad \text{for} \left|\vec{\mathbf{k}}\right| \geq K_{cut-off}.\end{aligned} \tag{C.13}$$

$$\hat{T}^{SLL}(\vec{\mathbf{k}},t,t_0) = -\left\langle [\hat{u}_i^S]^*(\vec{\mathbf{k}},t_0)\ \mathrm{FT}[u_j^L\partial_j u_i^L](\vec{\mathbf{k}},t)\right\rangle = \\ -\left\langle ik_j[\hat{u}_i^S]^*(\vec{\mathbf{k}},t_0)\sum_{k'}\hat{u}_j^L(\vec{\mathbf{k}}-\vec{\mathbf{k}}',t)\hat{u}_i^L(\vec{\mathbf{k}}',t)\right\rangle = \\ -\left\langle ik_j[\hat{u}_i^S]^*(\vec{\mathbf{k}},t_0)\sum_{\substack{|k'|<K_c\\ |\vec{\mathbf{k}}-\vec{\mathbf{k}}'|<K_c}}\hat{u}_j(\vec{\mathbf{k}}-\vec{\mathbf{k}}',t)\hat{u}_i(\vec{\mathbf{k}}',t)\right\rangle, \qquad \text{for}\left|\vec{\mathbf{k}}\right| \geq K_{cut-off}. \quad \text{(C.14)}$$

These terms represent the energy transfer between the small and large scales, the first term combines the energy exchanges with a small-scale mediator, while the second one - with the large-scale mediator. The equation for large scales would contain identical terms with the opposite sign.

Regarding the term $\hat{T}^{SLL}$, it is important to notice that although both velocity fields inside the convolution are large-scale pass filtered (with L superscript), this convolution can have a non-zero contribution to the mode $\vec{\mathbf{k}}$ belonging to the small-scale range. In other words, the convolution over filtered fields can generate a contribution to the modes outside the filter-pass range. Another important feature of this term is that it is exactly zero at $\left|\vec{\mathbf{k}}\right| > 2K_c$, which follows from the triangle inequality: $\left|\vec{\mathbf{k}}\right| = \left|\vec{\mathbf{k}}'+\vec{\mathbf{k}}\right| < \left|\vec{\mathbf{k}}'\right| + \left|\vec{\mathbf{k}}-\vec{\mathbf{k}}'\right| < 2K_c$. It signifies that the influence of this type of energy exchanges vanishes when one considers large wavenumbers which are far enough from the filter cut-off threshold so that $k > 2K_{cut-off}$.

Link with the two-point correlation function. These energy transfer terms can be related to the two-point spatio-temporal correlation function $\hat{C}_2(\vec{\mathbf{k}},t,t_0) = \left\langle \hat{u}_i(\vec{\mathbf{k}},t_0)\hat{u}_i^*(\vec{\mathbf{k}},t)\right\rangle$.

Using the notations introduced above, one can rewrite the equation (C.10) (here and after the superscript S is omitted, but one should keep in mind that it is valid for the small-scale part of the velocity field $\left|\vec{\mathbf{k}}\right| \geq K_c$):

$$\partial_t\hat{C}_2(\vec{\mathbf{k}},t,t_0) = \left[\hat{T}^{SSS}+\hat{T}^{SLS}+\hat{T}^{SSL}+\hat{T}^{SLL}\right](\vec{\mathbf{k}},t,t_0) - \nu k^2\hat{C}_2(\vec{\mathbf{k}},t,t_0) \quad \text{(C.15)}$$

$$\hat{T}^{total} = \hat{T}^{SSS}+\hat{T}^{SLS}+\hat{T}^{SSL}+\hat{T}^{SLL} \quad \text{(C.16)}$$

In the assumption of statistical stationarity, implying that the statistical quantities must depend only on the time difference $\Delta t = t - t_0$, the equation can be rewritten:

$$\left(\partial_{\Delta t}+\nu k^2\right)\hat{C}_2(\vec{\mathbf{k}},\Delta t) = \left[\hat{T}^{SSS}+\hat{T}^{SLS}+\hat{T}^{SSL}+\hat{T}^{SLL}\right](\vec{\mathbf{k}},\Delta t) \quad \text{(C.17)}$$

It should be noticed that the values of individual $\hat{T}$-terms on the right-hand side depend on the choice of the filter cut-off wavenumber K_c, while the two-point correlation function on the left-hand side does not depend on the choice of filter. The change of the filter only leads to a redistribution of the decomposition terms on the right-hand side.

C.2 Numerical results for the filtered velocity-advection correlation function

Energy transfers (zero time lag)

During the simulations, three different energy transfer terms were calculated:

1. $\hat{T}^{total}$ - the total energy transfer without any filter applied, which is equivalent to the sum of all four transfer functions of the right side in the equation (C.17);
2. $\hat{T}^{SS}$ - the energy transfer between the small scales, where the advection field is not filtered, which is equivalent to sum if two terms $\hat{T}^{SS} = \hat{T}^{SSS} + \hat{T}^{SLS}$;
3. $\hat{T}^{SSS}$ - the energy transfer computed with the use of all three fields filtered.

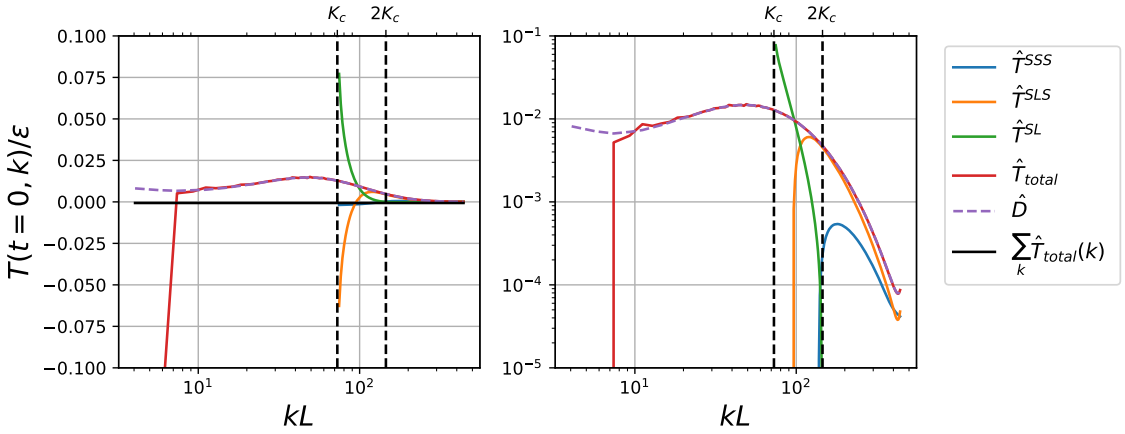

FIGURE *C.1 – Filtered and non-filtered energy transfer functions versus wavenumber k. The curves $\hat{T}^{SSS}, \hat{T}^{SLS}, \hat{T}^{SL}$ denote different filtered energy transfers according to definitions in the Sec. 3.3.2, while $\hat{T}^{total}$ is the total transfer without any filter applied. The curve $\hat{D}$ denotes the dissipation spectrum, the black continuous line gives the sum of the total energy transfer summed over all k, which is zero. The vertical lines show the filter cut-off wavenumber K_c and its doubled value. Left panel: the data in linear y scaling, right panel: the same in the logarithmic, so the zero and negative point are omitted.*

Results for these energy transfers allow to construct data for the other decomposition terms:

— $T^{SL} = \hat{T}^{total} - \hat{T}^{SS}$ - direct energy transfer from large scales to small ones, which would be non-local if we consider wavenumbers far enough from the cut-off filter value $K_{cut-off}$ (in this case, it is impossible distinguish the contributions of $\hat{T}^{SSL}$ and T^{SLL}, but we know that $T^{SLL} = 0$ for $k > 2K_{cut-off}$);

— $\hat{T}^{SLS} = \hat{T}^{SS} - \hat{T}^{SSS}$ - the energy transfer between two small scales with mediation of a large-scale mode.

In general, this type of decomposition does not allow to observe the cascade as clearly as the matrix of energy transfers between spectral shells as it is shown in Appendix B. However, it allows to estimate the contributions from different types of triads to energy transfer. The results presented in this section are obtained from the simulation on the grid of resolution $N^3 = 512^3$, at Taylor Reynolds number $Re_\lambda = 160$ with spectral spatial resolution $k_{max}\eta = 1.5$. The time dependency curves are averaged over 16 time windows. The filtering wavenumber is set at $K_c = 40$ which is close to the wavenumber corresponding to the Taylor length scale (the cut-off wavenumber was chosen with the use of the energy transfer matrix from Fig. B.3: it corresponds to the receiver wavenumber which interacts

negligibly weakly with the forcing modes, which means that the filtered field is free from the direct interactions with the forcing modes - see Appendix B).

Term $\hat{T}^{SLS}$ - "sweeping interactions". From the plot of the energy transfer function in the Fig. C.1 one can conclude that in the dissipation range, most of the energy is transferred by $\hat{T}^{SLS}$ term, meaning that the local energy transfers between small scales with a large-scale mode mediator are dominating, which is in agreement with previous studies (Domaradzki and Rogallo, 1990). It indicated that most of the energy transfers between two small scales occurs through the mediation of a mode of the large-scale velocity field, which advects both small scales.

Term $\hat{T}^{SL}$ - non-local transfers. The term $\hat{T}^{SL}$ denoting the direct energy transfer from the large-scale field towards the small-scale one, appears to be very large close to the cut-off wavenumber K_c, which is clear since in this zone the interaction between the two fields is local. At larger wavenumbers, this term measures non-local direct energy transfers. Note that at $k > K_c$ only one type of triad is involved in this term: $\hat{T}^{SL} = \hat{T}^{SSL}$ (large-scale mode as sender and a small-scale mode as a mediating advecting field). From the spectrum one can see that this term is very small compared to the local transfers $\hat{T}^{SLS}$, and can even become negative, which indicates the presence on a backward energy transfer from small to large scales, also known as backscattering (Piomelli et al., 1991). Apparently, this type of triads was also observed in the numerical simulations in the work of Ohkitani and Kida, 1992. The occurrence of backward non-local energy transfer has been also observed in the work of Domaradzki and Rogallo, 1990, and it is mentioned that this weak inverse energy transfer was also predicted by EDQNM theory.

Term $\hat{T}^{SSS}$ - small-scale-only interactions. The interactions involving the small scales only $\hat{T}^{SSS}$ are also relatively weak. This term is negative close to the cut-off frequency, which results from the fact that part of the local interactions with positive contribution in this zone is filtered out (the modes giving energy to the modes of this part of the spectrum are nullified by the filtering procedure), while the negative contribution due to energy transfer towards the smaller scales stays full. In other words, the disblance in local interactions close to the cut-off wavenumber is due to filtering. At wavenumbers $k > K_c$ the term $\hat{T}^{SSS}$ is positive. At $k > 2K_c$ one can consider that the effects of the filtering become minor.

The term $\hat{T}^{SSS}$ corresponds to a triadic interaction in which all three modes have large wavenumbers, thus, they are the only one possible to compare with the FRG prediction for the three-point correlation function (see section 3.3).

Time-dependent filtered advection-velocity correlation function (non-zero time lag).

Considering the terms of the decomposition (C.16) with a non-zero time lag allows to see the temporal dependence of the terms of the decomposition of $\hat{T}$. The results for the non-filtered $\hat{T}^{total}$ and and small-scale-only tetm $\hat{T}^{SSS}$ are provided in the main text in section 3.3. Here, in Fig. C.2 the examples of behaviors of the remaining two decomposition terms are shown. On the left panel, Fig. C.2a, the time dependence of the decomposition term $\hat{T}^{SL}$ is shown which gathers the contributions of the non-local energy exchanges. One can see that this type of correlation function tends to a symmetrical Gaussian form, but with a negative peak value, which indicates again the presence of the backscattering. On the right panel, Fig. C.2b, the time dependence of the decomposition term $\hat{T}^{SLS}$ is shown, which has the largest contribution to the energy transfer at zero-time lags. As it was mentioned

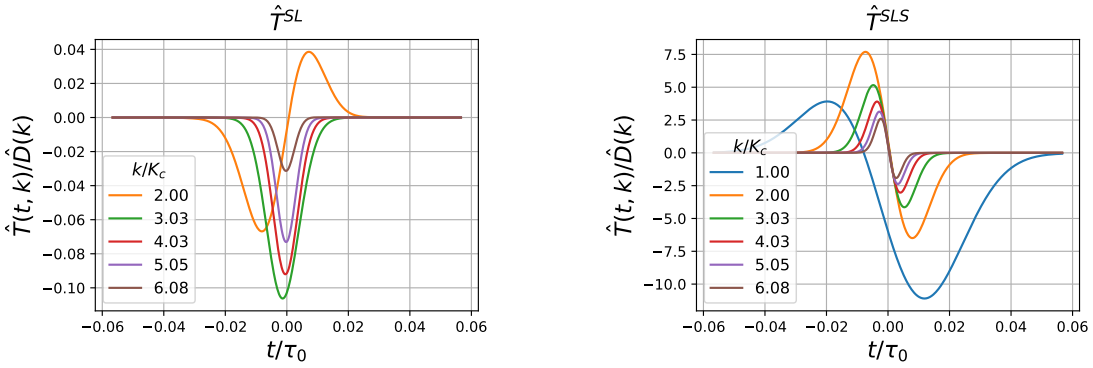

(a) Time dependence of $\hat{T}^{SL}$

(b) Time dependence of $\hat{T}^{SLS}$

FIGURE *C.2 – Time dependence of the filtered advection-velocity correlation functions $\hat{T}^{SLS}, \hat{T}^{SL}$ at various wavenumbers, from the simulation $R_\lambda = 160$, $N = 512$.*

above, these triads contain two small-scale modes, exchanging energy and one large-scale mode which plays the role of the mediator by advecting the two small-scale modes. One can see that the time dependence of this term is non-symmetrical and has clear maximum and minimum values. This result shows that the non-symmetrical temporal behavior of the non-filtered correlation function $\hat{T}^{total}$ (see Fig. 3.8a) is determined by the contribution of the decomposition term $\hat{T}^{SLS}$, and thus, by the sweeping of small scales by slowly varying in space and time large-scale velocity fields.

List of Figures

List of Tables

Bibliography

Adzhemyan, L. T. and N. V. Antonov (1998). "Renormalization Group in Turbulence Theory: Exactly Solvable Heisenberg Model". In: *Theoretical and Mathematical Physics* 115.2, pp. 562–574. DOI: 10.1007/BF02575456.

Adzhemyan, L. T. and S. V. Novikov (2006). "Anomalous Scaling in the Model of Turbulent Advection of a Vector Field". In: *Theoretical and Mathematical Physics* 146.3, pp. 393–410. DOI: 10.1007/s11232-006-0048-y.

Adzhemyan, L. T., N. V. Antonov, and A. N. Vasil'ev (1998). "Renormalization Group, Operator Product Expansion, and Anomalous Scaling in a Model of Advected Passive Scalar". In: *Physical Review E* 58.2, pp. 1823–1835. DOI: 10.1103/PhysRevE.58.1823.

Aluie, H. and G. L. Eyink (2009). "Localness of Energy Cascade in Hydrodynamic Turbulence. II. Sharp Spectral Filter". In: *Physics of Fluids* 21.11, p. 115108. DOI: 10.1063/1.3266948.

Alvelius, K. (1999). "Random Forcing of Three-Dimensional Homogeneous Turbulence". In: *Physics of Fluids* 11.7, pp. 1880–1889. DOI: 10.1063/1.870050.

Aoyama, T., T. Ishihara, Y. Kaneda, M. Yokokawa, K. Itakura, and A. Uno (2005). "Statistics of Energy Transfer in High-Resolution Direct Numerical Simulation of Turbulence in a Periodic Box". In: *Journal of the Physical Society of Japan* 74.12, pp. 3202–3212. DOI: 10.1143/JPSJ.74.3202.

Ballouz, J. G., P. L. Johnson, and N. T. Ouellette (2020). "Temporal Dynamics of the Alignment of the Turbulent Stress and Strain Rate". In: *Physical Review Fluids* 5.11, p. 114606. DOI: 10.1103/PhysRevFluids.5.114606.

Belinicher, V. I. and V. S. L'vov (1987). "A Scale-Invariant Theory of Fully Developed Hydrodynamic Turbulence". In: *Sov. Phys. JETP* 66.2, pp. 303–313.

Benzi, R., L. Biferale, and A. Wirth (1997). "Analytic Calculation of Anomalous Scaling in Random Shell Models for a Passive Scalar". In: *Physical Review Letters* 78.26, pp. 4926–4929. DOI: 10.1103/PhysRevLett.78.4926.

Bershadskii, A. (2008). "Near-Dissipation Range in Nonlocal Turbulence". In: *Physics of Fluids* 20.8, p. 085103. DOI: 10.1063/1.2969473.

— (2016). *Distributed Chaos and Inertial Ranges in Turbulence*. arXiv: 1609.01617 [nlin, physics:physics]. URL: http://arxiv.org/abs/1609.01617 (visited on 05/04/2020).

Biferale, L., G. Boffetta, A. Celani, and F. Toschi (1999). "Multi-Time, Multi-Scale Correlation Functions in Turbulence and in Turbulent Models". In: *Physica D: Nonlinear Phenomena* 127.3, pp. 187–197. DOI: 10.1016/S0167-2789(98)00277-2.

Biferale, L. and A. Wirth (1997). "A Minimal Model for Intermittency of Passive Scalars". In: *Turbulence Modeling and Vortex Dynamics*. Ed. by O. Boratav, A. Eden, and A. Erzan. Lecture Notes in Physics. Berlin, Heidelberg: Springer, pp. 65–73. ISBN: 978-3-540-69119-8. DOI: 10.1007/BFb0105030.

Biferale, L. (2003). "Shell Models of Energy Cascade in Turbulence". In: *Annual Review of Fluid Mechanics* 35.1, pp. 441–468. DOI: 10.1146/annurev.fluid.35.101101.161122.

Biferale, L., E. Calzavarini, and F. Toschi (2011). "Multi-Time Multi-Scale Correlation Functions in Hydrodynamic Turbulence". In: *Physics of Fluids* 23.8, p. 085107. DOI: 10.1063/1.3623466.

Blaizot, J.-P., R. Méndez-Galain, and N. Wschebor (2006). "A New Method to Solve the Non-Perturbative Renormalization Group Equations". In: *Physics Letters B* 632.4, pp. 571–578. DOI: 10.1016/j.physletb.2005.10.086.

Bourgoin, M. et al. (2018). "Investigation of the Small-Scale Statistics of Turbulence in the Modane S1MA Wind Tunnel". In: *CEAS Aeronautical Journal* 9.2, pp. 269–281. DOI: 10.1007/s13272-017-0254-3.

Buaria, D. and K. R. Sreenivasan (2020). *Dissipation Range of the Energy Spectrum in High Reynolds Number Turbulence*. Version 1. arXiv: 2004.06274 [physics]. URL: http://arxiv.org/abs/2004.06274 (visited on 05/04/2020).

Canet, L., B. Delamotte, and N. Wschebor (2015). "Fully Developed Isotropic Turbulence: Symmetries and Exact Identities". In: *Physical Review E* 91.5, p. 053004. DOI: 10.1103/PhysRevE.91.053004.

— (2016). "Fully Developed Isotropic Turbulence: Nonperturbative Renormalization Group Formalism and Fixed-Point Solution". In: *Physical Review E* 93.6, p. 063101. DOI: 10.1103/PhysRevE.93.063101.

Canet, L., V. Rossetto, N. Wschebor, and G. Balarac (2017). "Spatiotemporal Velocity-Velocity Correlation Function in Fully Developed Turbulence". In: *Physical Review E* 95.2, p. 023107. DOI: 10.1103/PhysRevE.95.023107.

Canuto, C., ed. (1988). *Spectral Methods in Fluid Dynamics*. Corr. 3rd print. Springer Series in Computational Physics. Berlin ; New York: Springer-Verlag. 567 pp. ISBN: 978-3-540-52205-8 978-0-387-52205-0.

Chen, S., G. Doolen, J. R. Herring, R. H. Kraichnan, S. A. Orszag, and Z. S. She (1993). "Far-Dissipation Range of Turbulence". In: *Physical Review Letters* 70.20, pp. 3051–3054. DOI: 10.1103/PhysRevLett.70.3051.

Chen, S. and R. H. Kraichnan (1989). "Sweeping Decorrelation in Isotropic Turbulence". In: *Physics of Fluids A: Fluid Dynamics* 1.12, pp. 2019–2024. DOI: 10.1063/1.857475.

— (1998). "Simulations of a Randomly Advected Passive Scalar Field". In: *Physics of Fluids* 10.11, pp. 2867–2884. DOI: 10.1063/1.869808.

Chertkov, M., G. Falkovich, and V. Lebedev (1996). "Nonuniversality of the Scaling Exponents of a Passive Scalar Convected by a Random Flow". In: *Physical Review Letters* 76.20, pp. 3707–3710. DOI: 10.1103/PhysRevLett.76.3707.

Chevillard, L., S. G. Roux, E. Lévêque, N. Mordant, J.-F. Pinton, and A. Arnéodo (2005). "Intermittency of Velocity Time Increments in Turbulence". In: *Physical Review Letters* 95.6, p. 064501. DOI: 10.1103/PhysRevLett.95.064501.

Clark di Leoni, P., P. J. Cobelli, and P. D. Mininni (2015). "The Spatio-Temporal Spectrum of Turbulent Flows". In: *The European Physical Journal E* 38.12, p. 136. DOI: 10.1140/epje/i2015-15136-x.

Corrsin, S. (1951). "On the Spectrum of Isotropic Temperature Fluctuations in an Isotropic Turbulence". In: *Journal of Applied Physics* 22.4, pp. 469–473. DOI: 10.1063/1.1699986.

Daems, D., S. Grossmann, V. S. L'vov, and I. Procaccia (1999). "Continued Fraction Representation of Temporal Multiscaling in Turbulence". In: *Physical Review E* 60.6, pp. 6656–6662. DOI: 10.1103/PhysRevE.60.6656.

Davidson, P. A. (2004). *Turbulence: An Introduction for Scientists and Engineers*. Oxford, UK ; New York: Oxford University Press. 657 pp. ISBN: 978-0-19-852948-4 978-0-19-852949-1.

Debue, P., D. Kuzzay, E.-W. Saw, F. Daviaud, B. Dubrulle, L. Canet, V. Rossetto, and N. Wschebor (2018). "Experimental Test of the Crossover between the Inertial and

the Dissipative Range in a Turbulent Swirling Flow". In: *Physical Review Fluids* 3.2, p. 024602. DOI: 10.1103/PhysRevFluids.3.024602.

DeDominicis, C. (1976). "Technics of Field Renormalization and Dynamics of Critical Phenomena". In: *J Phys (Paris), Colloq.* Techniques de Renormalisation de La Theorie Des Champs et Dynamique Des Phenomenes Critiques 1, pp. C1247–C1253.

DeDominicis, C. and P. C. Martin (1979). "Energy Spectra of Certain Randomly-Stirred Fluids". In: *Physical Review A* 19.1, pp. 419–422. DOI: 10.1103/PhysRevA.19.419.

Delamotte, B. (2012). "An Introduction to the Nonperturbative Renormalization Group". In: *Renormalization Group and Effective Field Theory Approaches to Many-Body Systems*. Ed. by A. Schwenk and J. Polonyi. Lecture Notes in Physics. Berlin, Heidelberg: Springer, pp. 49–132. ISBN: 978-3-642-27320-9. DOI: 10.1007/978-3-642-27320-9_2.

Domaradzki, J. A. (1992). "Nonlocal Triad Interactions and the Dissipation Range of Isotropic Turbulence". In: *Physics of Fluids A: Fluid Dynamics* 4.9, pp. 2037–2045. DOI: 10.1063/1.858373.

Domaradzki, J. A. and R. S. Rogallo (1990). "Local Energy Transfer and Nonlocal Interactions in Homogeneous, Isotropic Turbulence". In: *Physics of Fluids A: Fluid Dynamics* 2.3, pp. 413–426. DOI: 10.1063/1.857736.

Drivas, T. D., P. L. Johnson, C. C. Lalescu, and M. Wilczek (2017). "Large-Scale Sweeping of Small-Scale Eddies in Turbulence: A Filtering Approach". In: *Physical Review Fluids* 2.10, p. 104603. DOI: 10.1103/PhysRevFluids.2.104603.

Dupuis, N., L. Canet, A. Eichhorn, W. Metzner, J. M. Pawlowski, M. Tissier, and N. Wschebor (2021). "The Nonperturbative Functional Renormalization Group and Its Applications". In: *Physics Reports*. DOI: 10.1016/j.physrep.2021.01.001.

Eyink, G. L. (1994). "The Renormalization Group Method in Statistical Hydrodynamics". In: *Physics of Fluids* 6.9, pp. 3063–3078. DOI: 10.1063/1.868131.

— (2000). "Fluctuation-Response Relations for Multitime Correlations". In: *Physical Review E* 62.1, pp. 210–220. DOI: 10.1103/PhysRevE.62.210.

Fairhall, A. L., B. Galanti, V. S. L'vov, and I. Procaccia (1997). "Direct Numerical Simulations of the Kraichnan Model: Scaling Exponents and Fusion Rules". In: *Physical Review Letters* 79.21, pp. 4166–4169. DOI: 10.1103/PhysRevLett.79.4166.

Falkovich, G., K. Gawedzki, and M. Vergassola (2001). "Particles and Fields in Fluid Turbulence". In: *Reviews of Modern Physics* 73.4, pp. 913–975. DOI: 10.1103/RevModPhys.73.913. arXiv: cond-mat/0105199.

Favier, B., F. S. Godeferd, and C. Cambon (2010). "On Space and Time Correlations of Isotropic and Rotating Turbulence". In: *Physics of Fluids* 22.1, p. 015101. DOI: 10.1063/1.3276290.

Ferziger, J. H. and M. Perić (2002). *Computational Methods for Fluid Dynamics*. 3rd, rev. ed. Berlin ; New York: Springer. 423 pp. ISBN: 978-3-540-42074-3.

Foias, C., O. Manley, and L. Sirovich (1990). "Empirical and Stokes Eigenfunctions and the Far-dissipative Turbulent Spectrum". In: *Physics of Fluids A: Fluid Dynamics* 2.3, pp. 464–467. DOI: 10.1063/1.857744.

Fournier, J. .-D. and U. Frisch (1983). "Remarks on the Renormalization Group in Statistical Fluid Dynamics". In: *Physical Review A* 28.2, pp. 1000–1002. DOI: 10.1103/PhysRevA.28.1000.

Frisch, U. and A. Wirth (1996). "Inertial-Diffusive Range for a Passive Scalar Advected by a White-in-Time Velocity Field". In: *Europhysics Letters (EPL)* 35.9, pp. 683–688. DOI: 10.1209/epl/i1996-00170-7.

— (1997). "Intermittency of Passive Scalars in Delta-Correlated Flow: Introduction to Recent Work". In: *Turbulence Modeling and Vortex Dynamics*. Ed. by O. Boratav, A. Eden, and A. Erzan. Vol. 491. Lecture Notes in Physics. Springer Berlin Heidelberg, pp. 53–64. ISBN: 978-3-540-63051-7 978-3-540-69119-8. DOI: 10.1007/BFb0105029.

Frisch, U. (1995). *Turbulence: The Legacy of A. N. Kolmogorov*. Cambridge University Press. 314 pp. ISBN: 978-0-521-45713-2.

Fung, J. C. H., J. C. R. Hunt, N. A. Malik, and R. J. Perkins (1992). "Kinematic Simulation of Homogeneous Turbulence by Unsteady Random Fourier Modes". In: *Journal of Fluid Mechanics* 236, pp. 281–318. DOI: 10.1017/S0022112092001423.

Gkioulekas, E. (2007). "On the Elimination of the Sweeping Interactions from Theories of Hydrodynamic Turbulence". In: *Physica D: Nonlinear Phenomena* 226.2, pp. 151–172. DOI: 10.1016/j.physd.2006.11.012.

Gorbunova, A., G. Balarac, L. Canet, G. Eyink, and V. Rossetto (2021a). "Spatio-Temporal Correlations in Three-Dimensional Homogeneous and Isotropic Turbulence". In: *Physics of Fluids* 33.4, p. 045114. DOI: 10.1063/5.0046677. arXiv: 2102.02858.

Gorbunova, A., G. Balarac, M. Bourgoin, L. Canet, N. Mordant, and V. Rossetto (2020). "Analysis of the Dissipative Range of the Energy Spectrum in Grid Turbulence and in Direct Numerical Simulations". In: *Physical Review Fluids* 5.4, p. 044604. DOI: 10.1103/PhysRevFluids.5.044604.

Gorbunova, A., C. Pagani, G. Balarac, L. Canet, and V. Rossetto (2021b). "Eulerian Spatiotemporal Correlations in Passive Scalar Turbulence". In: *Physical Review Fluids* 6.12, p. 124606. DOI: 10.1103/PhysRevFluids.6.124606.

Gotoh, T. and P. Yeung (2012). "Passive Scalar Transport in Turbulence: A Computational Perspective". In: *Ten Chapters in Turbulence*. Ed. by K. R. Sreenivasan, P. A. Davidson, and Y. Kaneda. Cambridge: Cambridge University Press, pp. 87–131. ISBN: 978-0-521-76944-0. DOI: 10.1017/CBO9781139032810.004.

Gotoh, T., R. S. Rogallo, J. R. Herring, and R. H. Kraichnan (1993). "Lagrangian Velocity Correlations in Homogeneous Isotropic Turbulence". In: *Physics of Fluids A: Fluid Dynamics* 5.11, pp. 2846–2864. DOI: 10.1063/1.858748.

GRICAD (n.d.). URL: https://gricad.univ-grenoble-alpes.fr.

Guo, L., D. Li, X. Zhang, and G.-W. He (2012). "LES Prediction of Space-Time Correlations in Turbulent Shear Flows". In: *Acta Mechanica Sinica* 28.4, pp. 993–998. DOI: 10.1007/s10409-012-0088-5.

Gurvich, A. S. and A. M. Yaglom (1967). "Breakdown of Eddies and Probability Distributions for Small-Scale Turbulence". In: *The Physics of Fluids* 10.9, S59–S65. DOI: 10.1063/1.1762505.

He, G.-W., M. Wang, and S. K. Lele (2004). "On the Computation of Space-Time Correlations by Large-Eddy Simulation". In: *Physics of Fluids* 16.11, pp. 3859–3867. DOI: 10.1063/1.1779251.

He, G.-W. and J.-B. Zhang (2006). "Elliptic Model for Space-Time Correlations in Turbulent Shear Flows". In: *Physical Review E* 73.5, p. 055303. DOI: 10.1103/PhysRevE.73.055303.

He, G., G. Jin, and Y. Yang (2017). "Space-Time Correlations and Dynamic Coupling in Turbulent Flows". In: *Annual Review of Fluid Mechanics* 49.1, pp. 51–70. DOI: 10.1146/annurev-fluid-010816-060309.

He, X. and P. Tong (2011). "Kraichnan's Random Sweeping Hypothesis in Homogeneous Turbulent Convection". In: *Physical Review E* 83.3, p. 037302. DOI: 10.1103/PhysRevE.83.037302.

— (2014). "Space-Time Correlations in Turbulent Rayleigh-Bénard Convection". In: *Acta Mechanica Sinica* 30.4, pp. 457–467. DOI: 10.1007/s10409-014-0068-z.

Heisenberg, W. (1948). "Zur statistischen Theorie der Turbulenz". In: *Zeitschrift für Physik* 124.7, pp. 628–657. DOI: 10.1007/BF01668899.

Ishihara, T., T. Gotoh, and Y. Kaneda (2009). "Study of High–Reynolds Number Isotropic Turbulence by Direct Numerical Simulation". In: *Annual Review of Fluid Mechanics* 41.1, pp. 165–180. DOI: 10.1146/annurev.fluid.010908.165203.

Ishihara, T., Y. Kaneda, M. Yokokawa, K. Itakura, and A. Uno (2003). "Spectra of Energy Dissipation, Enstrophy and Pressure by High-Resolution Direct Numerical Simulations of Turbulence in a Periodic Box". In: *Journal of the Physical Society of Japan* 72.5, pp. 983–986. DOI: 10.1143/JPSJ.72.983.

— (2005). "Energy Spectrum in the Near Dissipation Range of High Resolution Direct Numerical Simulation of Turbulence". In: *Journal of the Physical Society of Japan* 74.5, pp. 1464–1471. DOI: 10.1143/JPSJ.74.1464.

Ishihara, T., K. Morishita, M. Yokokawa, A. Uno, and Y. Kaneda (2016). "Energy Spectrum in High-Resolution Direct Numerical Simulations of Turbulence". In: *Physical Review Fluids* 1.8, p. 082403. DOI: 10.1103/PhysRevFluids.1.082403.

Janssen, H.-K. (1976). "On a Lagrangean for Classical Field Dynamics and Renormalization Group Calculations of Dynamical Critical Properties". In: *Zeitschrift für Physik B Condensed Matter* 23.4, pp. 377–380. DOI: 10.1007/BF01316547.

Jensen, M. H., G. Paladin, and A. Vulpiani (1992). "Shell Model for Turbulent Advection of Passive-Scalar Fields". In: *Physical Review A* 45.10, pp. 7214–7221. DOI: 10.1103/PhysRevA.45.7214.

Jones, E., T. Oliphant, P. Peterson, et al. (2001). *SciPy: Open source scientific tools for Python*. URL: http://www.scipy.org/.

Kadanoff, L., D. Lohse, J. Wang, and R. Benzi (1995). "Scaling and Dissipation in the GOY Shell Model". In: *Physics of Fluids* 7.3, pp. 617–629. DOI: 10.1063/1.868775.

Kaneda, Y. (1993). "Lagrangian and Eulerian Time Correlations in Turbulence". In: *Physics of Fluids A: Fluid Dynamics* 5.11, pp. 2835–2845. DOI: 10.1063/1.858747.

— (2020). "Linear Response Theory of Turbulence". In: *Journal of Statistical Mechanics: Theory and Experiment* 2020.3, p. 034006. DOI: 10.1088/1742-5468/ab6de1.

Kaneda, Y., T. Ishihara, and K. Gotoh (1999). "Taylor Expansions in Powers of Time of Lagrangian and Eulerian Two-Point Two-Time Velocity Correlations in Turbulence". In: *Physics of Fluids* 11.8, pp. 2154–2166. DOI: 10.1063/1.870077.

Khurshid, S., D. A. Donzis, and K. R. Sreenivasan (2018). "Energy Spectrum in the Dissipation Range". In: *Physical Review Fluids* 3.8, p. 082601. DOI: 10.1103/PhysRevFluids.3.082601.

Khurshid, S., D. A. Donzis, and K. R. Sreenivasan (2021). "Slow Spectral Transfer and Energy Cascades in Isotropic Turbulence". In: *Journal of Fluid Mechanics* 908. DOI: 10.1017/jfm.2020.862.

Kit, E., H. J. S. Fernando, and J. A. Brown (1995). "Experimental Examination of Eulerian Frequency Spectra in Zero-mean-shear Turbulence". In: *Physics of Fluids* 7.5, pp. 1168–1170. DOI: 10.1063/1.868560.

Kolmogorov, A. (1941). "The Local Structure of Turbulence in Incompressible Viscous Fluid for Very Large Reynolds' Numbers". In: *Akademiia Nauk SSSR Doklady* 30, pp. 301–305. URL: http://adsabs.harvard.edu/abs/1941DoSSR..30..301K (visited on 07/05/2021).

Kraichnan, R. H. (1959). "The Structure of Isotropic Turbulence at Very High Reynolds Numbers". In: *Journal of Fluid Mechanics* 5.4, pp. 497–543. DOI: 10.1017/S0022112059000362.

— (1964a). "Kolmogorov's Hypotheses and Eulerian Turbulence Theory". In: *Physics of Fluids* 7.11, p. 1723. DOI: 10.1063/1.2746572.

— (1964b). "Mixed Lagrangian-Eulerian Approach to Turbulent Dispersion". In: *Physics of Fluids* 7.10, p. 1717. DOI: 10.1063/1.1711080.

— (1965). "Lagrangian-History Closure Approximation for Turbulence". In: *The Physics of Fluids* 8.4, pp. 575–598. DOI: 10.1063/1.1761271.

— (1968). "Small-Scale Structure of a Scalar Field Convected by Turbulence". In: *Physics of Fluids* 11.5, p. 945. DOI: 10.1063/1.1692063.

Kraichnan, R. H. (1987). "An Interpretation of the Yakhot–Orszag Turbulence Theory". In: *The Physics of Fluids* 30.8, pp. 2400–2405. DOI: 10.1063/1.866130.

— (1994). "Anomalous Scaling of a Randomly Advected Passive Scalar". In: *Physical Review Letters* 72.7, pp. 1016–1019. DOI: 10.1103/PhysRevLett.72.1016.

Kuczaj, A. K., B. J. Geurts, and W. D. McComb (2006). "Nonlocal Modulation of the Energy Cascade in Broadband-Forced Turbulence". In: *Physical Review E* 74.1, p. 016306. DOI: 10.1103/PhysRevE.74.016306.

Kupiainen, A. and P. Muratore-Ginanneschi (2007). "Scaling, Renormalization and Statistical Conservation Laws in the Kraichnan Model of Turbulent Advection". In: *Journal of Statistical Physics* 126.3, pp. 669–724. DOI: 10.1007/s10955-006-9205-9.

L'vov, V. and I. Procaccia (1996). "Towards a Nonperturbative Theory of Hydrodynamic Turbulence: Fusion Rules, Exact Bridge Relations, and Anomalous Viscous Scaling Functions". In: *Physical Review E* 54.6, pp. 6268–6284. DOI: 10.1103/PhysRevE.54.6268.

L'vov, V. S., E. Podivilov, and I. Procaccia (1997). "Temporal Multiscaling in Hydrodynamic Turbulence". In: *Physical Review E* 55.6, pp. 7030–7035. DOI: 10.1103/PhysRevE.55.7030.

Lagaert, J.-B., G. Balarac, G.-H. Cottet, and P. Bégou (2012). "Particle Method: An Efficient Tool for Direct Numerical Simulations of a High Schmidt Number Passive Scalar in Turbulent Flow". In: *Proceeding of the CTR Summer Program*. Stanford Univ., pp. 167–176.

Lesieur, M. (2008). *Turbulence in Fluids*. 4th ed. Fluid Mechanics and Its Applications. Springer Netherlands. ISBN: 978-1-4020-6434-0. DOI: 10.1007/978-1-4020-6435-7.

Lévêque, E., L. Chevillard, J.-F. Pinton, S. Roux, A. Arnéodo, and N. Mordant (2007). "Lagrangian Intermittencies in Dynamic and Static Turbulent Velocity Fields from Direct Numerical Simulations". In: *Journal of Turbulence* 8, N3. DOI: 10.1080/14685240600990266.

Li, Y., E. Perlman, M. Wan, Y. Yang, C. Meneveau, R. Burns, S. Chen, A. Szalay, and G. Eyink (2008). "A Public Turbulence Database Cluster and Applications to Study Lagrangian Evolution of Velocity Increments in Turbulence". In: *Journal of Turbulence* 9, N31. DOI: 10.1080/14685240802376389.

Liu, H., Y. Jin, N. Tobin, and L. P. Chamorro (2017). "Towards Uncovering the Structure of Power Fluctuations of Wind Farms". In: *Physical Review E* 96.6, p. 063117. DOI: 10.1103/PhysRevE.96.063117.

Lukassen, L. J., R. J. A. M. Stevens, C. Meneveau, and M. Wilczek (2018). "Modeling Space-Time Correlations of Velocity Fluctuations in Wind Farms". In: *Wind Energy* 21.7, pp. 474–487. DOI: 10.1002/we.2172.

Majda, A. J. and P. R. Kramer (1999). "Simplified Models for Turbulent Diffusion: Theory, Numerical Modelling, and Physical Phenomena". In: *Physics Reports* 314.4, pp. 237–574. DOI: 10.1016/S0370-1573(98)00083-0.

Manley, O. P. (1992). "The Dissipation Range Spectrum". In: *Physics of Fluids A: Fluid Dynamics* 4.6, pp. 1320–1321. DOI: 10.1063/1.858408.

Martin, P. C., E. D. Siggia, and H. A. Rose (1973). "Statistical Dynamics of Classical Systems". In: *Physical Review A* 8.1, pp. 423–437. DOI: 10.1103/PhysRevA.8.423.

Martínez, D. O., S. Chen, G. D. Doolen, R. H. Kraichnan, L.-P. Wang, and Y. Zhou (1997). "Energy Spectrum in the Dissipation Range of Fluid Turbulence". In: *Journal of Plasma Physics* 57.1, pp. 195–201. DOI: 10.1017/S0022377896005338.

Matsumoto, T., M. Otsuki, T. Ooshida, and S. Goto (2021). "Correlation Function and Linear Response Function of Homogeneous Isotropic Turbulence in the Eulerian and Lagrangian Coordinates". In: *Journal of Fluid Mechanics* 919. DOI: 10.1017/jfm.2021.357.

Matthaeus, W. H., J. M. Weygand, and S. Dasso (2016). "Ensemble Space-Time Correlation of Plasma Turbulence in the Solar Wind". In: *Physical Review Letters* 116.24, p. 245101. DOI: 10.1103/PhysRevLett.116.245101.

Mazzino, A. (1997). "Effective Correlation Times in Turbulent Scalar Transport". In: *Physical Review E* 56.5, pp. 5500–5510. DOI: 10.1103/PhysRevE.56.5500.

McComb, W. D. and S. R. Yoffe (2017). "A Formal Derivation of the Local Energy Transfer (LET) Theory of Homogeneous Turbulence*". In: *Journal of Physics A: Mathematical and Theoretical* 50.37, p. 375501. DOI: 10.1088/1751-8121/aa8379.

Mejía-Monasterio, C. and P. Muratore-Ginanneschi (2012). "Nonperturbative Renormalization Group Study of the Stochastic Navier-Stokes Equation". In: *Physical Review E* 86.1, p. 016315. DOI: 10.1103/PhysRevE.86.016315.

Mitra, D. and R. Pandit (2005). "Dynamics of Passive-Scalar Turbulence". In: *Physical Review Letters* 95.14, p. 144501. DOI: 10.1103/PhysRevLett.95.144501.

Monin, A. and A. M. Yaglom (2007). *Statistical Fluid Mechanics: Mechanics of Turbulence Volume I*. Courier Corporation. 786 pp. ISBN: 978-0-486-45883-0. Google Books: EtTyyI4_DvIC.

Mordant, N., J. Delour, E. Léveque, A. Arnéodo, and J.-F. Pinton (2002). "Long Time Correlations in Lagrangian Dynamics: A Key to Intermittency in Turbulence". In: *Physical Review Letters* 89.25, p. 254502. DOI: 10.1103/PhysRevLett.89.254502.

Nelkin, M. and M. Tabor (1990). "Time Correlations and Random Sweeping in Isotropic Turbulence". In: *Physics of Fluids A: Fluid Dynamics* 2.1, pp. 81–83. DOI: 10.1063/1.857684.

Novikov, E. A. (1961). "Energy spectrum of an incompressible fluid in turblent flow". In: *Dokl. Akad. Nauk SSSR* 139.2, pp. 331–334.

O'Gorman, P. A. and D. I. Pullin (2004). "On Modal Time Correlations of Turbulent Velocity and Scalar Fields". In: *Journal of Turbulence* 5, N35. DOI: 10.1088/1468-5248/5/1/035.

Obukhov, A. M. (1949). "Structure of Temperature Field in Turbulent Flow". In: *Izv. Akad. Nauk S.S.S.R., Ser. Geogr. and Geophys.* 13.1, pp. 58–69.

Ohkitani, K. and S. Kida (1992). "Triad Interactions in a Forced Turbulence". In: *Physics of Fluids A: Fluid Dynamics* 4.4, pp. 794–802. DOI: 10.1063/1.858296.

Orszag, S. A. (1971). "Numerical Simulation of Incompressible Flows Within Simple Boundaries. I. Galerkin (Spectral) Representations". In: *Studies in Applied Mathematics* 50.4, pp. 293–327. DOI: 10.1002/sapm1971504293.

Orszag, S. A. and G. S. Patterson (1972). "Numerical Simulation of Three-Dimensional Homogeneous Isotropic Turbulence". In: *Physical Review Letters* 28.2, pp. 76–79. DOI: 10.1103/PhysRevLett.28.76.

Pagani, C. (2015). "Functional Renormalization Group Approach to the Kraichnan Model". In: *Physical Review E* 92.3, p. 033016. DOI: 10.1103/PhysRevE.92.033016.

Pagani, C. and L. Canet (2021). "Spatio-Temporal Correlation Functions in Scalar Turbulence from Functional Renormalization Group". In: *Physics of Fluids* 33.6, p. 065109. DOI: 10.1063/5.0050515. arXiv: 2103.07326.

Pandit, R., S. S. Ray, and D. Mitra (2008). "Dynamic Multiscaling in Turbulence". In: *The European Physical Journal B* 64.3 (3), pp. 463–469. DOI: 10.1140/epjb/e2008-00048-6.

Pao, Y.-H. (1965). "Structure of Turbulent Velocity and Scalar Fields at Large Wavenumbers". In: *The Physics of Fluids* 8.6, pp. 1063–1075. DOI: 10.1063/1.1761356.

Perez, J. C. and S. Bourouaine (2020). "Eulerian Space-Time Correlation of Strong Magnetohydrodynamic Turbulence". In: *Physical Review Research* 2.2, p. 023357. DOI: 10.1103/PhysRevResearch.2.023357.

Perschke, C., Y. Narita, U. Motschmann, and K. H. Glassmeier (2016). "Observational Test for a Random Sweeping Model in Solar Wind Turbulence". In: *Physical Review Letters* 116.12, p. 125101. DOI: 10.1103/PhysRevLett.116.125101.

Piomelli, U. and E. Balaras (2002). "Wall-Layer Models for Large-Eddy Simulations". In: *Annual Review of Fluid Mechanics* 34.1, pp. 349–374. DOI: 10.1146/annurev.fluid.34.082901.144919.

Piomelli, U., W. H. Cabot, P. Moin, and S. Lee (1991). "Subgrid-scale Backscatter in Turbulent and Transitional Flows". In: *Physics of Fluids A: Fluid Dynamics* 3.7, pp. 1766–1771. DOI: 10.1063/1.857956.

Pope, S. B. (2000). *Turbulent Flows*. Cambridge University Press. 810 pp. ISBN: 978-0-521-59886-6.

Poulain, C., N. Mazellier, L. Chevillard, Y. Gagne, and C. Baudet (2006). "Dynamics of Spatial Fourier Modes in Turbulence: Sweeping Effect, Long-Time Correlations and Temporal Intermittency". In: *The European Physical Journal B* 53.2, pp. 219–224. DOI: 10.1140/epjb/e2006-00354-y.

Rogallo, R. S. (1981). *Numerical Experiments in Homogeneous Turbulence*. National Aeronautics and Space Administration. 98 pp. Google Books: 2eRCAQAAIAAJ.

Rubinstein, R. and G.-W. He (2003). "The Eulerian Time Correlation Function in Homogeneous Isotropic Turbulence". In: *Statistical Theories and Computational Approaches to Turbulence*. Ed. by Y. Kaneda and T. Gotoh. Tokyo: Springer Japan, pp. 229–238. ISBN: 978-4-431-67002-5. DOI: 10.1007/978-4-431-67002-5_15.

Saddoughi, S. G. and S. V. Veeravalli (1994). "Local Isotropy in Turbulent Boundary Layers at High Reynolds Number". In: *Journal of Fluid Mechanics* 268, pp. 333–372. DOI: 10.1017/S0022112094001370.

Sanada, T. and V. Shanmugasundaram (1992). "Random Sweeping Effect in Isotropic Numerical Turbulence". In: *Physics of Fluids A: Fluid Dynamics* 4.6, pp. 1245–1250. DOI: 10.1063/1.858242.

Sanada, T. (1992). "Comment on the Dissipation-range Spectrum in Turbulent Flows". In: *Physics of Fluids A: Fluid Dynamics* 4.5, pp. 1086–1087. DOI: 10.1063/1.858263.

Sankar Ray, S., D. Mitra, and R. Pandit (2008). "The Universality of Dynamic Multiscaling in Homogeneous, Isotropic Navier–Stokes and Passive-Scalar Turbulence". In: *New Journal of Physics* 10.3, p. 033003. DOI: 10.1088/1367-2630/10/3/033003.

Sato, Y. and K. Yamamoto (1987). "Lagrangian Measurement of Fluid-Particle Motion in an Isotropic Turbulent Field". In: *Journal of Fluid Mechanics* 175, pp. 183–199. DOI: 10.1017/S0022112087000351.

Schumacher, J. (2007). "Sub-Kolmogorov-Scale Fluctuations in Fluid Turbulence". In: *Europhysics Letters (EPL)* 80.5, p. 54001. DOI: 10.1209/0295-5075/80/54001.

Shraiman, B. I. and E. D. Siggia (2000). "Scalar Turbulence". In: *Nature* 405.6787 (6787), pp. 639–646. DOI: 10.1038/35015000.

Sirovich, L., L. Smith, and V. Yakhot (1994). "Energy Spectrum of Homogeneous and Isotropic Turbulence in Far Dissipation Range". In: *Physical Review Letters* 72.3, pp. 344–347. DOI: 10.1103/PhysRevLett.72.344.

Smith, L. M. and W. C. Reynolds (1991). "The Dissipation-range Spectrum and the Velocity-derivative Skewness in Turbulent Flows". In: *Physics of Fluids A: Fluid Dynamics* 3.5, pp. 992–994. DOI: 10.1063/1.857979.

Smith, L. M. and S. L. Woodruff (1998). "Renormalization-Group Analysis of Turbulence". In: *Annual Review of Fluid Mechanics* 30.1, pp. 275–310. DOI: 10.1146/annurev.fluid.30.1.275.

Sreenivasan, K. R. (1985). "On the Fine-Scale Intermittency of Turbulence". In: *Journal of Fluid Mechanics* 151, pp. 81–103. DOI: 10.1017/S0022112085000878.

Sreenivasan, K. R. (1995). "On the Universality of the Kolmogorov Constant". In: *Physics of Fluids* 7.11, pp. 2778–2784. DOI: 10.1063/1.868656.

— (2019). "Turbulent Mixing: A Perspective". In: *Proceedings of the National Academy of Sciences* 116.37, pp. 18175–18183. DOI: 10.1073/pnas.1800463115. pmid: 30545916.

Stepanov, R., F. Plunian, M. Kessar, and G. Balarac (2014). "Systematic Bias in the Calculation of Spectral Density from a Three-Dimensional Spatial Grid". In: *Physical Review E* 90.5, p. 053309. DOI: 10.1103/PhysRevE.90.053309.

Tarpin, M. (2018). "Non-Perturbative Renormalisation Group Approach to Some out of Equilibrium Systems : Diffusive Epidemic Process and Fully Developped Turbulence". PhD thesis. Université Grenoble Alpes. URL: https://tel.archives-ouvertes.fr/tel-02053156 (visited on 05/05/2020).

Tarpin, M., L. Canet, C. Pagani, and N. Wschebor (2019). "Stationary, Isotropic and Homogeneous Two-Dimensional Turbulence: A First Non-Perturbative Renormalization Group Approach". In: *Journal of Physics A: Mathematical and Theoretical* 52.8, p. 085501. DOI: 10.1088/1751-8121/aaf3f0.

Tarpin, M., L. Canet, and N. Wschebor (2018). "Breaking of Scale Invariance in the Time Dependence of Correlation Functions in Isotropic and Homogeneous Turbulence". In: *Physics of Fluids* 30.5, p. 055102. DOI: 10.1063/1.5020022.

Tatarskii, V. I. (1967). "Depolarization of Light by Turbulent Atmospheric Inhomogeneities". In: *Radiophysics and Quantum Electronics* 10.12, pp. 987–988. DOI: 10.1007/BF01073722.

Täuber, U. C. (2014). *Critical Dynamics: A Field Theory Approach to Equilibrium and Non-Equilibrium Scaling Behavior*. Cambridge: Cambridge University Press. 511 pp. ISBN: 978-0-521-84223-5.

Taylor, G. I. (1922). "Diffusion by Continuous Movements". In: *Proceedings of the London Mathematical Society* s2-20.1, pp. 196–212. DOI: 10.1112/plms/s2-20.1.196.

— (1938). "The Spectrum of Turbulence". In: *Proceedings of the Royal Society A: Mathematical, Physical and Engineering Sciences* 164.919, pp. 476–490. DOI: 10.1098/rspa.1938.0032.

Tennekes, H. (1975). "Eulerian and Lagrangian Time Microscales in Isotropic Turbulence". In: *Journal of Fluid Mechanics* 67.3, pp. 561–567. DOI: 10.1017/S0022112075000468.

Tomassini, P. (1997). "An Exact Renormalization Group Analysis of 3D Well Developed Turbulence". In: *Physics Letters B* 411.1, pp. 117–126. DOI: 10.1016/S0370-2693(97)00980-5.

Townsend, A. A. and G. I. Taylor (1951). "On the Fine-Scale Structure of Turbulence". In: *Proceedings of the Royal Society of London. Series A. Mathematical and Physical Sciences* 208.1095, pp. 534–542. DOI: 10.1098/rspa.1951.0179.

Uberoi, M. S. and S. Wallis (1969). "Spectra of Grid Turbulence". In: *The Physics of Fluids* 12.7, pp. 1355–1358. DOI: 10.1063/1.1692674.

Verma, M. K., A. Kumar, P. Kumar, S. Barman, A. G. Chatterjee, R. Samtaney, and R. A. Stepanov (2018). "Energy Spectra and Fluxes in Dissipation Range of Turbulent and Laminar Flows". In: *Fluid Dynamics* 53.6, pp. 862–873. DOI: 10.1134/S0015462818050166.

Verma, M. K. (2019). *Energy Transfers in Fluid Flows: Multiscale and Spectral Perspectives*. Cambridge University Press. 566 pp. ISBN: 978-1-108-22610-3. Google Books: fcmcDwAAQBAJ.

Verma, M. K., A. Kumar, and A. Gupta (2020). "Hydrodynamic Turbulence: Sweeping Effect and Taylor's Hypothesis via Correlation Function". In: *Transactions of the Indian National Academy of Engineering* 5.4, pp. 649–662. DOI: 10.1007/s41403-020-00161-3.

Wallace, J. M. (2014). "Space-Time Correlations in Turbulent Flow: A Review". In: *Theoretical and Applied Mechanics Letters* 4.2, p. 022003. DOI: 10.1063/2.1402203.

Wang, L.-P., S. Chen, J. G. Brasseur, and J. C. Wyngaard (1996). "Examination of Hypotheses in the Kolmogorov Refined Turbulence Theory through High-Resolution Simulations. Part 1. Velocity Field". In: *Journal of Fluid Mechanics* 309, pp. 113–156. DOI: 10.1017/S0022112096001589.

Warhaft, Z. (2000). "Passive Scalars in Turbulent Flows". In: *Annual Review of Fluid Mechanics* 32.1, pp. 203–240. DOI: 10.1146/annurev.fluid.32.1.203.

Wetterich, C. (1993). "Exact Evolution Equation for the Effective Potential". In: *Physics Letters B* 301.1, pp. 90–94. DOI: 10.1016/0370-2693(93)90726-X.

Wilczek, M. and Y. Narita (2012). "Wave-Number–Frequency Spectrum for Turbulence from a Random Sweeping Hypothesis with Mean Flow". In: *Physical Review E* 86.6, p. 066308. DOI: 10.1103/PhysRevE.86.066308.

Wilczek, M., R. J. A. M. Stevens, and C. Meneveau (2015). "Spatio-Temporal Spectra in the Logarithmic Layer of Wall Turbulence: Large-Eddy Simulations and Simple Models". In: *Journal of Fluid Mechanics* 769. DOI: 10.1017/jfm.2015.116.

Wilczek, M., R. J. A. M. Stevens, Y. Narita, and C. Meneveau (2014). "A Wavenumber-Frequency Spectral Model for Atmospheric Boundary Layers". In: *Journal of Physics: Conference Series* 524.1, p. 012104. DOI: 10.1088/1742-6596/524/1/012104.

Wilson, K. G. and J. Kogut (1974). "The Renormalization Group and the ϵ Expansion". In: *Physics Reports* 12.2, pp. 75–199. DOI: 10.1016/0370-1573(74)90023-4.

Wirth, A. and L. Biferale (1996). "Anomalous Scaling in Random Shell Models for Passive Scalars". In: *Physical Review E* 54.5, pp. 4982–4989. DOI: 10.1103/PhysRevE.54.4982.

Wu, T. and G. He (2021). "Stochastic Dynamical Model for Space-Time Energy Spectra in Turbulent Shear Flows". In: *Physical Review Fluids* 6.5, p. 054602. DOI: 10.1103/PhysRevFluids.6.054602.

Wu, X. (2017). "Inflow Turbulence Generation Methods". In: *Annual Review of Fluid Mechanics* 49.1, pp. 23–49. DOI: 10.1146/annurev-fluid-010816-060322.

Yakhot, V. and S. A. Orszag (1986). "Renormalization Group Analysis of Turbulence. I. Basic Theory". In: *Journal of Scientific Computing* 1.1, pp. 3–51. DOI: 10.1007/BF01061452.

Yakhot, V., S. A. Orszag, and Z.-S. She (1989). "Space-time Correlations in Turbulence: Kinematical versus Dynamical Effects". In: *Physics of Fluids A: Fluid Dynamics* 1.2, pp. 184–186. DOI: 10.1063/1.857486.

Yeung, P. K. and B. L. Sawford (2002). "Random-Sweeping Hypothesis for Passive Scalars in Isotropic Turbulence". In: *Journal of Fluid Mechanics* 459, pp. 129–138. DOI: 10.1017/S0022112002008248.

Yeung, P. K. and Y. Zhou (1997). "Universality of the Kolmogorov Constant in Numerical Simulations of Turbulence". In: *Physical Review E* 56.2, pp. 1746–1752. DOI: 10.1103/PhysRevE.56.1746.

Zhao, X. and G.-W. He (2009). "Space-Time Correlations of Fluctuating Velocities in Turbulent Shear Flows". In: *Physical Review E* 79.4, p. 046316. DOI: 10.1103/PhysRevE.79.046316.

Zhou, Y. (2010). "Renormalization Group Theory for Fluid and Plasma Turbulence". In: *Physics Reports* 488.1, pp. 1–49. DOI: 10.1016/j.physrep.2009.04.004.

— (2021). "Turbulence Theories and Statistical Closure Approaches". In: *Physics Reports*, S0370157321002763. DOI: 10.1016/j.physrep.2021.07.001.

Zhou, Y. and R. Rubinstein (1996). "Sweeping and Straining Effects in Sound Generation by High Reynolds Number Isotropic Turbulence". In: *Physics of Fluids* 8.3, pp. 647–649. DOI: 10.1063/1.868849.

Fonctions de corrélation en turbulence

Simulations numériques et comparaison avec l'analyse par le groupe de renormalisation fonctionnel

Correlation functions in turbulence

Numerical simulations and comparison with the functional renormalization group analysis

Résumé

L'objectif de cette thèse est une comparaison des données de simulations numériques directes (DNS) d'un écoulement turbulent isotrope homogène en trois dimensions avec des prédictions analytiques récentes obtenues au moyen de l'approche du groupe de renormalisation fonctionnel (FRG). Les principaux résultats de la thèse concernent la fonction de corrélation spatio-temporelle de la vitesse, qui devrait décroître comme une fonction gaussienne du temps aux petits décalages et exponentiellement aux grands décalages temporels. Les résultats numériques montrent que la fonction de corrélation à deux points des modes de Fourier de vitesse décroît effectivement comme une gaussienne dans le temps aux petits décalages temporels. Le même comportement est observé pour les corrélations triples de la vitesse, qui peuvent être liées à la fonction de transfert d'énergie spectrale. Cependant, le comportement aux grands décalages temporels est indiscernable en raison des amplitudes faibles des fonctions de corrélation.

Un autre résultat important de la thèse concerne les corrélations spatio-temporelles dans la turbulence du scalaire passif. Les simulations d'une quantité scalaire dans un champ de vitesse gouverné pas l'équation de Navier-Stokes démontrent également une décroissance gaussienne pour la fonction de corrélation du scalaire à de petits décalages, similaire à la corrélation de vitesse. L'influence des corrélations temporelles de vitesse sur le scalaire est étudiée dans des simulations avec des champs de vitesse synthétiques. Dans le cas d'une vitesse aléatoire delta-corrélée en temps (également connue sous le nom de modèle de Kraichnan), les corrélations du scalaire démontrent une décroissance purement exponentielle dans le temps. L'ajout d'un temps de corrélation fini à la vitesse synthétique conduit à l'émergence d'une partie gaussienne à de petits décalages temporels dans la décroissance de la fonction de corrélation scalaire, tandis qu'elle devient exponentielle à des décalages temporels plus grands que le temps de corrélation de vitesse typique. Ces résultats révèlent la transition entre les deux régimes de corrélation temporelle, comme prédit par le FRG.

La dernière partie de la thèse présente une étude préliminaire du modèle en couches de l'advection aléatoire du scalaire passif avec l'utilisation de l'approche FRG. La loi d'échelle normale dans la fonction de structure de second ordre du scalaire est obtenue, et les directions possibles d'études des lois d'échelle anormales sont discutées.

Mots-clés : Mécanique des fluides, Turbulence, Simulations numériques

Abstract

The aim of this thesis is a comparison of the data from direct numerical simulations (DNS) of a three-dimensional homogeneous isotropic turbulent flow with recent analytical predictions obtained by means of the functional renormalization group (FRG) approach. The main results of the thesis concern the spatio-temporal correlation function of velocity, which is expected to decay as a Gaussian function of time at small time lags and as an exponential at large time lags. The numerical results show that the two-point correlation function of the Fourier modes of velocity indeed decays as a Gaussian in time at small time lags. The same behavior is observed for triple velocity correlations, which can be linked to the spectral energy transfer function. However, the behavior at large time delays is indiscernible due to the low-level magnitude of the correlation functions. Another important result of the thesis concerns the spatio-temporal correlations in passive scalar turbulence. The simulations of a scalar in a Navier-Stokes velocity field demonstrate a Gaussian decay as well for the scalar correlation function at small time delays, similar to the velocity correlation. The influence of the velocity temporal correlations on the scalar is studied in simulations with synthetic velocity fields. In the case of a random white-in-time velocity (also known as Kraichnan's model), the scalar correlations demonstrate a purely exponential decay in time. Adding a finite correlation time to the synthetic velocity leads to the emergence of a portion of Gaussian decay at small time lags in the scalar correlation function, while it turns to the exponential at time delays larger than the typical velocity correlation time. These results reveal the crossover between the two temporal correlation regimes, as predicted by the FRG. The last part of the thesis presents a preliminary study of the shell model of random passive scalar advection with the use of the FRG approach. The normal scaling of the second-order scalar structure is obtained, and the possible directions for studying the anomalous scaling are discussed.

Keywords : Fluid mechanics, Turbulence, Numerical simulations